THE USE OF SYNCHROTRON X-RAY MICRO COMPUTED TOMOGRAPHY TO STUDY THE FAILURE MECHANISMS OF THERMAL BARRIER COATINGS

by

DANIAL KHOSHKHOU

A thesis submitted to the

University of Birmingham

for the degree of

DOCTORATE of ENGINEERING

Department of Metallurgy & Materials

College of Engineering and Physical Sciences

University of Birmingham

June 2017

UNIVERSITY OF
BIRMINGHAM

University of Birmingham Research Archive

e-theses repository

This unpublished thesis/dissertation is copyright of the author and/or third parties. The intellectual property rights of the author or third parties in respect of this work are as defined by The Copyright Designs and Patents Act 1988 or as modified by any successor legislation.

Any use made of information contained in this thesis/dissertation must be in accordance with that legislation and must be properly acknowledged. Further distribution or reproduction in any format is prohibited without the permission of the copyright holder.

Abstract

Thermal barrier coatings (TBCs) are used to protect high-pressure stage 1 turbine components in aero engines. At present the full potential high-temperature capabilities of TBCs cannot be utilised due to the difficulties in estimating the remaining useful life of in-service TBCs. State of the art non-destructive techniques, such as photo-luminescent piezospectroscopy (PLPS) have aided in furthering the understanding of damage evolution mechanism techniques, but are limited in applicability at temperature. In this work, a new force-balance model is presented for calculating the growth stress in a thermally grown oxide (TGO) layer at oxidation temperatures. Furthermore, a new experimental technique is explored for observation of the full-field strain distribution using synchrotron X-ray micro-tomography (SX μCT) coupled with digital volume correlation (DVC). The force-balance method relates the creep in bondcoats of precision-machined cylindrical micro-specimens to the stress acted on the bondcoat by the TGO. These precision-machined specimens were volumetrically imaged at the I12 JEEP beamline of Diamond Light Source (DLS) to reveal the three-dimensional evolution of TBC microstructure with time at temperature. The time-dependent volumetric image data acquired at DLS were processed using commercial digital volume correlation code to compute full-field displacement and strain distribution.

Optimus Parentibus

In loving memory of pedar

List of publications

D. Khoshkhou, M. Mostafavi, C. Reinhard, M. P. Taylor, D. S. Rickerby, I. M. Edmonds, H. E. Evans, T. J. Marrow, B. J. Connolly, “Three-dimensional displacement mapping of diffused Pt thermal barrier coatings via synchrotron X-ray computed tomography and digital volume correlation” Scripta Materialia, vol. 115, 1 April 2016, pp. 100–103.

S. Zhao, Z. C. Yang, X. G. Zhou, X. Z. Ling, L. S. Mora, D. Khoshkhou, and T. J. Marrow, “Design, Fabrication, Characterization and Simulation of PIP-SiC/SiC Composites,” Computers, Materials and Continua, vol. 42, no. 2, pp. 103–124, 2014.

L. S. Mora, M. Mostafavi, D. Khoshkhou, C. Reinhard, R. Atwood, S. Zhao, B. J. Connolly, T. J. Marrow, and Z. Shuang, “3D cellular automata finite element (CAFE) modelling and experimental observation of damage in quasi-brittle nuclear materials: Indentation of a SiC-SiC fibre ceramic matrix composite,” in Third International Workshop on Structural Materials for Innovative Nuclear Systems (SMINS-3), 2013, pp. 241–250.

Acknowledgements

My supervisors, Dr. Brian J. Connolly and Professor Hugh E. Evans are extensively thanked for their continued support, wisdom and faith in me. My gratitude is extended to Dr. Mary P. Taylor who has been an invaluable source of knowledge and direction, as has Dr. Christopher Cooper's practical support.

Dr. David S. Rickerby and Dr. Ian M. Edmonds both of Rolls-Royce Plc are kindly acknowledged for the generous provision of high-quality samples and continued interest in this work. Additional thanks are extended to Dr. Rob Jones of Turbine Surface Technologies Limited, Nottingham for insights into coating manufacturing and sample preparation. I would also like to extend my gratitude to Dr. Mahmoud Mostafavi for support during digital volume correlation work at the University of Oxford. My thanks also extend to Professor James Marrow for supporting the collaborative efforts between our two research groups and providing valuable feedback on publications.

The help and advice of the team at Diamond Light Source led by Dr. Michael Drakopoulos is gratefully acknowledged, in particular Dr. Christina Reinhard for support leading up to, during and after our beam-time allocation. For support during beamtime, Mr Matthew Bass and Mr Philip Baldock from our research group and Mr Bob Humphries of Diamond Light Source are thanked. The contributions of results from Mr Cameron Blackwell, for work at Diamond and analysis of Alstom specimens, in addition to sample preparation and analysis of a selection of cylindrical micro-specimens under the auspices of his final year project at the University of Birmingham are also acknowledged. The support of Mr Warren Hay and Mr Anthony Page at the University of Birmingham workshop in building the

cyclic oxidation rig, test cell and numerous other components is also appreciated. Theresa Morris and Paul Stanley at the Centre for Electron Microscopy, University of Birmingham are also thanked for their continued imaging and analysis support. Professor David Book, Dr. Daniel Reed and Dr. Alan Walton of the Hydrogen Materials Group at the University of Birmingham are thanked for access to and support using the group's confocal laser scanning microscope. The support of Dr. Yu-Lung Chiu of the Electron Microscopy group at Birmingham is also gratefully acknowledged for workstation and visualisation software access. The generous loan of a precision 4-axis goniometer used in the test cell used at Diamond Light Source by Mr Jeff Sutton of Birmingham is also appreciated.

Dr. John Nunn of the National Physical Laboratory, Teddington is warmly thanked for assistance with optical flash thermography experimental work as are Mrs Michelle Holder and Mr Michael Sandholzer both of the School of dentistry, University of Birmingham for assistance with SkyScan X-ray microCT work. Dr. Jifeng Sun is also thanked for FIB trials.

Dr. Yu Lu and Max Turner are also thanked for their support in organising access to the CHART Nikon XTH-225 microCT scanner at the University of Birmingham. Mr Dean Welton of the Precision Casting Facility at Rolls-Royce Plc is thanked for technical insights into the turbine blade casting process and useful discussions on the porosity within CMSX-4 turbine blades.

I would like to extend my thanks to the EPSRC and Rolls-Royce Plc for funding this project and finally to Professor Paul Bowen for facilitating the amicable environment in which this research took place.

Contents

List of figures

List of tables

List of symbols

ξ	Oxide thickness
t	Time
T	Temperature
σ	Stress
ε	Strain
$\dot{\varepsilon}$	Strain rate
ν	Poisson's Ratio
E	Elastic modulus
α	thermal expansion coefficient
Q	Activation energy
$\mathbb{E}_D$	Input energy
R	Universal gas constant
c	Specific heat capacity
κ	Thermal conductivity
ρ	Density
Ɛ	Photon energy
ϒ	Electron velocity
μ	Mass attenuation coefficient
ϕ	Photon flux
p	Projected attenuation
s	Shape function

Introduction

Thermal Barrier Coating (TBC) systems are used extensively in the hot section of aero and land-based gas turbines. They allow higher turbine entry temperatures (TET) and hence improve overall efficiency. This leads to a reduced specific fuel consumption (SFC) and over the life of the engine translates to significant commercial savings. An additional motive is the reduction in CO_x, NO_x and SO_x pollutants and unburnt residues. Achieving a TET of 1700K requires components to operate at elevated temperatures, which promotes elemental diffusion in alloys and chemical interaction with the operating environment.

TBCs systems typically consist of a 7-8wt% Yttria partially stabilized Zirconia (7YSZ) ceramic topcoat, deposited onto a metallic bondcoat, which is a layer either deposited on to, or is chemically part of the component alloy. Although the 7YSZ ceramic outer layer affords thermal protection to all subsequent layers beneath, the topcoat microstructure does not provide effective environmental protection. The bondcoat is thus designed to support the growth of a thermally grown oxide (TGO) layer of α-alumina that is a particularly effective environmental barrier in resisting hot corrosion and oxidation. The roughened bondcoat also provides improved adherence of the ceramic topcoat to the substrate alloy.

Because TBCs have allowed turbine blades to operate at temperatures noticeably higher than the melting temperature of the alloys, failure of the TBC is of paramount concern. At present, the full temperature capabilities of TBC systems cannot be realised due to the significant scatter observed in coating lifetimes under seemingly identical test conditions. Consequently, the temperature benefits of TBCs are designed conservatively into components. To accurately predict and extend the life

and operating envelope of these high-temperature components, it is necessary to fully understand the failure mechanisms of coatings. This is particularly the case in the stages of sub-critical defect formation as final failure generally occurs by the coalescence of such sub-critical defects. It is thus imperative to build an accurate picture of the interplay between stress and strain generation, and relief mechanisms. There is general agreement that failure occurs in and around the TGO and to this end, significant literature resources have been dedicated to the use of techniques such as photoluminescence piezospectroscopy (PLPS) and X-ray diffraction (XRD) to quantify the stress state within the TGO. Both of these methods, to some extent, allow examination of components without destructive sample preparation. However, both techniques suffer from drawbacks such as a lack of out-of-plane stress information in 3-D space and specifically in the case of the PLPS, limitations in numerical accuracy owing to room-temperature data acquisition.

X-ray Micro-tomography (X-ray μCT) is a non-destructive technique that allows three-dimensional, time-dependent observation of internal features. The technique is based on recording a series of digital radiographs (projections), formed by probing an object with a controlled beam of X-rays. The projections are formed through rotation of the object (or X-ray source and detector as in the case of most medical CT scanners) and using reconstruction algorithms to generate slice-by-slice images of the original object. These slices may then be visualised and analysed in three-dimensions (tomography).

The source of the X-rays plays an important role in the achievable resolution of the X-ray μCT reconstructions, with lab based sources offering convenient and relatively inexpensive scans at the expense of resolution. Synchrotron source X-

rays however require facilities on a national scale (e.g. Diamond Light Source in the UK with a storage ring of over 500 metres in diameter). The quality of the monochromatic beam produced and the auxiliary recording equipment at such facilities is unsurpassed and provides the highest resolution achievable today.

Digital volume correlation (DVC) is a three-dimensional computational strain measurement technique that can be used in calculating strains from X-ray μCT reconstructions. DVC is an extension of the digital image correlation (DIC) technique in the third spatial dimension. In two-dimensions, DIC is the numerical algorithm used to find the same group of features in a pixel set (an image subset of fixed, known dimensions) across two or more images of the same object. An applied 2D example is to spray a strip of material with particles followed by the application of an in-plane load and using DIC to measure the distribution of in-plane strains throughout the strip. Extending this concept in the third dimension allows calculation of three-dimensional strain fields from input data such as X-ray μCT reconstructions.

In this study, two themes relating to TBC failure mechanisms are explored. Firstly, conventional metallography and cyclic oxidation are used to establish a relationship between bondcoat creep and TGO stress. A force-balance approach is devised that couples empirical creep data from the open literature with measured oxidation-induced creep in specially designed cylindrical micro-specimens.

Secondly, synchrotron X-ray μCT imaging is used to capture the evolving 3-D microstructure of the cylindrical micro-samples at high resolution. This captured data is then coupled with DVC post-processing to compute full-field strains, from which TGO growth and the associated stress states are inferred.

Scope of work

A total of twenty-nine production Rolls-Royce stage 1 high pressure (HP1) turbine blades were examined as part of this study. All turbine blades consisted of a CMSX-4 second-generation nickel superalloy substrate and a diffusion bondcoat, of either a Pt or Pt-aluminide constituent. A small subset of samples was supplied with no topcoat present.

Thermal cycling to failure of aerofoil sections, derived from the supplied HP1 turbine blades was carried out under 20-hour exposure periods and the recorded time to spallation data was contrasted with in-house and literature data. The majority of tests were carried out at 1200°C with additional tests carried out at 1175°C, and 1100°C. Flat coupons, extracted from the trailing edge of aerofoil suction surfaces were also thermally cycled. Cross-section micrographs were analysed and TGO thickness measurements taken in addition to an analysis of interface morphology, namely the TGO/bondcoat and TGO/topcoat interfaces.

A novel slow-speed machining technique for the fabrication of cylindrical micro-specimens (1000μm or 500μm in diameter) with an intact TBC was devised by adding an additional rotating axis to a conventional diamond slow-speed saw. The miniature samples were used both in analysis of bondcoat creep and also for synchrotron X-ray micro-computed tomography. The cylindrical geometry and small size relative to the incident X-ray beam was ideal in minimising tomography reconstruction artefacts and maximising the imaging resolution. A purpose built cyclic oxidation rig was designed and constructed to aid with thermal cycling of cylindrical micro-specimens.

A mechanical constraint in the form of an air plasma sprayed (APS) overlay coating applied around the free cylindrical surface of micro-specimens was used to apply a physical boundary condition representative of flat coupons. Although interdiffusion occurred between the overlay coating and the diffusion TBC systems, delamination was induced in accordance with time-to-spallation observed in aerofoil sections.

Industrial, bench-top and synchrotron X-ray micro-tomography imaging was applied to cylindrical micro-specimens with progressively improving resolution. Industrial X-ray tomography using a Nikon XTH-225 scanner revealed little detail within cylindrical micro-specimens and was best suited to imaging full turbine blades. The limited resolution of a SkyScan 1172 benchtop device was used to support a proposal for beamtime allocation at the I12 beamline at Diamond Light Source. A 15-shift allocation followed by 2-shift allocation (8 hours per shift) at Diamond Light Source allowed near in-situ high-resolution scanning of cylindrical micro-specimens with thermal cycling carried out at 1150°C and 1200°C. The samples scanned in the first allocation were ones with an EB-PVD topcoat while the second shift was used to scan samples with and without topcoats under an 8.5-hour exposure period. A sample holder was designed and constructed to allow two specimens to be simultaneously scanned with one held over the other within the field of view. Phase contrast imaging (at the expense of resolution) was experimented with, however absorption contrast was found to yield a suitable combination of contrast and resolution. The experimental matrix was designed to allow a selection of samples (with and without an APS mechanical constraint) to be imaged and thermally cycled in a non-destructive manner. Samples of both Pt-only

and Pt-aluminide bondcoats (in addition to some Alstom Pt-aluminide cylindrical micro-specimens) were followed through time from the as-received state. Scans took place between every cycle and in the as-received condition. Reconstructed tomographs allowed visualisation of the full internal volume of a series of specimens through time. Volume slicing allowed TGO thickening, bondcoat phase transformation and topcoat sintering to be quantified and revealed good agreement with SEM cross-section measurements.

The 4-D (3-D spatial as a function of time) synchrotron tomography reconstructions acquired at Diamond were used to compute the internal oxidation-induced displacement field with the LaVision StrainMaster software package in collaboration with the University of Oxford. Matlab scripts were written to process the results and extract displacements in and around the TGO in addition to the topcoat. Inter-columnar separation within the topcoat was well-defined, as was the lateral displacement in the plane of the TGO. Thickening of the TGO was inferred from upward displacement of a plane of displacement vectors encompassing the TGO. Bondcoat phase transformation and elemental diffusion however, caused correlation to fail within some regions of the bondcoat. TGO displacement, both in-plane and inferred growth were compared to destructive SEM cross-sections and absolute displacements and thicknesses were seen to correspond accurately.

Chapter 1 Literature Review

1.1 Gas turbines

High-bypass ratio turbofans (Figure 1) used for aviation applications are a type of axial flow turbomachine that produce power by expanding the working fluid to a lower pressure [1]. In gas turbines, this process takes place over the three Brayton cycle stages of compression, combustion and expansion [2]. The thermal efficiency of a turbofan is chiefly a function of the compressor pressure ratio and turbine inlet temperature (Figure 2) [3]. Higher thermal efficiencies and increased work output are achieved by operating an engine at higher temperatures and at the correspondingly higher optimum pressure ratio. In addition to increased work output and increased thermal efficiency, there is also a need to reduce environmentally harmful emissions from gas turbines, including smoke (SN), hydrocarbons (HC), carbon monoxide (CO) and oxides of nitrogen (NO_x) [4]. As the combustion temperature of a turbofan increases, CO emissions generally decreases while NO_x outputs increase, with the ideal temperature to minimise both of these emissions being around 1577°C [5]. To achieve these high-temperature requirements, stage-1 high pressure turbine (HPT1) blades immediately after the combustion chamber are typically fashioned from nickel-based superalloys (Figure 3).

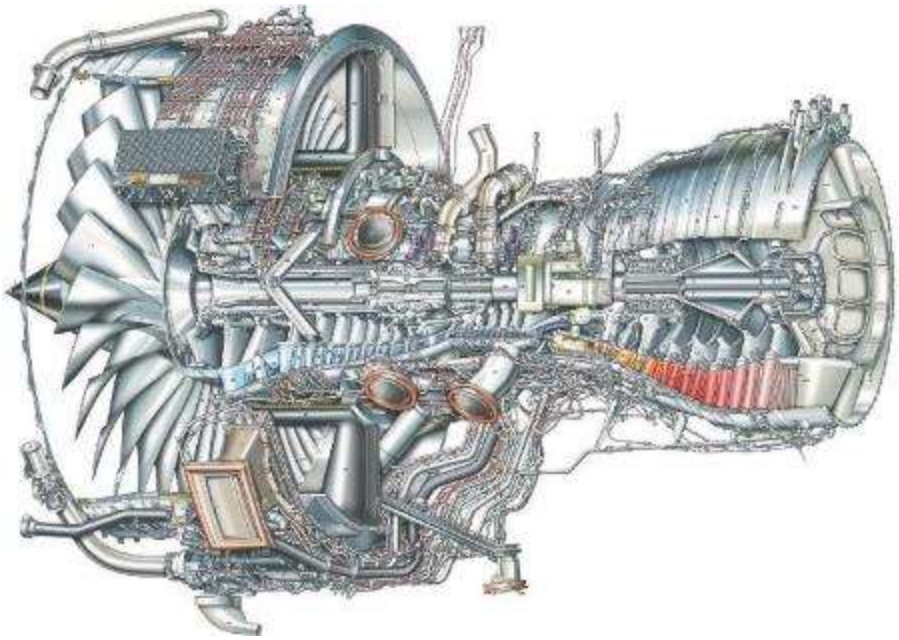

Figure 1 – High bypass ratio Rolls-Royce Trent 500 engine cutaway [6]*. The relative temperature of the core flow is shown through the compressor (blue), combustion chamber (yellow) and turbine stages (red).*

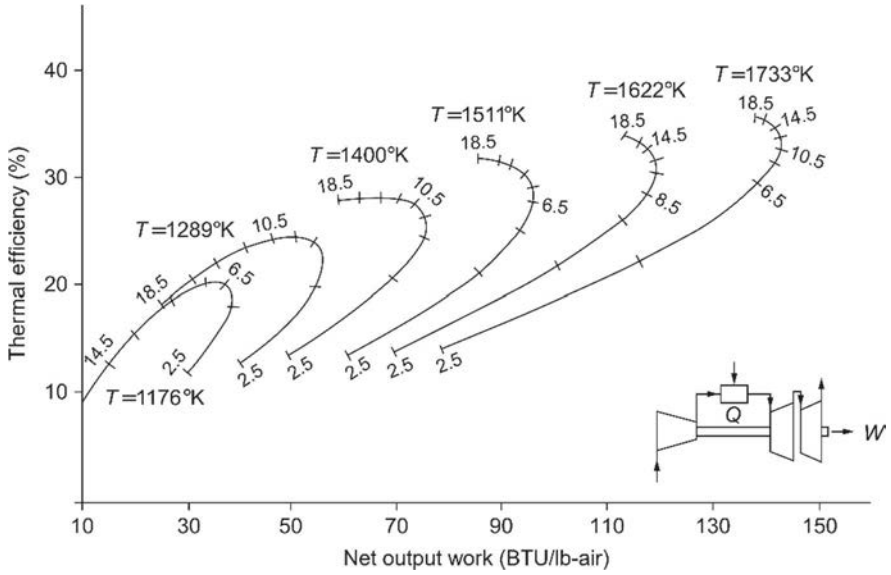

Figure 2 – Performance map showing influence of turbine entry temperature and pressure ratio on thermal efficiency and power output of a split-shaft gas turbine, adapted from [3].

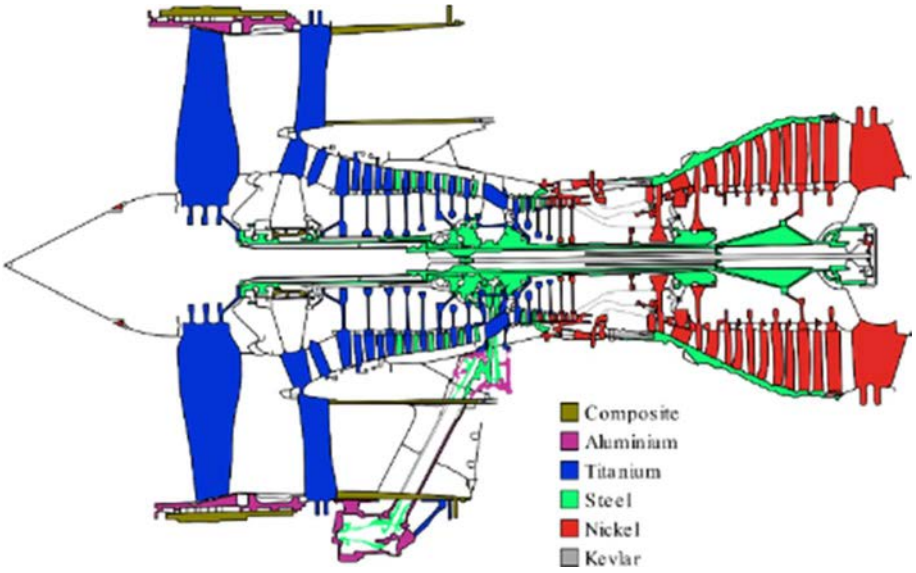

Figure 3 – Cross-section of Rolls-Royce Trent 800 showing material usage throughout engine, adapted from [7].

1.2 Nickel-base superalloys

1.2.1 Introduction

Nickel, a transition group metal with a melting temperature of 1455°C exhibits resistance to oxidation and corrosion while retaining high temperature strength and toughness. The FCC crystal structure of nickel is retained up to the melting point of the metal and this, combined with the partially filled 3d-orbital, affords nickel good alloying solubility [8]. Nickel superalloys contain varying amounts of Cr, Co, Mo, W, Al, Ti and Ta (Figure 4) with other alloying elements depending on the alloy generation. In second generation superalloys, the amount of refractories (Mo, W) were reduced and replaced with rhenium (3-4%) and in third generation superalloys, the rhenium content was increased further (6%) [9]. The role of rhenium in later superalloy generations has been linked to the partitioning of rhenium to the γ matrix [10].

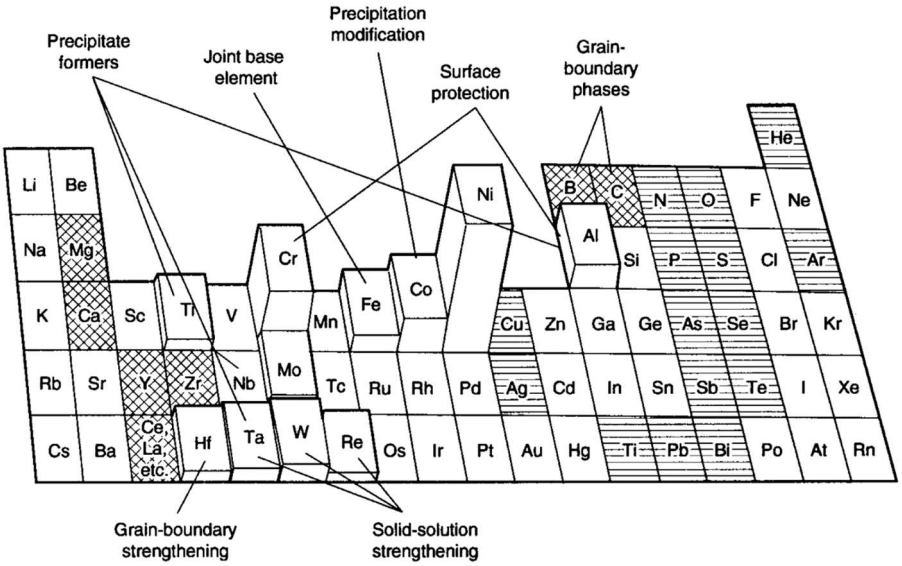

Figure 4 – Role of alloying elements in nickel-based superalloys [11].

1.2.2 Turbine blade casting

Improvements in casting processes since the use of wrought alloys have allowed complex superalloy components to be produced with refined microstructures (Figure 5). Conventionally cast components provide equi-axed grains that provide good mechanical properties in all directions while directionally solidified (both columnar grain and single crystal) components provide superior performance along the solidification direction (Figure 6). The lack of grain boundaries in single crystal components, in contrast with equi-axed blades provides superior mechanical properties and improved high-temperature performance.

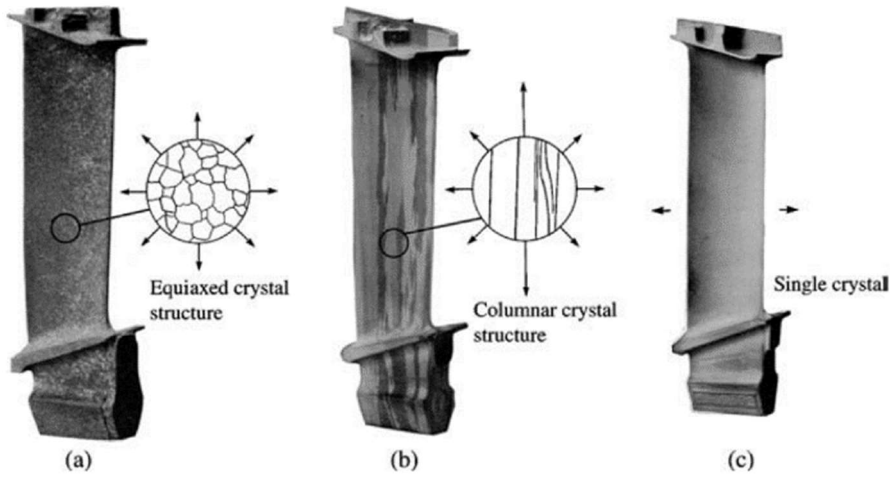

Figure 5 – Cast turbine blades with (a) polycrystalline equiaxed microstructure, (b) columnar microstructure resulting from directional solidification and (c) single crystal microstructure resulting from directional solidification and grain growth control [7].

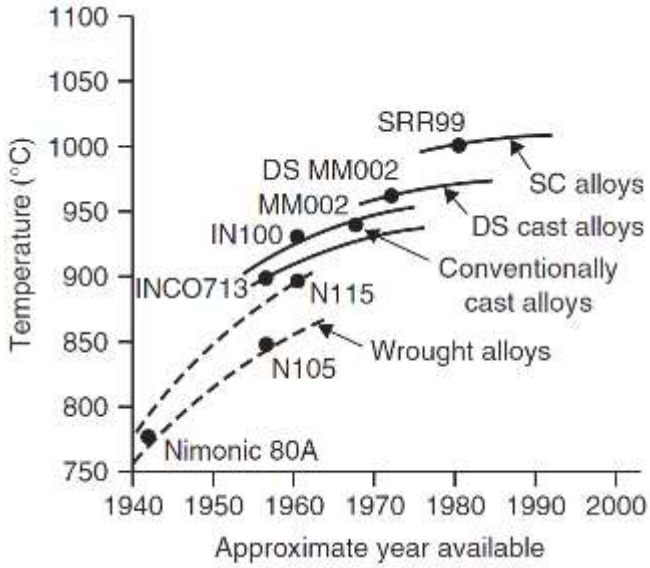

Figure 6 – Improvements in high temperature capability of components with casting methods [12].

The casting process employed at the Rolls-Royce precision casting facility (PCF), utilises a high throughput wax-loss method. A precision machined ceramic core is the starting component for blade manufacture that is the inverse of the internal serpentine cooling channels. This ceramic core is designed to be crushed at the interfaces during solidification later in the manufacturing process to prevent near surface residual stresses that may cause recrystallization. The core is then suspended within a die, also machined to exacting tolerances, via platinum or alumina pins. The die is filled with a wax that sets with low surface roughness and shrinkage. Wax moulds are then combined onto a multi-blade mount to allow casting of numerous blades from a single melt. The wax mould combination is then dipped into combinations of zircon, alumina and silica to form a multi-layered shell that can withstand deformation and oxidation when molten alloy is poured into the shell. The wax within the shell is burned off at 300 – 400°C and the shell is subsequently sintered around 900°C. A three-zone Bridgeman furnace (Figure 7) with melt, mould and withdrawal zones is then used to melt a superalloy billet and pour downwards into the shell. A penny-shaped diaphragm that sits below the superalloy billet is used to prevent pouring until complete melting has occurred by having the diaphragm

melting temperature slightly above that of the superalloy. Filling of the shell can either be bottom-up or top-down, depending on the required microstructural and geometric tolerances. In bottom-up filling, a spiral or pig-tail grain selector is used to achieve grain orientations within ±18° of the <001> direction, while in top-down filling, a precision machined seed with a flat surface is at the bottom of the blade to achieve orientations of ±5° of the <001> direction. In general, tighter tolerances are required for HP1 blades (Figure 8a) while less so for the later turbine stages.

The molten superalloy-filled shells are slowly withdrawn into a cooler chamber to control the solidification interface. Generally, complex geometries are not cast directly and extra material is added, that is later machined away. This approach, although produces more waste, reduces the likelihood of surface porosity, recrystallization and secondary grain formation within the blade. Once cooled, the shells are removed by the application of high-frequency vibrations and the ceramic core is leeched out by soaking the blade in NaOH at 80°C.

A solution heat treatment at 1314°C for 8 hours is then applied to the blades to homogenise the as-cast dendritic microstructure followed by a four-hour primary age at 1140°C and a sixteen-hour secondary age at 870°C [13]. Following this heat treatment, hot isostatic pressing (HIP) of the blades is carried out to close internal pores. Pores within the substrate act as fatigue crack initiation sites and are considered detrimental to blade life.

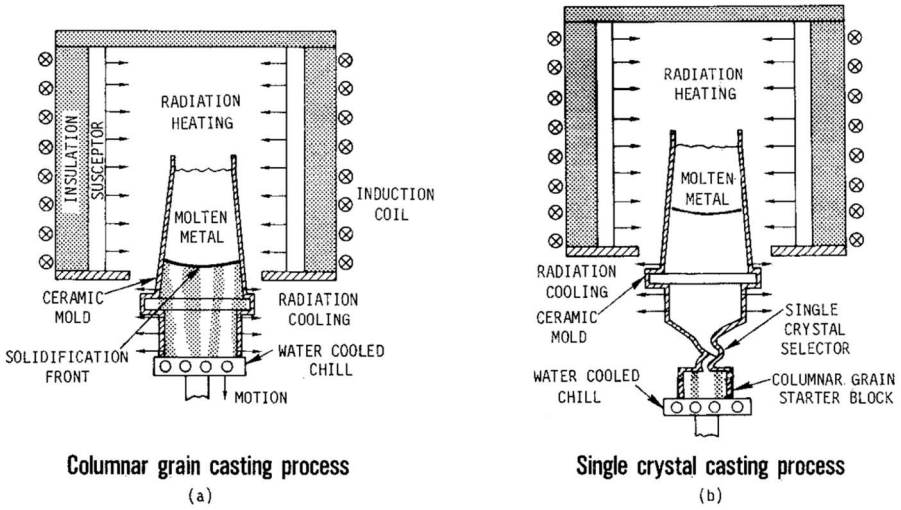

Figure 7 – Directional solidification of (a) columnar grain and (b) single crystal superalloy components [14].

Single crystal components such as HP1 turbine blades (Figure 8a) are manufactured in a similar way to columnar grain components in which a thermal gradient is maintained between the cooled component base and the molten metal pool at the component top (Figure 7). A controlled downward withdrawal that maintains a stable solidification front creates the columnar crystal structure in directionally solidified blades. In single crystal blades, a starter block and crystal selector combination may be used at the base of the component to force a single grain to solidify in the component mould. The as-cast single crystal solidifies with a dendritic microstructure (Figure 9) that consists of primary,secondary and tertiary dendrite arms, in addition to inter-dendritic regions. The dendritic arms are formed as the solidification front extends into the neighbouring molten liquid. The spacing, size and orientation of these dendrites is controlled by the temperature gradient and solidification rate along the <001> withdrawal direction [15]. These casting parameters also control solidification defects, primarily observed in the inter-dendritic regions. Heat treatment of the as-cast dendritic microstructure facilitates partitioning of elements between the dendrite arms and inter-dendritic regions and homogenisation of the microstructure to γ/γ’ (Figure 10).

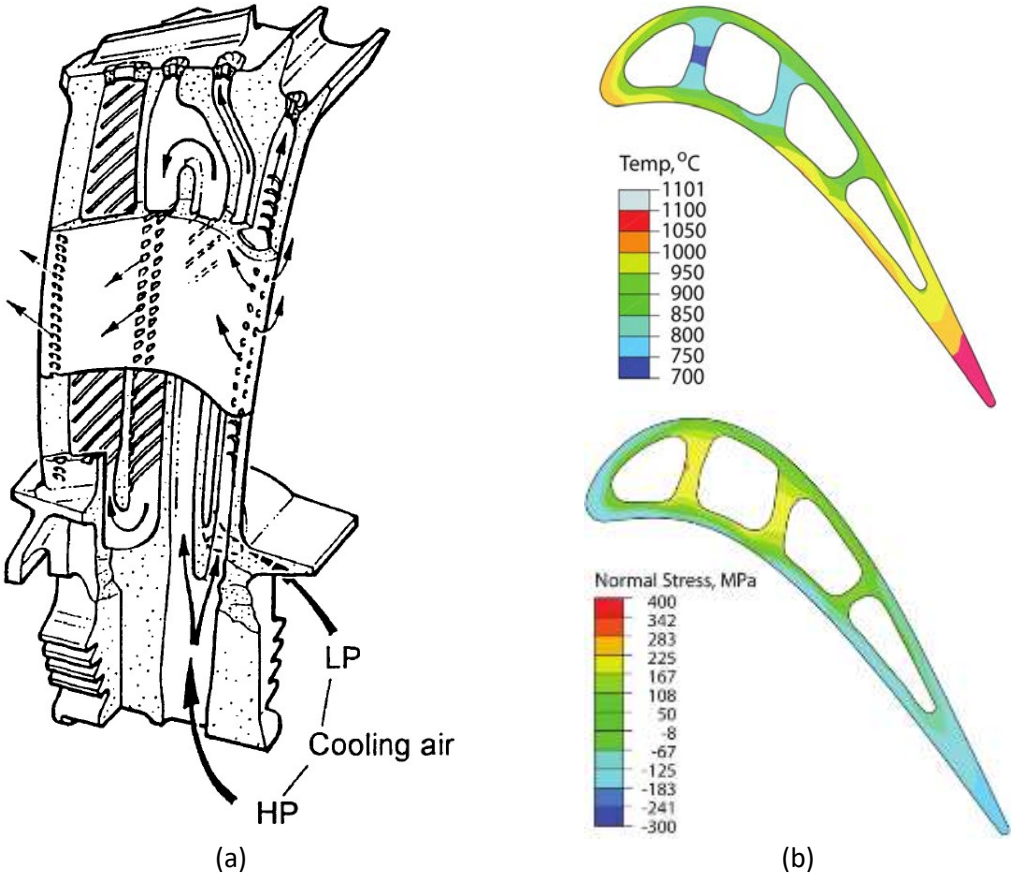

Figure 8 – (a) Rolls-Royce stage 1 high-pressure turbine blade revealing ribbed internal cooling channels and position of cooling holes for escape paths [16] *and (b) top: operating temperature distribution of CMSX-4 aerofoil sections and bottom: resulting normal stresses under thermal loading only in <001>* [17].

1.2.3 Microstructure of single crystal castings

The microstructure of as-cast single crystal superalloys is dendritic owing to the controlled withdrawal and solidification front of the Bridgman process. The morphology of the dendrites is such that primary dendrites (on the order of 500μm wide) are aligned with the <001> withdrawal direction with secondary dendritic arms emanating normal to the primary dendrites. The dendritic arms contain heavier elements including W, Co, Re and Cr while the interdendritic regions contain lighter elements such as Al, Ni, Ti and Ta. A homogenisation heat treatment with a final ageing is applied to the as-cast microstructure to diffuse heavier elements out of the dendrites and lighter elements into the dendrites and to form the ordered γ/γ' microstructure [18]. On the scale of the primary

dendrites, this heat treatment is seen as a homogenisation of the dendritic microstructure and at the finer scale, the γ/γ' microstructure (Figure 11) is observed.

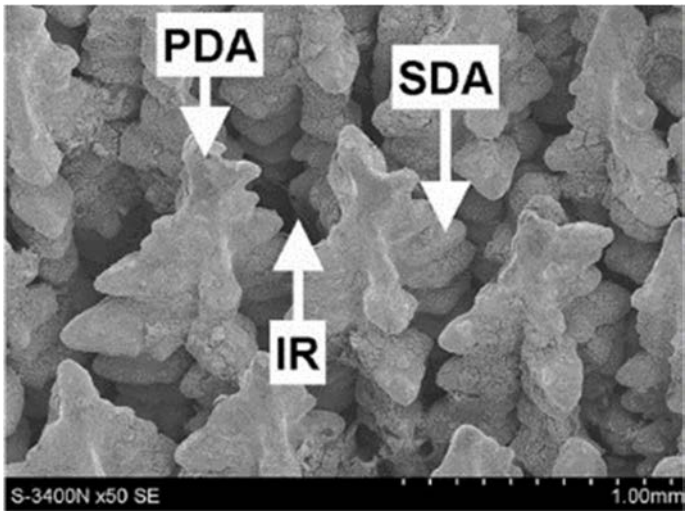

Figure 9 – Dendrites in as-cast CMSX-4 showing primary dendrite arms (PDA), secondary dendrite arms (SDA) and inter-dendritic regions (IR) [18].

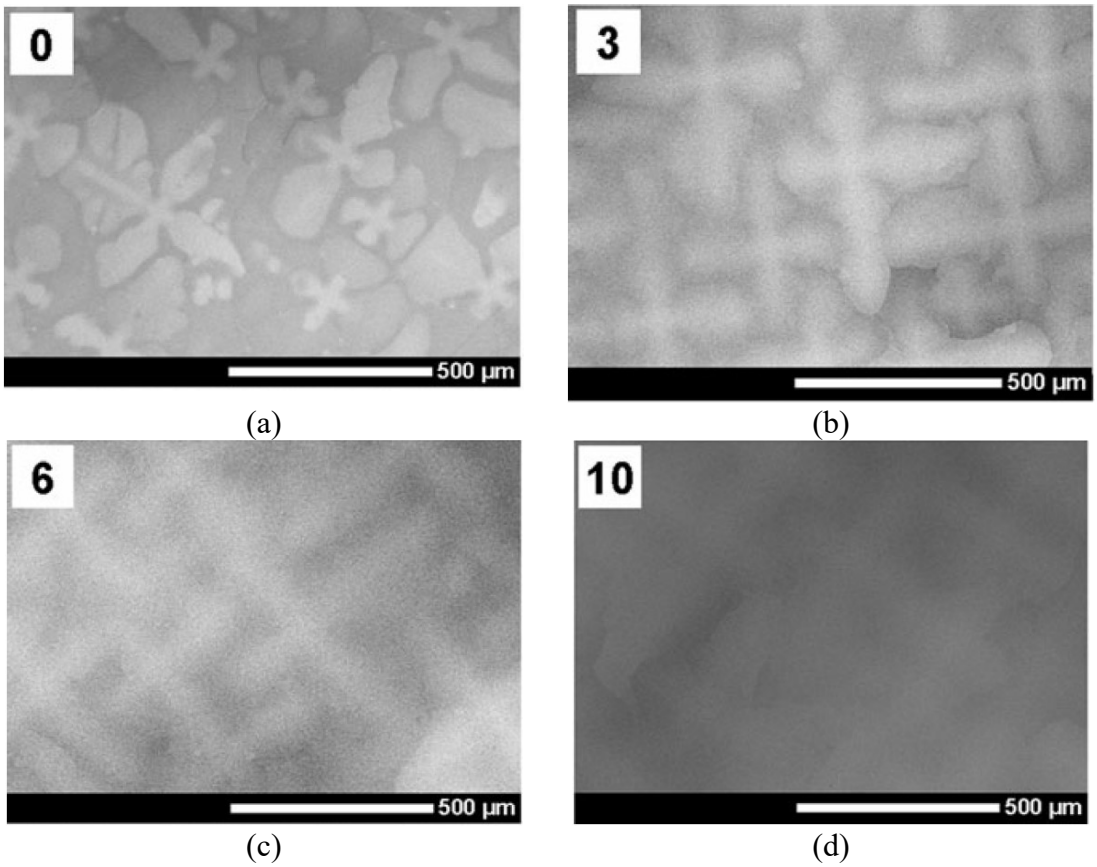

Figure 10 – Effect of heat treatment on dendritic microstructure of CMSX-4, adapted from [18]*, showing (a) as-cast state, (b) 1277°C for 2h + 1288°C for 2 h + 1296°C for 3h, (c) as previous with an additional 1304°C for 3 h + 1313°C/2 h + 1316°C for 2 h and (c) as previous step with an additional + 1321 C/2 h and ageing of 1140°C for 6 h + 870°C for 20 h.*

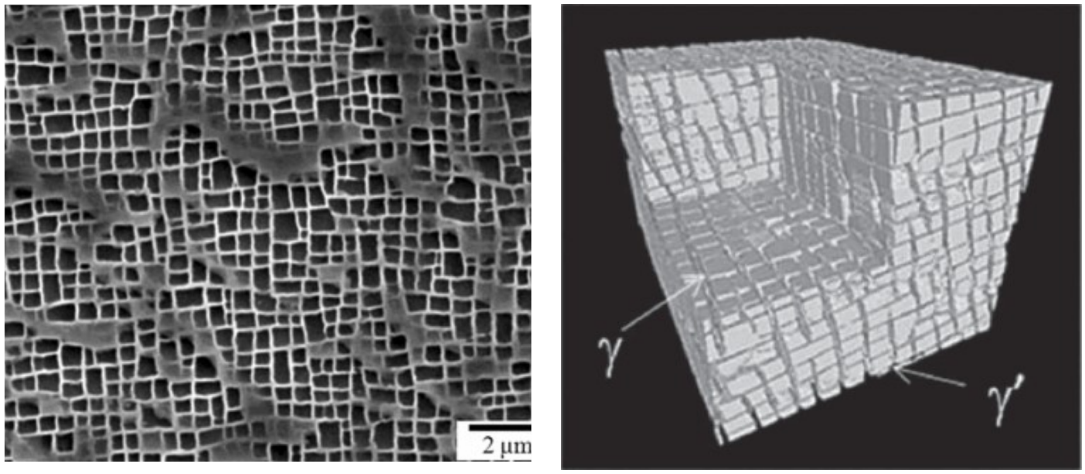

(a) (b)

Figure 11 – As-heat-treated microstructure of CMSX-4 showing γ-γ' microstructure via (a) cross-sectioning [19] *and (b) serial sectioning tomography (volume of 7.7×4.4×3.5µm)* [20].

One of the challenges faced with casting single crystal blades is the formation of porosity that is detrimental to fatigue and creep properties [21–23]. Solidification (S-type) porosity, linked to shrinkage on cooling and homogenisation (H-type) porosity are the two prevalent forms [24]. The pores are generally of the order of tens of micrometres (Figure 12) and are prevalent within the interdendritic regions. Homogenisation porosity tends to increase with homogenisation time (Figure 13a) and is marked in later generation superalloys with increased refractory elements that require longer homogenisation time. Porosity in single-crystals is a 3-D phenomenon and although conventional metallography allows investigation of the microstructure of porosity, X-ray tomography may be used to characterise the distribution and geometry of pores within a 3-D volume (Figure 12b) [25,26].

Hot isostatic pressing (HIP) is the preferred method of reducing porosity of aged components (Figure 13b). Pore annihilation during the HIP process takes place via plastic deformation by dislocation glide [27].

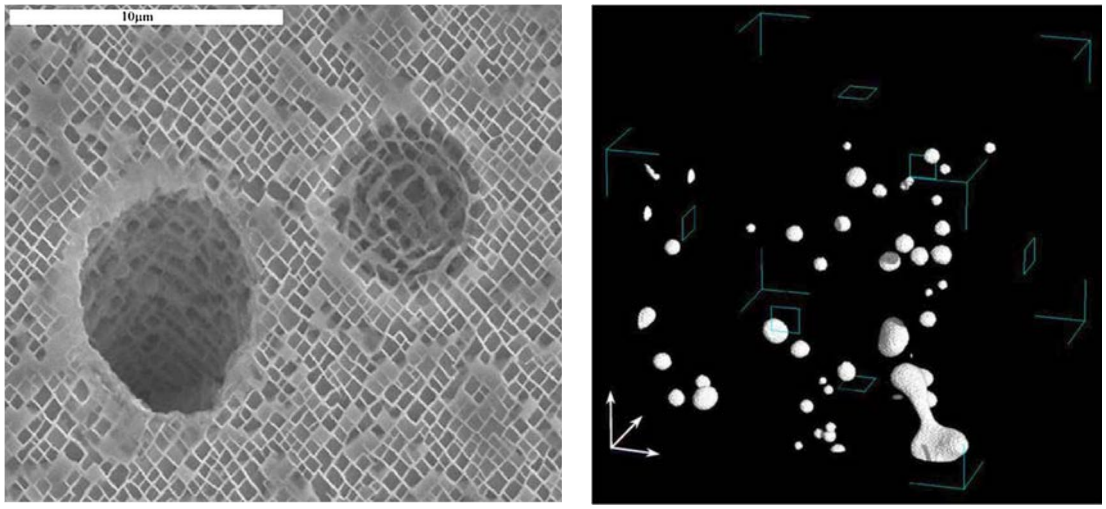

(a) (b)

Figure 12 – Porosity in CMSX-4 observed through (a) cross-sectioning [28] *and (b) via 3-D synchrotron X-ray micro-tomography (volume of 295×180×210μm)* [26].

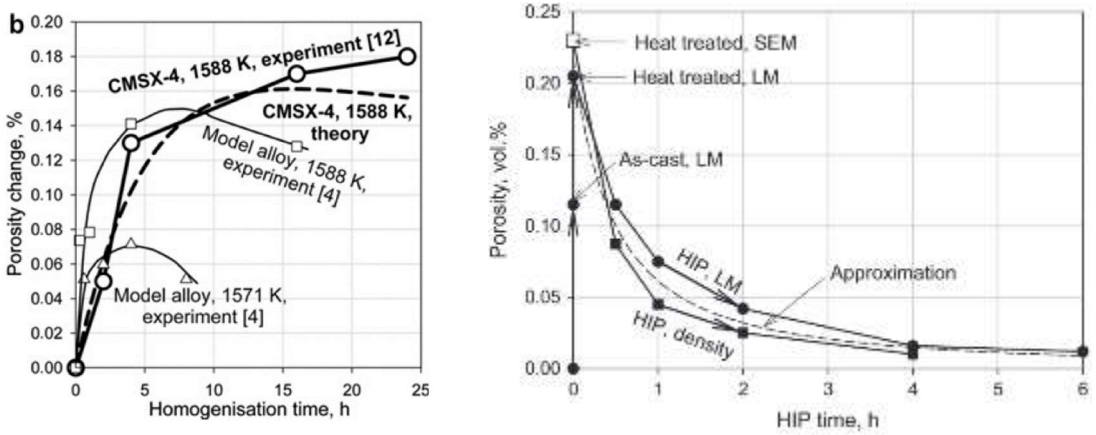

(a) (b)

Figure 13 – (a) Porosity increase during the homogenisation of CMSX-4 [24] *and (b) pore annihilation in CMSX-4 as a result of hot isostatic pressing (HIP)* [27].

1.3 High Temperature Oxidation

1.3.1 Introduction

Oxidation is the phenomenon that occurs when solid materials such as metals and alloys are exposed to oxygen containing reactive gaseous environments. Oxidation of materials can be both a detrimental and advantageous occurrence. As in the case of the thermally grown oxide (TGO) of thermal barrier coatings (TBCs) discussed later, a dense slow growing alumina oxide forms a protective barrier to the environmental attack of the base alloy. In the uncoated case however, oxidation of the base alloy may cause undesirable changes in microstructural and mechanical properties that can lead to critical component failure.

1.3.2 Thermodynamics of oxidation

The currently accepted definition of oxidation in terms of electron transfer as opposed to the classical oxygen or hydrogen transfer states that oxidation is the loss of electrons from a reducing agent to an oxidising agent. The general equation for the oxidation of a pure solid metal M in a pure gaseous oxygen environment to form an oxide product is given by

$$^{2x}/_{y}\, M(s) + O_2(g) \rightarrow {}^{2}/_{y}\, M_x O_y(s) \qquad \textit{Eq. 1}$$

In order to determine whether a reaction that follows the above equation is thermodynamically possible, although not strictly predictive because of kinetic factors (the rate of reaction may be particularly low), the Gibbs free energy G, of the system must be evaluated. This energy relates the enthalpy H, entropy S and temperature T of an isothermal and isobaric system and is a measure of the thermodynamic driving force for

a reaction. Enthalpy is a measure of heat energy, entropy energy related to atomic, molecular, ionic and/or electronic arrangement and rearrangement and free energy the quantity of the same that may be converted into useful energy [29]. This relation is given by

$$G = H - TS \qquad \textit{Eq. 2}$$

For a reaction of the form $aA + bB \rightarrow cC$, the Gibbs free energy change ΔG, is given by

$$\Delta G = \Delta G^{\circ} + RT \ln\left(\frac{a_C^c}{a_A^a \cdot a_B^b}\right) \qquad \textit{Eq. 3}$$

where ΔG° refers to the free energy change when all species are present in their standard states (alternatively, the free energy released by combining one mole of oxidising agent with the metal [30]), $a_x = \frac{p_x}{p_x^{\circ}}$ is the thermodynamic activity, defined as the ratio of vapour pressures or partial pressures of a species relative to the standard state of the same species [31] and R is the molar gas constant. For a system having $\Delta G > 0$ the reaction is thermodynamically impossible, while for the condition where $\Delta G = 0$ the process is in equilibrium. In the case where $\Delta G < 0$, the reaction can spontaneously occur without external inputs, though this is a necessary but not sufficient condition as described later. This equation may be rewritten in terms of the generalised oxidation equation to yield

$$\Delta G = \Delta G^{\circ} + RT \ln\left(\frac{a_{M_xO_y}^{2/y}}{a_A^{2x/y} \cdot a_{O_2}}\right) \qquad \textit{Eq. 4}$$

However, noting that the activity is only applicable to condensed (vapour pressure) and gaseous species (partial pressure), the solid metal and oxide activities tend to unity. Noting that all elements in their standard states have $\Delta G = 0$ and $a = 1$, the above may be rewritten as

$$\Delta G = \Delta G^{\circ} + RT \ln\left(\frac{1}{p_{O_2}/p^{\circ}_{O_2}}\right) = \Delta G^{\circ} + RT \ln p^{\circ}_{O_2} - RT \ln p_{O_2} = \Delta G^{\circ} - RT \ln p_{O_2}$$

For a system in equilibrium, the above may be rewritten as

$$\Delta G^{\circ} = RT \ln p_{O_2} \qquad \textit{Eq. 5}$$

For an oxide in equilibrium with the pure metal and oxygen at 1 atmosphere pressure (i.e. $\Delta G = 0$ as above), the temperature at which this condition holds is known as the standard dissociation temperature. Since the temperature of a system is also a function of pressure, the above equation may be rewritten in terms of the equilibrium dissociation pressure at a certain T as

$$p_{O_2} = e^{\Delta G^{\circ}/RT} \qquad \textit{Eq. 6}$$

For pressures below this value, the oxide will dissociate and if raised above this pressure the oxide is stable. The relationship between temperature, standard free energy of formation and pressure is summarised for oxides using the Ellingham diagram (Figure 14).

The noble metals that are easily reduced and resist oxidation are found at the top of the diagram having the least negative ΔG° values with the least stable oxides and conversely the more reactive metals at the bottom having the most stable oxides. As temperatures are increased, the numerical value of ΔG° typically increases, corresponding to decreased entropy and the oxide hence becomes less stable. The slope at a particular temperature corresponds to $-\Delta S$ and the intercept with the ordinate axis is equal to ΔH. Changes in slope are generally associated with changes in state, with sublimation typically causing a larger change in slope than melting.

Such diagrams are useful in determining the oxidation product that is most likely to form in a given environment and allow comparisons of relative oxide stabilities. However, as will be discussed in the following section, the principal oxide that will form in a system is also a function of the kinetics of oxide growth. For example, metals such as Al, Ti and Zr resist oxidation at low temperatures even though they are found at the lower portions of the diagram, owing to coherent and relatively impermeable oxide films that prevent further oxidation [30]. Additionally, the Ellingham diagram does not take into account non-stoichiometric compounds that are frequently observed at high temperatures [32].

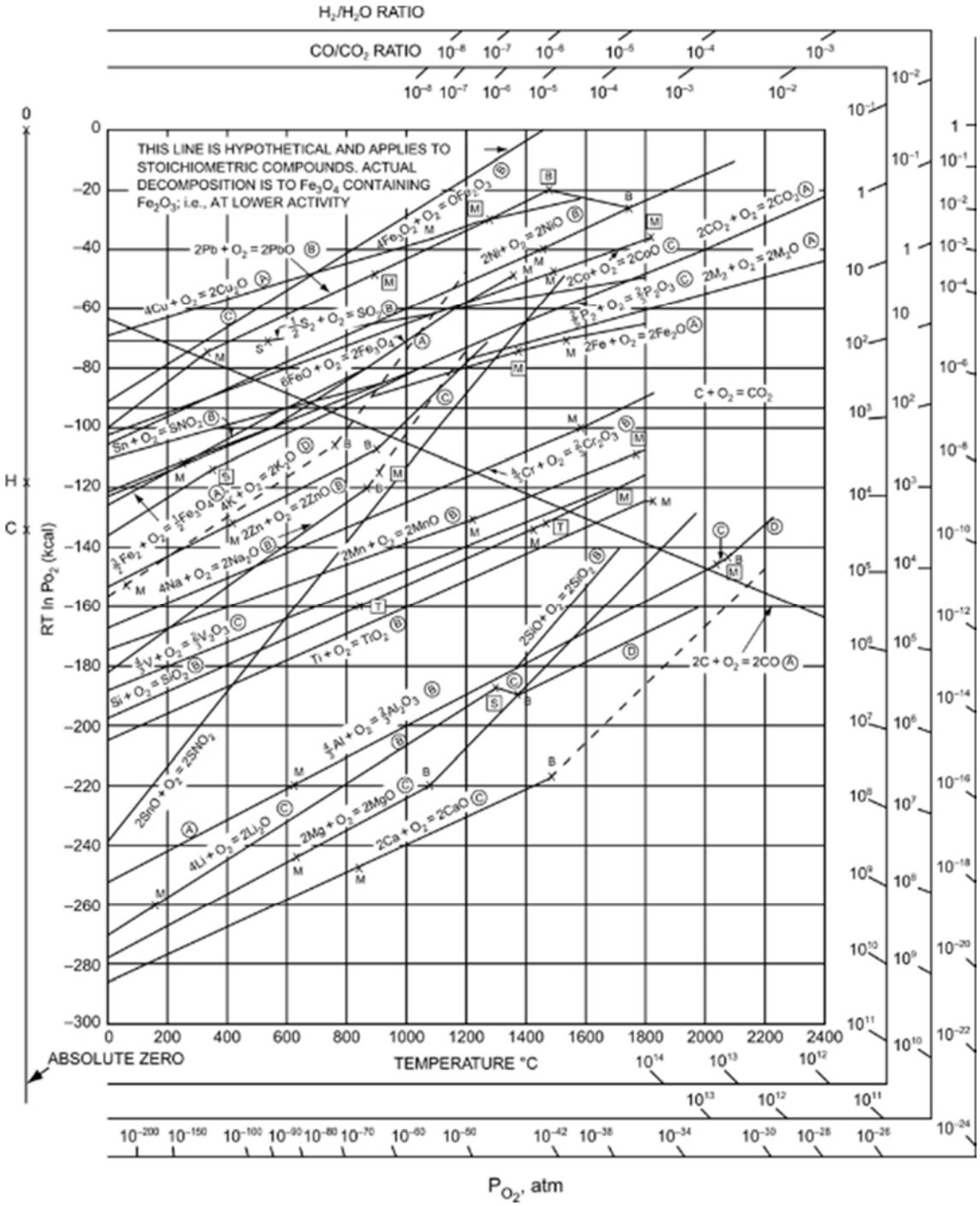

Figure 14 – Ellingham diagram adapted from [33]. *A, B, C and D refer to suggested accuracies of ±1, ±3, ±10 and ±>10 kcal respectively. Points marked M, B, S and T refer to melting, boiling, sublimation and transition points respectively.*

1.3.3 Oxidation kinetics

The thermodynamic considerations of oxide formation presented previously do not provide information on the rate at which oxidation occurs or its likelihood. The process

of oxide formation consists of several stages, each of which may have its own growth rate and influence on the overall behaviour of the oxide. The stages generally start with chemisorption (dissociation and ionisation), followed by oxide nucleation at favourable sites. Nucleated regions continue to grow and impinge on each other until a full film is formed [30]. The individual steps leading to the formation of an oxide film may thus be detailed quantitatively as follows [33]: adsorption of molecular oxygen on the metal surface first occurs followed by dissociation of molecular oxygen into atomic oxygen. Atomic oxygen then migrates to low-energy sites on the metal surface, such as dislocations and impurity atoms. Ionization of atomic oxygen takes place and subsequent bond formation with atomic metal. A build-up of multiple adsorbed layers, described by the early-stage lateral oxide growth model [34] (as opposed to the classical uniform film growth) is seen followed by growth and overlap of oxide islands to form transient oxide film. Diffusion of ionic metal and/or oxygen through the film takes place to form and continue the growth of a stable oxide.

The mechanism for the transport of ions in the last stage of the steps outlined above usually occurs by solid state diffusion, which in turn depends on the imperfections in the oxide or its defect structure. In oxides, the most common imperfections are vacancies, interstitials and impurities [35].

The rate at which an oxide layer thickens is a function of temperature and the material. A number of different growth laws (Figure 16) may be observed including parabolic, sub-parabolic, logarithmic, linear and breakaway. Logarithmic growth rates are typically experienced at low temperatures for thin films. Because atomic oxygen acquires electrons from surface atomic metal, under Wagner's theory of oxidation [36], a strong electric field is set up across the thin film pulling metal atoms through the oxide (Figure 15).

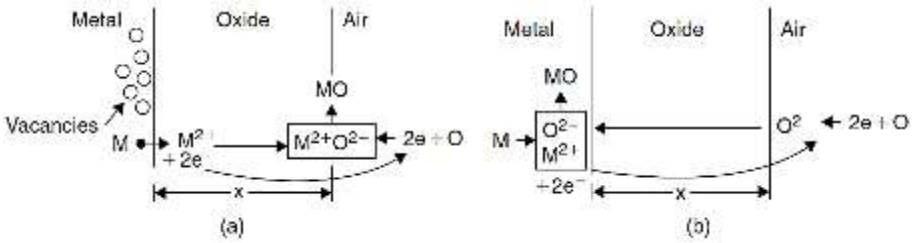

Figure 15 – Diffusion processes leading to oxide growth at a) oxide/gas interface and b) metal/oxide interface [30].

As the oxide thickens, the field strength diminishes and the oxide thickness is proportional to $\ln t$. Wagner's treatment of transport across the oxide layer envisaged the movement of cations, anions and electrons but the approach is often simplified by assuming that only one of the ionic fluxes dominates and that the oxide is an electronic conductor. The flux of ions, j_i, is then given as

$$j_i = -\frac{D_i C_i}{kT}\left(\frac{1}{N_A}\frac{d\mu_i}{dx} + z_i e \frac{d\varphi}{dx}\right) \qquad \textit{Eq. 7}$$

where C_i is concentration, D_i the appropriate diffusion coefficient, K is Boltzmann's constant, T is absolute temperature, N_A is Avogadro's number, μ_i is the chemical potential, x is the spatial coordinate, z_i is the ionic valency, e is the electronic charge and φ is the electrical potential. Integration and manipulation of Eq. 7 leads to the expression for the flux of defects (equal to the flux of ions, j_i) as:

$$j_i = (1 + z_i) B_v kT \left(\frac{C_v^{outer} - C_v^{inner}}{\xi}\right) \qquad \textit{Eq. 8}$$

where B_v is the mobility of the defects (assuming cation vacancies), C_v^{outer} is their concentration at the oxide/gas interface and C_v^{inner} that at the oxide /metal interface, ξ is the thickness of the oxide layer. For cation vacancies$C_v^{outer} \gg C_v^{outer}$. Eq. 8 shows that the kinetics of oxide growth are predicted to be parabolic since the flux of ions is proportional to the oxide thickness. Also, the flux is proportional to the defect concentration gradient across the oxide layer, albeit modified by the term $(1 + z_i)$.

Evaluation of this term is not straightforward because in many cases the charge on defects is not well established. For cases where it is, e.g doubly-charged cation vacancies in NiO, satisfactory agreement is obtained with the Wagner model [37] since the ion diffusion coefficient is also known for this system.

Parabolic growth rates are generally observed at temperatures where ionic diffusion rates are significant through the oxide. The speed of ion movement is controlled by the defect structure of the oxide lattice.

Parabolic breakaway or linear growth rates may be experienced under the repeated breakaway of the oxide. The interfacial stresses (tensile or compressive) generated due to the growth of an oxide layer may be such that the oxide layer repeatedly cracks and spalls away. The action of repeated breakaway leads to a linear or faster growth rate.

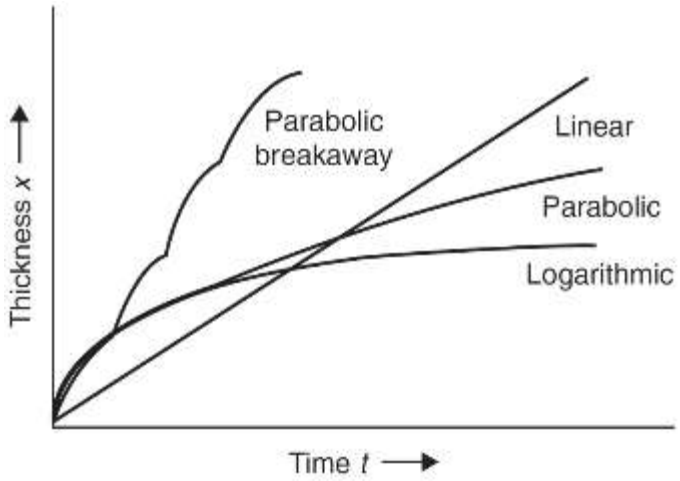

Figure 16 – Various oxide thickening rates in metals, controlled by temperature and material [30].

The Pilling-Bedworth ratio (PBR) is the ratio of the molecular volume of the oxide to the molecular volume of the metal of which the oxide is formed such that

$$PBR = {}^{V_{oxide}}/_{V_{metal}} \qquad \textit{Eq. 9}$$

The PBR is a useful criterion in estimating the spallation stability of an oxide. For oxides having a PBR value of less than unity, as in the case of light elements e.g. Mg, Na and K,

the coverage of the scale formed is insufficient to provide protection against further oxidation and hence a linear growth rate is observed. For oxides having PBR much greater than unity, the volume of the oxide formed is greater than the volume of metal replaced and hence is highly compressed and has a tendency to buckle and spall. Hence, for a stable and protective oxide scale PBR should be close to unity. There are however, complications in estimating PBR values as a result of factors such as geometry effects, oxide volatility and preferential oxidation and other chemical effects. In addition to isothermal oxidation, the action of thermal cycling and a mismatch in coefficient of thermal expansion (CTE) between the oxide and base material may also drive repeated breakaway. . In the Wagner model for thick oxide layers, the assumptions made [35] are that (1) the oxide scale is compact and adherent, (2) migration of charged species is the rate-controlling process (3) at both the metal/oxide and oxide/gas interface thermodynamic equilibrium is achieved, (4) the oxide is almost stoichiometric and that (5) oxygen solubility in the metal is ignored.

The growth rate of an oxide of thickness ξ having a diffusion coefficient D and a concentration difference Δc under Wagner's model is given by

$$\frac{d\xi}{dt} \propto D \cdot {\Delta c}/{\xi} \qquad \textit{Eq. 10}$$

The oxide thickens according to the following parabolic rate law

$$\xi^2 = k_p t \qquad \textit{Eq. 11}$$

where the parabolic scaling constant is given by

$$k_p = k_0 e^{-{Q}/{RT}} \qquad \textit{Eq. 12}$$

where Q is the activation energy for the rate controlling diffusion process.

The oxides of practical engineering significance are those that exhibit slow growth rates in addition to thermodynamic oxide stability. Rate constants for a selection of oxides (Figure 17) suggest that chromia, silica and α-alumina exhibit the lowest growth rate. Alumina (α phase), is the preferred oxide for high temperature (1000°C) components such as turbine blades. Alloy chemistry and coatings are optimised to promote the growth of stable alumina in such components. In lower temperature applications (800°C), for example turbine discs, chromia forming alloys are preferred.

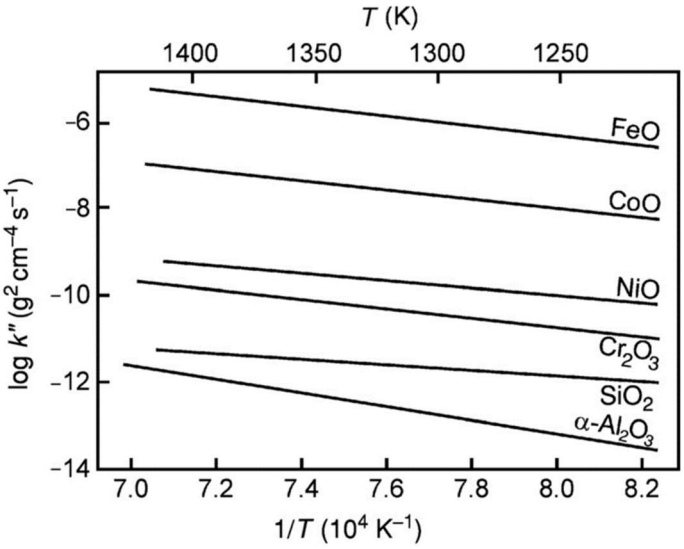

Figure 17 - Parabolic rate constants for a number of technologically important oxides (α-alumina, silica and chromia) compared to the primary constituents of typical superalloys (Ni, Co and Fe) [38].

The growth of stable α-alumina scales initiates with the formation of a transition alumina oxide layer, consisting of the cubic θ and or γ phase, with growth dominated by outward Al transport [39]. Randomly orientated grains of hexagonal α-Al_2O_3 nucleate at the alloy/alumina interface eventually forming a complete layer at the interface. With further time, the remainder of the θ and γ phases transform to the thermodynamically most stable α phase with growth dominated by inward oxygen diffusion. Of the alumina phases, the α form exhibits the lowest growth rates (Figure 18).

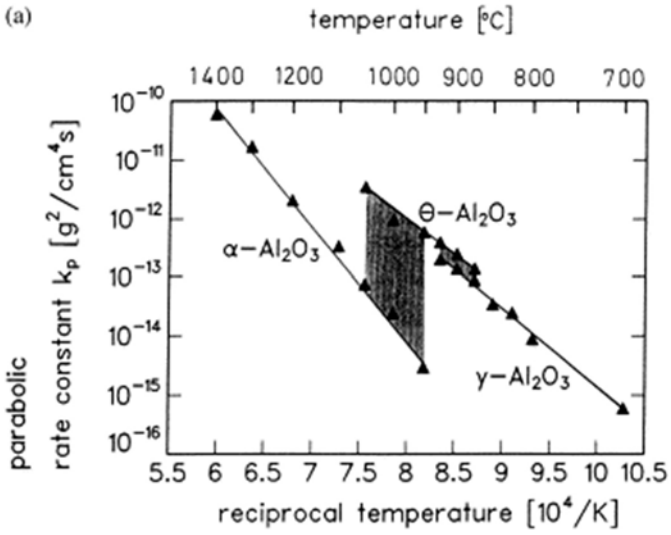

Figure 18 - Rate constants of the alumina phases as a function of temperature [40].

The formation of a dense adherent surface oxide layer is usually associated with growth stresses within that layer [41–43]. These can be relatively small (approximately 0 for NiO) or up to a few hundred (-ve) megapascals [44]. Further discussion on growth stresses to be examined here will be made in Chapter 4. It needs to be recognised however, that the predominant source of stress in the oxide layer is that induced thermally during temperature changes. The coefficient of thermal expansion of the oxides of relevance here are less than that of the alloy itself and so the oxide experiences in-plane compressive stresses during cooling. This in plane stress may be calculated adequately from

$$\sigma_{th} = \frac{E_{ox} \cdot \left(\alpha_{ox} - \alpha_{alloy}\right) \cdot \Delta T}{\left(1 - \nu_{ox}\right) + \frac{\xi_{ox}}{\xi_{alloy}} \cdot \frac{E_{ox}}{E_{alloy}} \cdot \left(1 - \nu_{alloy}\right)} \qquad \textit{Eq. 13}$$

where the subscripts o and m represent oxide and underlying metal alloy respectively and the elastic modulus E (Pa) and thermal expansion coefficient α (K^{-1}) are a function of temperature.

The thermal stress developed during cooling for say 1000°C can be substantial and 3 GPa to 4 GPa have been measured using the photoluminescence technique [45]. Such large

stresses can prejudice the mechanical stability of the oxide layer resulting in its cracking and spallation. Evans [44] described two routes to spallation (Figure 19) depending on the relative strengths of the oxide and oxide/metal interface. Buckling (Route II) will arise for thin oxides but requires decohesion at the oxide/medal interface to be induced. For a weak interface and strong oxide, the critical temperature drop to initiate buckling (ΔT_b) is given by

$$\Delta T_b = \frac{1.22}{\Delta\alpha(1-\nu_{ox}^2)}\left(\frac{\xi}{R}\right)^2 \qquad \textit{Eq. 14}$$

where ξ is the oxide thickness, R the radius of decohesion and ν_{ox} the Poission's ratio of the oxide. Wedging (Route I) occurs in systems where the oxide is weak relative to the interface and the oxide is thick. In this model, the elastic strain energy to form shear cracks in a four-sided array is considered. The critical temperature drop for spallation ΔT_s in a four-sided array of side length λ (modelling the spacing between shear cracks) through the oxide layer is given by

$$\Delta T_s = \left(\frac{4\gamma_o}{(1-\nu_{ox})E_{ox}\lambda(\Delta\alpha)^2}\right)^{\frac{1}{2}} \qquad \textit{Eq. 15}$$

where γ_o is the fracture surface energy of the oxide. Experimentally observed spallation on a model alloy at varying oxide thicknesses (Figure 20) reveals a buckling mode for an oxide of thickness less than 1 μm and a wedging mode for an oxide thicker than 10 μm.

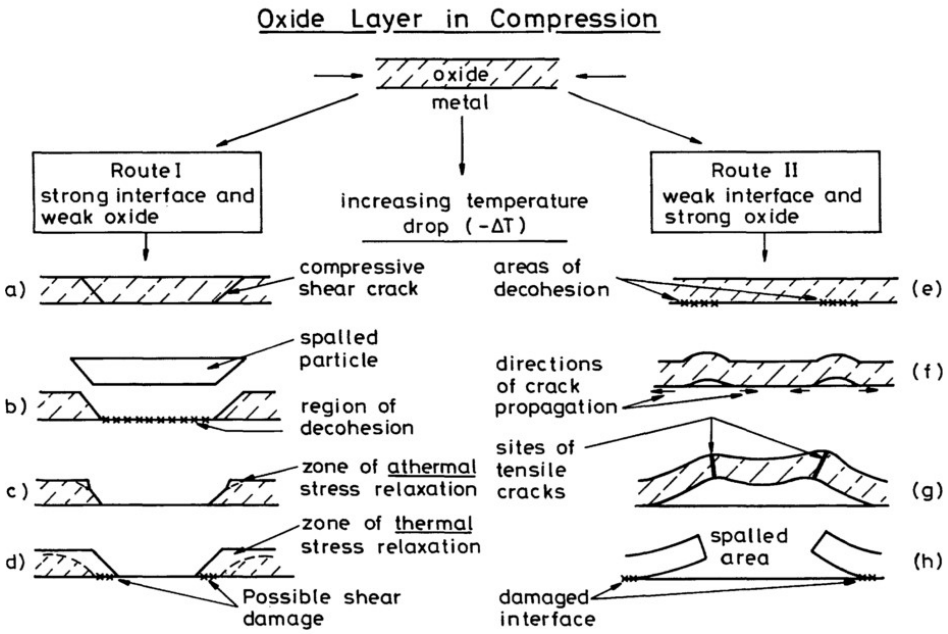

Figure 19 - Oxide cracking and subsequent spallation by compressive stress via Route I for a weak oxide and a strong interface and Route II for a weak interface and a strong oxide [44].

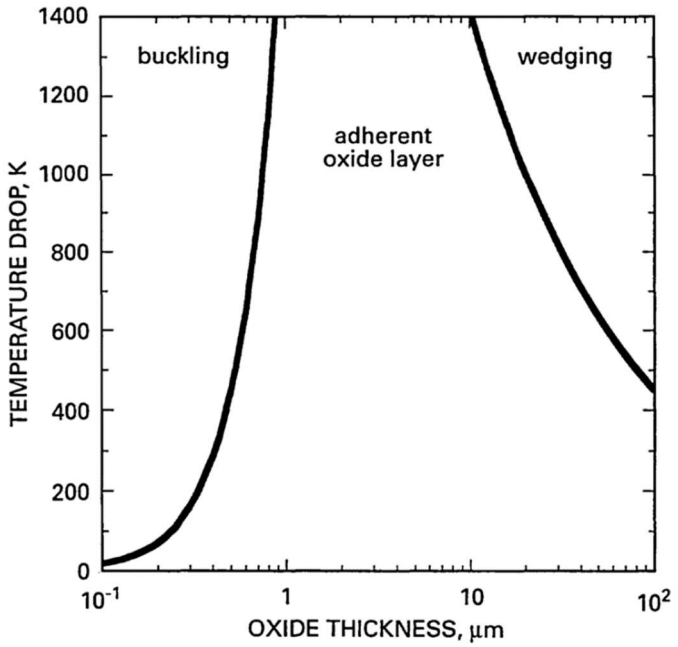

Figure 20 - Spallation map for alumina on Fecralloy showing the relation between oxide thickness, temperature drop and failure mode [44].

In practice, commercial nickel-based superalloys are complex (see Table 2). Some elements have high affinity for oxygen, for example Co, Ni and Ti and these can affect the oxidation behaviour of the alloy. On exposure to air at 1100°C, CMSX-4 exhibits a

bi-layer structure (Figure 21) with an inner protective α-Al_2O_3 oxide and an outer layer consisting of (Ni,Co)Al_2O_4, (Ni,Cr)$_2O_4$ and simple Ti and Ta oxides [46].

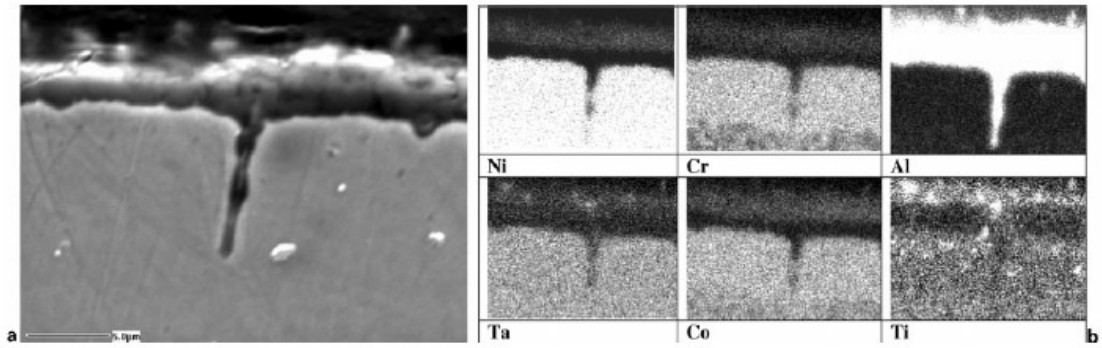

Figure 21 - Cross-section of bi-layer oxide formed on CMSX-4 following 100 hours of exposure in air at 1100°C [46].

1.3.4 High temperature coatings

The aluminium and chromium content of nickel superalloys alloys (5.6 wt% Al in CMSX-4), are insufficient to meet the long-term service requirements of turbine components. Consequently, coatings rich in Al and/or Cr are required to allow extended high-temperature operation. Chromia forming coatings are preferred in Type II hot corrosion environments (600°C to 800°C) and alumina formers in higher-temperature (≥950 °C) Type I environments as chromia layers can be converted to gaseous CrO_3.[47]. Coating strategies are broadly divided into two categories of overlay (M-Cr-Al-X where M is any combination of Ni, Co or Fe and X any of Y, Hf and Si [48]) and diffusion coatings (typically either β(Ni,Pt)-Al or γ/γ', Figure 22). An overlay system does not chemically alter the component composition and microstructure (apart from the formation of a diffusion zone after high temperature exposure) of the component surface (Figure 23). A hybrid SMART coating system [49] has been developed to operate effectively in hot corrosion environments. Such coatings are suited to land-based gas turbines where the range of fuels and long-term operating temperatures are subject to change. The chemically graded MCrAlY bondcoat forms an alumina layer under Type-I hot corrosion and a

chromia layer under Type-II hot corrosion [47]. Prior to coating deposition, substrate surfaces are typically grit-blasted with alumina to remove surface oxides and roughen the surface to improve adhesion [50]. This process may cause trapped alumina blast particles to remain in the coating system, visible as a grit-line.

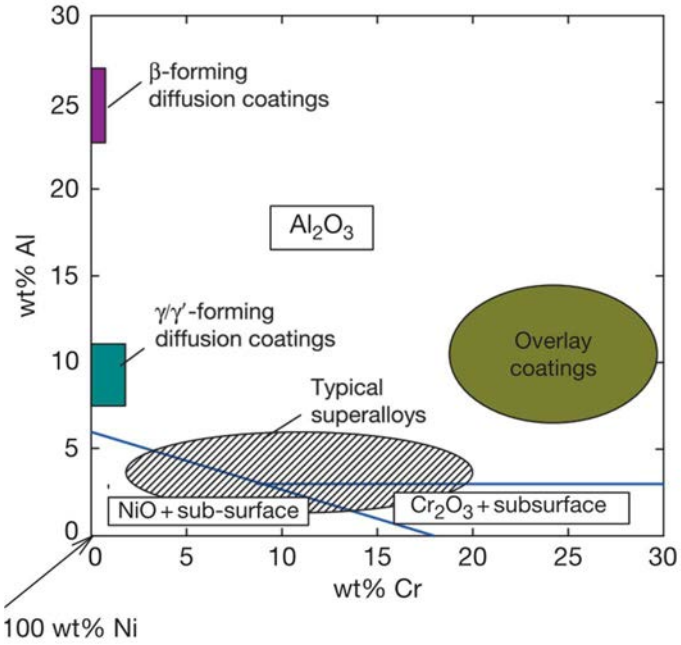

Figure 22 - Schematic Al-Cr composition map showing relative positions of typical nickel superalloys, overlay coatings and diffusion coatings for applications between 1000°C and 1200°C [47].

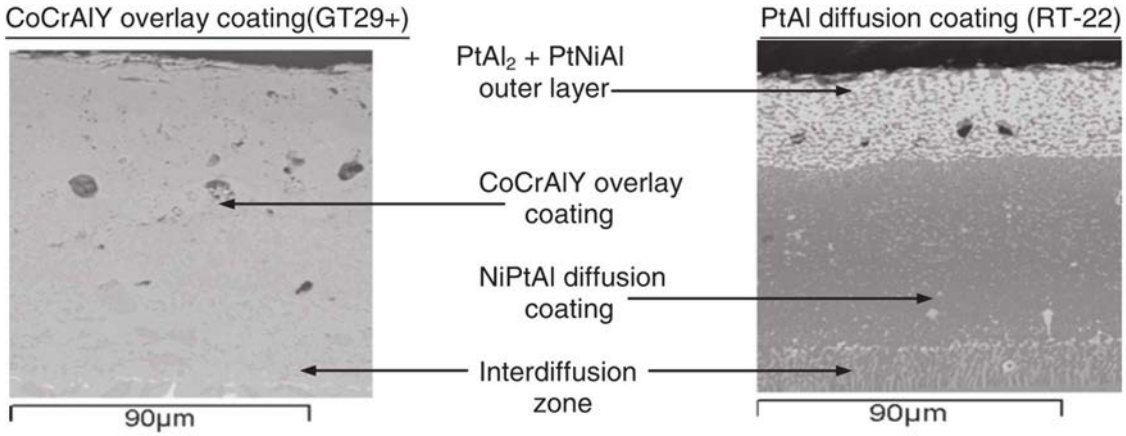

Figure 23- IN738LC nickel superalloy with CoCrAlY overlay coating and Pt-aluminide diffusion coating [51].

Diffusion coatings (Figure 24), either β(Ni,Pt)-Al or γ/γ' form the bondcoat of thermal barrier coatings (see next section). β(Ni,Pt)-Al coatings may either be formed via a low-activity (outward-grown) route or a high-activity (inward route), depending on the

aluminising method employed. Both diffusion coating types make use of platinum to either enhance the oxidation and corrosion protection of β(Ni,Pt)-Al coatings [52] or remove the need for aluminising entirely in γ/γ' coatings [53]. Both β(Ni,Pt)-Al and γ/γ' coatings are expected to form α-alumina. Following depletion of aluminium reserves, the system enters into breakaway oxidation [54] forming non-protective Ni and Co oxides.

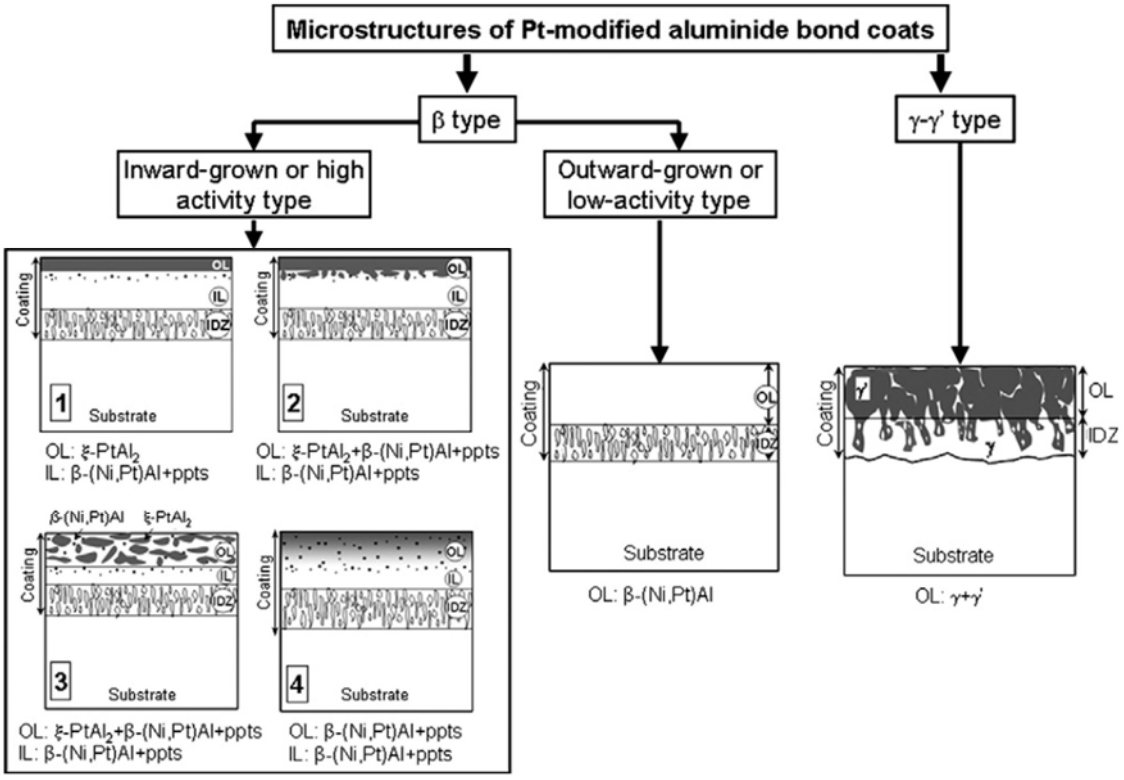

Figure 24 – Schematic microstructures of Pt-aluminide β-(Ni,Pt)Al and Pt-modified (γ/γ') diffusion bondcoats on nickel-base superalloys. Both inward-grown (high-activity) and outward-grown (low activity) β-(Ni,Pt)Al bondcoats are indicated. Where indicated, OL refers to the outer layer, IDZ the inter-diffusion zone, IL the intermediate layer [55].

The binary Ni-Al (Figure 25) phase diagram indicates that β-NiAl is the most stable phase at the highest temperature in the system. The ternary Ni-Pt-Al phase diagram (Figure 26) indicates the range of Pt addition required to form β(Ni,Pt)-Al.

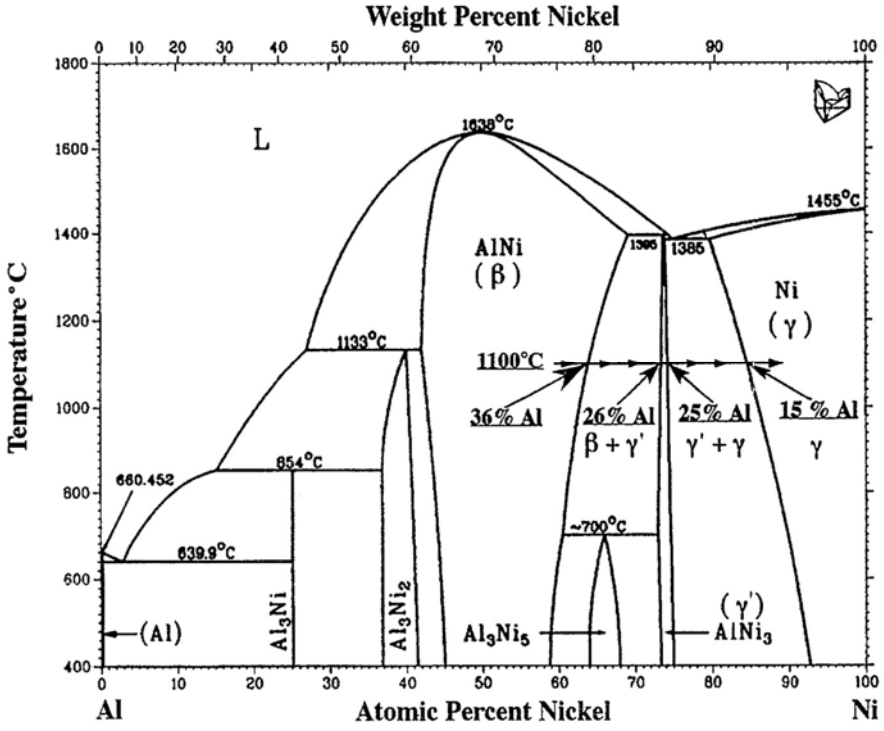

Figure 25 - Binary phase diagram for Ni-Al with reference made to phase transformation following the depletion of aluminium at temperature [56].

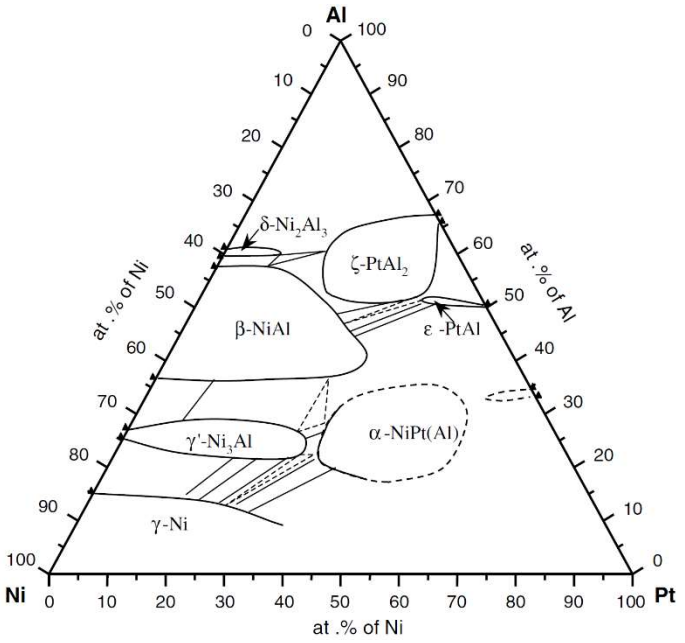

Figure 26 – Tertiary Ni-Pt-Al phase diagram at 1100°C [52]. *Note that bottom axis refers to Pt at%.*

1.4 Thermal Barrier Coatings

1.4.1 Introduction

Thermal barrier coatings (TBCs) are a class of protective coatings designed to be used with aerodynamic cooling features of turbine blades. When combined with a cooling film around the blade aerofoil the surface temperature of the superalloy substrate may be reduced substantially (≥100°C) [47,57]. In addition to reducing the heat transfer to the underlying component, the role of the TBC system is to reduce the oxidation attack of the superalloy substrate through preferential oxidation of the bondcoat to form a dense oxide barrier that resists further oxidation. Reduction in heat transfer is achieved through the use of a stable ceramic material as the contact surface with the hot gas stream (topcoat) with a low thermal conductivity [58]. Oxidation protection is provided through preferential oxidation of a slow-growing alumina (thermally grown oxide or TGO). Alumina is chosen because of stability at engine operating temperatures and its slow growth rate. The growth of the alumina layer (0.5µm – 10µm) is promoted by the addition of aluminium to the surface region of the superalloy (below the topcoat) and may be one of two types of bondcoat. The bondcoat may either be overlaid (mechanically adherent) or a diffusion type (chemical surface modification). It is still unclear which of the bondcoats offer longer coating lives (Figure 29 shows that both are essentially the same). Diffusion coatings have higher aluminium contents but are thinner than the MCrAlY type even though the latter has less aluminium. For rotating components at the highest temperature (i.e. HP1 stage) where the total mass is critical (turbine blades can rotate up to 12,000 rpm), diffusion type coatings are preferred.

Overlay coatings may be applied through a variety of spraying methods, for example air plasma spraying (APS) [59] low pressure plasma spraying (LPPS) [60] or high velocity oxy-fuel (HVOF) [61] spraying. These methods may also be used to apply both overlay bondcoats and overlay topcoats. A further method of applying the ceramic topcoat is electron beam physical vapour deposition (EB-PVD). This process results in a columnar microstructure with the preferred orientation normal to the surface. One of the key advantages of EB-PVD topcoats over the equivalent overlay type is in strain tolerance. EB-PVD topcoats, owing to their columnar nature, are free to laterally expand to a certain extent without cracking at the base. This strain tolerance is advantageous both in terms of thermal cycling where upon expansion and contraction residual stresses will be lower but also in terms of remaining adherent to complex geometries. A downside of the inter-columnar spaces, of course, is that oxygen diffusion is not prevented and the oxidation rates are slightly impacted.

1.4.2 Topcoat

The ceramic topcoat component of TBCs consists primarily of zirconia that is partially stabilised with 7-8wt% yttria (7-YPSZ). The addition of yttria delays the onset of tetragonal to monoclinic phase transformation [62,63]. EB-PVD topcoats are deposited atop a roughened bondcoat (rotating specimen) in a vacuum chamber where ingots of YSZ are laser heated [64]. This leads to a columnar microstructure (Figure 27) with a growth direction perpendicular to the substrate surface owing to cooling on contact. Near the surface, a zone of competitive growth exists. The individual columns display a feathery microstructure (Figure 28) that coalesce on exposure to high temperatures.

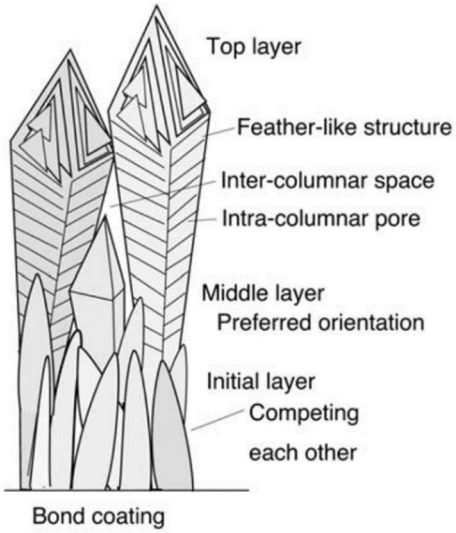

Figure 27 - Columnar microstructure of EB-PVD topcoat of thermal barrier coating [65].

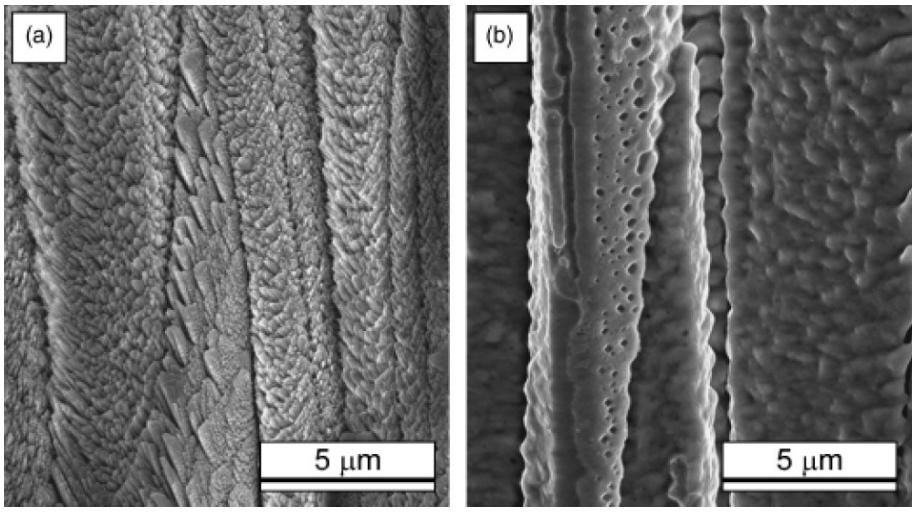

Figure 28- EB-PVD columns (a) in as received condition and (b) showing sintering following 200 hours at 1150°C [66].

1.4.3 Failure of TBC systems

Final failure of the TBC system often occurs by buckling [67]. A zone of decohesion a few mm in diameter is needed to produce an initial buckle during the final, fatal cool. Coating life is determined by the rate of development of this zone. TGO growth is implicated as a possible damage mechanism proposed by Evans [68] through a critical strain energy criterion. The controversial aspect of this model is that he argues that the strain energy in the top coat itself only has a second order effect and it is the strain energy

in the TGO that drives the failure process. For an oxide/metal system with a flat interface and thin oxide, the effective interfacial fracture energy per unit area [69] is given by

$$\gamma_F = h\left(\frac{\left(\sigma_g + E_{ox}(\Delta T)(\Delta\alpha)\right)^2 (1-\nu_{ox})}{E_{ox}}\right) = hW^*$$

For NiCrAlY [70] and NiAl [71], $\sigma_g \sim 0$ so that re-arranging the previous equation for γ_F gives the critical temperature drop, ΔT_c, for spallation to occur as

$$\Delta T_c = \left[\frac{\gamma_F}{E_{ox}(1-\nu_{ox})(\Delta\alpha)^2 h}\right]^{0.5}$$

For an MCrAlY system without a topcoat a critical oxide thickness of 3 μm was required to initiate oxide spallation [72]. This corresponds to an interfacial fracture energy of approximately 55 Jm^{-2}. When comparing TBC failure times a similar value of γ_F produces reasonable agreement with the data (Figure 29). It was on this basis that Evans [68] argued that the contribution to the total strain energy could only be second order.

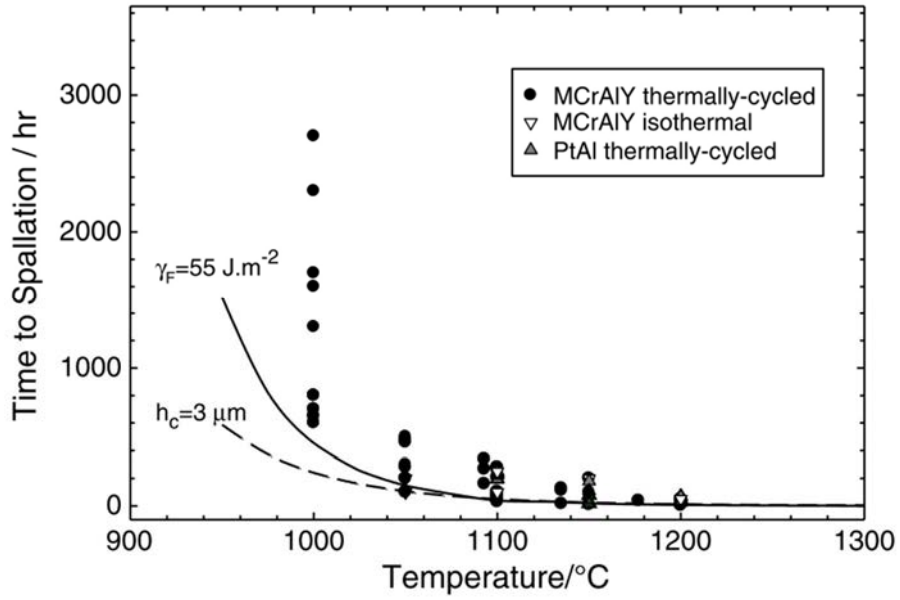

Figure 29 – Calculated TGO critical strain energy for spallation shown alongside experimental time to spallation for MCrAlY and Pt-aluminide diffusion bondcoat TBC systems [68].

Alternative failure mechanisms envisage the formation of a rumpled bondcoat under thermal cycling conditions and this reduces the adhesion of the topcoat [73,74]. The difficulty with this approach is that rumpling has not been seen on actual TBC systems, that is, with a topcoat present. It certainly does occur in the absence of a topcoat as shown in Figure 30a.

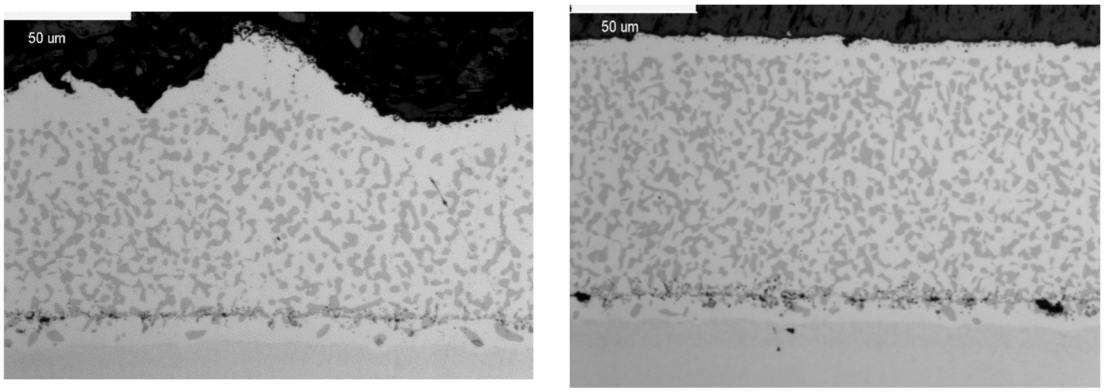

(a) (b)

Figure 30 – MCrAlY bondcoat applied to the same superalloy substrate (a) without a topcoat showing rumpling and (b) with a topcoat showing no rumpling [68]. *Image courtesy of D. S. Rickerby, Rolls-Royce.*

A more satisfactory model of failure derives from the work of A.G. Evans [75–77] and is termed ratcheting. Examples are shown in Figure 31 and demonstrate how the bondcoat can detach from the topcoat.

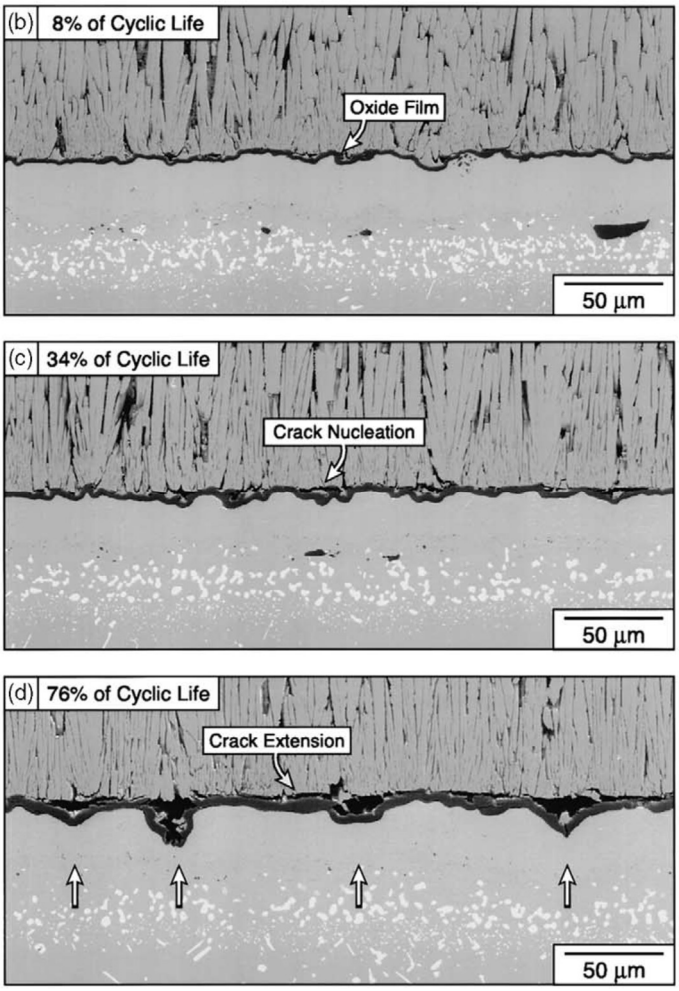

Figure 31 - Ratcheting (downward displacement of TGO/bondcoat interface) showing periodic separation of the topcoat from the TGO with cyclic oxidation [75].

The complexity of the failure mechanisms may be appreciated from Figure 32. Here failure times for a variety of coating systems are compiled and demonstrate clearly that a factor of 10 in TBC lifetimes at any given temperature is not uncommon. The causes of this variation have not been properly identified but Meier [67] has shown that surface roughness of the bondcoat is an important factor in TBC life but is a somewhat uncontrolled variable in TBC manufacture.

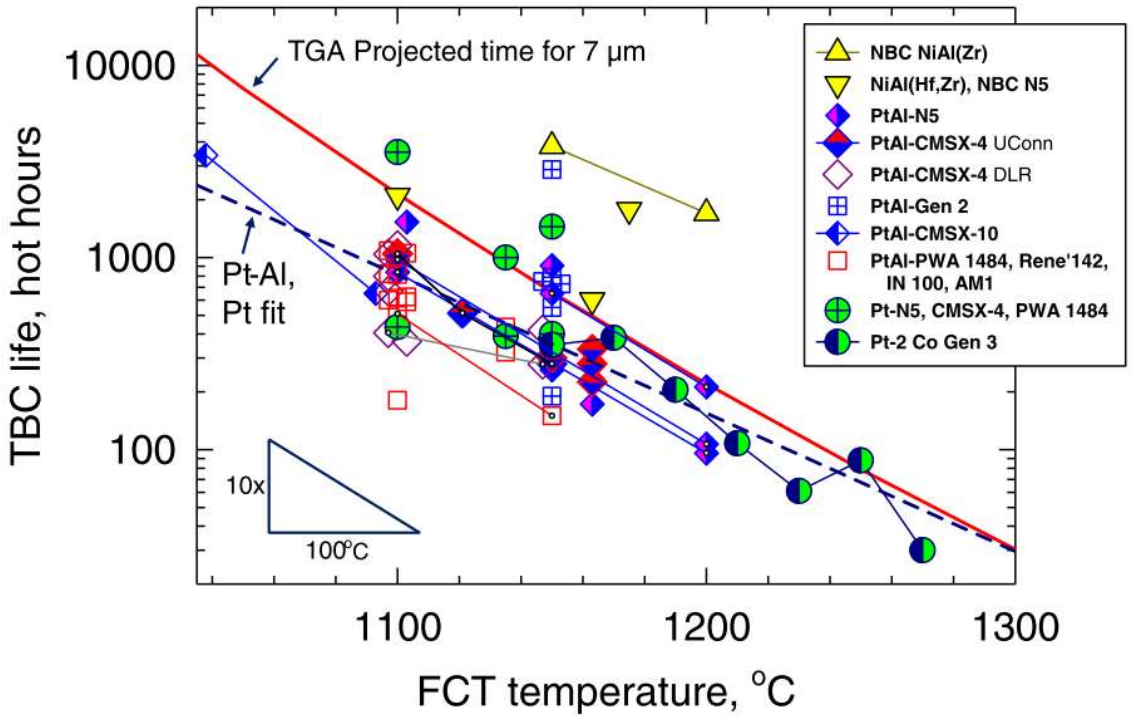

Figure 32 Compiled literature time to spallation for a variety of diffusion bondcoats and superalloy substrates under thermal cycling conditions [78].

Busso et al. [54,79] has used observations such as this to undertake a model analysis of stress development within the TBC system for different bondcoat roughness. They find that the rougher the bondcoat the higher the stresses developed at the base of the topcoat (Figure 33). Peak out of plane stresses occur at the flanks of the asperities where cracks in the topcoat are often found (see Figure 31 for horizontal cracks emanating from flanks into the topcoat).

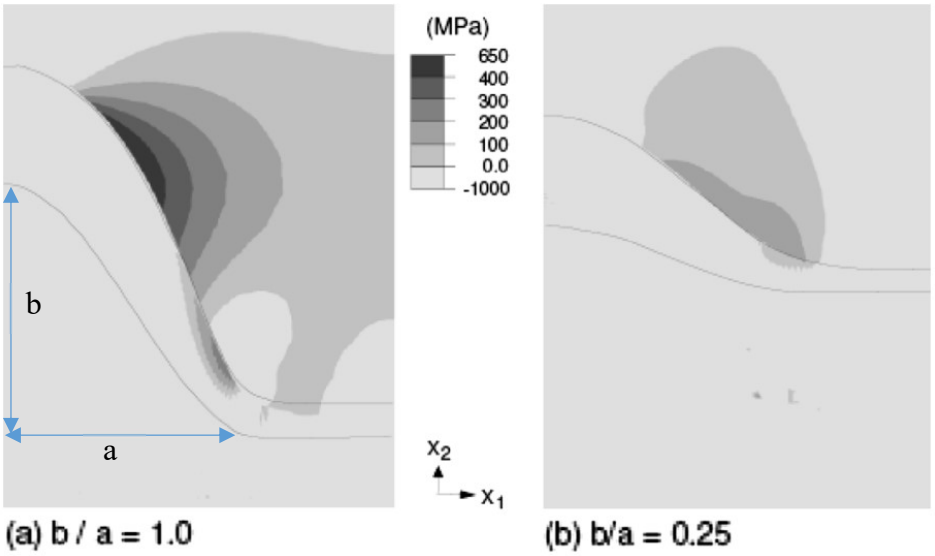

Figure 33- The influence on bondcoat roughness on out-of-plane stress predicted using finite element model at 1100C following 200 hours [54]. *Bondcoat roughness is defined by the aspect ratio b/a.*

In addition to oxidation-induced failure described, topcoat failure may occur by foreign object damage (erosion) or corrosion (or a combination) from calcium-magnesium-alumina-silicate (CMAS) infiltration [80]. Other failure models favour void formation at the TGO bondcoat interface [81,82].

The TBC system of choice examined in this work is the single-crystal CMSX-4 single crystal nickel-based superalloy substrate coated with either the commercially available RT22 β(Ni,Pt)-Al bondcoat or the patented Rolls-Royce γ/γ' low-cost bondcoat [83]. The topcoat in the TBC systems considered is an EB-PVD topcoat.

1.5 Non-destructive analysis techniques

1.5.1 Optical flash thermography

There are many variants of thermography however all the methods rely on the principle that objects above 0 K emit a finite level of infra-red (IR) radiation and that by applying heat energy to a body the amount of IR emitted will rise [84]. By applying heat then

recording the IR levels emitted by a body, the heat distribution on that body may be recorded. The heat source need not be external to the body, for example cyclic loading may provide the thermal excitation [85] or in the case of fully passive thermography, making use of existing thermal differences between voids and a continuous body [86]. The many options available in applying this heat energy permit variations of the method. For example, the use of lasers in laser excited thermography [84] allow a controlled, local application of heat whereas the indiscriminate burst of heat applied by pulsed thermography allows rapid and large-scale analysis of say, concrete structures. The heat dissipated by the body may be approximated using the equation [87] given by

$$T(t) - T_0 = \frac{\mathbb{E}}{\kappa\rho c\sqrt{\pi t}} \qquad \textit{Eq. 16}$$

for a semi-infinite defect-free plate. The difference in temperature T at time t and $t = 0$ is thus a function of $\mathbb{E}Q$, the input energy (per unit area), the specific heat capacity c and thermal conductivity κ.

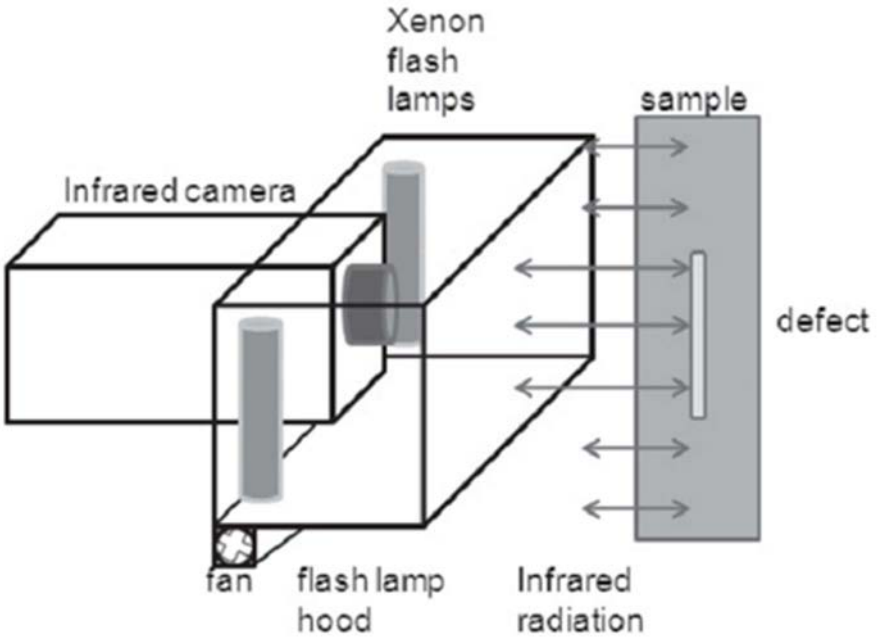

Figure 34 – Schematic of optical flash thermography system used to detect sub-surface damage.

1.5.2 Photoluminescence piezospectroscopy

Piezospectroscopy is used for analysing the wavelength shifts induced by crystal fields. Applications include analysis of optical materials, high pressure calibration of diamond anvils and stress analysis of polycrystalline alumina [88]. In thermal barrier coatings, fluorescence occurs through the emission of photons from Cr^{3+} ions in the TGO. A 514nm [89] green laser excitation source applied to these ions promotes them to an unstable, high-energy state. On decay to their ground state, photon emission occurs with a corresponding R line doublet fluorescence (R1 and R2) having wavelengths of 14402 and 14432 cm^{-1} respectively [90]. The R2 peak shift relative to a ruby standard is used for calculation of stress state [91]. The R2 peak is preferred over the R1 peak owing to the non-linear dependence on stress of the R1 peak [92]. The technique takes advantage of the fact the EB-PVD topcoat is somewhat transparent to visible light [93]. Upon straining of the crystal, the crystal field is perturbed and shifts in the wavelengths of the R lines occur (Figure 35). This process is termed the piezospectroscopy effect. In order to achieve high spatial resolutions, the laser beam is shone through the optics of a microscope (Figure 36).

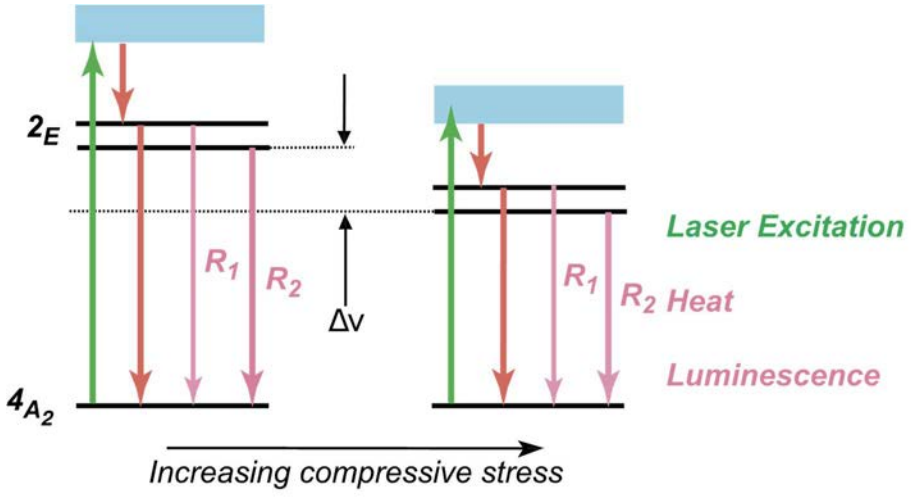

Figure 35 – Schematic of experimental setup for photoluminescence piezo-spectroscopy and b) example R-shift in photoluminescence spectra following the application of a stress to the TGO [94].

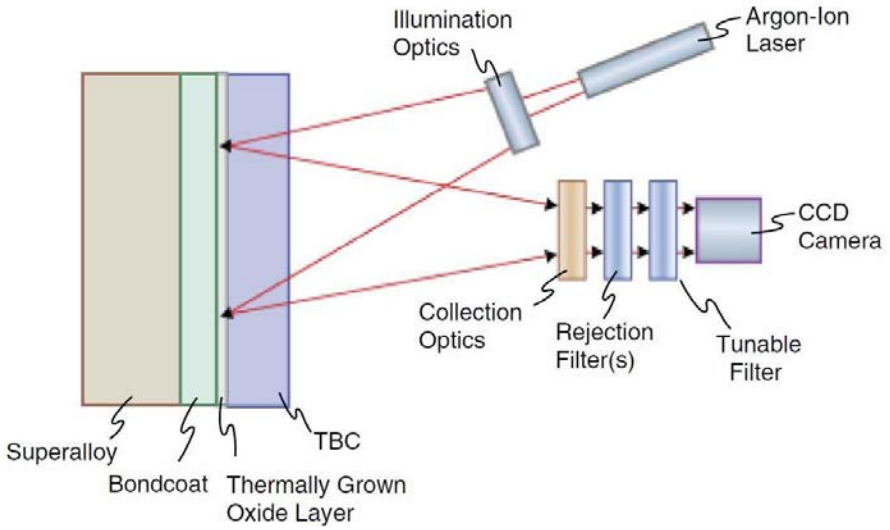

Figure 36 – Schematic of luminescence process under the action of a compressive stresses in the TGO from the presence of Cr^{3+} [94].

For a biaxially constrained thin scale, the local stress-induced frequency shift is given by [95]:

$$\Delta\nu = {}^{2}/_{3}\,\Pi_{ii}\sigma_{R}^{mis} \qquad \textit{Eq. 17}$$

in which the peak shift $\Delta\nu$ (cm^{-1}), is related to the crystallographic stress (σ) through the piezospectroscopic tensor Π_{ii} $(cm^{-1}GPa^{-1})$. From measured peak shifts through the topcoat, the TGO stress may be inferred through the experimentally determined relationship [92]:

$$\Delta\nu = 5.07\sigma \qquad \textit{Eq. 18}$$

For peak shifts measured from cross-sections the normal components of the stresses must vanish and the measured frequency shift is lowered by a factor of $\frac{1-\upsilon_{TGO}}{2}$ to give [92]:

$$\Delta\nu_{cross\ section} = 1.98\sigma \qquad \textit{Eq. 19}$$

Numerous authors have applied the technique to study the stress state of Pt-aluminide and Pt diffusion bondcoat systems [45,92,94,96–104], overlay bondcoat systems [100,105–108] and model alloys [90]. Two approaches are generally taken, the first of which directs

the laser beam through the topcoat and back for analysis while the second examines destructive cross-sections.

Heeg et al. [94] applied the technique to study the TGO stress of four samples at various stages of what they considered total coating life (185 hours at 1150°C under one-hour thermal cycling) of platinum modified aluminide bondcoats on René N5. Maps over 4.4mm × 5.6mm sample areas indicate an average compressive residual stress of 1.4GPa following 2 hours (1%) while after approximately 100 hours (55%) this fell to approximately 0.75GPa.

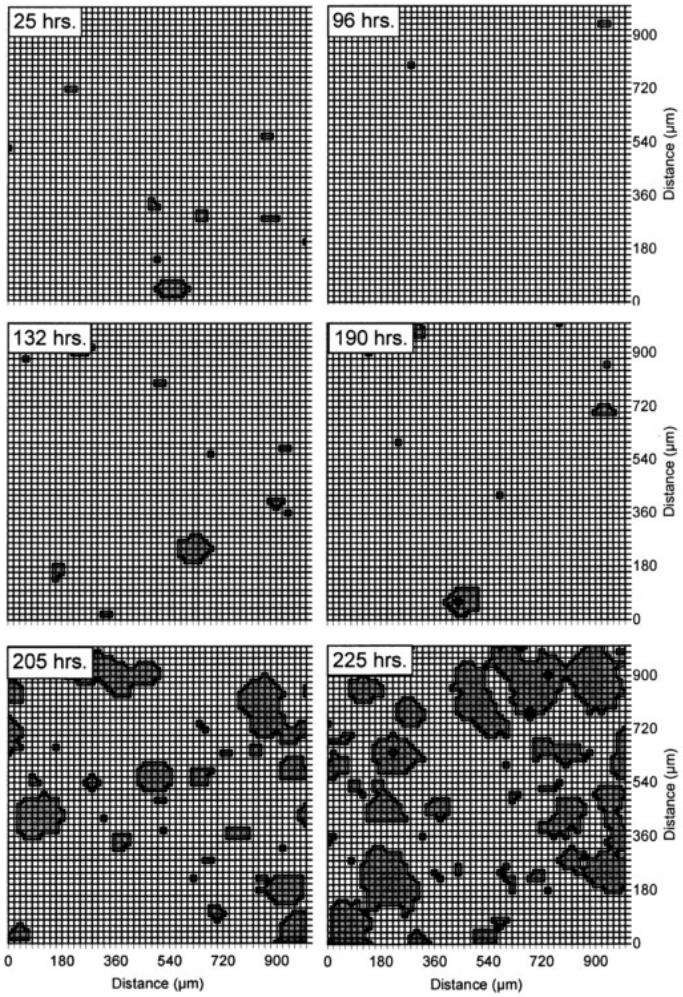

Figure 37 - PLPS maps showing low-stress damage areas (dark) for a specimen undergoing 225 1-hour cycles under a heating/cooling programme between 200 °C and 1150 °C [109].

In other work by Wen, Jordan and Gell [97] on samples at 1151°C, results (Figure 38) indicate a similar downward trend from a range of 2.0GPa to 2.3GPa decreasing to a range of 1.6GPa to 2.1GPa, following an initial increase from 1.5GPa in the as-received state. In contrast, Wang, Lee and Atkinson [96] noted a steady peak shift as a function of time (following an initial increase) when examining platinum-modified aluminide aerofoil sections similar to that used in this work under twenty-hour thermal cycles (Figure 39). A combination of these literature data in addition to contributions from Wang et al. [102], Lee, Atkinson and Selçuk [103], Wen Jordan and Gell [97], Tolpygo, Clarke and Murphy [45] and Sridharan et al. [98] are summarised in Figure 40. These results tend to show a decrease in room temperature TGO stress with increasing time but are complicated by the fact that the measurements include growth as well as thermal stresses.

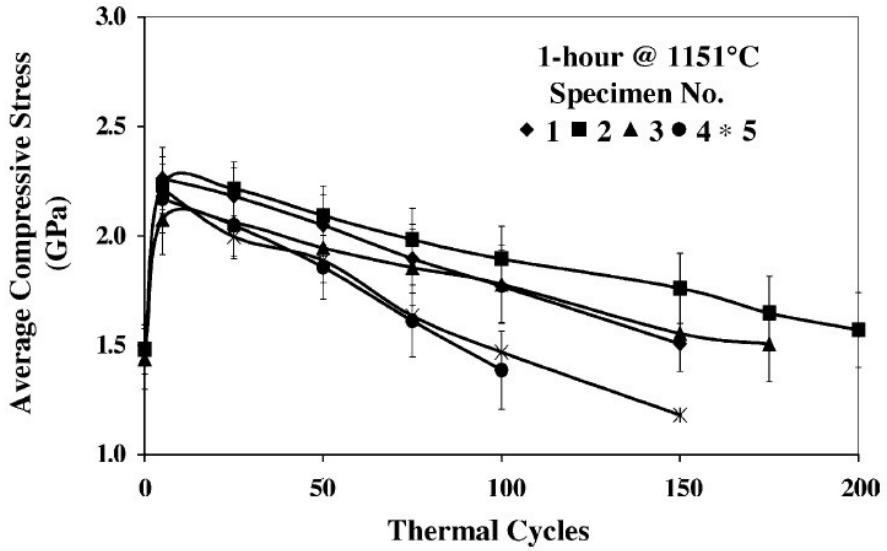

Figure 38 – Compressive stress measured by photoluminescence piezospectroscopic mapping as a function of time [97].

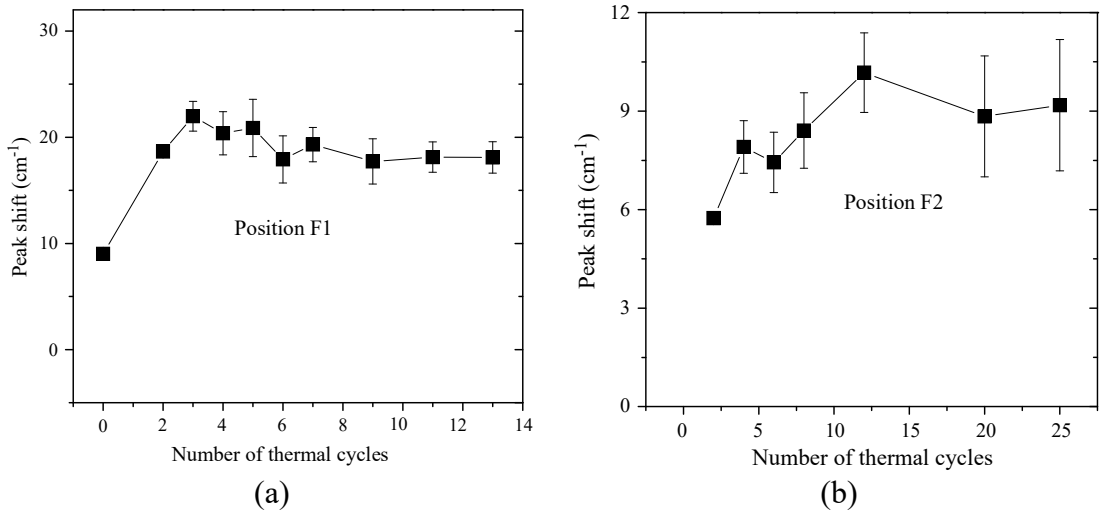

Figure 39 – Peak shift maps for two different samples undergoing twenty-hour thermal cycles at 1150°C.

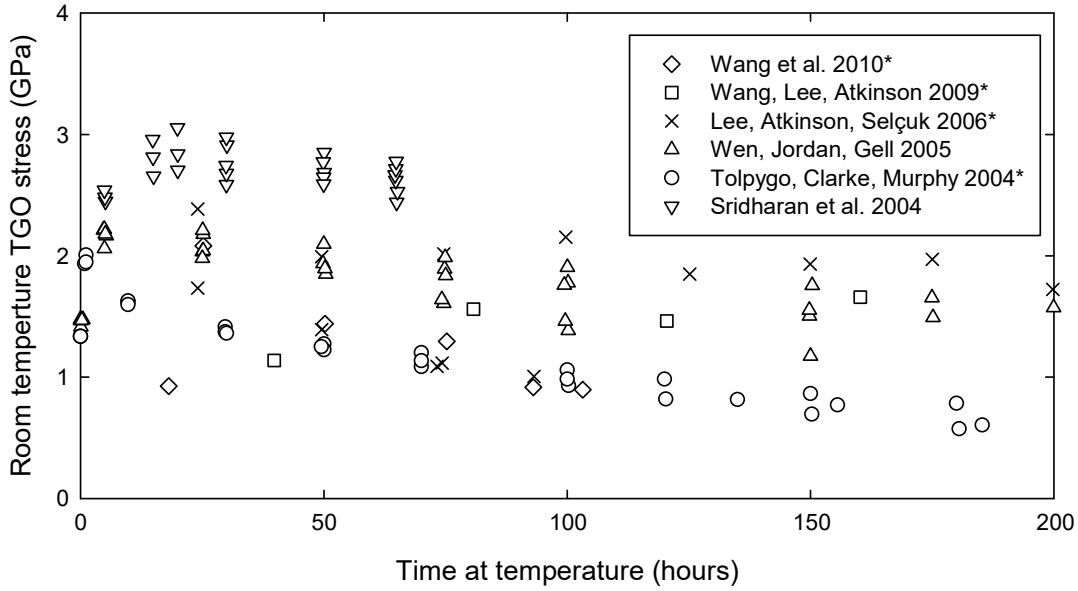

Figure 40 – Combined literature PLPS measurements (growth stress and thermal stress) of Pt-aluminide bondcoats under one-hour cycles (except where noted) from the work of Wang et al. [102], *Wang, Lee and Atkinson* [96] *(twenty-hour cycles), Lee, Atkinson and Selçuk* [103], *Wen Jordan and Gell* [97], *Tolpygo, Clarke and Murphy* [45] *and Sridharan et al.* [98]. *Legend entries denoted by an asterisk indicate TGO stresses calculated from peak shift using Eq. 18.*

1.6 Synchrotron X-ray tomography

1.6.1 Introduction

Synchrotrons (Figure 41) are experimental facilities that enable a wide range of scientific disciplines to make use of high energy X-rays. The synchrotron radiation exploits the loss of energy associated with alteration of electron trajectories such that changes in direction result in radiation emission. By controlling the trajectory of electrons travelling in a near-circular orbit close to the speed of light, a range of tuneable X-ray emissions are generated. A synchrotron is designed so that a number of experimental beamlines can manipulate such X-rays for specific applications, ranging from X-ray tomography to protein crystallography. At the time of writing, the Diamond Light Source is the sole such facility in the United Kingdom (Figure 41) and the beamline of interest to the study of thermal barrier coatings is I12, the joint engineering and environmental processing (JEEP) beamline.

1.6.2 The physics of third generation synchrotrons

A third-generation synchrotron typically consists of a main storage ring (of the order of 500m diameter) and a series of beamlines. The purpose of the storage ring is two-fold, (1) to maintain the velocity, trajectory, profile (100μm × 100μm [110]) and energy (3GeV) of the electrons and (2) to condition the X-ray beam before supplying to the beamline. Electrons are generated using a filament source and accelerated using a linear accelerator (linac). A booster ring is used to further accelerate electrons before transfer to the main storage ring (under ultra-high vacuum). The storage ring (Figure 42) consists of a series of arcs and straight sections with dipole bending magnets to apply directional

changes while maintaining electron velocities near the speed of light. Each time the electron path is changed, radiation emission occurs which may directly be used by a beamline or further conditioned with a wiggler or undulator insertion device (ID, see later for definition). Regardless of whether a beamline is situated after an arc section of the storage ring, the lost energy of the electron beam through emission must be replaced to prevent the electron beam from colliding with the storage ring inner wall. Radio frequency cavities are used to replace lost electron energy using a klystron vacuum amplifier [111].

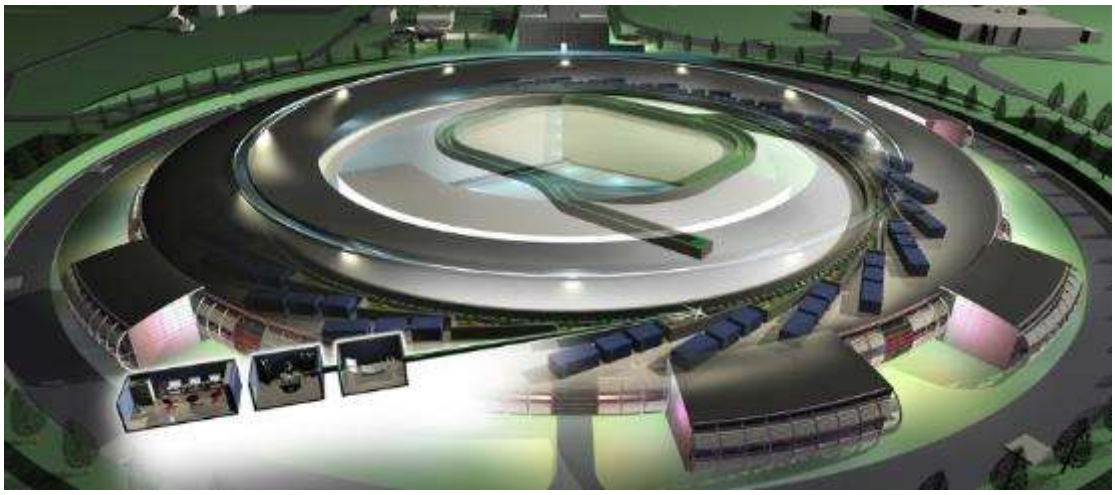

Figure 41 – Schematic of Diamond Light Source showing linear accelerator and booster ring within main storage ring, approximately 500m in diameter. A series of beam-lines are visible emanating from the main storage ring with the insert showing experimental hutches.

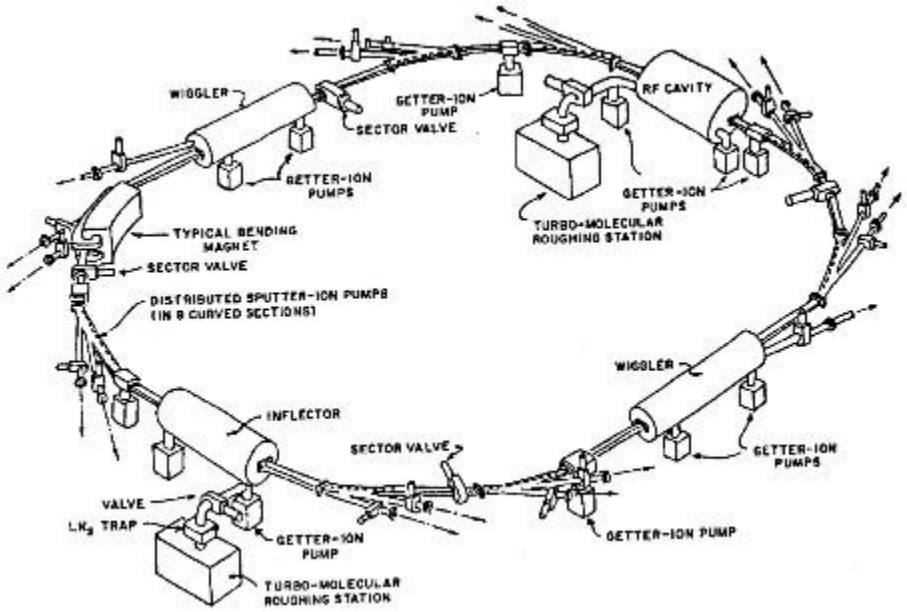

Figure 42 – Schematic of a small-scale electron storage ring showing a typical bending magnet to direct the electron path, wigglers to intensify the emission beam and RF cavities to replace lost energy from the beam [112].

By operating near the speed of light, the X-ray emission pattern can be substantially more focused and collimated when compared to lower velocity electrons (Figure 43b) where the emission is in a dipole pattern [112]. Near the speed of light (Figure 43a), relativistic effects distort the angular distribution and the emissions become concentrated tangentially to the orbital direction [113].

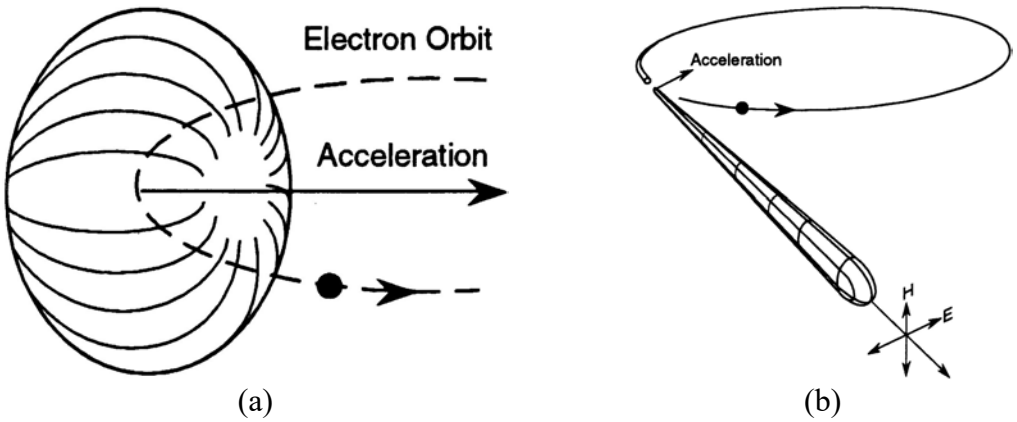

Figure 43 – The effect of velocity on the radiation emission pattern from electrons in a circular orbit for (a) low velocity electrons resulting in a dipole pattern and (b) high velocity electrons near the speed of light emitting radiation in a collimated beam [112].

Orbital motion is maintained through a series of bending magnets but recent generation configurations also make use of wigglers and undulators (Figure 44) combined with

bending magnets at arc sections to refine the X-ray emission trajectory and energy bandwidth. Undulators and wigglers placed before the entry to a beamline are referred to as insertion devices (ID). These insertion devices consist of alternating magnetic fields that cause the electron beam to repeatedly change direction. A distinction between the two types of Insertion devices is made through the energy band given by the K_U value [114] of the insertion device:

$$K_U = \frac{eB\lambda}{2\pi\gamma m_c} \qquad \textit{Eq. 20}$$

Where γ is the electron velocity, λ is the distance between magnets in the same orientation. Undulator IDs have $K_U \ll 1$ while wiggler IDs have $K_U \gg 1$.

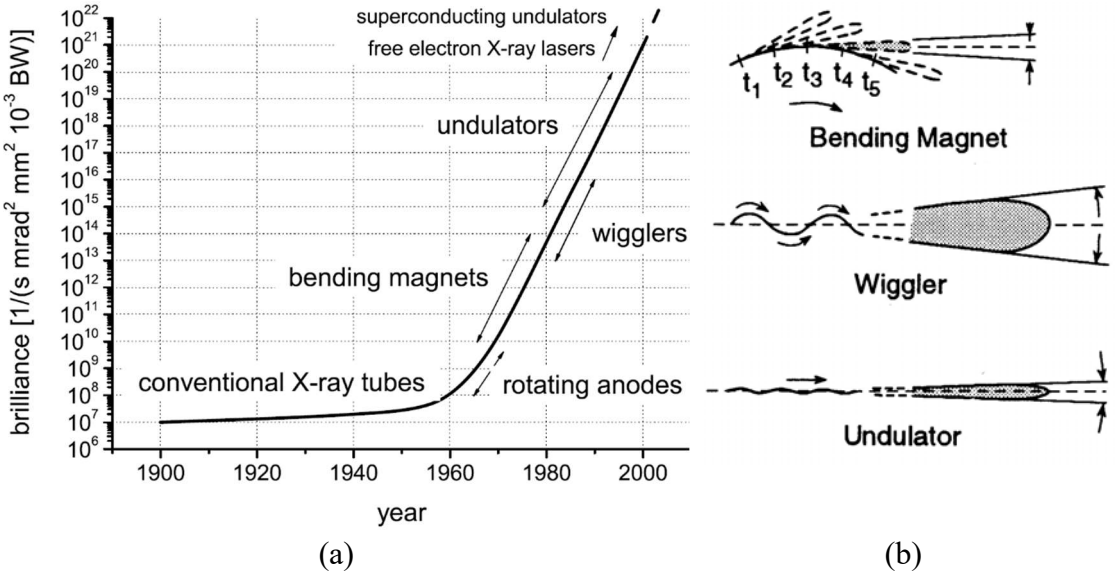

Figure 44 – Improvements in synchrotron (a) brilliance (or spectral brightness) achieved through development of wigglers and undulators [115] *and (b) schematic of emission beam geometry with successive developments in electromagnet technology* [112].

1.6.3 The interaction of X-rays with matter

Atomic absorption of X-rays is through scattering following interaction with the electronic configuration of an atom and consists of coherent (Rayleigh) scattering, incoherent (Compton) scattering and the photo-electric effect. The total energy loss by the X-rays and hence attenuated (the reduction in beam energy by atomic absorption) by

an atom is given by the total of these scattering energies in addition to the pair electron and nuclear production energies (Figure 45 for energies of alumina, for instance). Mass attenuation is the key material property used to distinguish between elements, compounds and mixtures. In general, the energy of a photon $\mathcal{E}$ in vacuum is given by de Broglie's wavelength of a particle with rest mass zero [116] as

$$\mathcal{E} = hv = hc/\lambda$$

Where $h = 6.626\times10^{-3}\ Js$ (Planck's constant), v the frequency of radiation in Hz, $c = 2.9979\times10^{8}ms^{-1}$ is the speed of light in vacuum and λ is the wavelength of light in metres. To compute the attenuation of X-rays through a homogeneous material, Beer's law states

$$\phi(x) = \phi_0 e^{-\mu}$$

Where ϕ_0 is the incident photo flux (photons per second per unit area), $\phi(x)$ is the photon flux after traveling a distance x and μ is the linear attenuation coefficient of the medium being traversed. In the case where the material is not homogeneous and the attenuation coefficient varies with distance traversed by the beam, a projected attenuation p is used, given by

$$p = \int_0^X \mu(x)\,dx \qquad \textit{Eq. 21}$$

Hence the flux is given by

$$\phi(x) = \phi_0 e^{-\int_0^X \mu(x)dx} \qquad \textit{Eq. 22}$$

The mass attenuation coefficient μ/ρ is defined as the ratio of the linear attenuation coefficient and density. It is used to calculate the mass of a material required to attenuate a primary beam by a prescribed amount such that

$$\frac{\phi}{\phi_0} = e^{-\left(\mu/\rho \cdot x\right)} \qquad \textit{Eq. 23}$$

In this case, x is the thickness of the attenuating material per unit area of beam, and ρ the density of that material. In relation to the energy of an incident X-ray beam the chemical binding energies are so small such that chemical compounds may be treated as mixtures. Hence the mass attenuation coefficient of a mixture consisting of n components is given by

$$\left(\mu/\rho\right)_{mixture} = \sum_{i=1}^{n} \left(\mu/\rho\right)_i \cdot w_i \qquad \textit{Eq. 24}$$

where w_i is the weight fraction of each compound component. Databases of X-ray absorption such as XCom [117] are widely available and software applications such WinXCom [118,119] allow automatic calculation of mixtures and compounds from elemental data.

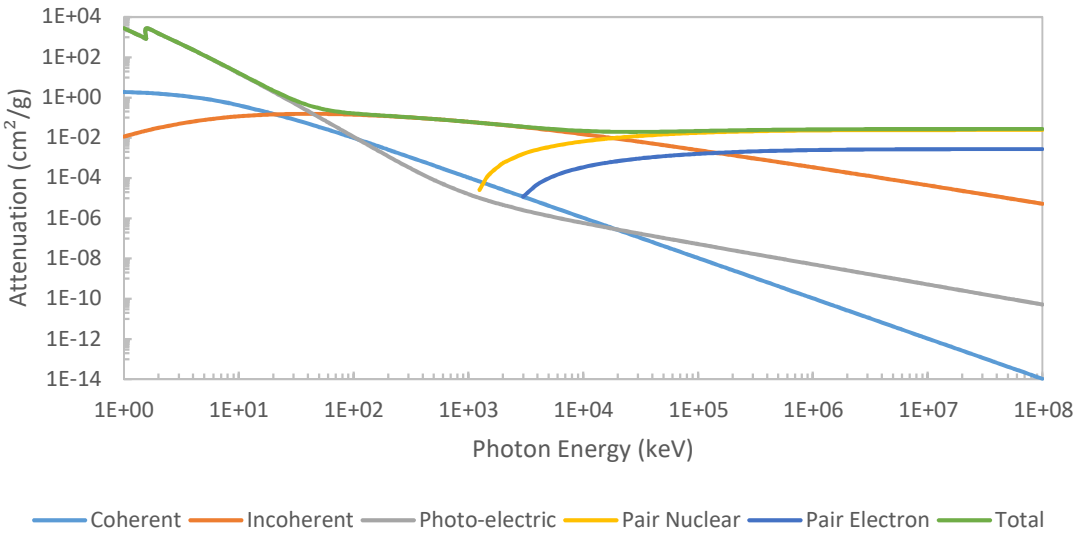

Figure 45 – Attenuation components of Al_2O_3 from different scattering sources including coherent (Rayleigh), incoherent (Compton) photo-electric and the total attenuation, data generated using WinXCom [118].

1.6.4 X-ray micro-computed tomography

X-ray tomography is a volumetric imaging technique that utilises the difference in attenuation (a function of atomic number and density) of materials to generate through-thickness contrast. It is a non-destructive imaging method that allows the internal structure of an object to be revealed when only the surface is visible. The technique consists of recording a series of two-dimensional radiographs at known rotations and back-tracing the radiographs to reconstruct the original object in three-dimensional space. In general, two methods are used to generate X-rays, cone-beam (or fan-beam) point sources that are polychromatic in wavelength (and divergent in nature) and parallel beam sources that generate monochromatic X-rays. Fan-beam X-ray tomography systems are compact and relatively simple whereas parallel beam configurations require highly specialist facilities, typically a synchrotron. A recent addition to the field is the development of the compact light source [120] in which an improvement in resolution and beam quality is achieved at a smaller scale than a synchrotron.

1.6.4.1 Reconstruction from filtered back-projection

The Radon transform [121] is the mathematical operation used to produce cross-sectional slices from a series of radiographs [122]. For each cross-sectional slice, a sinogram is computed using the Radon transform (Figure 46).

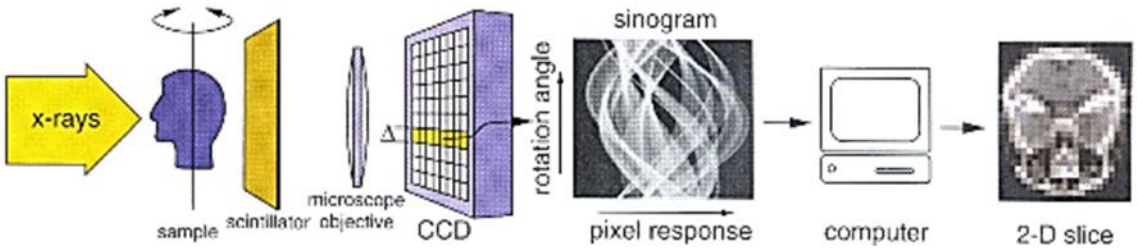

Figure 46 – The general sequence of image acquisition and reconstruction in X-ray tomography for both parallel and cone-beam source. A series of 2-D radiographs are captured with the sample rotating about a centre of rotation which are then reconstructed using back-projection to reveal 3-D slices showing the internal volume of the original sample [123].

1.6.4.2 Laminography

Conventional computed tomography, given the rotating nature of image acquisition, performs best with cylindrical-shaped specimens that have a relatively low aspect ratio and fit within the detector field of view. These requirements can complicate the imaging of planar samples; however, by modifying the image acquisition process and reconstruction algorithm, computed laminography [124,125] allows one to overcome the dimensional constraints of planar computed tomography (Figure 47). The method is very closely related to conventional tomography with the key difference being that the centre of rotation in inclined relative to the incident X-ray beam and consequently the way in which reconstructions are computed.

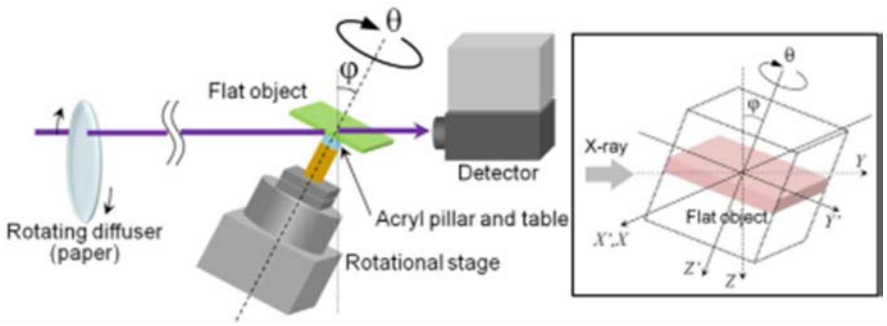

Figure 47 – Schematic of stage and detector configuration for synchrotron laminography [126]*, a variation of synchrotron tomography.*

1.6.4.3 X-ray tomographic imaging of TBCs

Numerous studies have applied X-ray micro-tomography to study TBCs, however in almost all such work, a single point in time is considered without consideration of the initial state of the TGO. Imaging of an APS TBC [127] for example, was carried out using a lab-source 160keV Xradia XRM-510 following 60% of time to spallation (the authors do not reveal cycle and temperatures). Although cracks (primarily in the topcoat) were segmented (the method of 3-D feature extraction, see section 2.8.6), the minimum crack length detected was approximately 50μm which is a direct reflection of the limited

resolution of that experiment. In similar work carried out at the Henry Mosely X-ray imaging facility, Manchester [128], an APS specimen was thermally cycled from the as-received state at 1150°C. The equipment used however was lab-based and consequently limited in resolution. To overcome this challenge, the samples were ground to a wedge shape and in the as-received case, the TGO was not detectable. Other recent work examining the bondcoat roughness of disk-shaped APS coatings [129] were also limited by resolution.

At the other resolution extreme, ultra-high resolution nano tomography has been applied by Yan et al. at the Advanced Photon Source, Argonne National Laboratory [130]. This work however, did not consider TBCs and the samples were cylindrical pins 20μm in diameter. One of the limitations of TBC samples this small is that the oxidation behaviour and subsequent stress states are unlikely to be representative of in-service conditions.

In other, earlier synchrotron work carried out at at the Advanced Photon Source, on TBCs, artificially thick (800μm) EB-PVD topcoats were imaged and porosity analysed using neutron and X-ray scattering [131]. The authors claim a resolution of 1.3μm per pixel for the tomography aspect of the work and their scans were only carried out on the as-received condition of the coatings. In related work by the same authors [132], the effect of thermal exposure on the porosity in topcoats (with 250μm thickness) was analysed at the at the Advanced Photon Source and the porosity under the influence of sintering shown to decrease from 20% to 10% following 500 hours at 1200°C.

Recent work by Maurel et al. [133] using synchrotron laminography at the European synchrotron radiation facility (ESRF, Grenoble) showed the TGO of a pre-oxidised Pt-aluminide TBC system. Although their work revealed detail of the TGO/bondcoat interface, the as-received case was not imaged. In subsequent work [134], the same group

applied laminography to different samples exposed to cyclic oxidation conditions. It is noteworthy that the same specimen was not repeatedly scanned but a selection of thermally cycled specimens were extracted from a larger test piece.

1.6.5 Wide, small and ultra-small angle scattering

Small and wide-angle X-ray and neutron scattering (SAXS, WAXS, and SANS respectively) are techniques that may be used to measure matrix inhomogeneities such as porosity [135]. In general, small angle scattering is categorised as $\theta < 1°$ and wide angle scattering as $5° < \theta < 60°$ where θ is the scattering angle. Features between 1nm and 1μm may be resolved with SAXS and up to tens of micrometres under ultra-small angle conditions (USAXS). Generally, neutron scattering methods are used for thick samples (order of millimetres) where resolutions are lower while X-ray sources for thinner samples [136]. Much of the work surrounding small angle scattering (SAS) to date, has been performed at the APS, Argonne in which topcoat porosity under various conditions has been quantified [137,138]. The preferred orientation of the Y-PSZ columns and range of different pore sizes (inter-columnar, intra-columnar and nano-pores within feathers) lend themselves well to SAS techniques (Figure 48).

Although SAS from synchrotron sources are very capable in resolving a range of porosity within the topcoat; it should be noted that the data extracted from the scattered beam is an average of the through-thickness porosity. For example, work carried out by Renteria et al. [139] analysed EB-PVD topcoats (400μm topcoat thickness) that were 200μm long (in the direction of the incident beam). The computed porosity volume fractions are thus an average of the 200μm thickness and a single slice through the topcoat, for example cannot be isolated. USAXS has also been applied to TBC topcoats by Hass et al. [140]

in which changes in porosity of the topcoat with manufacturing process parameters were observed. They noted a monotonic increase in porosity with increased deposition pressure.

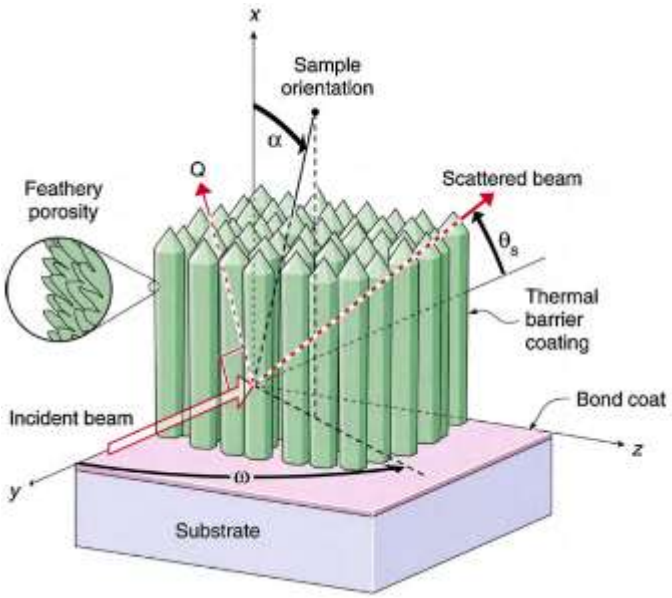

Figure 48 – Schematic of synchrotron-based ultra-small angle X-ray scattering (USAXS) configuration [140].

1.7 Digital volume correlation

1.7.1 Introduction

In three dimensions, digital volume correlation (DVC) is an extension of the two dimensional in-plane digital image correlation technique (DIC). At its simplest and in two dimensions, the concept is to compare two images of the same specimen (before and after a deformation) and attempt to locate the same pixel set (image subset) in both images and compute the displacements for that pixel. DIC requires that a texture covering at least a few pixels of the recorded image be present to allow algorithms to detect patterns [141]. To improve the accuracy of the determined pixel match (the correlation), a subset of pixels surrounding the interrogated pixel is chosen and compared between images (Figure 49) and the displacement vector of this subset determined [142]. The displacement field over the entire domain is evaluated to sub-pixel or sub-voxel accuracies via an appropriate interpolation function [143]. This approach, i.e. quantizing the domains of interest and individually correlating them is referred to as a local correlation algorithm. An alternative approach, referred to as a global correlation algorithm, computes displacements based on a continuous input field (similar in principle to the finite element method) [144].

In the software system used in this work (LaVision StrainMaster 8.0), a local correlation algorithm is used that utilises a fast Fourier Transform (FFT) cross-correlation to compare sub-volumes in three dimensions. A multi-pass approach is used to deform the sub-volumes to compute the strain vectors using displacement gradient information from the previous passes [145]. The size of the sub-volumes (referred to as window size in this software package) is variable and a progressively decreasing window size may be selected for analysis. In general, increasing the window size enhances the numerical accuracy of

the displacement field computation over a larger averaged sub-volume at the expense of displacement field resolution. An additional consideration when utilising information obtained from DVC analysis is the generation of random displacement error, although this may be estimated by measuring the background strain in a region where only rigid body movement is observed [146].

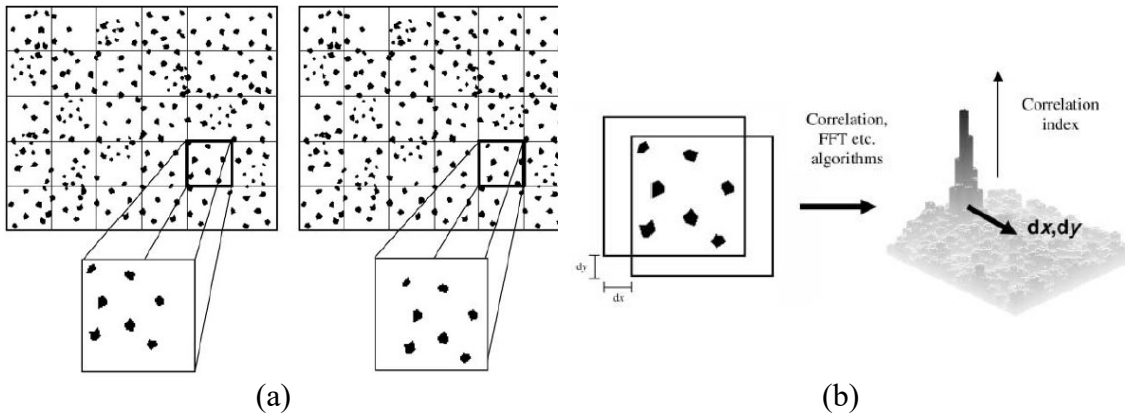

Figure 49 – The steps involved in Digital Image Correlation analysis of images, (a) schematics of textured images before and after deformation and (b) computation of the correlation index across all pixel groups to determine matching pixel groups [147].

1.7.2 Mathematical formulation

On the reference or undeformed image, a region of interest (ROI) must be defined along with subsets within this ROI. The two parameters used to define these subsets are the number of pixels for the subset dimension followed by the separation between subset. Square subsets containing a representative number of pixels are tracked individually between images. In addition to rigid-body displacement of these subsets, deformation is also expected to occur and hence displacement mapping functions are used that may be of first or second order [148]. In the following, (x, y) refer to coordinates within the defined ROI. The point P refers to the centre of defined subsets and primed variables refer to those found in the deformed state. The shape functions (or displacement mapping functions) s for first order deformation is given by

$$s_u(x_i, y_j) = u + u_x \Delta x + u_y \Delta y$$

$$s_v(x_i, y_j) = v + v_x \Delta x + v_y \Delta y$$

Extending to second order, the shape functions may be written as

$$s_u(x_i, y_j) = u + u_x \Delta x + u_y \Delta y + \frac{1}{2} u_{xx} \Delta x^2 + \frac{1}{2} u_{yy} \Delta y^2 + u_{xy} \Delta x \Delta y$$

$$s_v(x_i, y_j) = v + v_x \Delta x + v_y \Delta y + \frac{1}{2} v_{xx} \Delta x^2 + \frac{1}{2} v_{yy} \Delta y^2 + v_{xy} \Delta x \Delta y$$

where

$$\Delta x = x_i - x_0$$

$$\Delta y = y_j - y_0$$

In order to compare the similarity of two subsets at different temporal points, it is necessary to use a correlation function. These functions measure and optimise the grey level contrast distribution in the small domain around a subset to determine similarity between subsets across images [149]. There are two categories of these similarity indices, namely the cross correlation (CC) and sum of squared differences (SSD) criterion. Of the various indices, zero-normalised cross correlation (ZNCC) or zero-normalised sum of squared differences (ZNSSD) demonstrates the lowest impact from noise and is also insensitive to illuminating lighting fluctuations [148]. The equations are given as follows

$$C_{ZNCC} = \sum_{i=-M}^{M} \sum_{j=-M}^{M} \left\{ \frac{[f(x_i, y_j) - f_m] \times [g(x_i', y_j') - g_m]}{\Delta f \Delta g} \right\}$$

$$C_{ZNSSD} = \sum_{i=-M}^{M} \sum_{j=-M}^{M} \left[\frac{f(x_i, y_j) - f_m}{\Delta f} - \frac{g(x_i', y_j') - g_m}{\Delta g} \right]^2$$

Where

$$f_m = \frac{1}{(2M+1)^2} \sum_{i=-M}^{M} \sum_{j=-M}^{M} f(x_i, y_j)$$

$$g_m = \frac{1}{(2M+1)^2} \sum_{i=-M}^{M} \sum_{j=-M}^{M} g(x_i', y_j')$$

In three dimensions the zero centred normalised cross-correlation function may be written as [150]:

$$C = \frac{\sum_{\underline{X} \in D} \left(f(\underline{X}) - \overline{f_D}\right) \cdot \left(g\left(\varphi(\underline{X})\right) - \overline{g_D}\right)}{\sqrt{\sum_{\underline{X} \in D} \left(f(\underline{X}) - \overline{f_D}\right)^2} \cdot \sqrt{\sum_{\underline{X} \in D} \left(g\left(\varphi(\underline{X})\right) - \overline{g_D}\right)^2}}$$

Where X refers to voxels within the domain D, f and g are grey levels in the deformed and un-deformed states, with the corresponding overbar values indicating the averaged values over the domain.

1.7.3 Applications to thermal barrier coatings

Most applications of DIC to TBCs to date have concentrated on determining mechanical properties [151–160]. In general, studies have measured displacements under load at room temperature and do not explore volumetric strains or the influence of high temperature oxidation. Reported high temperature applications of DIC have been limited to CTE measurement [161] and instantaneous 2-D thermal shock response analysis [156]. The work of Eberl et al. [151–153] has focused on the application of 2-D DIC in measuring strain fields within EB-PVD topcoats under micro-beam bending. The authors use low-resolution optical imaging to measure inter-columnar separation and interfacial cracking and quantify strain fields (Figure 50). Although the work presents a novel technique in measuring mechanical properties at room temperature, out-of-plane displacement and strain fields at temperature or under thermal cycling are not reported. In addition, pre-cracks are introduced as part of the experimental method which may alter out-of-plane strain distributions.

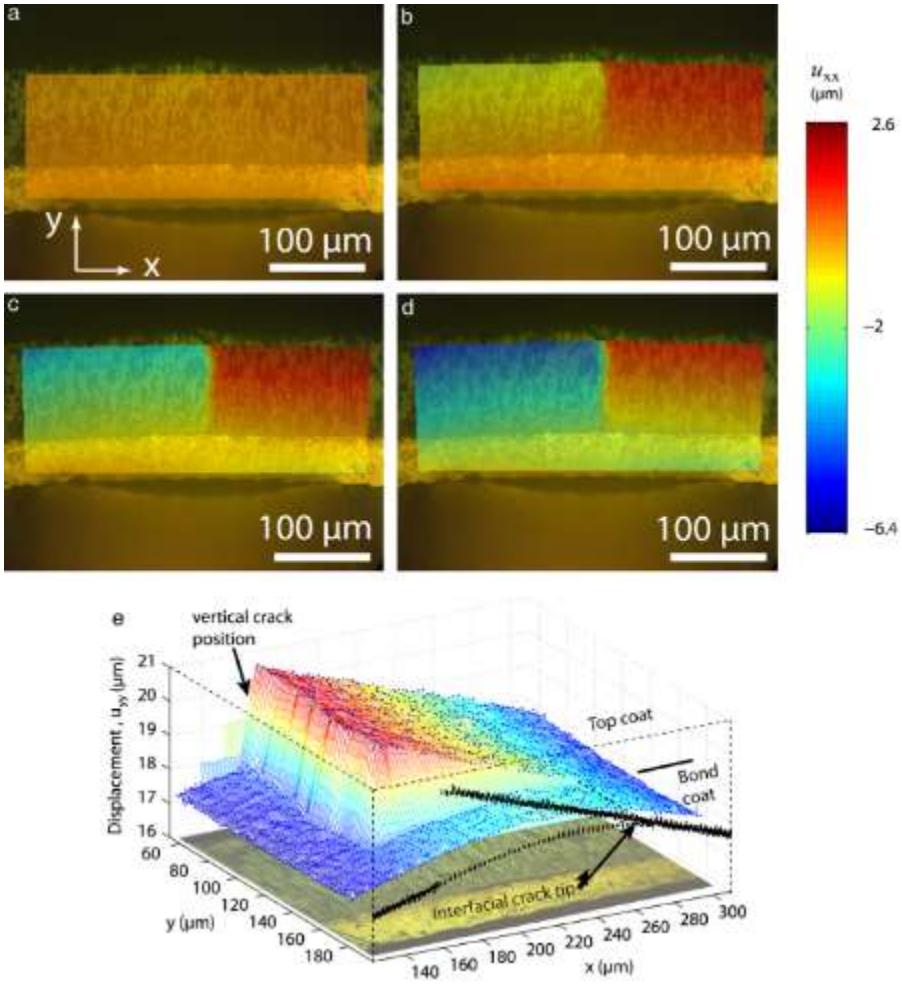

Figure 50 – 2-D Digital Image Correlation strain map under bending at room temperature from the work of Eberl et al. [153].

Similar work by Mao et al. [154] on air plasma sprayed coatings used cross-sectional optical imaging of three-point bend tests at room temperature to couple failure events with local strains. This work, in addition to other room-temperature studies [155,157,158,160] neglected the influence of time at temperature and thermal cycling. The work of Donohue et al. [159] used a wedge to drive a crack into a section of APS topcoat (Figure 51) to measure fracture toughness and determine failure modes. The work only examined the topcoat in isolation from the rest of the TBC system.

Figure 51 – Digital Image Correlation of speckle patterned double cantilever beam [159].

Although the work presented by Zhu et al. [162] measures out of plane strains, it is actually the bending strains of a flat 2-D thermal spray topcoat and bondcoat system that are measured (Figure 52). The technique is a modification of conventional 2-D DIC that employs stereoscopic imaging with a camera pair to quantify normal displacements to the flat image surface. This method neglects any through-thickness volumetric displacement but is useful in quantifying out-of-plane surface deformation.

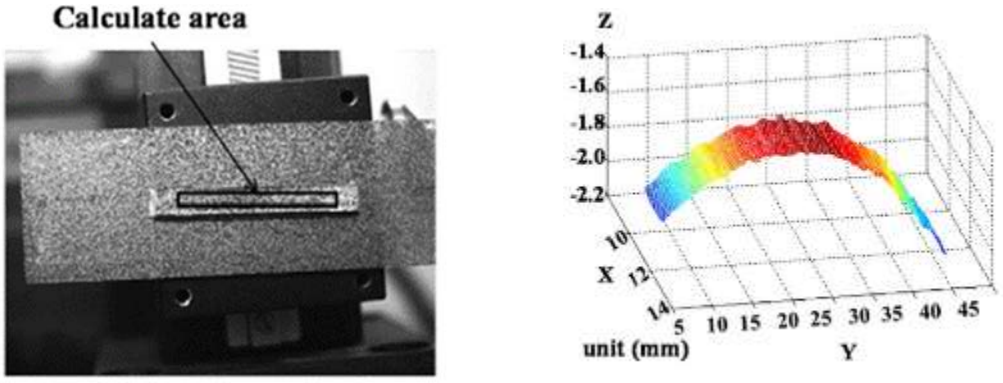

(a) (b)

Figure 52 – Stereo DIC data computed from surface sections of coating [162] *showing (a) the view seen by cameras and (b) displacements measured by curvature based on 2-D digital image correlation.*

In other work [161], DIC was used to measure thermal expansion coefficients of a NiCoCrAlY bondcoat (without a substrate) and Rene N5 (substrate only) from room temperature to 1100°C. The CTE data indicate good correlation with other reported literature however, the influence of oxidation, cyclic or otherwise, is not explored. Additionally, the 2-D optical image data is on the order of centimetres indicating that local damage is not explored. In other macroscopic studies [163], substrate strain anisotropy was demonstrated by 2-D DIC imaging of a cylindrical specimen under compressive testing (Figure 53). The tests were carried out at 20°C and under mechanical loading, with DIC computations revealing only in-plane displacements.

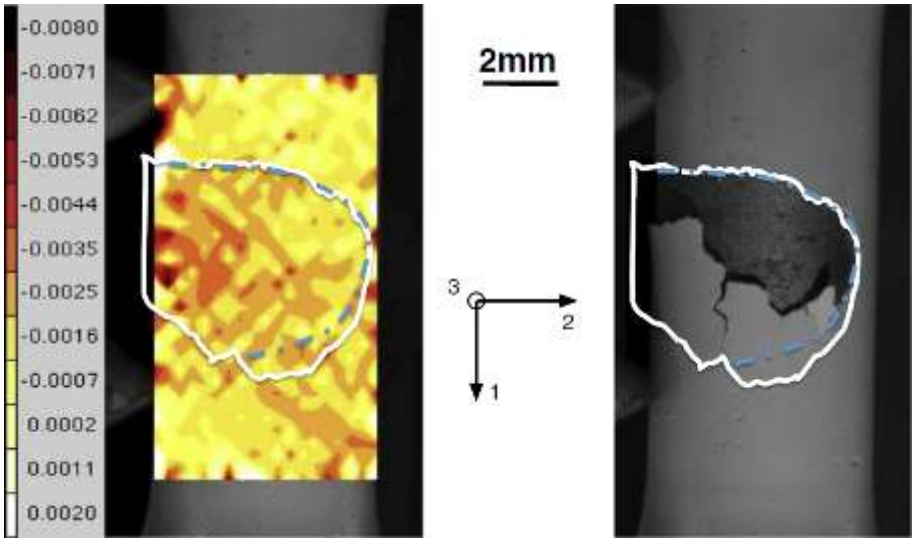

Figure 53 – 2-D DIC computations of compressive testing of an EB-PVD topcoat with and AM1 substrate showing in-plane displacements [163].

The influence of thermal shock between 20°C and 1100°C was explored by Yang et al. [156] in which a thermally supressed CCD camera was used to measure the displacement distributions. The work examined both the topcoat surface and the cross-section of an APS TBC system (Figure 54). Although strong correlation exists from the surface speckles applied, this approach, like those previously examined, neglect the through thickness displacement field.

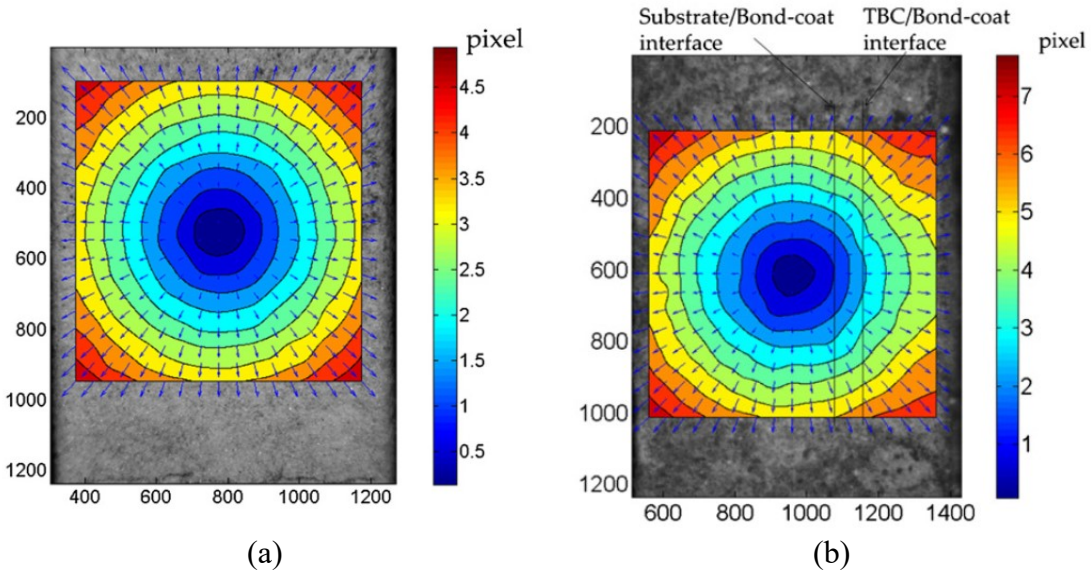

Figure 54 – Displacement fields from DIC calculations of surface deformations of APS and MCrAlY coatings under thermal shock using a speckled field [156] *showing (a) topcoat surface and (b) sample cross-section.*

1.8 Literature summary and aims

To date, a definitive approach to predicting the time to spallation of thermal barrier coating life has yet to be conclusively established, seen by the factor of 10 commonly reported in the literature. Fracture damage, particularly in the early stages in and around the TGO is a known cause coating system failure. The role of the bondcoat has also been shown to strongly influence TGO stress states, particularly bondcoat roughness. Numerous failure mechanisms have been proposed in the literature, both with and without topcoats, including rumpling, ratcheting, critical oxide thickness and critical strain energy. The experimental method frequently used to report the in-situ TGO stress state is photoluminescence piezospectroscopy (PLPS). For TBC systems with a topcoat, the technique suffers from a large spot size owing to beam scattering within the topcoat. Alternative techniques include 3-D synchrotron X-ray tomography for imaging and 2-D digital image correlation for strain calculation.

In this work, two new approaches to observation of the stress state and strain response under oxidation of the TGO bondcoat are sought. The first relating bondcoat stress relaxation, computed using literature creep data, to TGO growth stress and compared with PLPS. The second aims to couple 3-D synchrotron X-ray with 3-D digital volume correlation to computed strains within the entire sample domain. 3-D X-ray tomography will allow visualisation of bondcoat roughening and 3-D digital volume correlation will allow quantification of bondcoat and TGO displacements.

Chapter 2 Experimental Method

2.1 Introduction

The experimental work carried out herein focused on cyclic oxidation testing of samples derived from production turbine blades. A purpose-built cyclic oxidation rig was designed and constructed as part of this work to aid furnace testing. In addition to conventional metallography, X-ray micro-tomography analysis of exposed and unexposed samples was carried out using a variety of X-ray sources, namely bench-top, industrial and synchrotron tomography. The majority of the X-ray tomography imaging was performed at the Diamond Light Source facility that required miniature specimens for the highest resolution. A cylindrical micro-specimen machining technique was devised to produce such specimens by adapting existing sample preparation practices. A sample cell was also designed and constructed for use on the manipulation stage at Diamond Light Source to allow scanning two specimens simultaneously.

2.2 Materials

Twenty-nine production HP1 turbine blades were supplied for this work (Appendix B). The blades were cast at the Rolls-Royce precision casting facility (PCF) and thermal barrier coatings were applied by Turbine Surface Technologies Limited (TSTL, a joint venture between Rolls-Royce and Chromalloy).

Two types of bondcoats were present in the collection of supplied blades, the RT22 Pt-Al bondcoat and the Rolls-Royce low-cost Pt-only γ/γ’ bondcoat (Table 1). For each type of bondcoat, blades were provided either with or without an EB-PVD topcoat. The

substrate consisted of CMSX-4 (Table 2), the single-crystal nickel-based superalloy [164]. The elemental composition of nickel includes impurities consisting of S (<20 ppm), B (<30 ppm), Si (<400 ppm), C (<60ppm) and Zr (<75ppm) [165].

Table 1 – Turbine blades examined in this work, consisting of two types of bondcoats and either with or without an EB-PVD topcoat

Substrate	Bondcoat	Topcoat	Quantity
CMSX-4	Pt-Al	EB-PVD	10
CMSX-4	Pt-Al	None	5
CMSX-4	Pt	EB-PVD	12
CMSX-4	Pt	None	2

Table 2 – Chemical composition of CMSX-4 nickel superalloy substrate for all turbine blades used in this work [164,165].

Element	Hf	Mo	Ti	Re	Al	W	Ta	Cr	Co	Ni
wt.%	0.1	0.6	1.0	3.0	5.6	6.4	6.5	6.6	9.6	60.6
at%	0.03	0.26	0.93	0.97	11.62	1.70	1.87	6.61	11.25	64.76

2.3 Sample preparation

Three types of specimen were extracted and machined from these turbine blades (Figure 55). These specimens were either aerofoil sections (Figure 56 for schematic and nomenclature) obtained by cutting a single blade into sections, flat coupons extracted from the suction surface at the trailing edge of an aerofoil section (position M through N) or cylindrical micro-specimens obtained by further cutting and machining of the flat coupons.

Turbine blades were cut into aerofoil sections using a Buehler IsoMet 4000 high-speed cutting saw with a water-based Struers DP-Suspension lubricant. Cutting parameters were set at 3000 rpm with a feed rate of 1.2 mm/min using a cubic boron nitride cut-off wheel. Aerofoil sections were then washed in acetone using a Guyson KC2 ultrasonic bath for three minutes to remove lubricant and cutting residues.

Flat coupons were cut from the suction surface at the trailing edge of aerofoil sections using a South Bay Technologies (SBT) Model 650 low speed diamond wheel. A 100mm cubic boron nitride cut-off wheel was used in Struers DP-Suspension lubricant with two cuts performed between the last spar of the aerofoil (position M) and the trailing edge (position N). Flat coupons and the remaining aerofoil section were washed in acetone for three minutes each using the ultrasonic bath to remove lubricant and cutting residues.

Figure 55 – Stages of sample preparation for aerofoil sections and flat coupons extracted from the suction surface of the trailing edge of aerofoil sections. Left, Rolls-Royce Pt-only bondcoat HP1 turbine blade, centre, Rolls-Royce Pt-Al bondcoat with no topcoat cut into four aerofoil sections and right, cut aerofoil section showing flat coupons extracted from suction surface of trailing edge.

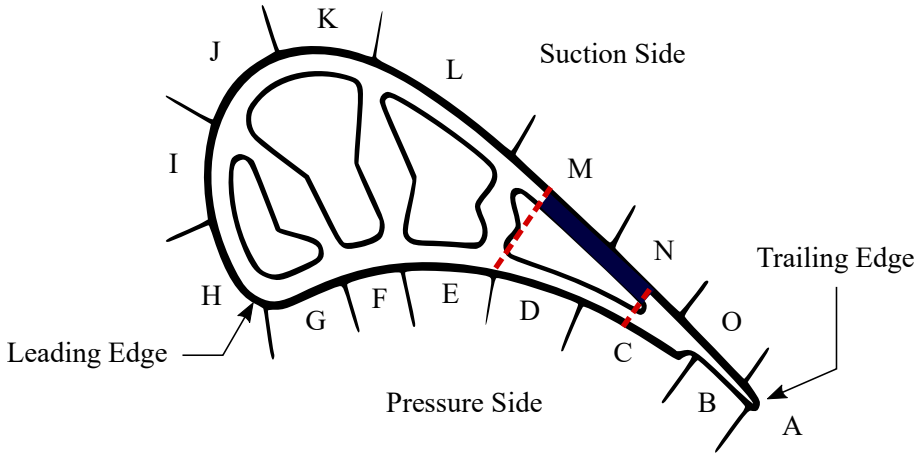

Figure 56 – Schematic diagram of cross-section through turbine blade aerofoil showing position naming convention and surface profile/contour and internal cooling holes. Adapted from schematic courtesy of Dr. R. Jones, TSTL. Dashed lines indicate locations of cuts to extract flat coupons (highlighted portion of positions M through N).

Specimens with a cylindrical geometry were required for tomography imaging in order to minimise imaging artefacts associated with corners and sharp features. Great care was needed so as not to introduce defects and to produce the required geometry. Cylindrical micro-specimens were machined using a modified SBT model 650 slow speed diamond wheel (Figure 57). A small, geared 12V DC motor was attached to the sample holder arm, powered by a variable DC generator (Figure 58 for schematic). Care was taken to match the speeds of the DC motor and low speed diamond wheel resulting in an even cylindrical surface finish with bondcoat diameters of 1000µm or 500µm.

To produce the micro-specimens, a 2mm thick section of flat coupon (extracted from position M through N of aerofoil sections) was affixed onto an aluminium block with a Cyanoacrylate adhesive for ease of manipulation. The slow speed saw, with micrometre control was used to section the flat coupon into 2mm × 2mm square sections. These were subsequently released from the aluminium block by ultrasonically soaking in acetone. The technique allowed precise control over the sample diameter (with frequent manual measurements) and the surface finish (Figure 59 demonstrates the smallest sample produced using the technique).

To assist with alignment of specimens, primarily for digital volume correlation (DVC) computations, three reference holes, 100µm in diameter were micro-drilled into the substrate of the cylindrical micro-specimens. The holes were positioned 500µm from the top of the topcoat and drilled to a depth of 100µm with 20° separating each pair of holes. This work was carried out by Drill Service Ltd, Horley and Partridge Microdrilling Services, Crawley.

The application of a mechanical constraint to the exposed surface of selected cylindrical micro-specimens was carried out by air plasma spraying (carried out by Zircotec Ltd, Abingdon) a NiCoCrAlY bondcoat and a 7wt% yttria partially-stabilised zirconia (7-YPSZ) topcoat to the cylindrical surface sides such that the spraying direction was perpendicular to the cylindrical axis (Figure 60). This approach ensured that the oxygen path through the topcoat columns remained as in the case of the cut aerofoil section and flat coupon specimens while applying a physical boundary condition.

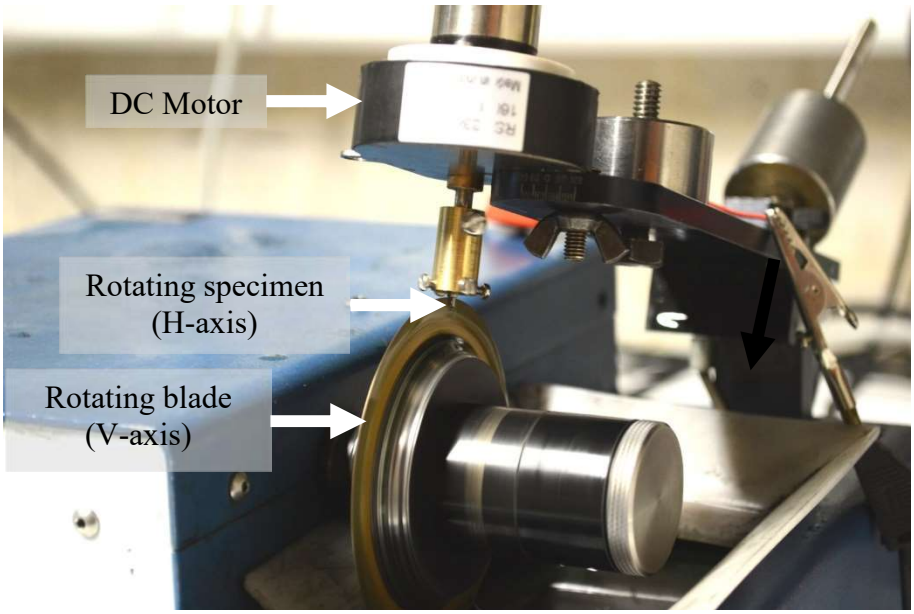

Figure 57 – Modified slow-speed cutting wheel to fabricate cylindrical micro-specimens. External power supply (not shown) drives a secondary motor attached to the sample holder arm. This rotates the specimen about a secondary axis perpendicular to the blade. The motor and blade speeds are matched to achieve a uniform finish. The specimen arm is moved towards the blade at five-minute intervals using the positioning micrometre (not shown).

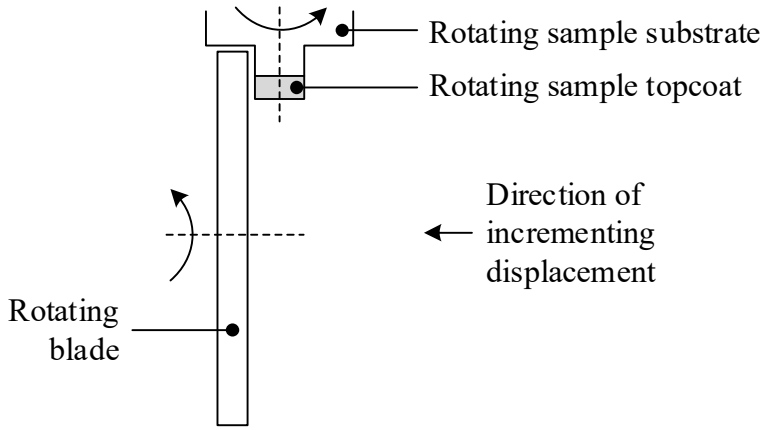

Figure 58 – Schematic diagram of cylindrical micro-specimen sample preparation method. Axes of blade rotation and sample rotation indicated by dashed lines and location of EB-PVD topcoat indicated by shaded portion of sample.

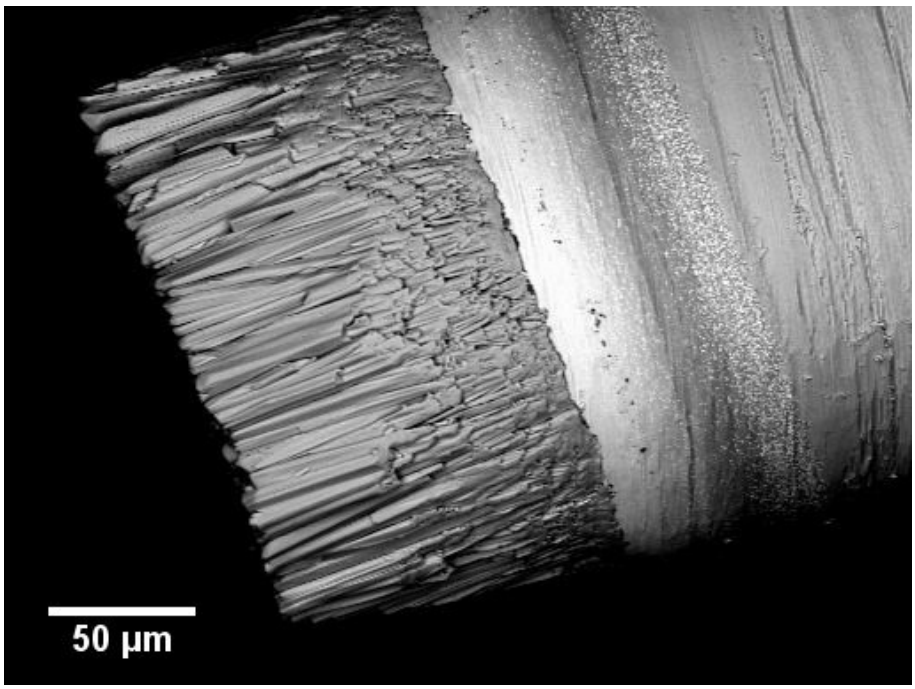

Figure 59 – Backscatter micrograph showing one of the smallest cylindrical micro-specimens fabricated (a Rolls-Royce Pt-aluminide specimen approximately 150µm in diameter) using the biaxial slow-speed saw technique.

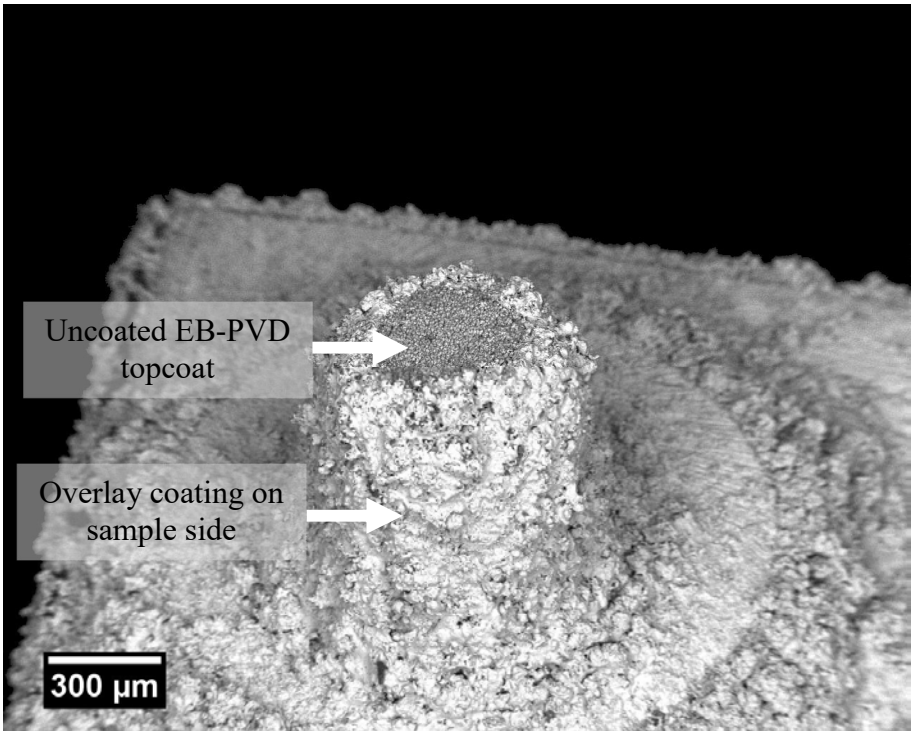

Figure 60 – Overlay coating of NiCoCrAlY bondcoat and overlay 7-YPSZ topcoat applied to cylindrical surfaces of micro-specimens. Column tips of EB-PVD topcoat remain exposed to allow oxygen ingress while a mechanical constraint is applied to the cylindrical free surface. Overlay coatings applied by Zircotec Ltd., Abingdon.

2.4 Thermal Cycling

Thermal cycling oxidation tests were carried out in laboratory air using a Lenton Thermal Designs horizontal tube furnace rated at 1300°C. The calibrated furnace was heated by four 995mm long, 20mm OD Sandvik Kanthal Globar SD SiC heating elements with recrystallized silicon carbide hot zones rated at 41 Amps – 56 Amps at 109 Volt with aluminium sprayed cold ends. A 99.7% purity recrystallized alumina tube of 1200mm length, 80mm OD and 70mm ID, open both ends (OBE) was used as the main work tube. For high-throughput tests of aerofoil sections a fire-brick shelf 200mm in length (Figure 61) was machined and positioned in the centre of the work tube to double sample capacity in the furnace hot zone.

Figure 61 – Firebrick shelf used to load multiple aerofoil sections into furnace for high-throughput testing, showing a selection of alternating pairs of Pt (larger) and Pt-aluminide (smaller) aerofoil sections following three 20-hour cycles at 1200°C.

Cylindrical micro-specimens (Figure 62) and flat specimens from aerofoils were placed in 99.5% purity recrystallized alumina boats before loading into the furnace. One of the challenges faced with handling the cylindrical micro-specimens was the relative ease with which the micro-specimens would be ejected from the sample boat. This was most likely to occur at the crucial loading and unloading stages. To counter the likelihood of sample loss and also to enable automatic short-cycle testing, a programmable cyclic rig was designed and built with particular attention paid to the sample holding section.

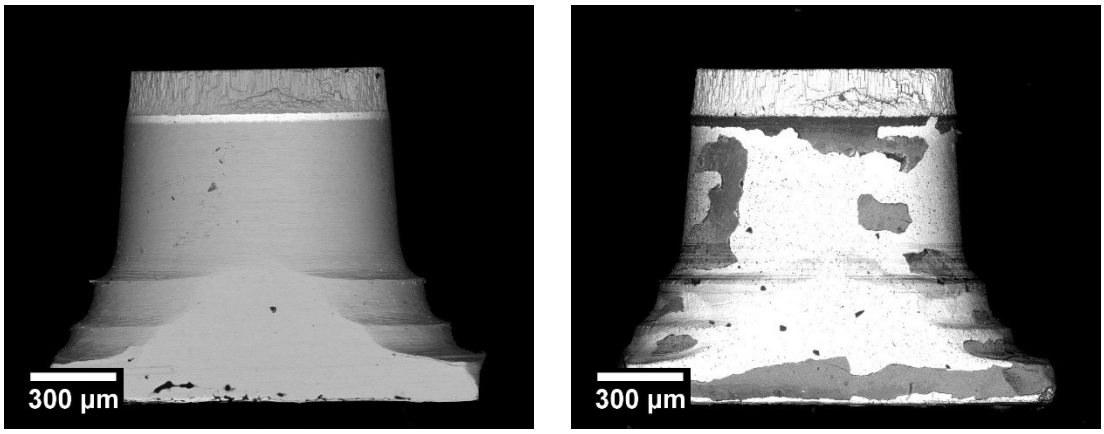

(a) (b)

Figure 62 – Backscatter micrographs of Rolls-Royce Pt bondcoat cylindrical micro-specimen exterior in (a) as-received state and (b) following two 20-hour exposures at 1200°C. Stepped features at base of specimen are formed at each manual rotation of the positioning micrometre of the modified slow-speed cutting wheel.

2.5 Cyclic oxidation rig

A computer-controlled programmable cyclic-oxidation rig was built in-house to facilitate the timing of thermal exposures and aid with handling of small specimens. The rig was designed (Figure 63) to fit the Lenton Thermal Designs horizontal tube furnace described previously for thermal cycling work. The system consisted of a sample holder arm, machined from a stock closed one end (COE) 99.7% recrystallized alumina tube attached to an aluminium runner-block and a Thompson Linear Motion 1000mm precision ball-screw drive assembly (Figure 64). The rig frame was constructed using lengths of extruded aluminium (Valuframe Series 8 profiles) with no-drill connectors. The drive system consisted of a Pololu TReX Jr Dual Motor Controller (DMC02) that powered a 12V 7.2A Parvalux DC motor. A Windows Forms application was written in the C# programming language using Microsoft Visual Studio (Appendix C for source code).

A Eurotherm 6100E temperature logger with three thermocouple input channels with integrated cold-junction compensation was also designed into the rig. Two thermocouple channels on this temperature logger were used, one permanently monitoring the furnace hot-zone temperature and a second at the tip of the sample holder arm to measure sample heating/cooling rates on loading/unloading. Temperatures were recorded every three seconds and transferred to the controlling computer every hour.

Calibration of both of these R-type thermocouples (platinum/platinum-13% rhodium), in addition to the main furnace controller and over-temperature alarm R-type thermocouples was carried out using a UKAS certified calibrated R-type thermocouple (NPL Instrument number NPL10/07/B, certificate reference PM03/E08070355/1). The instrument was certified between 0°C and 1600°C and was used to verify the accuracy of all thermocouples to within ±2°C. Copper/cupronickel compensating thermocouple cable

was used for all connections between thermocouples and the temperature logger. A second temperature logger (Eurotherm 6100A) with 6 input channels was used to verify the readings of the primary temperature logger connected to the cyclic rig.

The size of the furnace hot-zone was measured and found to be 15cm centred about the mid-point of the furnace length. The temperature of the hot zone was found to vary within ±5°C in either direction about the mid-point within the hot-zone.

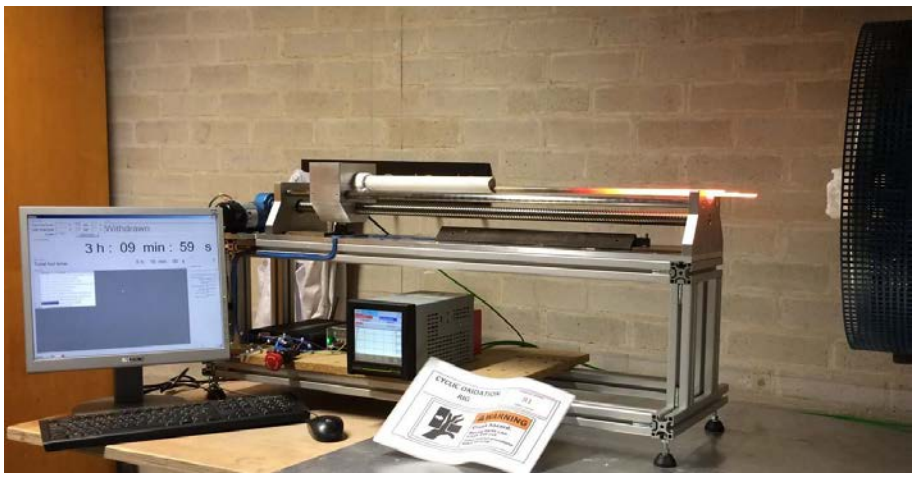

Figure 63 – Cyclic oxidation rig showing red-hot sample holder immediately after withdrawal from tube furnace. The rig consists of a software-programmable motor controller interface and a Eurotherm 6100A temperature logger.

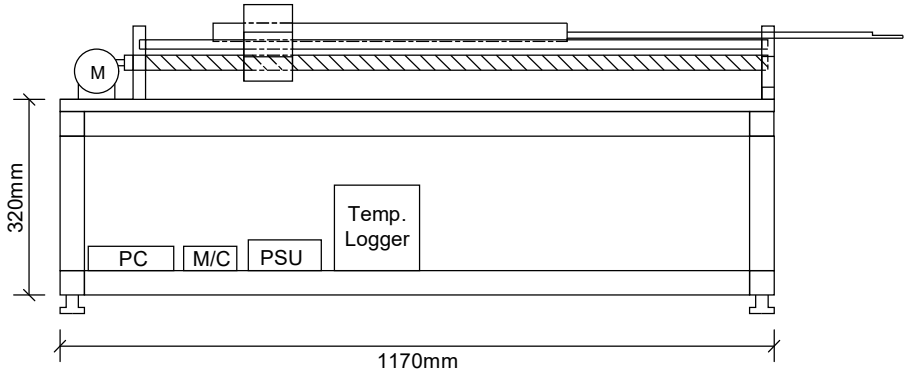

Figure 64 – Schematic diagram of purpose-built cyclic oxidation rig showing main drive systems and sample holder tip. Electro-mechanical drive system consists of a motor controller (M/C), power supply unit (PSU) and computer (PC) to drive the motor (M) connected to a ball-screw and runner block mechanism (PC, M/C and PSU not to scale).

2.6 Metallography

2.6.1 Vacuum mounting

The low-shrink Struers EpoFix cold-mounting kit was used to vacuum-mount specimens. Fifteen parts by volume of resin were mixed with two parts by volume of hardener (Triethylenetetramine) and the mixture was stirred for three minutes and left for a further two minutes before being used for mounting. To assist the filling of cracks and pores with the mounting mixture, a Struers Epovac with Air Ejector Pump vacuum impregnator was used at 100 – 200mBar with compressed air. The mixture was drawn through a rubber tube under the low chamber pressure in 30mm mounting cups. Once filled, three minutes at low pressure were allowed for the resin to fill voids and cracks, and draw out air bubbles.

A manufacturer recommended curing time of 12 hours at room temperature was allowed before the grinding and polishing of vacuum mounted specimens. In rare instances where the cures resulted in a soft mount, post-curing was carried out at 50°C for a further two hours.

Following curing, mounted aerofoil sections and flat specimens extracted from aerofoil sections were cut at the mid-point of the specimen thicknesses using the slow speed diamond wheel used previously.

2.6.2 Grinding and polishing

Sample grinding was carried out using 200mm diameter SiC grinding paper of 120, 240, 400, 800 and 1200 grit sizes. At each stage, 3 minutes of grinding at light manual pressure was performed, rotating opposite to the direction of the grinding paper. For cylindrical

specimens of 1000µm and 500µm diameter, grinding times at 800 and 1200 grit were significantly longer as width measurements of the specimen cross-section were made at regular intervals to match the external diameter measured prior to mounting. The last 15 seconds of each stage was held fixed against the rotating grinding paper such that all grinding scratches were aligned. This assisted in judging an extra grinding time for the next grinding stage.

Polishing was carried out using the Struers 200mm diameter MD-Cloth system and monocrystalline diamond polishing suspensions. Between each polishing stage, the polished surface was washed using ethanol and force dried using a heat gun. The following polishing sequence was carried out for all specimens: 6µm monocrystalline diamond suspension on MD-Dur for 5 minutes, 1µm monocrystalline diamond suspension on MD-Plus for 5 minutes and a final polish using Struers OP-S colloidal silica on an MD-Chem disc for 5 minutes.

2.6.3 Scanning electron microscopy

In preparation for electron microscopy, polished samples mounted in non-conducting EpoFix resin were sputtered with a thin layer (10 – 50nm) of any one of Au, Pt or C. An Emscope Laboratories SC500 sputter coater was used for sputtering Au or Pt. The sputter coating chamber was evacuated to 0.1 torr using an Edwards B2M5 high vacuum pump and a 3-minute deposition of Au or Pt was applied at a current of 25mA.

An Au coating was applied for general imaging whereas a Pt layer was deposited for high-resolution imaging as sputtered Pt forms finer surface particles. A carbon coating was applied for energy and wavelength dispersive spectroscopy as carbon exhibits a single

peak in the spectrum whereas those of Au and Pt can overlap with those being analysed [166].

Imaging and compositional analysis was carried out using a JEOL 7000F FEG-SEM equipped with an Oxford Instruments WDX and EDS detector, with analysis carried out through the INCA software package. Geometric calibration for TGO thickness measurements was carried out by imaging a reference graticule with a known spacing of 0.479μm.

Calibration of energy and wavelength dispersive spectroscopy was carried out using a forty-six element Micro-Analysis Consultants compositional standard with a Faraday cup. EDS quantitative calibration for electron beam current and temperature fluctuations was carried out using a pure cobalt block from the forty-six element standard at 20keV in addition to probe current measurement every 2 hours [167].

2.6.4 Free-edge lateral displacement measurement

To record the outward displacement of the topcoat/TGO interface with time at temperature, the exterior of cylindrical samples were imaged non-destructively between thermal cycles prior to mounting. Each sample was imaged both top down and from the side. Side view measurements (single value) were made at the maximum diameter that corresponded to the topcoat/TGO interface. Top view measurements were made by fitting a rectangle (length and width measurements) to the largest diameter at the topcoat/TGO interface.

Following sample cross-sectioning, one bondcoat/TGO interfacial extension measurements was made at either end of each sectioned sample. A reference line was drawn parallel to the substrate edge and the normal distance from this line to the furthest

bondcoat point was measured (Figure 65). The bondcoat was chosen as opposed to the oxide edge extremities to reduce the influence of repeated scale spallation on measurements.

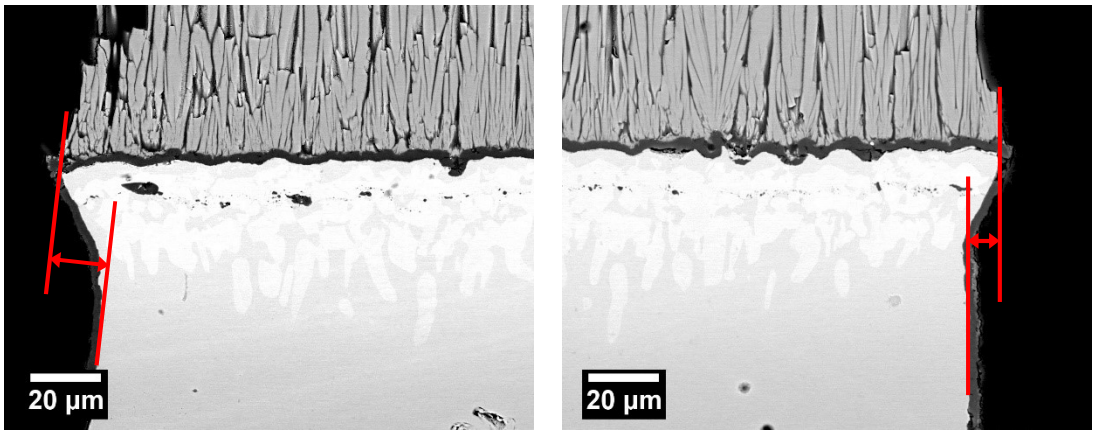

(a) (b)

Figure 65 – Backscatter micrographs showing edge detail of Rolls-Royce Pt cylindrical micro-specimens for (a) left and (b) right edge following one 20-hour exposure period. Markers indicate location of measurements for lateral extension of the TGO/bondcoat interface, relative to the substrate.

2.6.5 TGO thickness measurements

Image analysis of micrographs was carried out using Fiji (ImageJ) [168]. For cylindrical micro-specimens, to ensure uniform spacing between measurements, the whole width of the specimen cross section was imaged. The sequence of micrographs was then stitched together using the MosaicJ plugin for ImageJ [169] to produce a single image spanning the entire sample cross-section. A uniformly spaced grid was then applied using the Grid Overlay plugin for ImageJ [170] such that the stitched image contained two-hundred grid points. Individual TGO thicknesses (normal to the TGO/bondcoat interface) were added to the region-of-interest manager of ImageJ at the intersection of each vertical gridline and the TGO/bondcoat interface (Figure 66). In regions of the TGO where the oxide had locally delaminated and a new layer grown underneath (Figure 67), the total thickness of the oxide excluding space between the two layers was considered as the TGO thickness.

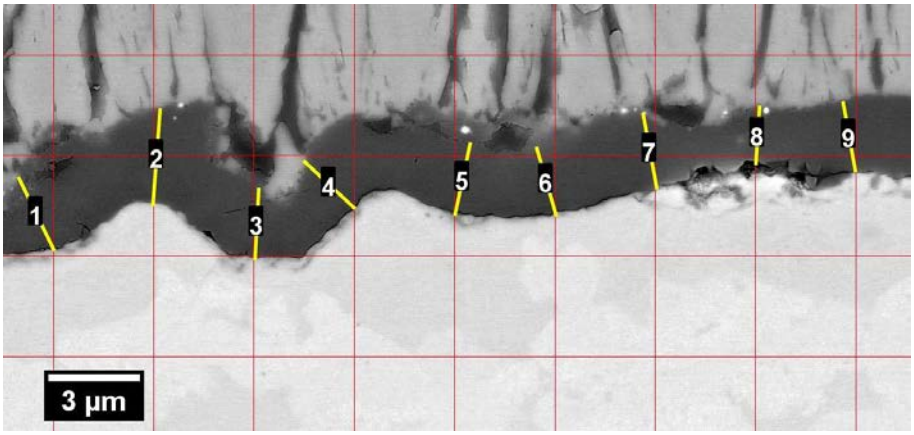

Figure 66 – Backscatter micrograph of cross-section through Rolls-Royce Pt cylindrical micro-specimen exposed for 20 hours at 1200°C showing intervals for TGO thickness measurements. Continuous micrographs were produced using the MosaicJ [169] *plugin and the Grid Overlay plugin for ImageJ* [170].

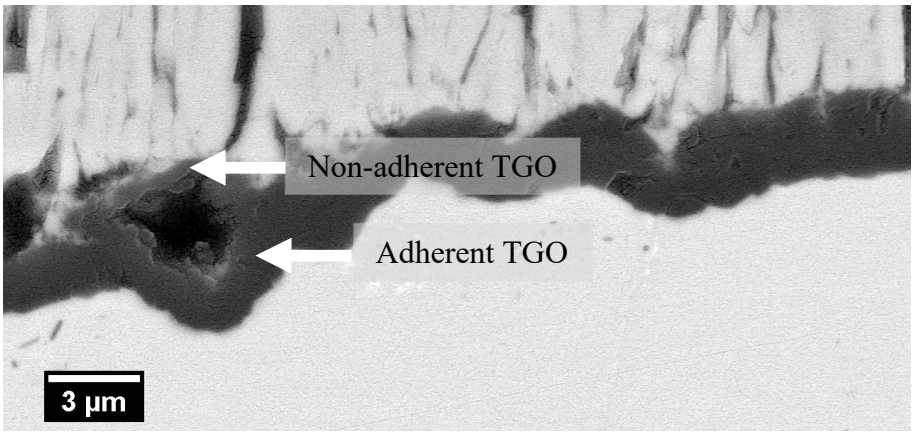

Figure 67 – Backscatter micrograph of cross-section through Rolls-Rolls Pt-aluminide coupon exposed for 20 hours at 1200°C showing two continuous TGO regions separated by a void. Oxide thickness measurements for such features excluded the void between the oxide portions.

Probably density functions were fitted to TGO thickness datasets including Wald (inverse Gaussian), normal and Weibul distributions (see Chapter 3).

2.6.6 TGO/bondcoat interface profile measurements

The two-dimensional profiles of TGO/bondcoat interfaces were processed using a combination of Fiji (ImageJ) and Matlab (Appendix D for script). The stitched mosaic micrograph used for TGO thickness measurements was used to extract the TGO/bondcoat interface through the binarisation function of Fiji (ImageJ) with appropriate thresholding. Individual grit line features were also processed using the particle analyser utility of Fiji

(ImageJ). The centroid of each grit-line feature (an artefact of alumina grit blasting during bondcoat manufacture) was computed and imported into Matlab. The combination of grit line centroids, binary TGO/bondcoat interface and original SEM micrograph (Figure 68) were used to produce a profile map relative to the mean grit line position (Figure 69).

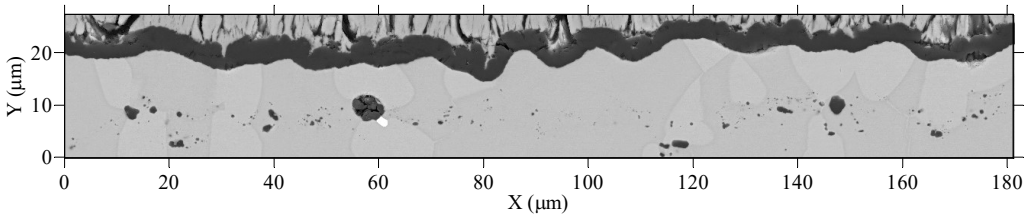

Figure 68 – Backscatter micrograph of Rolls-Royce Pt-aluminide cylindrical micro-specimens after 80 hours at 1200°C, used as input image for TGO/bondcoat interface extraction.

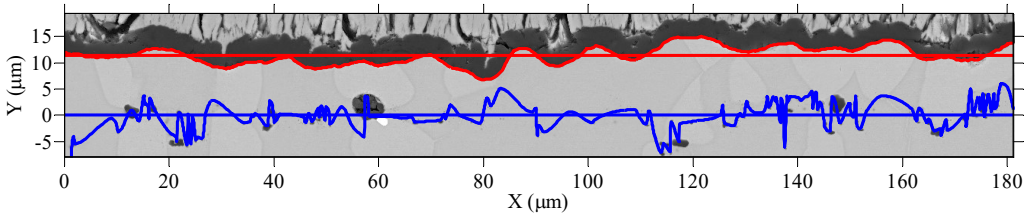

Figure 69 – Bondcoat/TGO interface extracted from micrograph, showing distance above and below mean profile for Rolls-Royce Pt-aluminide cylindrical micro-specimens after 80 hours at 1200°C.

2.7 Confocal laser scanning microscopy

An Olympus LEXT OLS-3100 confocal laser microscope was used for surface profile analysis. The system consisted of a 408nm laser with a 1024x1024x12-bit image detector that was rasterised over the imaging plane. A motorised precision x-y stage was available on the microscope and the entire system was mounted above a Table Stable TS-140 dynamic vibration isolation stage.

A Matlab script was written to process the height data produced from the microscope and incorporated a noise reduction and spike removal algorithm. The script allowed extracting an individual horizontal and/or vertical height profile from a data set in addition

to a rectangular region of interest for further examination of three-dimensional topography.

2.8 X-ray micro-tomography

X-ray micro-CT was carried out using three different scanning systems, a Nikon XTH-225 industrial unit, a SkyScan 1172 benchtop system and the I12 JEEP beamline at Diamond Light Source, Didcot. Details of each system are given in the following sections. Emphasis was placed on maximising the imaging resolution of all systems and consequently cylindrical micro-specimens of the smallest diameter (500μm) were scanned. The effective resolutions of each of the Nikon XTH-225, SkyScan 1172 and I12 JEEP beamlines were 20μm, 10μm and 2μm respectively.

To better configure the beam conditions of each of the three X-ray μ-CT systems, the mass attenuation coefficients of the alumina, 7wt%-YPSZ, β-(NiAl) [171] and γ/γ' [172] bondcoat phases and CMSX-4 were calculated (Figure 70) using WinXCom [118,119]. The mass attenuation of CMSX-4 was calculated using the compositions given in Table 2, assuming no impurities. Dry air at sea level was also evaluated for the background reference [166]. It is evident that at energies at and beyond 100keV, the mass attenuation of alumina and air converge. This creates the undesirable situation in which alumina may be misinterpreted as voids or otherwise. Consequently, the lowest energy possible for each system was chosen. Lowering the beam energy however means that for low brilliance laboratory-based systems, i.e. the SkyScan 1172 and Nikon XTH-225 systems used here, X-ray throughput is lower resulting in longer scan times and lower quality reconstructions.

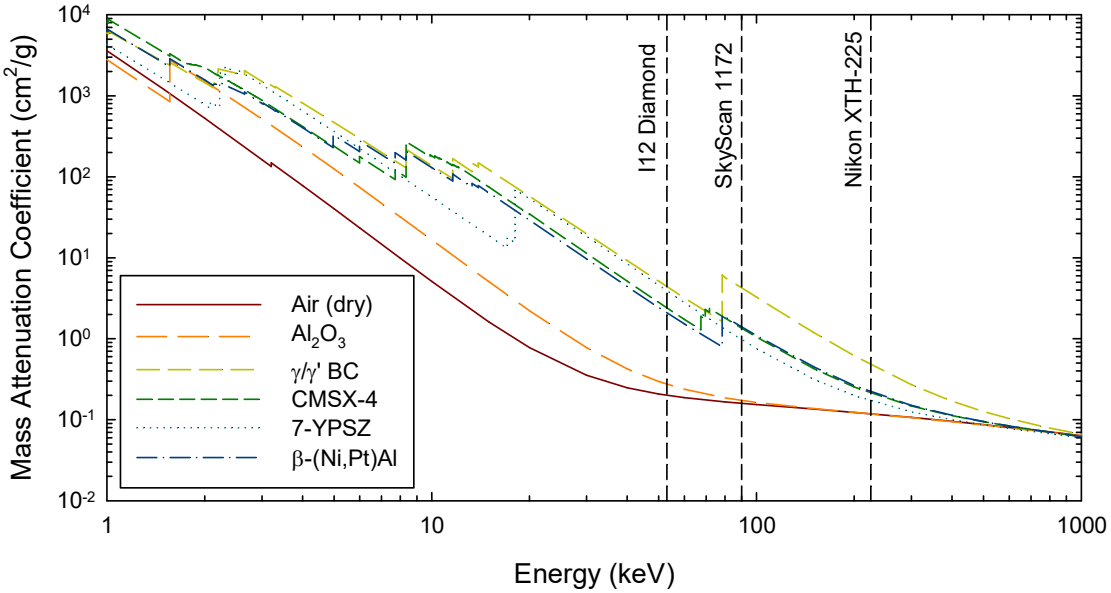

Figure 70 – Mass attenuation coefficients calculated using WinXCom [118,119] *for CMSX-4 substrate* [165]*, β-(NiAl)* [171] *and γ/γ'* [172] *bondcoat phases, 7-YPSZ topcoat, alumina TGO and dry air at sea level* [173].

2.8.1 Nikon XTH-225 industrial scanner

A Nikon Metrology XTH-225 (Figure 71) with a 225keV reflection target with a minimum focal spot size of 3µm at 7W was used. The detector resolution and beam configuration of this device was such that imaging cylindrical micro-specimens yielded little detail particularly in the topcoat. The Nikon XTH-225 however, was particularly suited to imaging larger specimens of the order of centimetres and was used to image full HP1 turbine blades. A 14-bit Varian 4030 detector was used with a pixel resolution of 20µm at 2300x3200. The sample stage allowed manipulation about four axes (X, Y, Z and R_z – rotation about the Z axis).

Figure 71 – Nikon XTH-225 industrial X-ray tomography system with sample chamber open.

2.8.2 SkyScan 1172 benchtop scanner

Benchtop X-ray MicroCT work was carried out using a SkyScan 1172 scanner (Figure 72). The device consisted of a Hamamatsu 100keV, 10W cone-beam X-ray tube-source with an 11Mpix cooled CCD detector to deliver a theoretical resolution of 0.5µm per pixel at a maximum resolution of 4200 x 2300 pixels. The effective resolution was at least an order of magnitude lower (10µm) owing to the high attenuation of the CMSX-4 and TBC system. The stage consisted of a 4-axis system (X, Y, Z and R_z – rotation about Z) and samples were manually attached to the smallest available sample holder using adhesive.

To compensate for beam hardening effects (the absorption of low-energy X-rays suggesting an artificially more dense sample surface), two filters, 1mm Al and 0.05mm Cu were available. For scans carried out in this work, both Al and Cu filtering was applied due to the highly attenuating nature of the nickel substrate. An exposure time of 4 seconds was thus used for unconstrained specimens with a step size of 0.28° per projection over 180°.

Prior to each high-resolution scan, two reference scans were carried out using the supplied 2mm diameter alignment tool at a distance corresponding to a resolution of 1.0µm followed by a scan with a resolution of 0.5µm. These reference scans provided pixel misalignment correction and inclination compensation when generating projections. Reconstructions were carried out using the SkyScan proprietary software, nRecon that utilised a modified Feldkamp cone-beam reconstruction algorithm with adjustable ring-artefact reduction, additional misalignment compensation and thermal shift correction (stage temperatures typically increased by 2-3°C over the course of a scan).

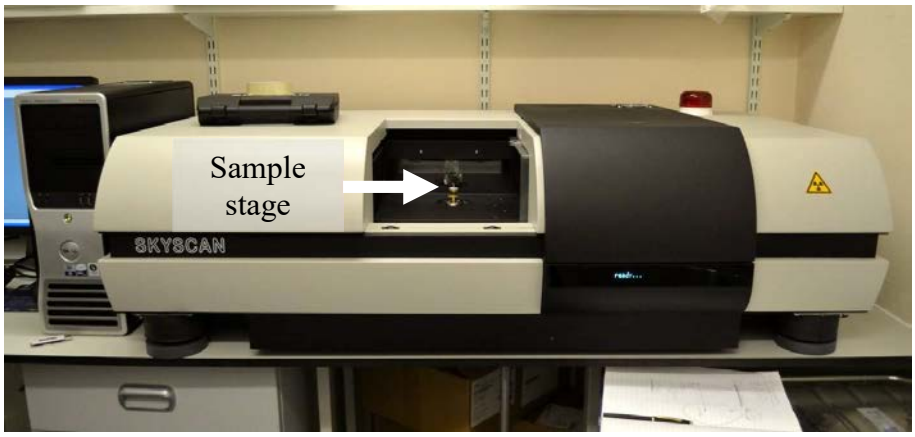

Figure 72 – SkyScan 1172 Bench-top X-ray micro-tomography system with sample chamber open. X-ray generation is through a 100keV Hamamatsu tube-source X-ray and the detector is an 11MPix CCD camera coupled to the device X-ray scintillator.

2.8.3 Synchrotron tomography at I12 Diamond Light Source

Synchrotron X-ray micro tomography was carried out at the I12 Joint Engineering, Environmental and Processing (JEEP) beamline (Figure 73) at Diamond Light Source, Didcot, UK. Two beamtime allocation blocks were provided under Diamond experiment numbers EE-8331-1 (January 2013) and CM-4693-5 (November 2014). The first of these consisted of fifteen 8-hour shifts and a team of five persons, while the second constituted three 8-hour shifts and a team of three persons. The first allocation block was used primarily to carry out 20-hour thermal cycles on APS constrained and unconstrained

specimens and the second for scans of samples without topcoats. In both experiments, a monochromatic beam of 53keV was used in absorption contrast configuration. A PCO 4000 camera with a field of view of 3.6mm×2.4mm was used to deliver a nominal voxel resolution of 0.9µm in EE-8331-1 and 1.3µm in CM-4693-5. The effective imaging resolutions achieved were 1.5µm and 3µm owing to the highly tuned and monochromatic synchrotron beam when compared to the Nikon XTH-225 and SkyScan 1172.

To maximise the throughput of scanned specimens, a sample holder was constructed using machined aluminium and cut Perspex piping (Figure 74). This casing housed a four-axis goniometer with an additional z-axis lead screw adjustment and was designed to fit the existing Huber goniometer system on the 50kg sample stage at I12. The design of the sample holder allowed positioning of one cylindrical micro-specimen over another. Specimens were scanned over 180° with 0.06° separating each step with an exposure time of 2.0s per step for samples without an APS constraint (both with and without topcoats) and 3.0 seconds for constrained specimens. Reconstructions were carried out using the in-house reconstruction algorithm at I12 incorporating ring artefact suppression [174].

Near in-situ thermal cycling of a collection of samples, in which the same sample was repeatedly scanned over a number of thermal cycles was supported by two Lenton Thermal Designs horizontal tube furnaces running at 1200°C and 1150°C. For example, Rolls-Royce low-cost bondcoat cylindrical micro-specimens were scanned in the as-received state, then scanned again following one 20-hour thermal cycle, once again following a second 20-hour thermal cycle, etcetera.

Furnace temperatures were calibrated using the NPL-certified R-type thermocouple referenced previously. Samples were loaded and unloaded manually and both furnace work-tubes were configured with a firebrick shelf to permit numerous sample boats to be

exchanged from both ends of each furnace. Samples were allowed to cool in laboratory air to 21°C without forced cooling over a period of 20 minutes before either scanning or storing in a desiccator to fit the scanning schedule.

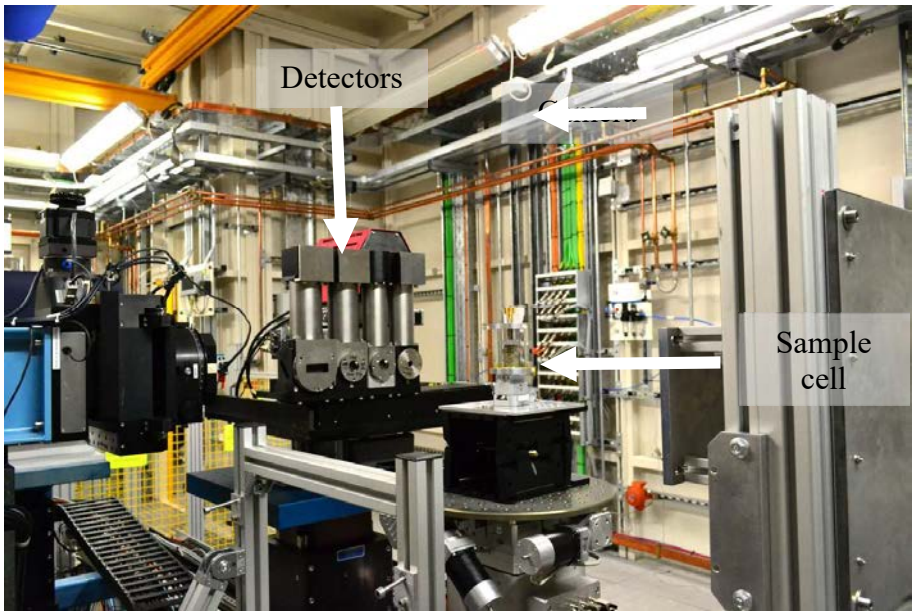

Figure 73 – Experimental hutch at I12 beamline (JEEP) at Diamond Light Source, Didcot. The four camera modules are visible behind the sample holder.

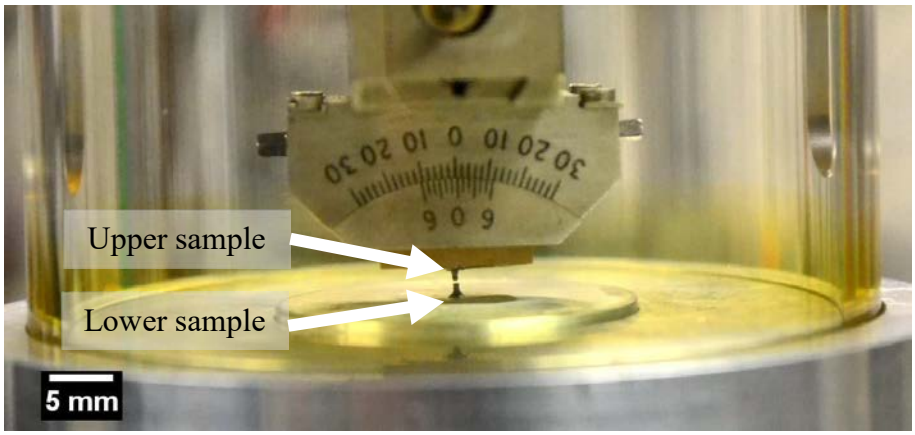

Figure 74 – Twin sample cell fabricated for use on the small-specimen stage in experimental hutch 1 at the I12 beamline that holds one sample over another. The cell consists of a 4-axis goniometer (two rotation and two translation) inverted and mounted to a z-translation plinth. The cell casing is derived from a Perspex tube (note radiation damage at base of Perspex case).

Both Rolls-Royce Pt and Pt-Al bondcoat specimens, in addition to Alstom Pt-Al bondcoat specimens, were scanned (Table 3). A selection of samples with a mechanical constraint in the form an APS coating applied to the cylindrical free surface of the samples were also imaged.

Table 3 – Summary of near in-situ synchrotron X-ray tomography scans carried out at Diamond Light Source on Rolls-Royce Pt-Al, Rolls-Royce Pt and Alstom Pt-Al cylindrical micro-specimens.

Coating	Temperature	Constraint	Scan times (hours)				
RR Pt-Al	1200°C	No	0h	20h	40h	60h	80h
		Yes	0h	11h	19h	25.5h	38.8
	1150°C	No	0h	20h			
		Yes	0h	20h			
RR Pt	1200°C	No	0h	20h	40h	60h	80h
		Yes	0h	11h	19h	25.5h	
	1150°C	No	0h	20h			
		Yes	0h	20h			
Alstom Pt-Al	1200°C	No	0h	20h	40h	60h	80h
		Yes	0h	5h	10h	18h	31.3h
	1150°C	No	0h	11h			

2.8.4 Image processing

Image processing of reconstructed synchrotron datasets was carried out using the Fiji software package (Fiji Is Just ImageJ) [168], an extension of the open-source ImageJ platform [175]. Translation and rotation correction of image stacks for the same specimen over thermal cycles was carried out in Fiji, assisted by the micro-drilled reference holes. The source of these unwanted rotations and translations was primarily from removing and returning samples to the stage between thermal exposure periods.

In addition to unwanted rotations and translations, another form of image processing that became necessary was due to variations in pixel intensity, visible as differences in brightness and contrast between timesteps. Differences in beam intensity, stage movement and detector response contributed to these variations in pixel intensity. In order to correct for these variations, image stacks were normalised using the greyscale values of the CMSX-4 substrate bulk between timesteps for each sample. The substrate was used as the reference as it showed the least deformation and microstructural evolution. Correcting for these variations was important both during segmentation when

determining the sizes of features (cracks, pores and voids) and also for the accuracy of digital volume correlation (DVC) calculations.

The normalisation procedure was a three-stage process, the first of which was to compute the histogram for the entire image stack for all timesteps of each specimen (Figure 75a). The pixel intensities ranged from 0 (black) to 255 (white) corresponding to the 8-bit (256 value) greyscale spectrum and the integral of each histogram corresponds to the total number of pixels in the image stack. The first peak from the ordinate of each histogram corresponds to the background (air) and the second peak to the sample itself. The second step was to adjust the histograms relative to each other such that pixels corresponding to the background were truncated (set to 0) at the trough between the bimodal histogram peaks (Figure 75b). Subsequent to background normalisation, the third step was to adjust the brightness and contrast such that all the histogram peaks were coincident with the substrate bulk in the as-received scan (approximately 127 in the case of Figure 75b).

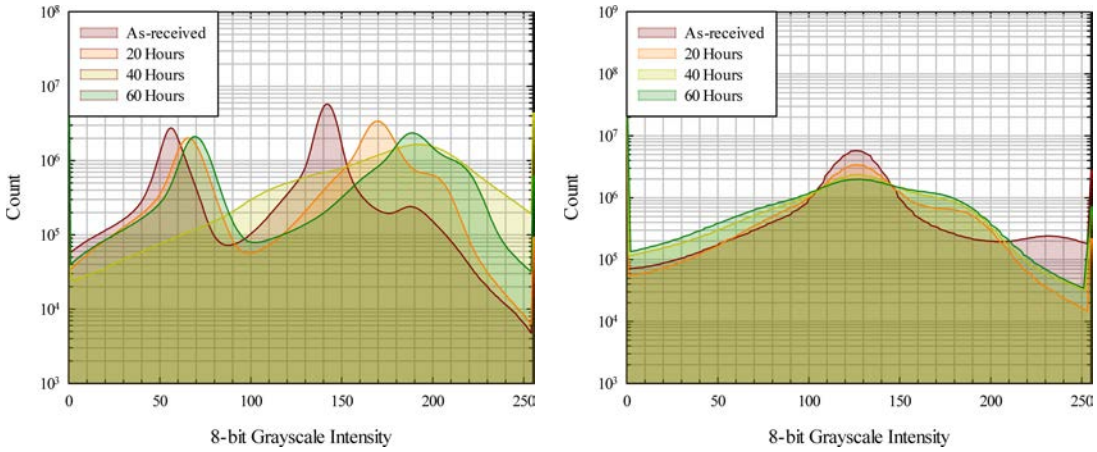

Figure 75 – Pixel intensity adjustment to remove background noise and normalise brightness and contrast. Histograms of unconstrained Rolls-Royce Pt-Al specimens (a) before and (b) after normalisation respectively, for the same specimen through time.

2.8.5 Calculation of greyscale intensity profiles

The variation in greyscale intensities was used as a means to identify and monitor the evolution of interfaces, features and oxide thickening. A Matlab script was written to read an image stack and output a single line profile with averaging over a region of interest.

2.8.6 3-D segmentation

3-D feature analysis of the reconstructions was carried out using the Amira and Avizo Fire software packages. For each of the data sets, a label field was attached and using the segmentation editor (Figure 76), materials were created for each of the pore types (i.e. pores in the substrate, bondcoat, TGO and topcoat) in addition to the default exterior and inside materials of the editor. One voxel was assigned to only one material at any given time and materials were locked sequentially. The complete volume of the specimen and background were first assigned to the interior material and locked, using the thresholding tool (0 – 255 selected). The remaining background voxels were selected using the magic wand tool (0 – 1 range with the 'All Slices' option enabled to select contiguous background voxels), assigned to the exterior material and locked. Features of interest from within the interior material (temporary unlocked) were assigned to the desired material. At any one time, only the source and destination materials were unlocked to avoid inadvertently replacing voxels. To discard outliers, having volume less than a desired amount, the remove islands tool was used and features with less than 15 voxels in 3D with a fraction less than 25% were removed.

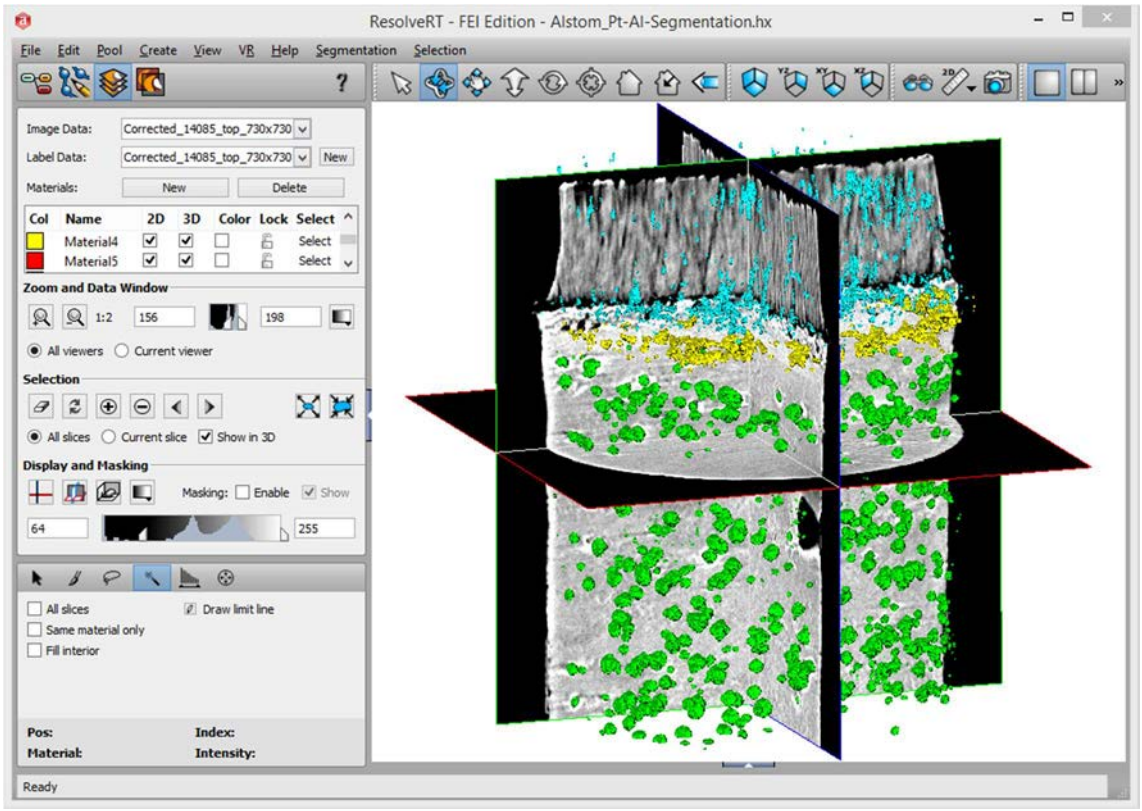

Figure 76 – Amira image segmentation editor showing final result of voxel assignment to appropriate materials.

2.9 Digital volume correlation

DVC using the Davis Strain Master 8.2.2 software package (Figure 77) was applied to reconstructions and computations were carried out between image stack pairs, i.e. as-received and 20 hours exposure, 20 hours and 40 hours exposure, etcetera. This allowed the three-dimensional, oxidation-induced internal displacement field to be computed as a function of thermal cycles.

Optimisation of software processing parameters was first necessary, with the key variables including the windows sizes, the number of passes (iterations), the fraction of window overlap and the peak search radius.

A series of known rotations were applied to the Rolls-Royce Pt-only bondcoat as-received image stack using Fiji and the effect of the number of processing passes was investigated (Figure 77). Firstly, a fixed number of passes was chosen and the applied rotation was

varied from 0.5° to 2° (Figure 78a). The window sizes were progressively deceased from 512 to 256 to 128 to 64 to 32 to 16 pixel cubes with a 50% window overlap. There was a continuous improvement in the precision of the computed output with an increase in the number of passes at the expense of computational time. Subsequent to this investigation, a fixed rotation of 1° was applied to the same as-received image stack using the same window sizes and the number of computational passes increased from 1 to 5 (Figure 78b). This further confirmed the strong dependence of the output precision on the number of passes with precision improving from 92.0% to 97.6% from 2 to 5 passes. This behaviour is expected as the domain outputs of one pass is used as the inputs to the following pass. Three passes for each window size was chosen as the optimum number of passes to balance numerical precision and computational time.

The next parameters investigated were the peak search radius and the window overlap. A decrease in precision of 0.3% was observed at a quarter of a window and a decrease of 1.98% precision at an eighth of a window. Consequently, the maximum peak search radius of 50% of the window was chosen as the optimum peak search radius. A 50% window overlap was also chosen as this value presented the highest precision compared to 25%, 75% and no overlap.

In addition to the settings optimised above (summarised in Table 4) the minimum required correlation coefficient (i.e. how likely the same pixel group was mapped between two timesteps) was set at 0.5, the optimum value to filter local image artefacts in the tomographic reconstructions [146]. Vectors having a correlation coefficient less than 0.5 were automatically deleted at each step. In addition, all post-processing utilities were disabled, including outlier detection/removal/insertion and vector field smoothing.

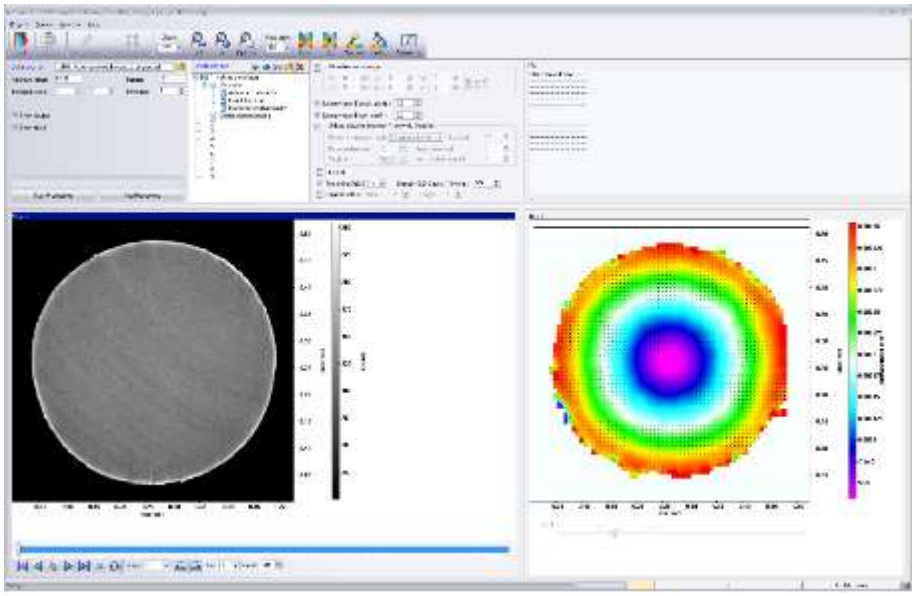

Figure 77 – LaVision DaVis 8.2.2 analysis environment showing source (left) and result (right) of 0.1° rigid body rotation.

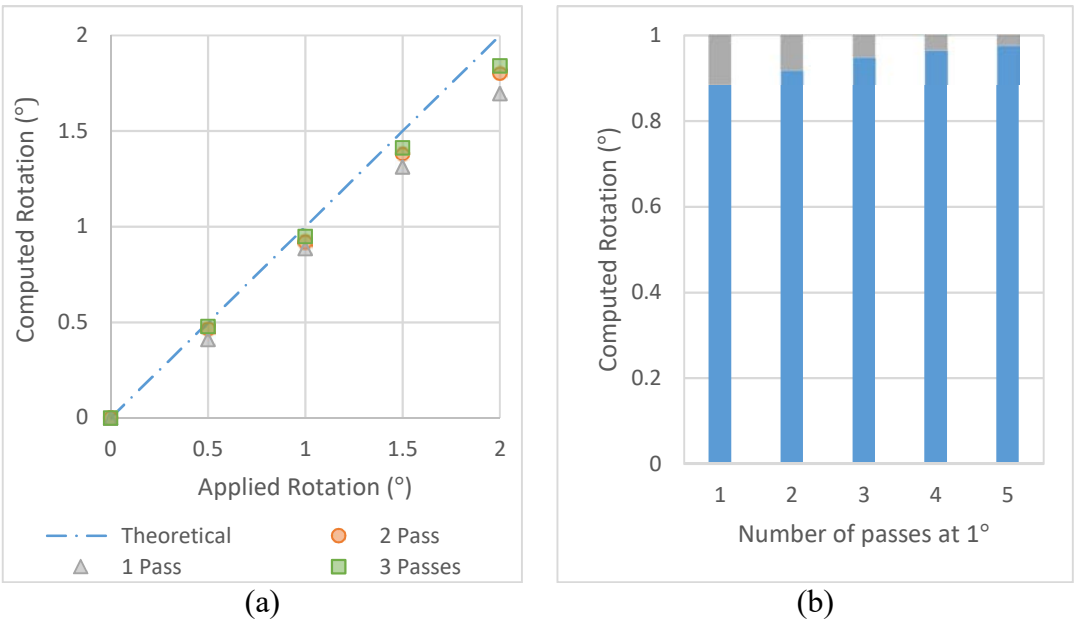

Figure 78 – The effect of the number of passes on the precision of the computation of a rigid body rotation of the as-received Rolls-Royce Pt specimen, (a) using a fixed number of passes and varying the applied rotation and (b), fixing the applied rotation and varying the number of passes.

Table 4 – Sequence of DVC correlation window sizes, correlation window overlaps, number of passes and peak search radius used at each stage.

Step	X	Y	Z	Overlap	Passes	Peak Search Radius
1	512	512	512	50%	3	Window/2
2	256	256	256	50%	3	Window/2
3	128	128	128	50%	3	Window/2
4	64	64	64	50%	3	Window/2
5	32	32	32	50%	3	Window/2
6	16	16	16	50%	3	Window/2

2.9.1 Rigid body correction

The removal from and return to the scanning stage of specimens generated displacements and rotations which were corrected using Euler angle and quaternions [176] written using a Matlab script [177]. A complete derivation of this algorithm is presented in Appendix G. It is computationally more efficient to estimate and correct rigid body movements after DVC processing as opposed to iteratively aligning the image stacks as the data set is significantly reduced. For example, an input dataset for the specimens considered here are of the order of 600×600×600px whereas as an output dataset following DVC computation is of the order of 80×80×80px. The results of the calculated rigid body translation for unconstrained specimens are presented in Table 5.

Table 5 – Calculated rigid body rotations using Euler rotations and quaternions for 20-hour cycles at 1200°C. Step 1 data corresponds to the DVC computation of As-received and 20 hours exposure image pair, step 2 the 20-hour and 40-hour pair and step 3 40-hour to 60-hour pair.

	Rolls-Royce Pt-Al			Alstom Pt-Al			Rolls-Royce Pt		
Step	1	2	3	1	2	3	1	2	3
R_x	0.21°	-0.37°	0.24°	0.02°	0.76°	-0.78°	-0.19°	0.02°	-0.03°
R_y	0.19°	-0.29°	0.11°	0.22°	-0.05°	0.28°	0.06°	-0.11°	0.05°
R_z	1.01°	-1.06°	-0.01°	-1.93°	2.59°	0.32°	-0.48°	0.64°	0.12°

2.9.2 Displacement visualisation and analysis

A Matlab script (Appendix H) was written to combine tomography data sets with a computed DVC vector field (Figure 79). Such a script was necessary to determine the location of the TGO within the resulting DVC vector fields in addition to the fact that the

DVC data sets were scaled down by approximately a factor of eight. Regions that did not correlate, where the correlation coefficient fell below 0.5, do not display displacement data.

The script also allowed orthogonal slices (Figure 80) to be extracted from the displacement data. In and around the TGO, an X-Y plane could also be radially analysed with in-plane and out-of-plane displacements extracted (Figure 81). For in-plane displacements, the local Cartesian coordinate system of each vector was transformed into cylindrical coordinates and determined whether the displacement was negative (inward) or positive (outward). Where appropriate, the average strain was computed by fitting a first order polynomial to the displacement set (Figure 81). In the case of Pt bondcoat shown here for example, the TGO displays a linear distribution of lateral extension relieving the compressive stress acted upon the oxide. This allows calculation of strains within the oxide layer, discussed further in Chapter 4 and Chapter 6.

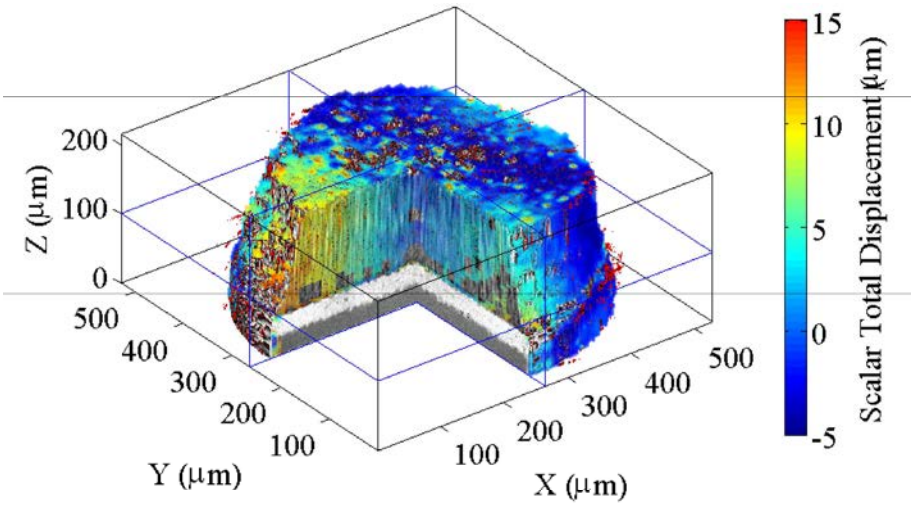

Figure 79 – 3-D visualisation of Rolls-Royce Pt specimen showing corner cut-away of scalar total DVC displacement field (as-received to 20-hour computation) overlaid with transparency onto as-received tomographs of Rolls-Royce Pt-only bondcoat cylindrical micro-specimen.

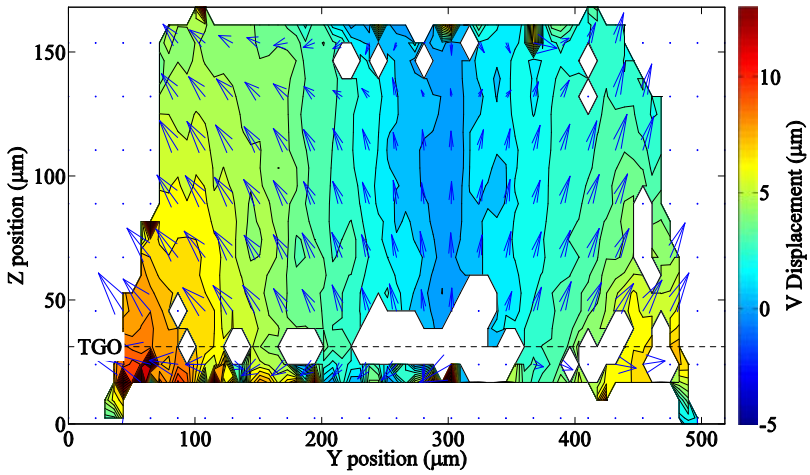

Figure 80 – 2-D DVC displacement vector field for a Rolls-Royce Pt only specimen at the central Y-Z plane after 20 hours at 1200°C. Contour map shows displacement components in the plane of the TGO.

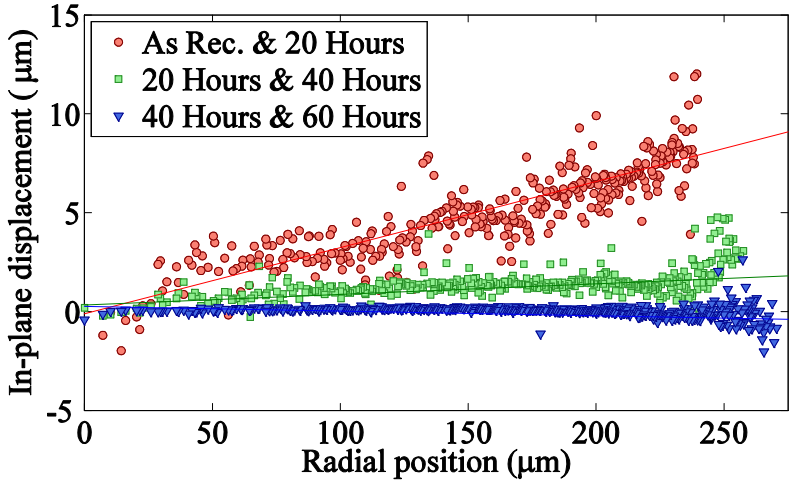

Figure 81 – In-plane displacements in the TGO for Rolls-Royce Pt-only bondcoat cylindrical micro-specimen extracted in a cylindrical coordinate system for incrementing 20 hour cycles at 1200°C.

Chapter 3 Cyclic oxidation of β-(Ni,Pt)Al and γ/γ' TBC systems

3.1 Macroscopic characterisation of aerofoil section spallation

Aerofoil sections of both Pt and Pt-aluminide bondcoats were thermally cycled to room temperature from peak temperatures in the range 1100°C – 1200°C, undergoing 20-hour cycles until TBC failure. A total of fourteen aerofoil sections were cyclically exposed to 1200°C, eight samples at 1175°C, four at 1150°C and two at 1100°C. The criterion for coating section failure was defined as a minimum spallation of 20% of the coated surface area. The blade position nomenclature described previously (Figure 56) was used to characterise the location of spallation around aerofoil sections. Macrographs of a selection of spalled Pt (Figure 82) and Pt-aluminide (Figure 83) aerofoil sections at 1200°C illustrate the extent of TBC loss on failure. In cases where minor local spallation had occurred but was below the global 20% criterion, cyclic oxidation was continued and a zone of repeated spallation-oxidation was observed (for example, between positions G and H, Figure 82c).

In some instances, local delaminations were observed (for instance, position F through G, Figure 83b) that did not lead to immediate spallation. Other samples exhibited sub-surface delaminations, the extent of which was only revealed following spallation (for example, position E through G Figure 83a). Spallation was also noted in which only the near-edge TBC remained adherent (demonstrated at position J in both Figure 82a, and Figure 82b).

The time to spallation of all aerofoil sections tested (Figure 84) indicates that at higher temperatures there is a decrease in spread of time to spallation. At the test temperature of 1175°C, visible failure occurs between 40 hours and 480 hours (40 hours – 240 hours for Pt-aluminide bondcoat and 140 hours – 480 hours for Pt bondcoat) while at 1200°C, a narrow band of time to failure is observed between 60 hours – 100 hours for both bondcoats.

Of the fourteen aerofoil sections tested at 1200°C, the failure lives (Figure 85a) indicate that Pt and Pt-aluminide aerofoil sections displayed similar times to spallation. The distribution of failure around each aerofoil section (Figure 85b) suggests that spallation is more prevalent around complex geometries (positions D through J Figure 56) around aerofoil sections for both bondcoats at 1200°C.

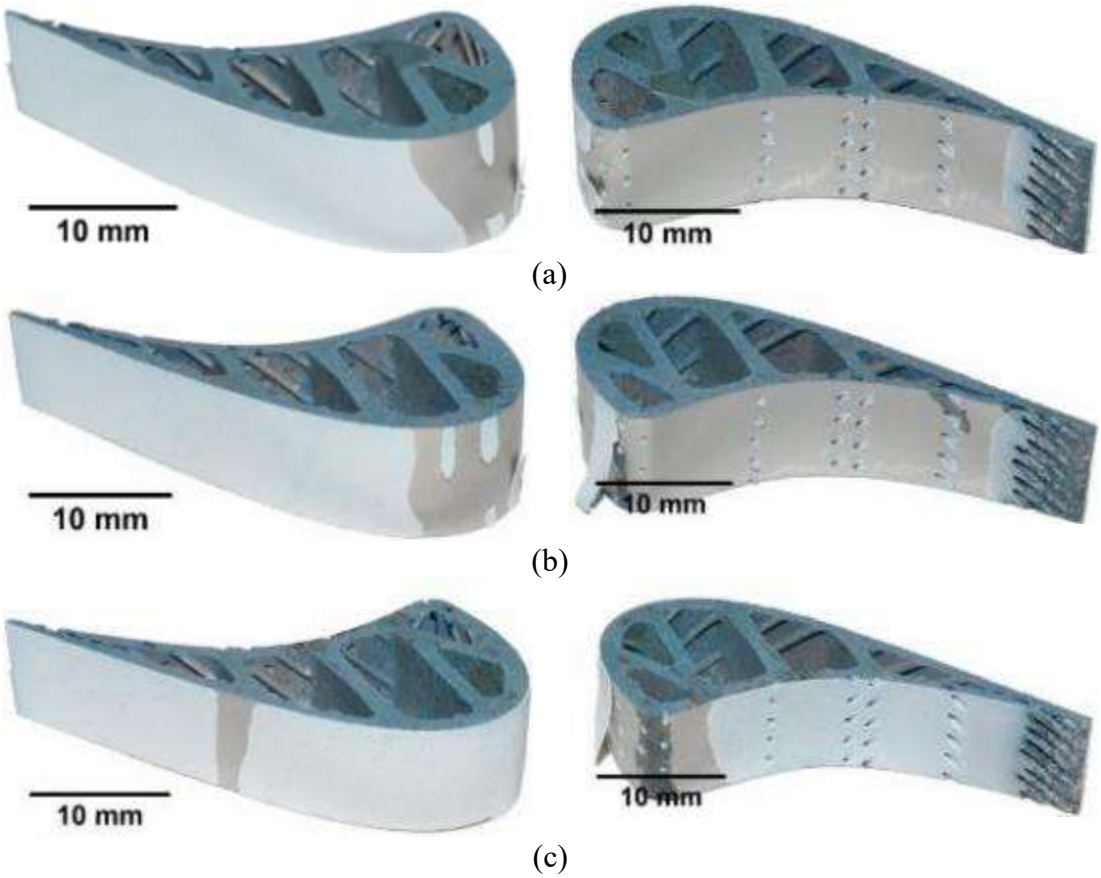

Figure 82 – Rolls-Royce Pt bondcoat aerofoil sections, all after five 20-hour thermal cycles to spallation at 1200°C showing (a) sample 09-C after five cycles (b) sample 09-A after five cycles and (c) sample 11-A. Each pair of images shows the front upper (suction) surface and lower (pressure) surface of a single aerofoil section.

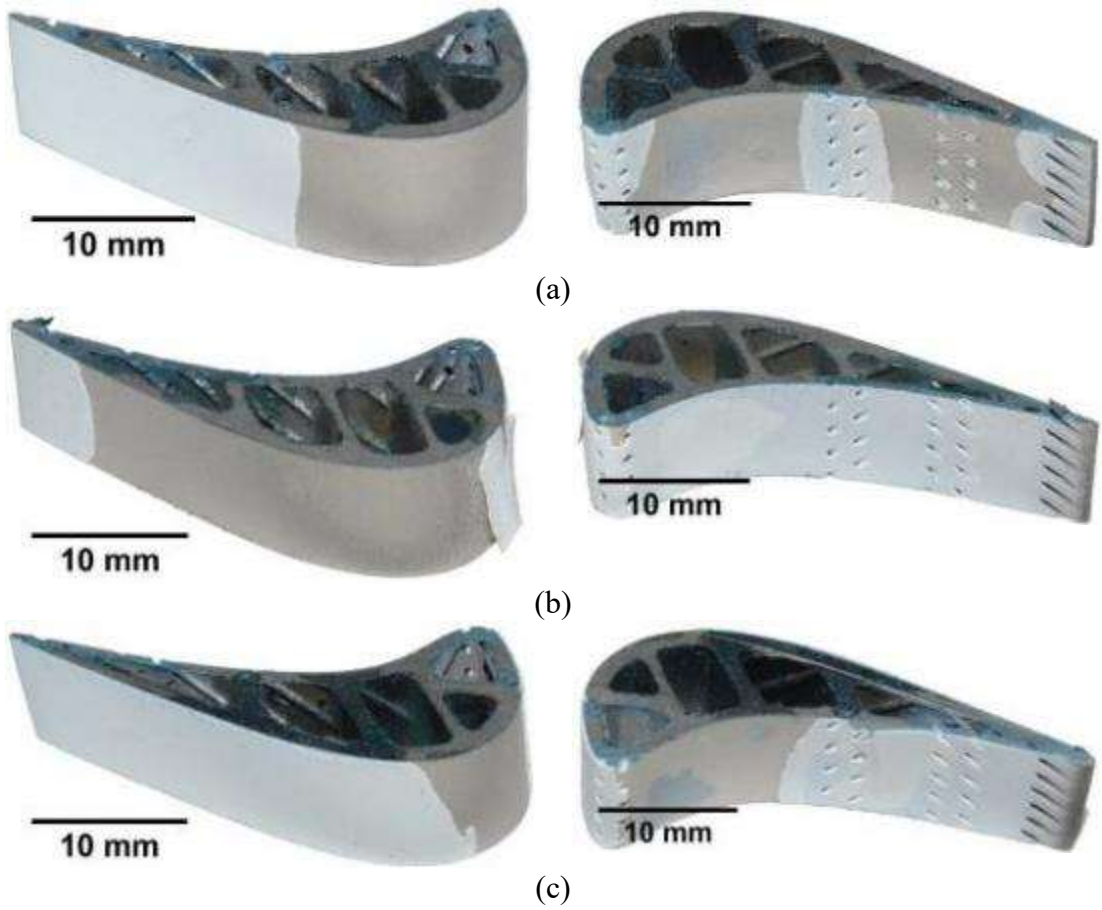

Figure 83 – Rolls-Royce Pt-Al bondcoat aerofoil sections following 20-hour thermal cycling to spallation at 1200°C showing (a) sample 13-C after four cycles (b) sample 14-C after five cycles and (c) sample 16-A after three cycles. Each pair of images shows the front upper (suction) surface and lower (pressure) surface of a single aerofoil section.

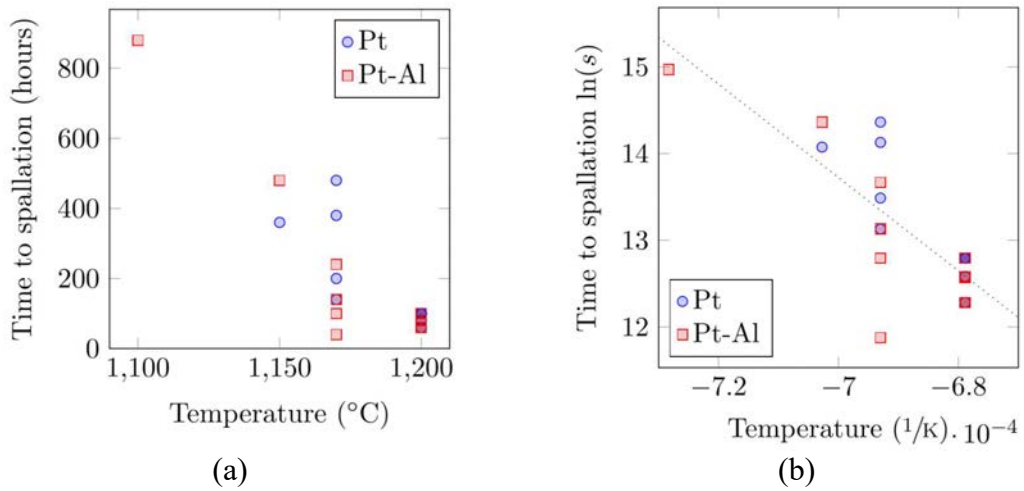

Figure 84 – Summary of time to >20% area spallation for all aerofoil sections tested at 1100°C, 1150°C, 1175°C and 1200°C shown as (a) standard axes and (b) Arrhenius plot.

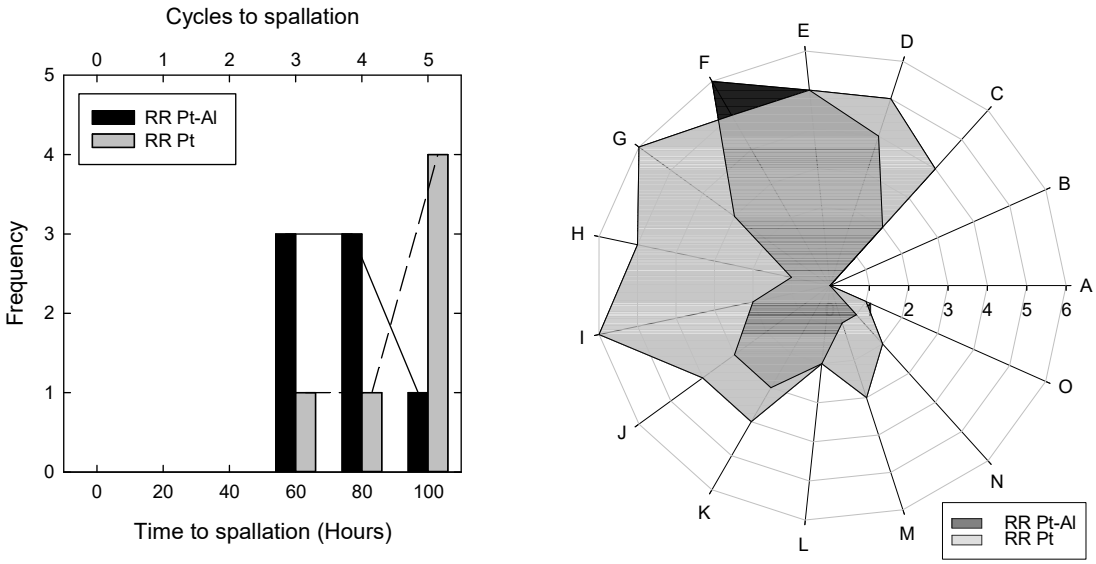

Figure 85 – (a) Histogram showing Rolls-Royce Pt and Pt-Aluminide aerofoil section lives as a function of the number of 20-hour thermal cycles at 1200°C and (b) polar plot showing the spallation locations around aerofoil perimeter where each concentric ring represents the number of aerofoil sections exhibiting spallation.

Samples thermally cycled at 1150°C were analysed using optical flash thermography to investigate the nature of sub-surface defects, visible and otherwise. Thermographs (Figure 86a) of the Pt-Al aerofoil section (sample 21-C, Figure 86b) and the Pt aerofoil section (sample 07-B, Figure 86c) were recorded alongside reference as-received samples of the both bondcoat types. The thermally cycled images appear brighter in contrast to the reference samples, likely due to a reduction in thermal dissipation rate from the optical flash owing to a thicker TGO and sintering within the topcoat. The section of visibly spalled TBC is clearly mapped in the thermograph (position A) but the technique reveals a subtle area of local damage not noticeable on visual inspection (position B).

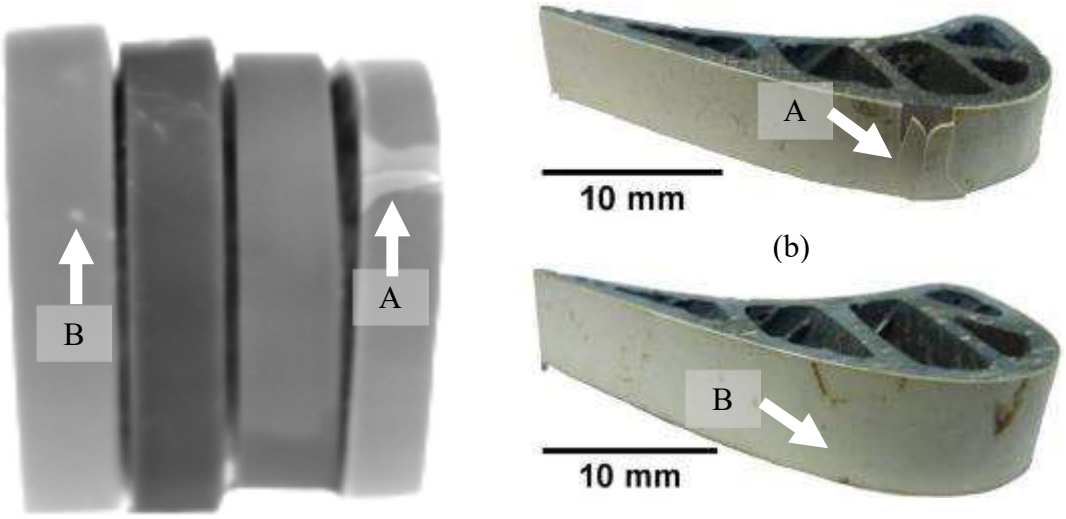

Figure 86 – (a) Optical flash thermograph of samples (far-left and far-right) thermally cycled for 880 hours (forty-four 20-hour cycles) at 1150°C with as-received reference samples (inner two) and (b) Sample 21-C after 880 hours showing local edge cracking and spallation that corresponds to far-right sample in optical flash thermograph and (c) Sample 07-B showing no visible damage that corresponds to far-left sample in optical flash thermograph.

3.2 Cyclic Oxidation of coupons and cylindrical micro-specimens

It is noted from the previous section that at higher temperatures (1200°C), the scatter in time to spallation is minimised and that suction surfaces nearest trailing edges are relatively immune from widespread and catastrophic TBC failure. For these reasons, coupons were extracted from the suction surface at the trailing edge (positions M through N, Figure 56). These coupons served two purposes, firstly used directly as samples for cyclic oxidation tests and secondly as the starting point for the fabrication of miniaturised cylindrical micro-specimens. Where possible and between thermal cycles of both coupon and cylindrical micro-specimens, the exterior state of each sample was documented from the as-received state.

3.2.1 Exterior morphology

Backscatter micrographs were recorded of coupon specimens in plan-view (Figure 87). In general, and at low magnification, the topcoat bulk displayed little change. At the

sample edges however, the formation of inter-columnar separation was observed, manifest as cracks parallel to a sample edge. Plan-view examination of cylindrical micro-specimens derived from coupons (Figure 88) also showed the evolution of inter-columnar separation with a preferred orientation. This behaviour was noted on both Pt and Pt-aluminide cylindrical micro-specimens but to a greater extent on Pt-aluminide samples.

The application of an APS mechanical constraint (Figure 89) alters the uniform topcoat appearance by introducing a continuous and concentric area of inter-columnar separation. This feature is likely to be associated with contraction upon cooling of the metallic APS bondcoat following the spraying process. Following twenty hours at 1200°C this prominent, circular separation is noted as increasing to a small extent.

Micrographs of cylindrical micro-specimens lacking a topcoat in the as-received state are indicative of the surface finish for Pt (Figure 90a) and Pt-aluminide (Figure 91a) bondcoats. These micrographs suggest a coarser finish with larger features on the Pt-aluminide than that of the Pt surface. This difference in as-received morphology is further confirmed by cross-sections of the rougher Pt (Figure 96a) and Pt-aluminide (Figure 97a) bondcoats, suggesting the bondcoats did not have the same surface finish. Although direct measurements of the bondcoat roughness were made, the difference in morphology becomes more pronounced with exposure at temperature. Following one twenty-hour cycle at 1200°C the TGO morphology of both Pt (Figure 90b) and Pt-aluminide (Figure 91b) surfaces appear continuous with the scales following the underlying profile.

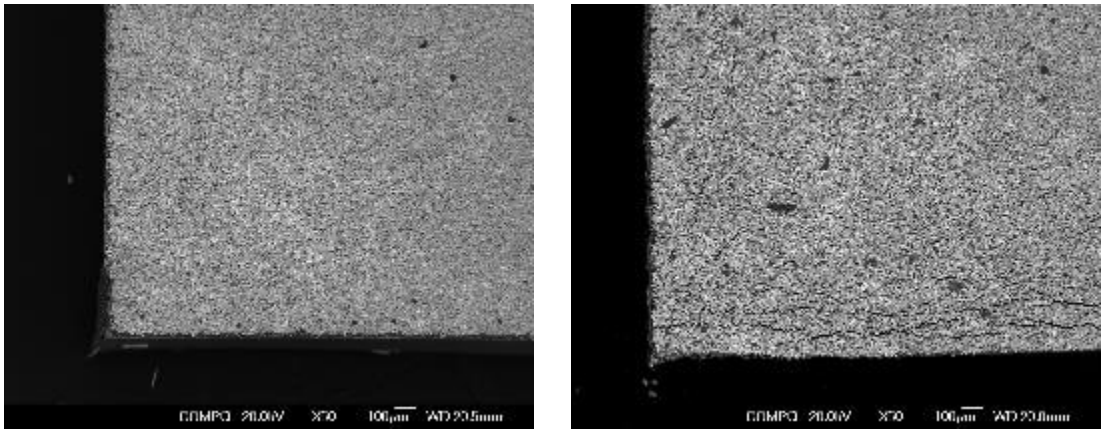

(a) (b)

Figure 87 – Backscatter micrographs showing topcoat plan view of the same Rolls-Royce Pt-aluminide coupon corner having a topcoat in (a) as-received state and (b) following 60 hours at 1200°C (three 20-hour cycles), showing evidence of inter-columnar separation with a preferred orientation.

A Rolls-Royce Pt-Al sample (17-A-1), from which the topcoat had spalled following eighty hours (four twenty-hour cycles) at 1200°C (Figure 92) was further analysed. Examination of the remaining bondcoat bulk revealed cavitation (Figure 93) breaching the surface near edges in addition to alumina islands located in the minima of local bondcoat undulations. Analysis of the underside of the remaining topcoat (Figure 92b) revealed an almost continuous alumina layer save for islands of missing alumina corresponding to those found on the bondcoat surface. Quantification of plan-view bondcoat bulk micrographs revealed 58.4% area retention of TGO (spallation at the TGO/topcoat interface), suggesting a 41.6% area spallation at the TGO/bondcoat interface.

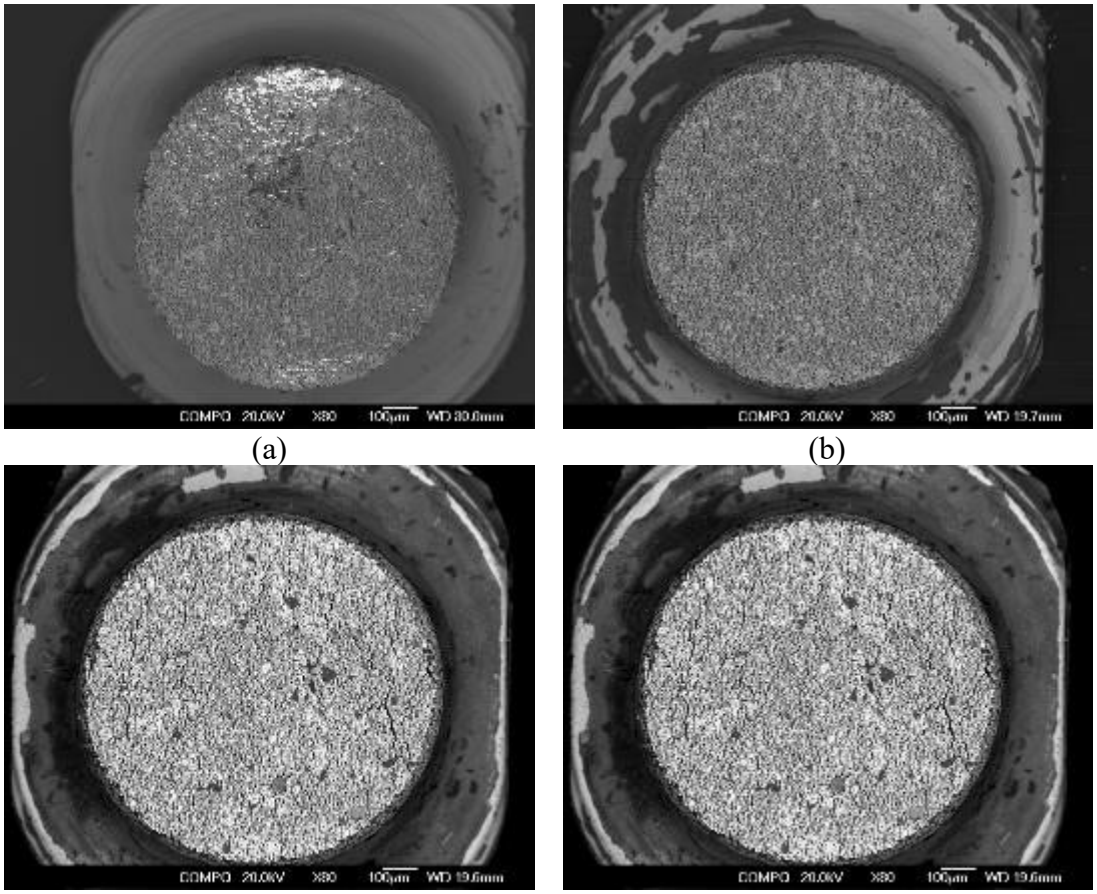

(a) (b)

(c) (d)

Figure 88 – Backscatter micrographs showing top view of EB-PVD topcoat of the same Rolls-Royce Pt cylindrical micro-specimen (a) as-received, (b) after one 20-hour exposure, (c) following two 20-hour cycles and (d) after three 20-hour cycles.

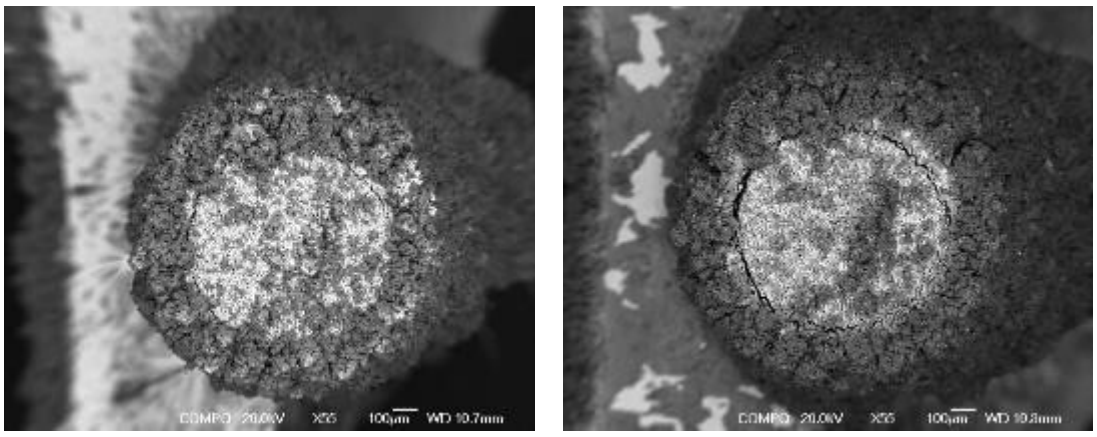

(a) (b)

Figure 89 – Backscatter micrographs showing top surface of APS coated Rolls-Royce Pt-Al cylindrical micro-specimen (a) as-received and (b) after one 20-hour period at 1200°C.

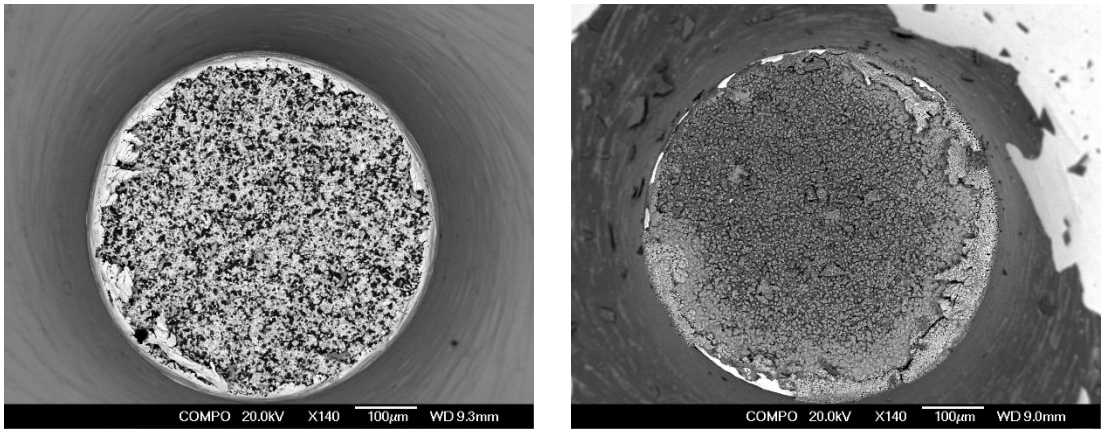

(a) (b)

Figure 90 – Backscatter micrographs showing top view of the same Rolls-Royce Pt cylindrical micro-specimen without a topcoat in (a) as-received state and (b) after one 20-hour exposure at 1200°C. Micrographs courtesy of C. Blackwell.

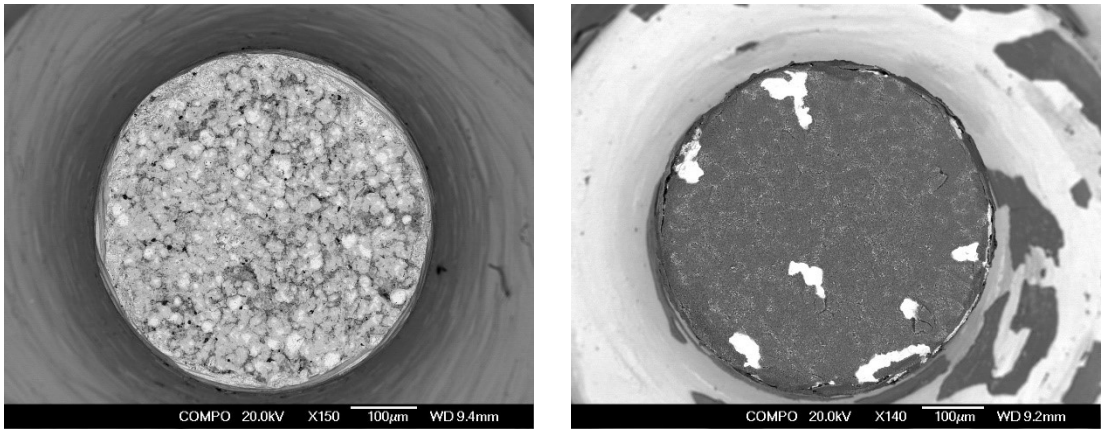

(a) (b)

Figure 91 – Backscatter micrographs showing top view of the same Rolls-Royce Pt-aluminide cylindrical micro-specimen without a topcoat in (a) as-received state and (b) after one 20-hour exposure at 1200°C. Micrographs courtesy of C. Blackwell.

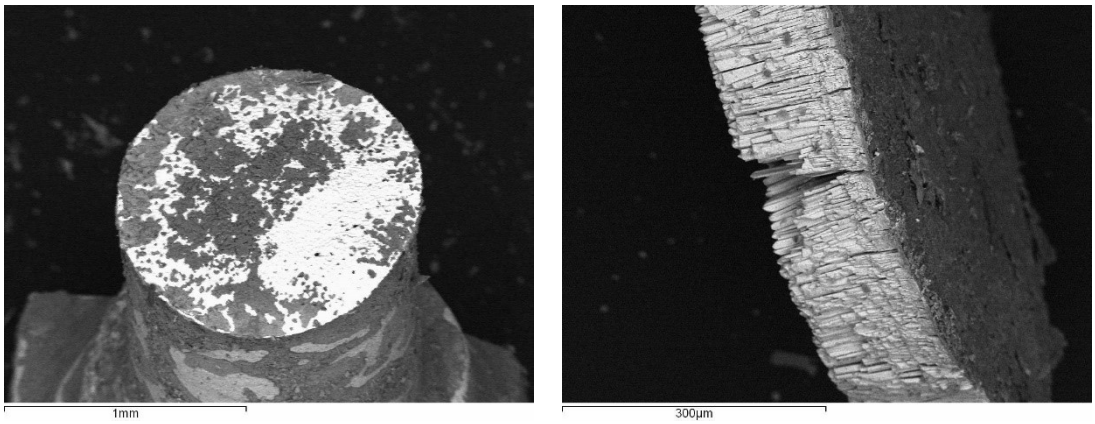

(a) (b)

Figure 92 – Backscatter micrograph of spalled Rolls-Royce Pt-Al cylindrical micro-specimen following four 20-hour cycles at 1200°C showing (a) elevated view of sample top surface in which dark regions correspond to alumina and brighter regions the bondcoat, and (b) corresponding topcoat section. Quantification of (a) in plan-view revealed a 41.6% area spallation at the TGO/bondcoat interface, with 58.4% of the sample retaining its TGO.

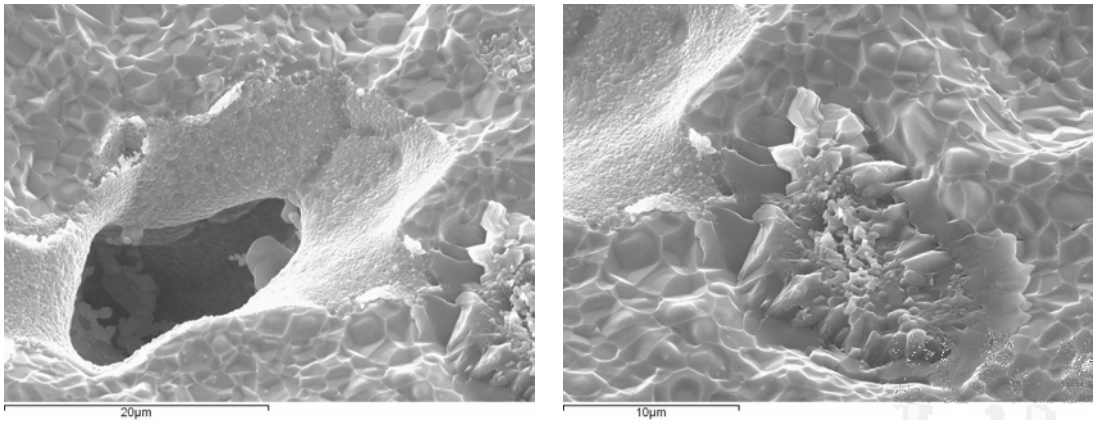

Figure 93 – SE micrographs of spalled Roll-Royce Pt-Al cylindrical micro-specimen following four 20-hour cycles at 1200°C revealing (a) morphology of cavitation breaching the surface and (b) islands of alumina at the minima of local bondcoat/TGO undulations.

3.2.2 Cross section overviews

The samples of the previous section examined in three dimensions were subsequently cross-sectioned. Coupons were sectioned normal to the direction of preferred inter-columnar separation at the midpoint. The cause of the preferred inter-columnar separation is not entirely clear but is likely attributable to the lateral bondcoat extension as the effect is limited to sample edges. Cylindrical micro-specimens were cross-sectioned such that the plane of analysis was coincident with the sample diameter.

Low-magnification cross-sections reveal that although coupons are seemingly flat in relation to the complex aerofoil geometry, some curvature over the width of the coupons exist (Figure 100). This curvature is associated with blade twist along the span of the HP1 turbine blades (Figure 55) that increases with distance from the blade root. Consequently, coupons originating from nearest the blade root display a near-symmetrical curvature (Figure 100a) while coupons derived from sections near the blade tip (Figure 100d) feature more pronounced curvature with bias toward the aerofoil trailing edge.

Cross-sections of Pt (Figure 94) and Pt-aluminide (Figure 95) cylindrical micro-specimens reveal a noticeable difference between the bondcoat behaviour and substrate homogeneity. The extent of substrate porosity between the two bondcoat types is equal in the as-received state. With time at temperature however, it is clear that Pt micro-specimens exhibit increased substrate porosity confined to sample edges. Of greater interest however, is the behaviour of the TGO/bondcoat at the exposed surface of each sample, in addition to the TGO profile across the sample width. A comparison of Pt (Figure 94d) and Pt-aluminide (Figure 95d) samples exposed for twenty hours at 1200°C shows that relative to the perpendicular substrate edge, there is significant outward lateral displacement of the TGO/bondcoat interface. This is accompanied by an arced deflection of the Pt-aluminide TGO along the sample width contrasted with a relatively flat TGO/bondcoat plane in the Pt sample.

Cylindrical micro-specimens, both Pt (Figure 96) and Pt-aluminide (Figure 97) lacking a topcoat were similarly exposed. As with samples having a topcoat, the micrographs show that the weaker Pt-aluminide bondcoat undergoes deformation significantly more so than the Pt equivalent. A comparatively large upward deflection of the TGO/bondcoat free surface is also visible for the Pt-aluminide specimen without a topcoat when contrasted with the equivalent sample with a topcoat.

The application of a mechanical constraint to the cylindrical edges of Pt-aluminide (Figure 98a) and Pt (Figure 98b) samples show the complete retention of any lateral displacements. The consequence of this restraint in the case of the Pt specimen is a crack driven through the entire radius (Figure 99b) of the sample along frequent alumina stress concentrators of the grit line. In the case of the Pt-aluminide specimen, it would appear that a crack at 45° to the TGO/bondcoat interface has been driven into the inter-diffusion

zone. The presence of an oxide layer around this crack supports this argument, suggesting that the crack-tip grew into the interdiffusion zone at temperature.

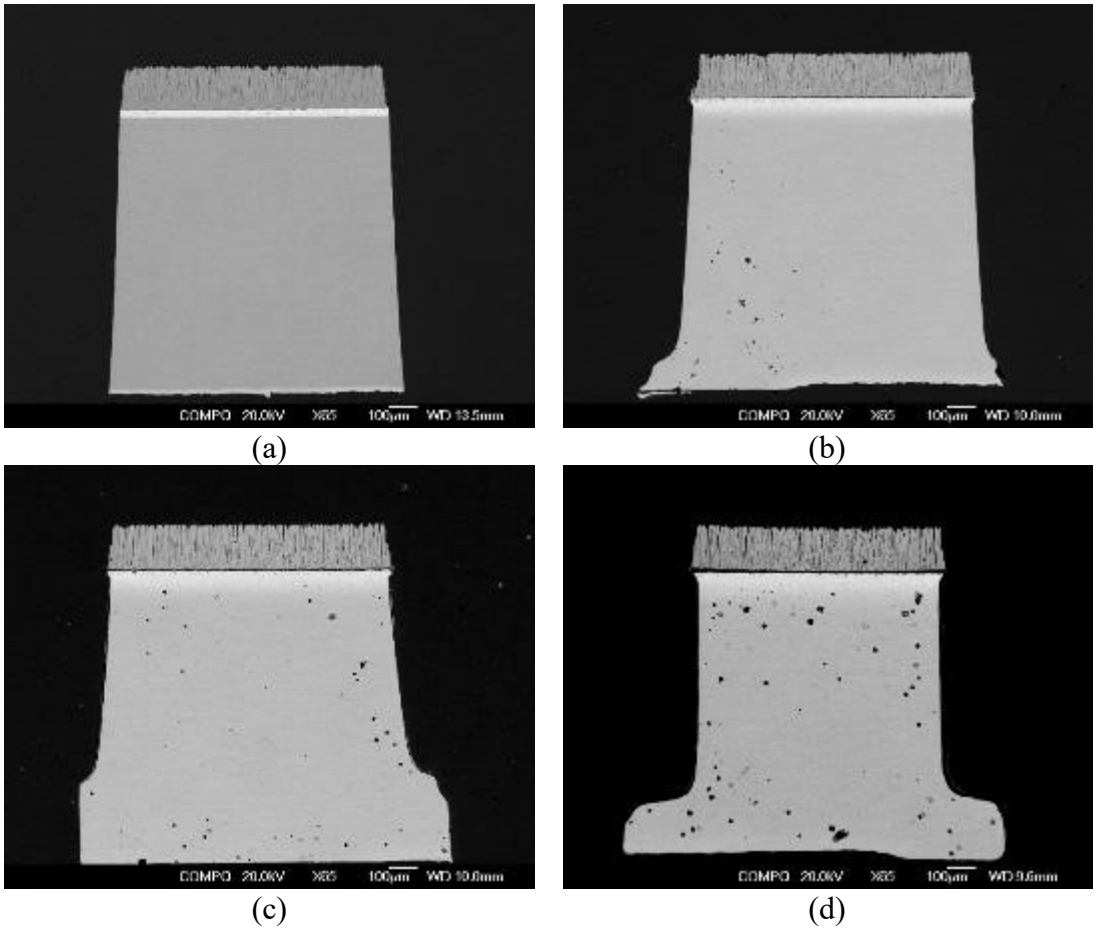

Figure 94 – Backscatter micrographs of Rolls-Royce Pt cylindrical micro-specimens (a) as-received, (b) following one 20-hour exposure, (c) following two 20-hour cycles and (d) following 4 20-hour cycles (80 hours) at 1200°C. Substrate pore fraction calculated as 0.26% 0.47% 1.32% area fraction for 20, 40 and 80 hours.

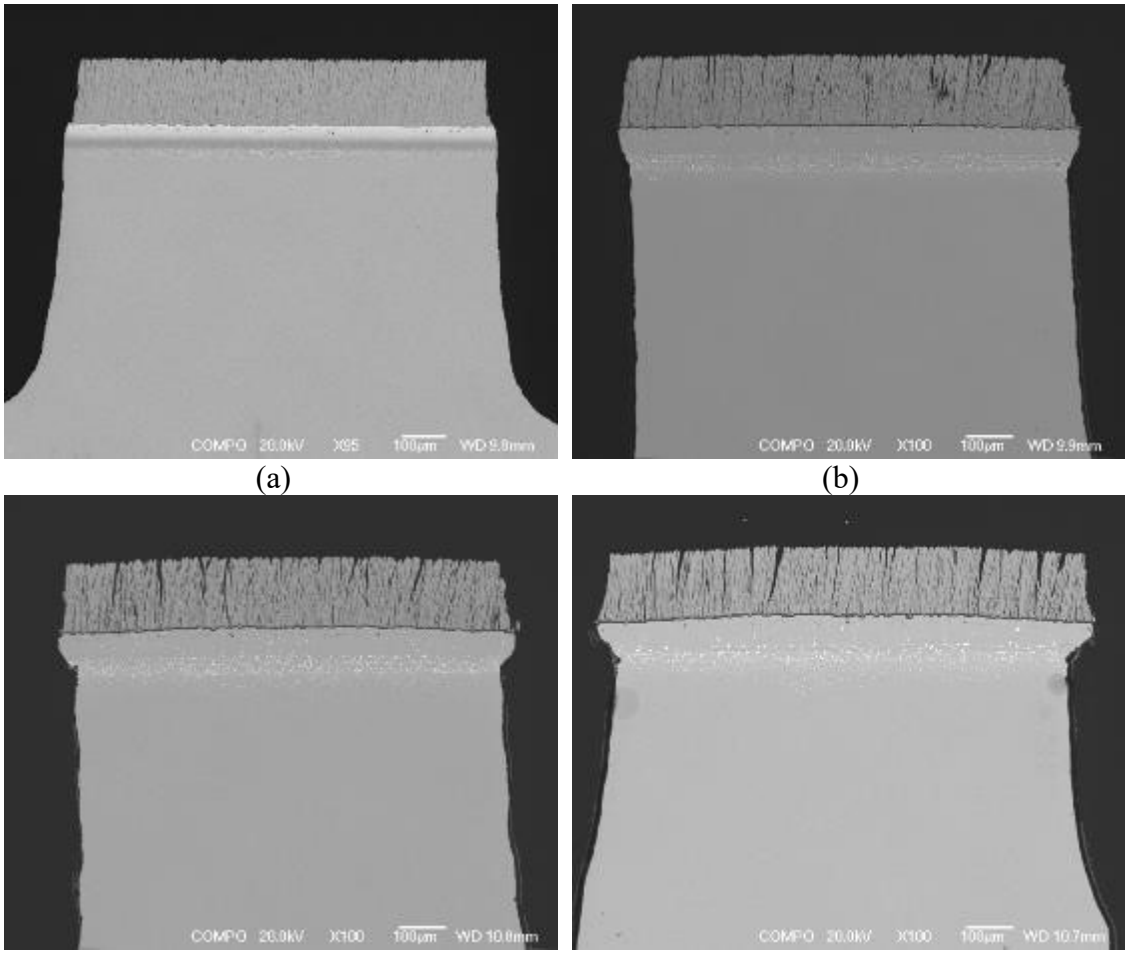

(a) (b)

(c) (d)

Figure 95 – Backscatter micrographs of Rolls-Royce Pt-Al cylindrical micro-specimens showing (a) as-received state, (b) following one 20-hour exposure, (c) following two 20-hour cycles and (d) following 4 20-hour cycles (80 hours) at 1200°C.

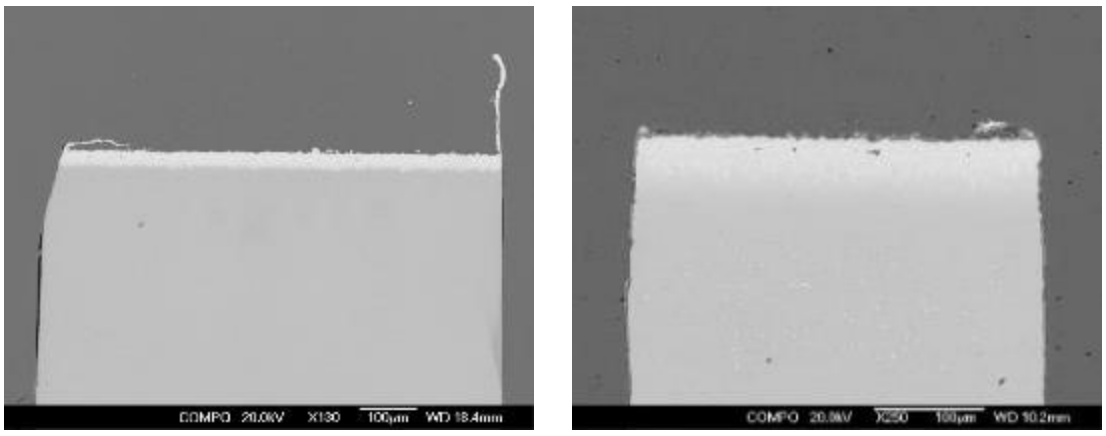

(a) (b)

Figure 96 – Backscatter micrographs showing cross-sections of Rolls-Royce Pt cylindrical micro-specimens without a topcoat in (a) as-received state and (b) after one 20-hour exposure at 1200°C. Micrographs courtesy of C. Blackwell.

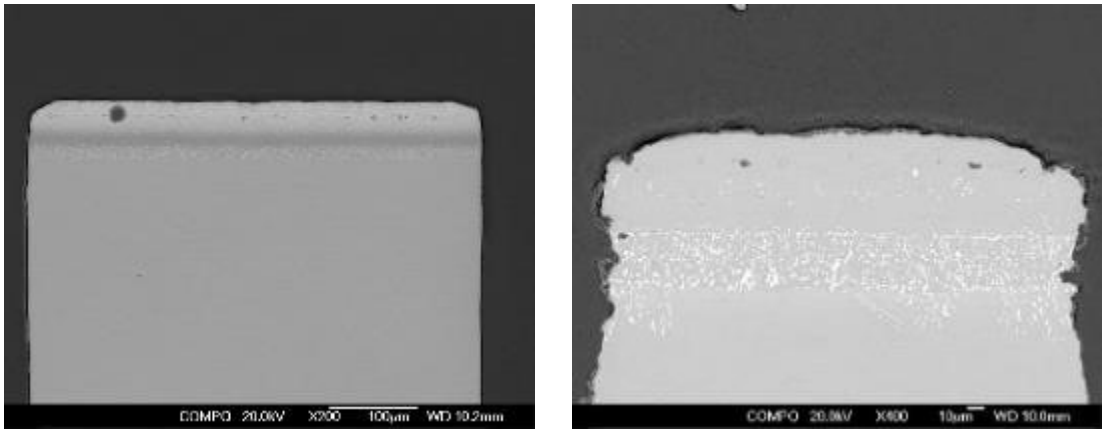

(a) (b)

Figure 97 – Backscatter micrographs showing cross-sections of Rolls-Royce Pt-aluminide cylindrical micro-specimens without a topcoat in (a) as-received state and (b) after one 20-hour exposure at 1200°C. Micrographs courtesy of C. Blackwell.

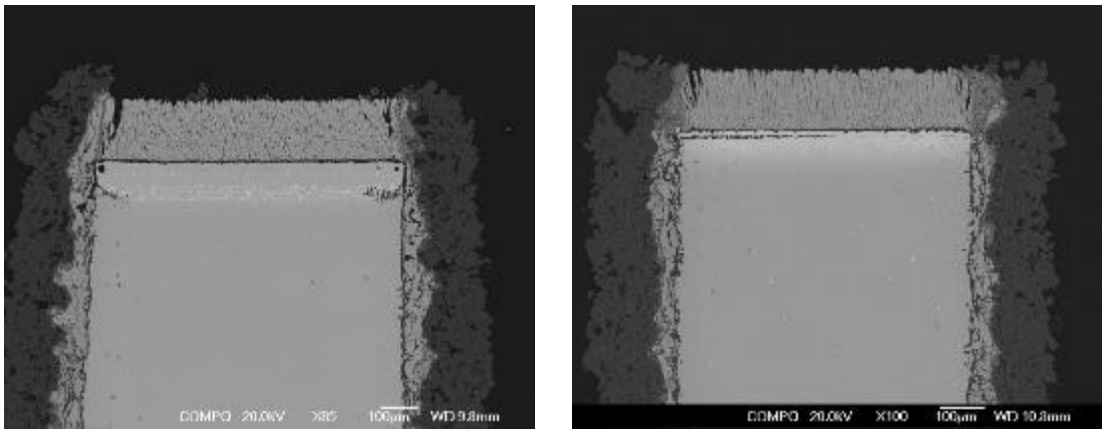

(a) (b)

Figure 98 – Backscatter micrographs showing cross-sections of Rolls-Royce (a) Pt-aluminide (sample 12-A-e-2) and (b) Pt (sample 02-E-k-2) cylindrical micro-specimens without a cylindrical APS mechanical edge constraint following one 20-hour exposure at 1200°C.

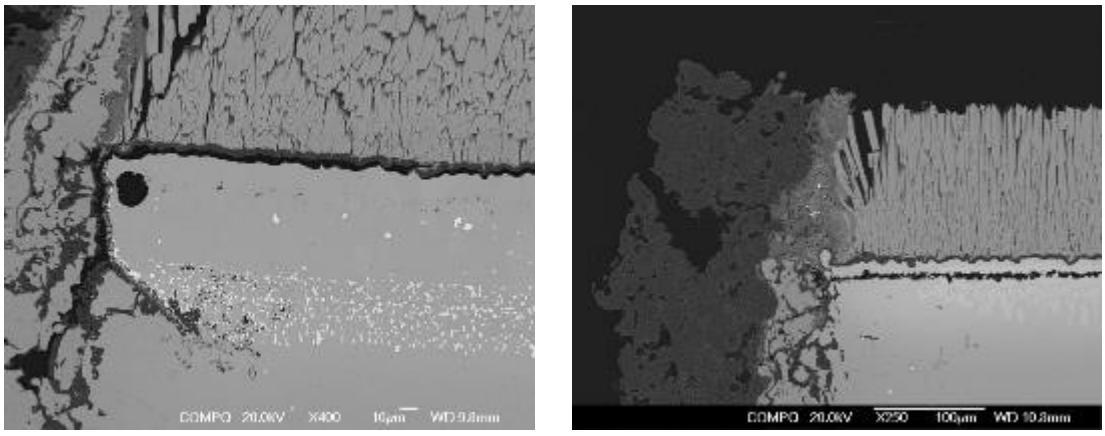

(a) (b)

Figure 99 – Backscatter micrographs showing left-hand edge of Rolls-Royce (a) Pt-aluminide (sample 12-A-e-2) showing a 45° crack at the interdiffusion zone and (b) Pt (sample 02-E-k-2) cylindrical micro-specimen with a crack driven through the grit-line; both with a cylindrical APS mechanical edge constraint following one 20-hour exposure at 1200°C.

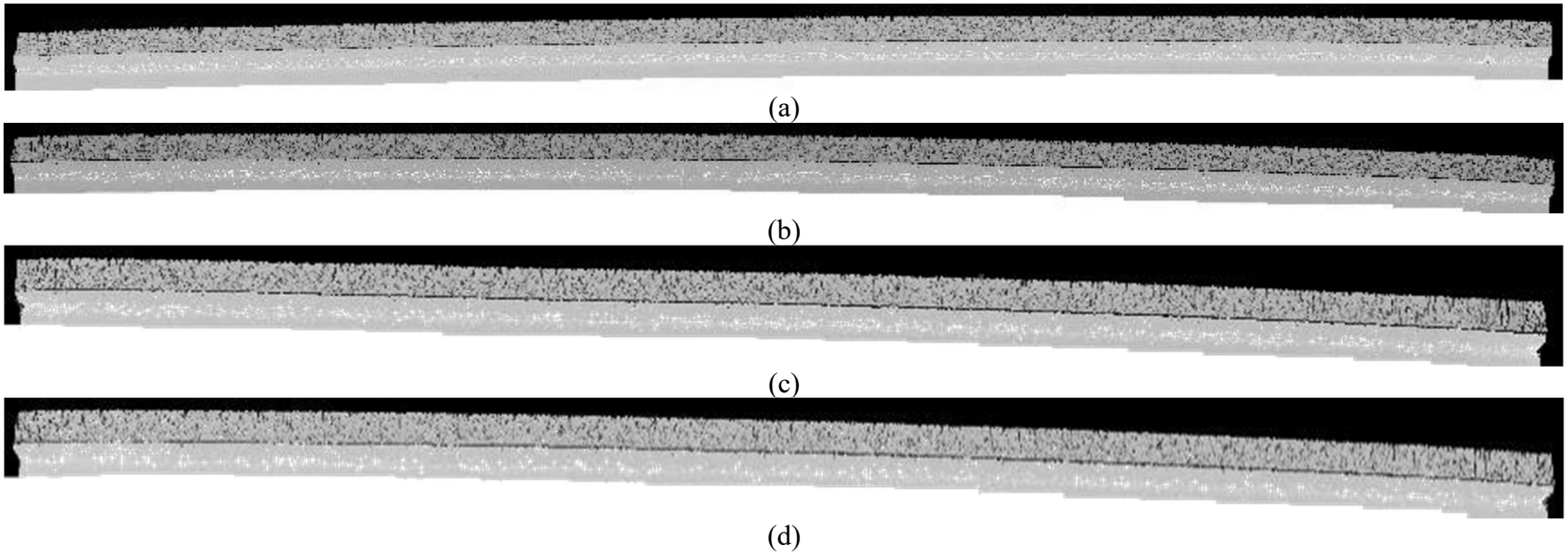

Figure 100 – Backscatter micrographs of flat coupons extracted from aerofoil sections (all derived from turbine blade number 23) following (a) 20 hours, (b) 40 hours (two 20-hour cycles), (c) 60 hours (three 20-hour cycles) and (d) 80 hours (four 20-hour cycles) at 1200°C. For each micrograph, approximately 25 smaller micrographs were stitched together using the MosaicJ [169] *plugin for Fiji (ImageJ)* [168].

3.2.3 Free-edge lateral displacement quantification

Cross-section microscopy of coupon edges was carried out with focus placed on the behaviour of the free edge in the vicinity of the TGO. As noted previously, Pt-aluminide specimens displayed notable lateral displacements and further examination (Figure 101) suggests a correlation with the inter-columnar separation observed in plan-view. Similar microscopy was carried out on samples without topcoats (Figure 102). In the case of the Pt-aluminide specimen after one twenty-hour exposure, the sample with a topcoat (Figure 101a) shows an edge profile resembling a quarter-circle while the sample without a topcoat (Figure 102a) shows an almost three-quarter-circle profile at the free edge. This is also seen in the Pt-aluminide cylindrical micro-specimen with no topcoat (Figure 97b). Numerical quantification of coupon lateral displacements (Figure 103) shows very clearly that the absence of a topcoat reduces the lateral displacement by a factor of approximately 2.3 (see Figure 105 for a comparison between coupon and cylindrical micro-specimens between different bondcoat types). Pt-aluminide specimens typically show double the lateral displacement of Pt specimens regardless of the presence of a topcoat, owing to the inherent γ/γ' bondcoat creep strength. When a topcoat is present however, the total lateral displacements are significantly higher (10μm without a topcoat and 30μm with a topcoat after forty hours). The difference made by a topcoat in the case the Pt specimen is not as pronounced, although a difference of 10μm is present at forty and sixty hours. It is also noted that samples without topcoats show little change in lateral growth rate following the first 20-hour exposure period. This trend is a result of the oxide formed on the sample side dominating the measured lateral displacement at the over the first exposure period. In other words, measured lateral displacements were small relative to the oxide scale formed on the bondcoat free edge. Fitted power law coefficients of the form $\xi = at^b$

(coefficients given in Table 6) indicate time exponent terms of 0.24 without a topcoat and 0.45 with a topcoat (Pt-aluminide) and 0.16 without a topcoat and 0.64 with a topcoat (Pt). These exponents indicate a slow lateral extension rate without a topcoat. Similar lateral displacement quantification of cylindrical micro-specimens with topcoats (Figure 104) was carried out. Fits suggest a similar trend (time exponents of 0.45 and 0.47 for Pt-aluminide coupon and cylindrical micro-specimens respectively) and between zero and forty hours the lateral extensions are comparable. At eighty hours however, the cylindrical micro-specimens show an increase in lateral displacement of approximately 10μm over the coupon counterpart.

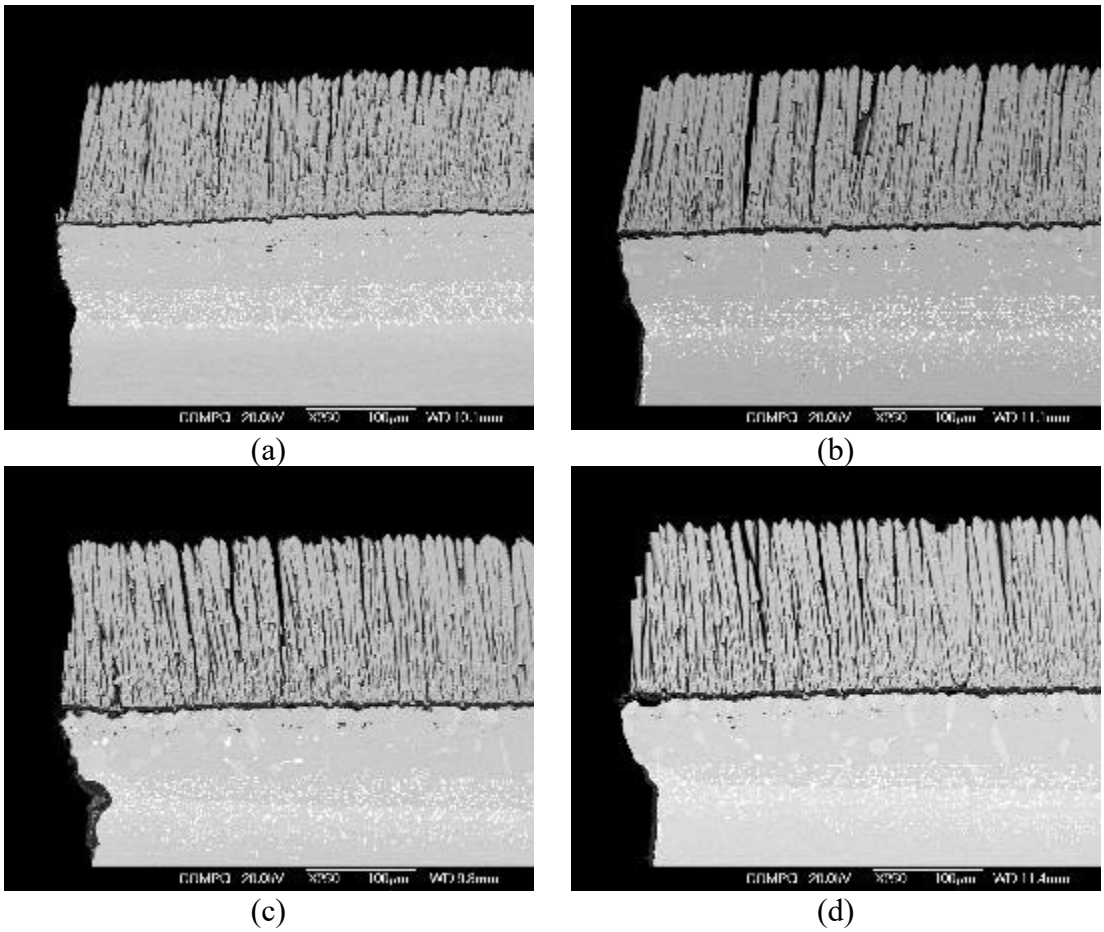

Figure 101 - Cross-section micrographs showing left-hand edge of Rolls-Royce Pt-aluminide bondcoats coupons (a) after 20 hours, (b) after 40 hours (two 20-hour cycles) (c) after 60 hours (three 20-hour cycles) and (d) after 80 hours (four 20-hour cycles).

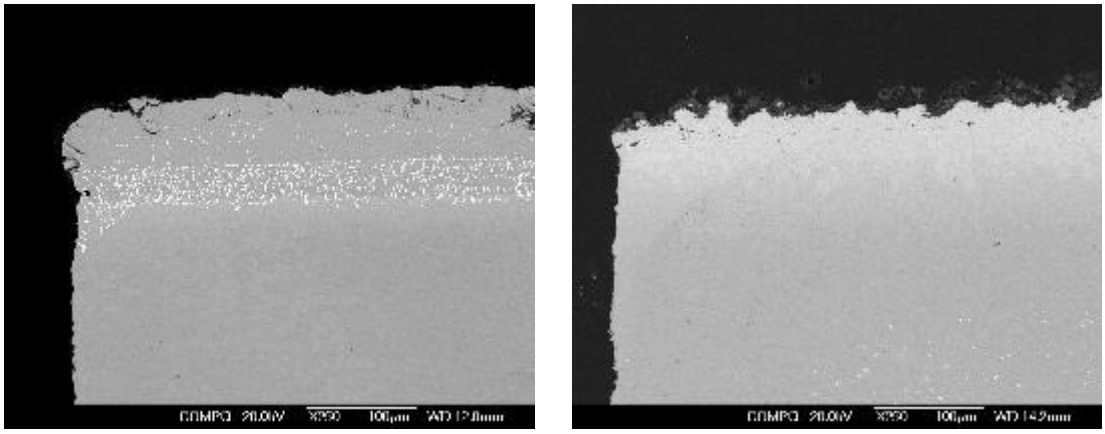

(a) (b)

Figure 102 – Backscatter micrographs showing left-hand edge of Rolls-Royce (a) Pt-aluminide and (b) Pt coupons without topcoats following one 20-hour exposure at 1200°C.

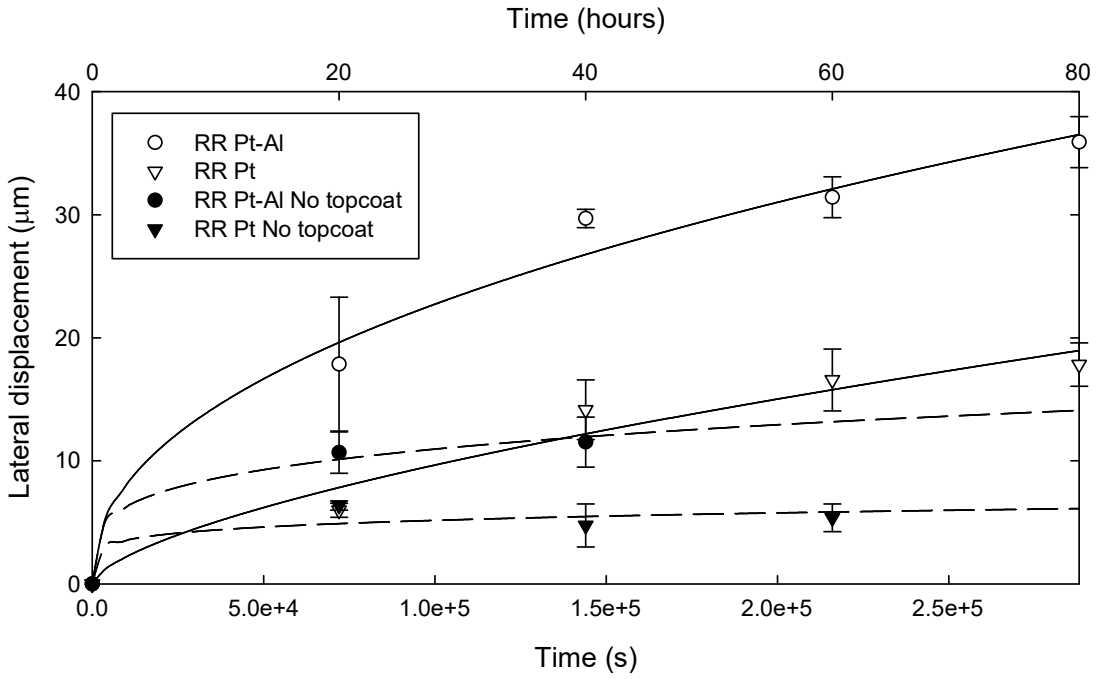

Figure 103 – Lateral extension of TGO/bondcoat interface at free edge of coupon specimens, for both Rolls-Royce Pt and Pt-aluminide with and without a topcoat. Two data points measured for each bondcoat at each time step (left and right edges). Mean values plotted with errors given by the minimum and maximum measurement. Data fitted to a power law of the form $\xi = at^b$ with constants given in Table 6.

Table 6 – Power law constants for fits to lateral extension rates of Rolls-Royce Pt and Pt-aluminide coupons with and without a topcoat. Time exponent term (b) indicates sub-parabolic lateral extension kinetics with lower rates for samples without topcoats.

Constant	Coupon		Cylindrical		Cylindical NT	
	Pt-Al	Pt	Pt-Al	Pt	Pt-Al	Pt
a	5.136	1.932	5.916	2.887	3.812	1.145
b	0.448	0.495	0.473	0.450	0.322	0.413

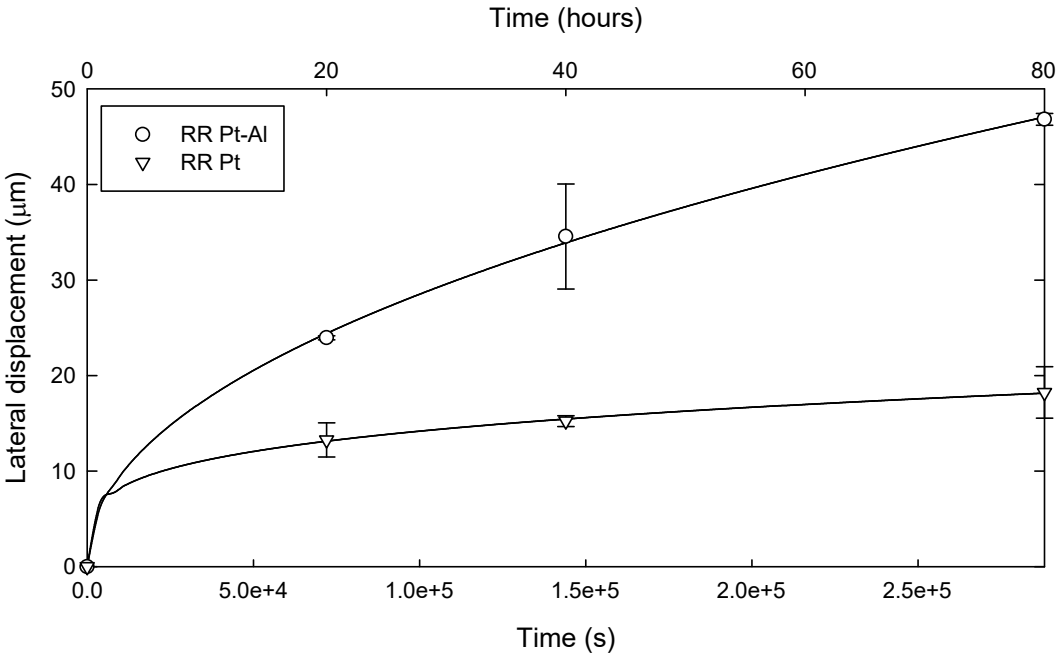

Figure 104 – Lateral extension of TGO/bondcoat interface at free edge of cylindrical micro- specimens, for both Rolls-Royce Pt and Pt-aluminide. Two data points measured for each bondcoat at each time step (left and right edges). Mean values plotted with errors given by the minimum and maximum measurement. Data fitted to a power law of the form $\xi = at^b$ with constants given in Table 6.

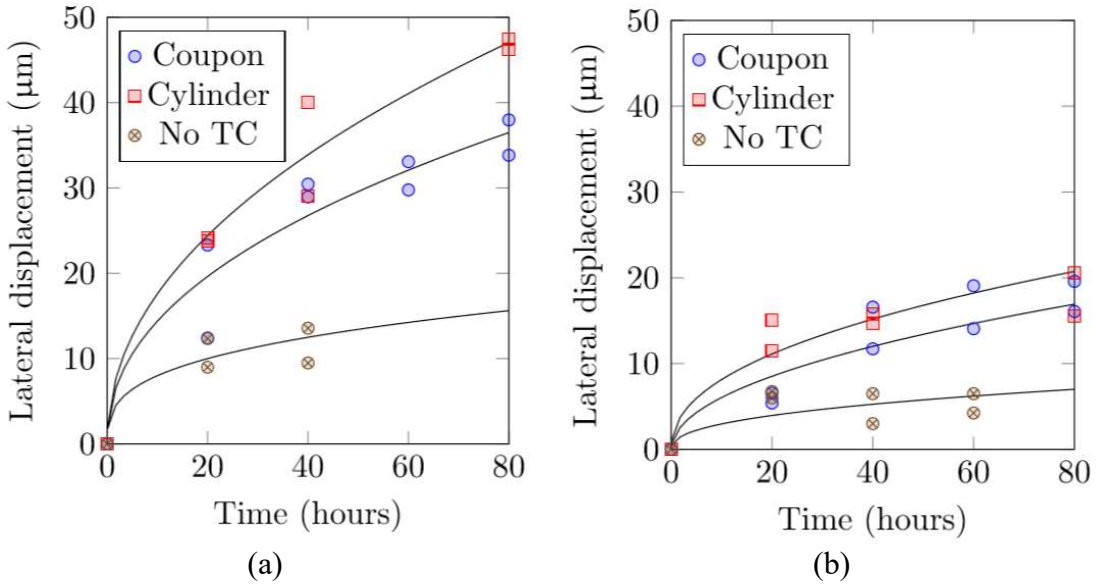

Figure 105 - Lateral extension of TGO/bondcoat interface at free edge of coupon and cylindrical micro-specimens, for both Rolls-Royce (a) Pt-aluminide and (b) Pt, with and without a topcoat (No TC). Two data points measured for each bondcoat at each time step (left and right edges). Data fitted to a power law of the form $\xi = at^b$ with constants given in Table 6.

3.2.4

3.2.4 Bondcoat and TGO/bondcoat interface characterisation

Cross-sections from central portions of cylindrical micro-specimens of both Pt-aluminide (Figure 106) and Pt (Figure 107) show the change in bondcoat morphology to support the growth of the TGO. Detailed oxide thickness measurements are given in section 3.2.6. The Pt-aluminide bondcoat shows the transition from β to γ' and the increase in heavy-element precipitates within the interdiffusion zone (Figure 106). Pt cross-sections (Figure 107) indicate downward platinum diffusion from the upper bondcoat region. The mechanically constrained Pt-aluminide cylindrical micro-specimen (Figure 109) shows fracture along the entire TGO/bondcoat interface. It is also noteworthy that the TGO/bondcoat interface exhibits a differing roughness profile than the equivalent unconstrained profile (Figure 108). The mechanically-constrained specimen shows longer amplitude undulations compared to the higher frequency of shorter undulations in the unconstrained case. In the mechanically constrained specimen, cracks and separation from the bondcoat appear to give a thicker TGO. Apparent oxide thickness is at least partly attributable to cracking. The long-range separation may have initiated from cracks in the topcoat associated with flanks of asperities (see section 1.4.3).

Detail of samples without topcoats indicate that Pt-aluminide (Figure 110) coupons experience extensive fracture within the bondcoat as well as the TGO and that the Pt coupons display thick and non-protective islands of oxide (Figure 111). The composition of Pt-aluminide bondcoats is primarily an intermetallic beta-phase structure, whereas the Pt bondcoat is γ/γ'. Consequently, the beta phase is likely to become more brittle as the temperature drops resulting in extensive fracture compared to the Pt bondcoat.

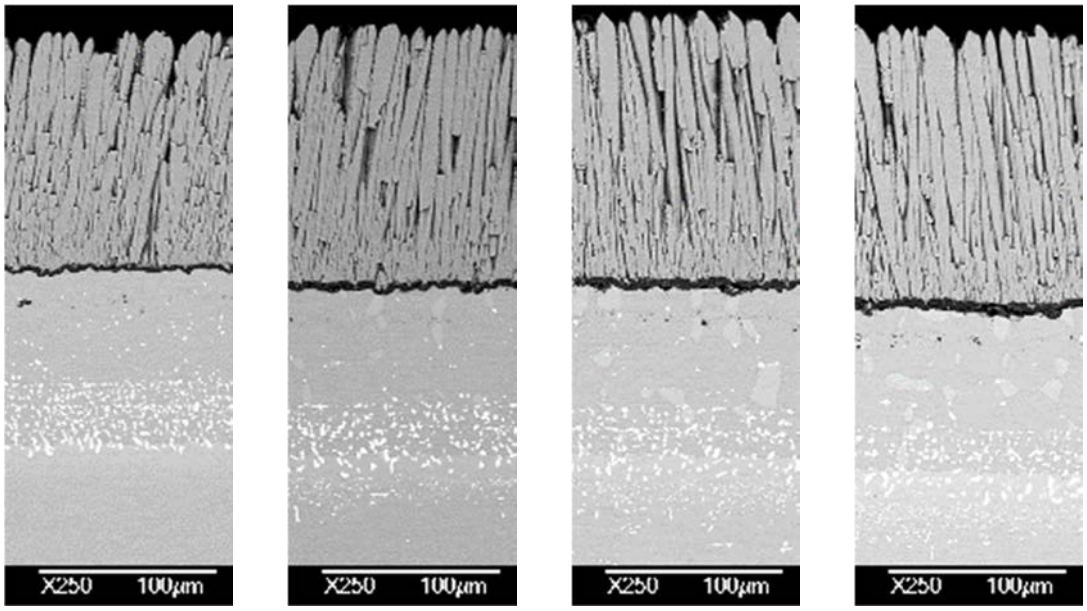

Figure 106 – Sections from Rolls-Royce Pt-aluminide cylindrical micro-specimens (a) as-received, (b) following one 20-hour thermal cycle and (c) following three 20-hour cycles (60 hours) and four 20-hour cycles at 1200°C. Detailed oxide thickness measurements given in section 3.2.6.

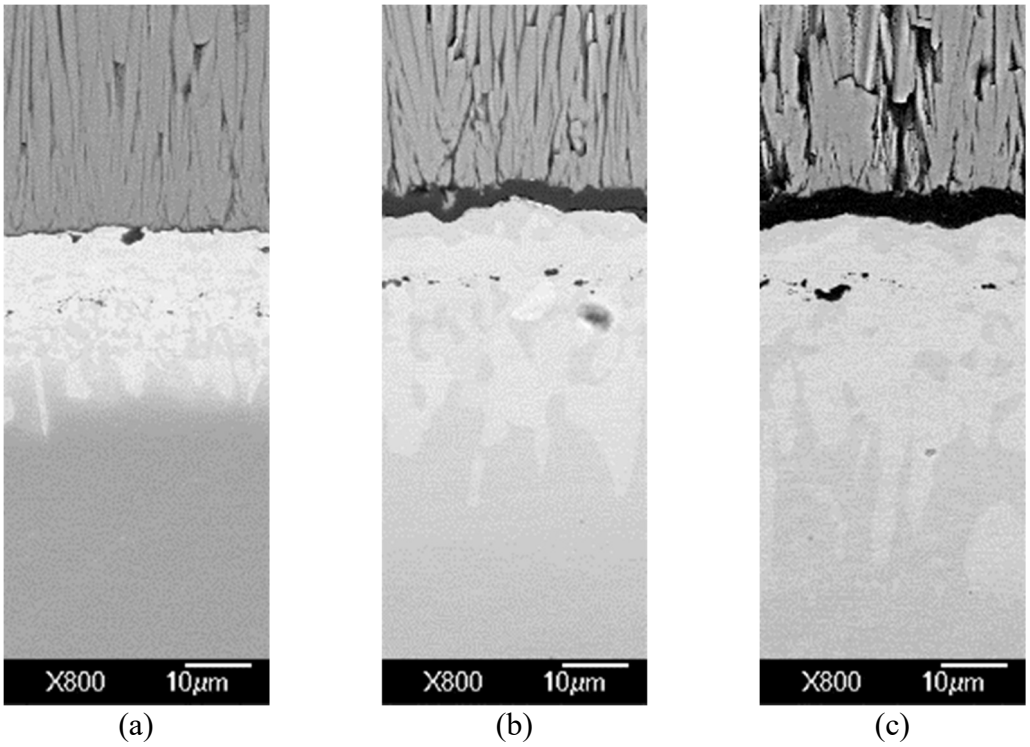

Figure 107 – Sections encompassing TGO from Rolls-Royce Pt cylindrical micro-specimens showing (a) as-received, (b) following one 20-hour thermal cycle and (c) following three 20-hour cycles (60 hours) at 1200°C. Detailed oxide thickness measurements given in section 3.2.6.

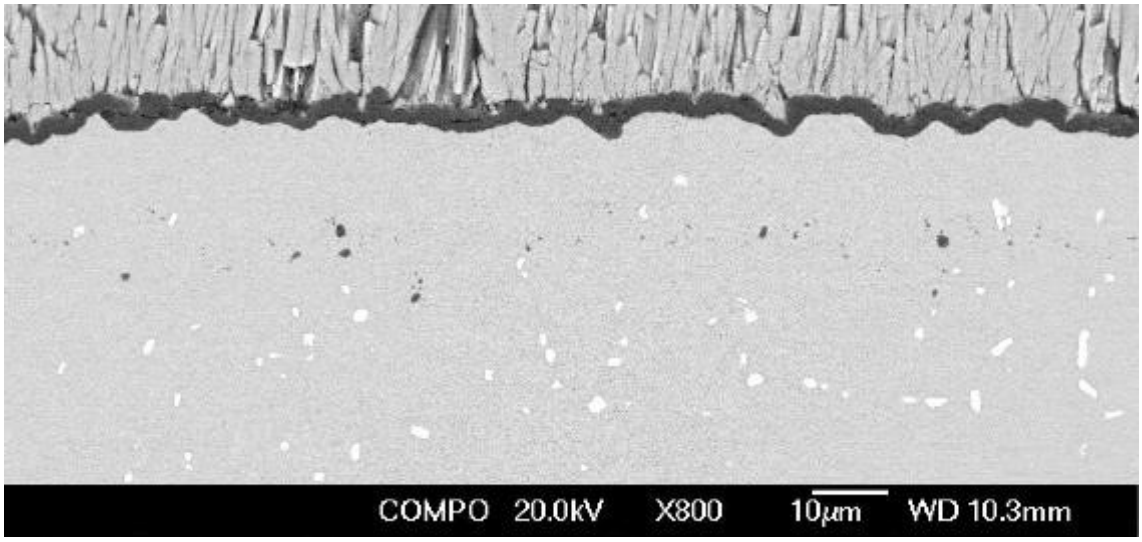

Figure 108 – Cross-section backscatter micrograph of Rolls-Royce Pt-aluminide coupon (central region) following 20 hours at 1200°C.

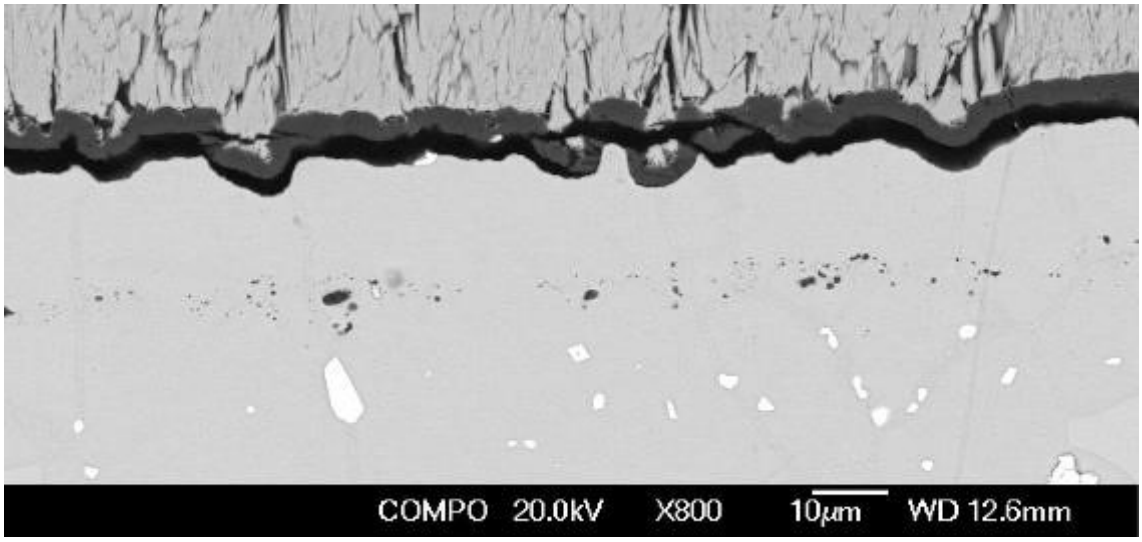

Figure 109 – Cross-section backscatter micrograph of Rolls-Royce Pt-aluminide cylindrical micro-specimen (central region) with a mechanical cylindrical edge constraint following 20 hours at 1200°C, in which total delamination at the TGO/bondcoat interface is observed.

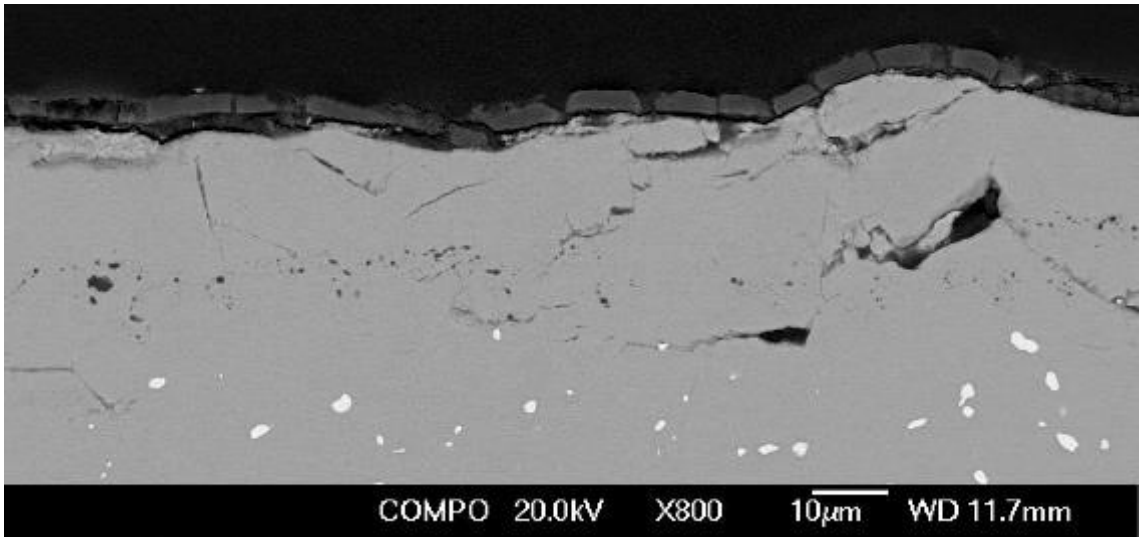

Figure 110 – Cross-section backscatter micrograph of Rolls-Royce Pt-aluminide coupon lacking a topcoat following 20 hours at 1200°C. Widespread damage to bondcoat microstructure is observed and a non-continuous TGO with multiple and periodic cracks.

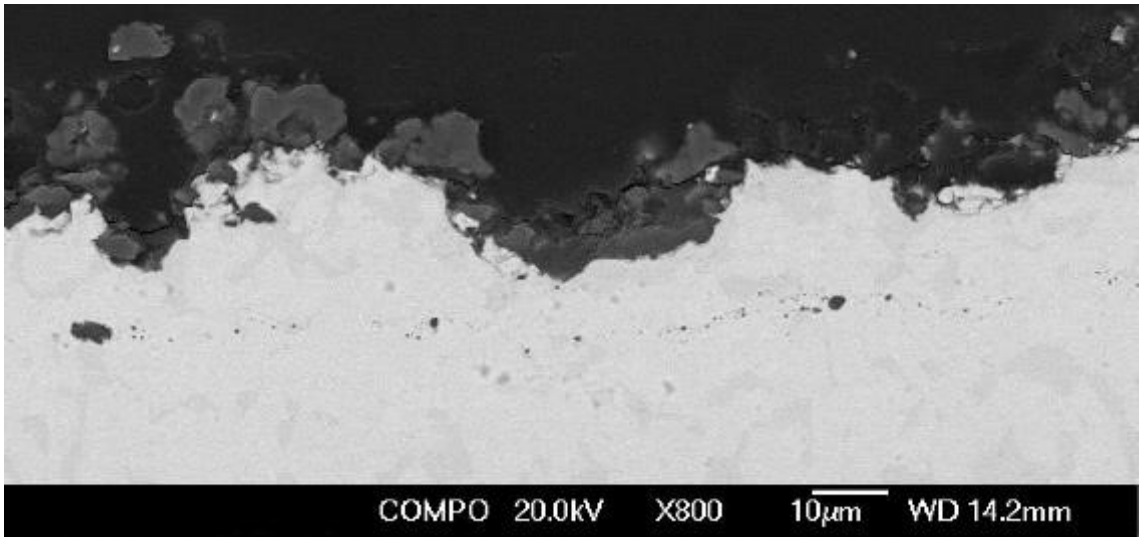

Figure 111 – Cross-section backscatter micrograph of Rolls-Royce Pt coupon lacking a topcoat following 20 hours at 1200°C, in which a non-continuous TGO is observed.

3.2.5 TGO morphology

The nature of the oxide morphology for Pt-aluminide coupons (Figure 112) indicates progressive thickening of the layer accompanied by a proliferation of micro-cracks. Such cracking is a combination of interfacial fracture (Figure 113) at either the TGO/bondcoat interface or the TGO/topcoat interface or through the TGO (Figure 114).

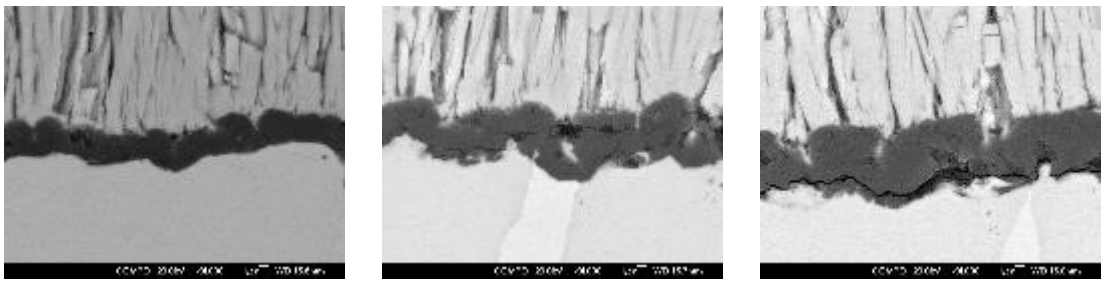

(a) (b) (c)

Figure 112 - Cross-section backscatter micrographs showing TGO thickening in central region of Rolls-Royce Pt-aluminide bondcoats (a) after 20 hours, (b) after 40 hours (2 cycles) and after 80 hours (4 cycles) at 1200°C.

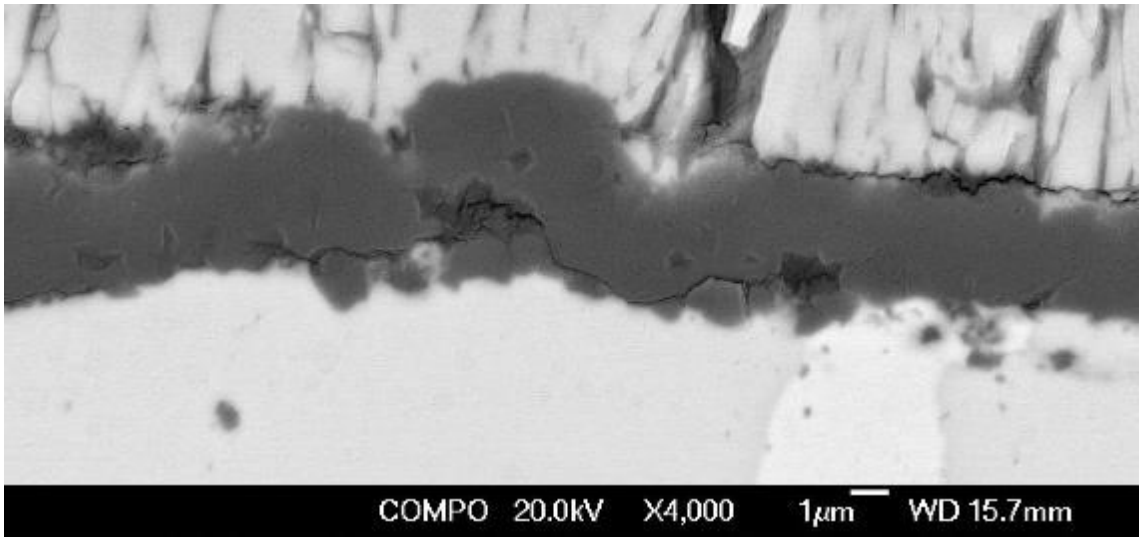

Figure 113 – Cross-section backscatter micrograph showing cracks at both the TGO/topcoat interface and at the TGO/bondcoat interface at central region of Rolls-Royce Pt-aluminide bondcoat coupon following 40 hours (two 20-hour cycles) at 1200°C.

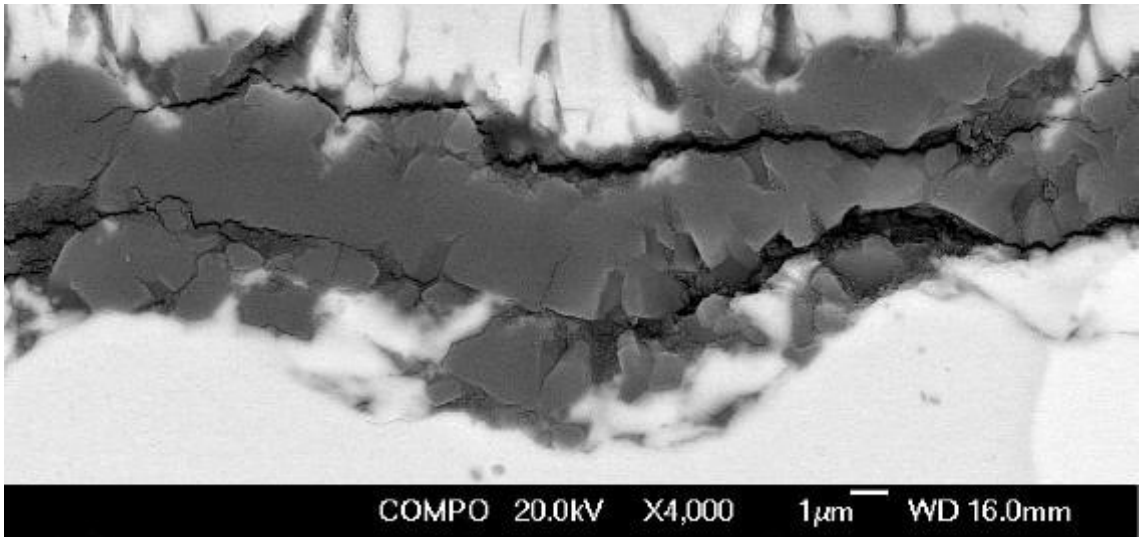

Figure 114 – Cross-section backscatter micrograph showing cracks through the TGO of Rolls-Royce Pt-aluminide bondcoat coupon following 80 hours (four 20-hour cycles) at 1200°C.

3.2.6 TGO thickness measurements

Twenty-five oxide thickness measurements were taken at each of the left, right and central positions for each coupon and cylindrical micro-specimen. For each set of measurements (spanning 150μm, equally spaced), the median, upper and lower quartiles were calculated. The median values were used to compute the power law fit of the form:

$$\xi = at^b + c \qquad \textit{Eq. 25}$$

in which the oxide thickness ξ, relates to the time at temperature t by the constants a, b and c (oxide thickness at time $t = 0$). This two-term general parabolic rate law [178] was found to best fit the data and represent the initial state of the as-received oxide over interpolant, rational, sum of sine and Gaussian fits. The fits were calculated separately for the Rolls-Royce Pt-aluminide (Figure 116) and Rolls-Royce Pt bondcoats (Figure 117). Oxide thicknesses in general show a sub-parabolic growth rate with a time exponent ranging from 0.22 to 0.46 (Table 8). TGO thicknesses at the sample edges (left and right) appear to show no particular difference between TGO thicknesses at the centre in the Pt-aluminide case.

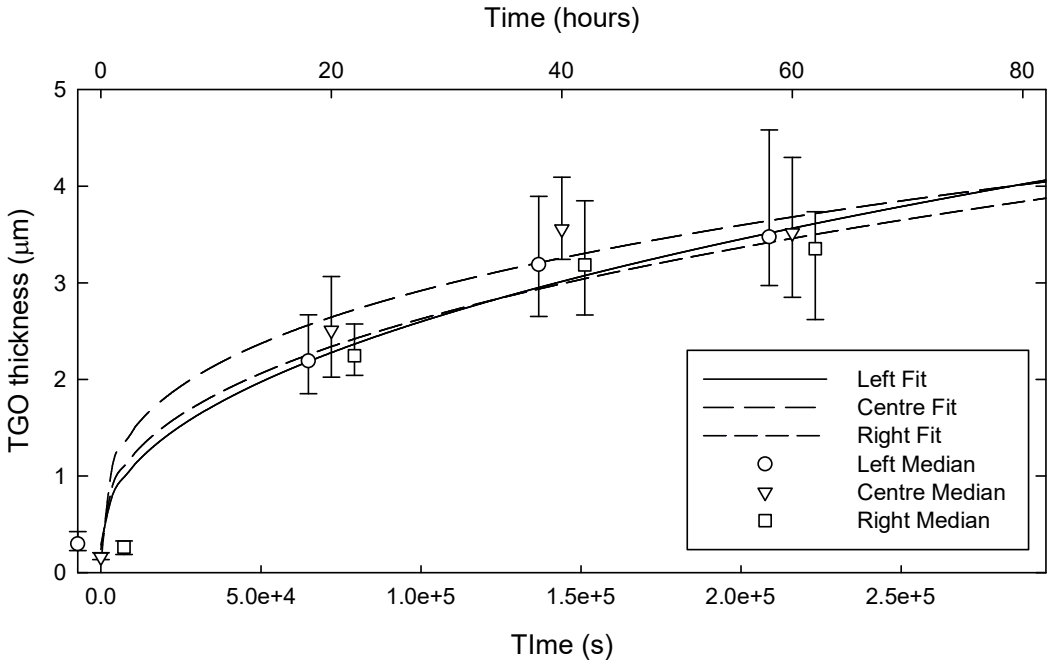

Figure 115 – TGO thickness measurements for Rolls-Royce Pt-aluminide coupon specimens at 1200°C. Twenty-five thickness measurement were taken at each time step over a length of 120μm. Error bounds indicate 25th and 75th percentiles. For clarity of illustration, left and right TGO thicknesses have been offset in the respective directions. Fitted curves are of the form $\xi = at^b + c$ with constants given in Table 7.

Table 7 – Power law constants for fits to TGO growth rates of Rolls-Royce Pt-aluminide coupons with time exponents indicating sub-parabolic growth rates.

Constant	Left	Centre	Right
a	0.01254	0.07918	0.02726
b (time exp.)	0.45320	0.31040	0.38850
c	0.28470	0.09773	0.24020

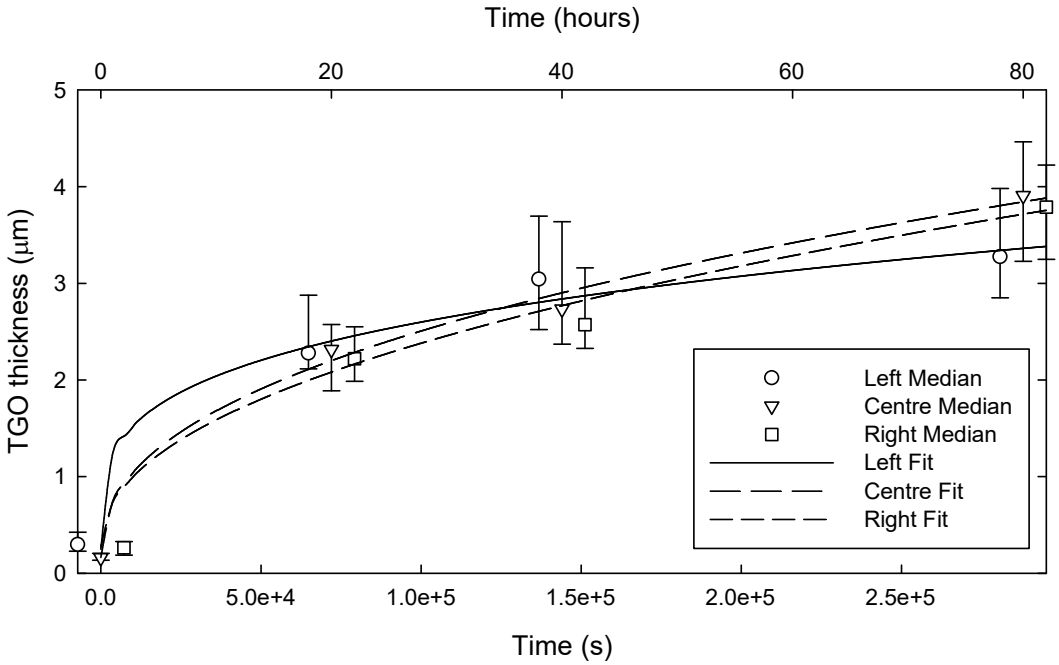

Figure 116 – TGO thickness measurements of Rolls-Royce Pt-Al cylindrical micro-specimens as a function of time at 1200°C. Twenty-five thickness measurement were taken at each time step over a length of 120μm. Error bounds indicate 25th and 75th percentiles. For clarity of illustration, left and right TGO thicknesses have been offset in the respective directions.

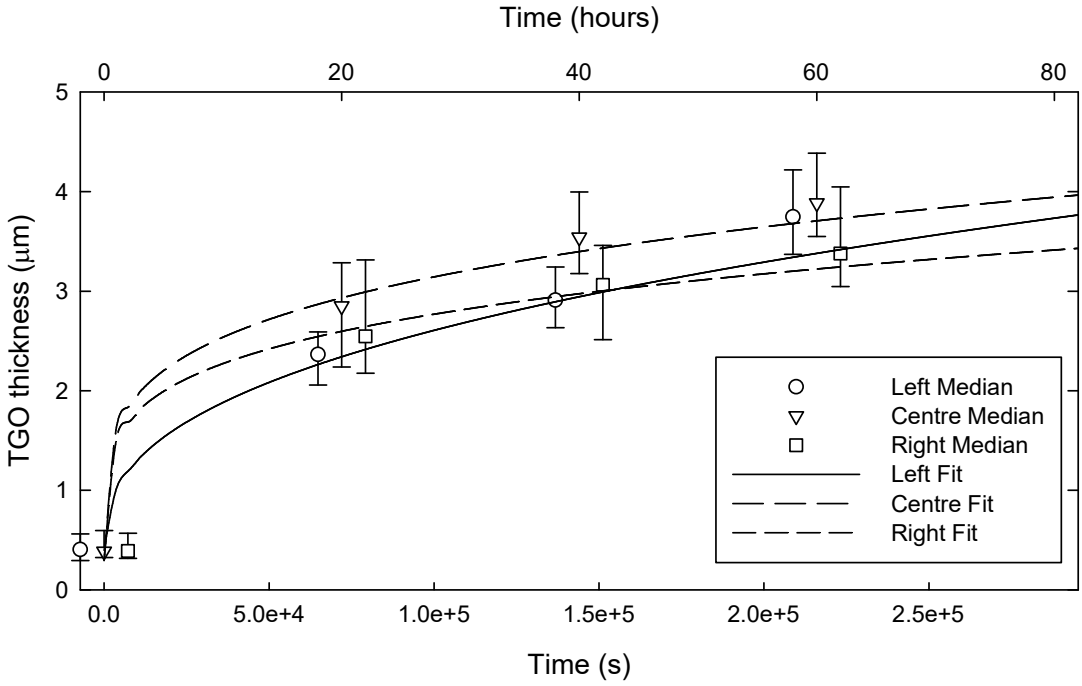

Figure 117 – TGO thickness measurements of Rolls-Royce Pt cylindrical micro-specimens as a function of time at 1200°C. Twenty-five thickness measurement were taken at each time step over a length of 120μm. Error bounds indicate 25th and 75th percentiles. For clarity of illustration, left and right TGO thicknesses have been offset in the respective directions.

Table 8 – Power law constants for fits to TGO growth rates at 1200°C of cylindrical micro-specimens with Rolls-Royce Pt and Pt-aluminide bondcoats.

Constant	Pt			Pt-Al		
	Left	Centre	Right	Left	Centre	Right
a	0.6056	1.3100	1.1980	0.9727	0.5689	0.4528
b (time exp.)	0.3894	0.2338	0.2185	0.2655	0.4261	0.4631
c	0.3974	0.2951	0.2930	0.2484	0.1633	0.2712

For each set of measurements (spanning 150 µm each, equally spaced), a probability density function was fitted and normality checks carried out. Specifically, Inverse Gaussian (Wald), Normal and Weibull distributions were fitted to Rolls-Royce Pt-Al (Figure 118) and Pt-aluminide (Figure 119) cylindrical micro-specimens.

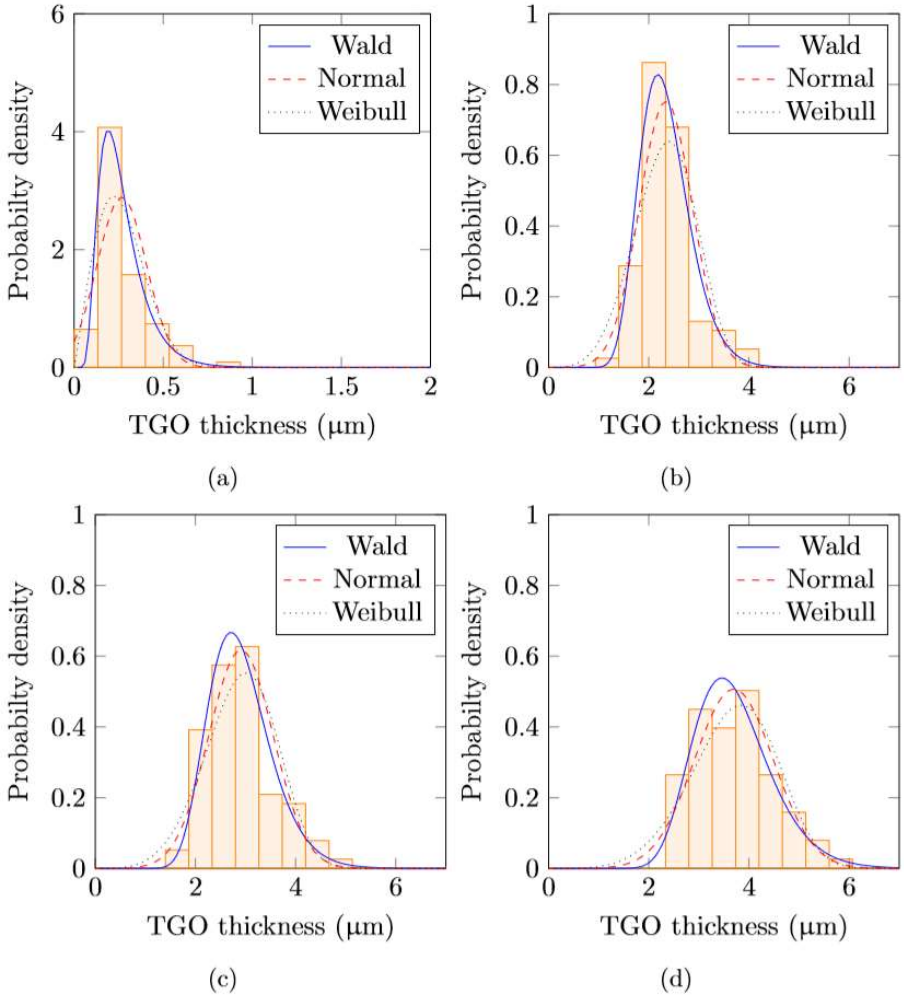

Figure 118 - Probability density functions (Wald or inverse Gaussian, Normal and Weibull) fitted TGO measurements of Rolls-Royce Pt-aluminide cylindrical micro-specimens (a) as-machined, (b) after 20 hours, (c) after 40 hours and (d) after 80 hours at 1200 °C.

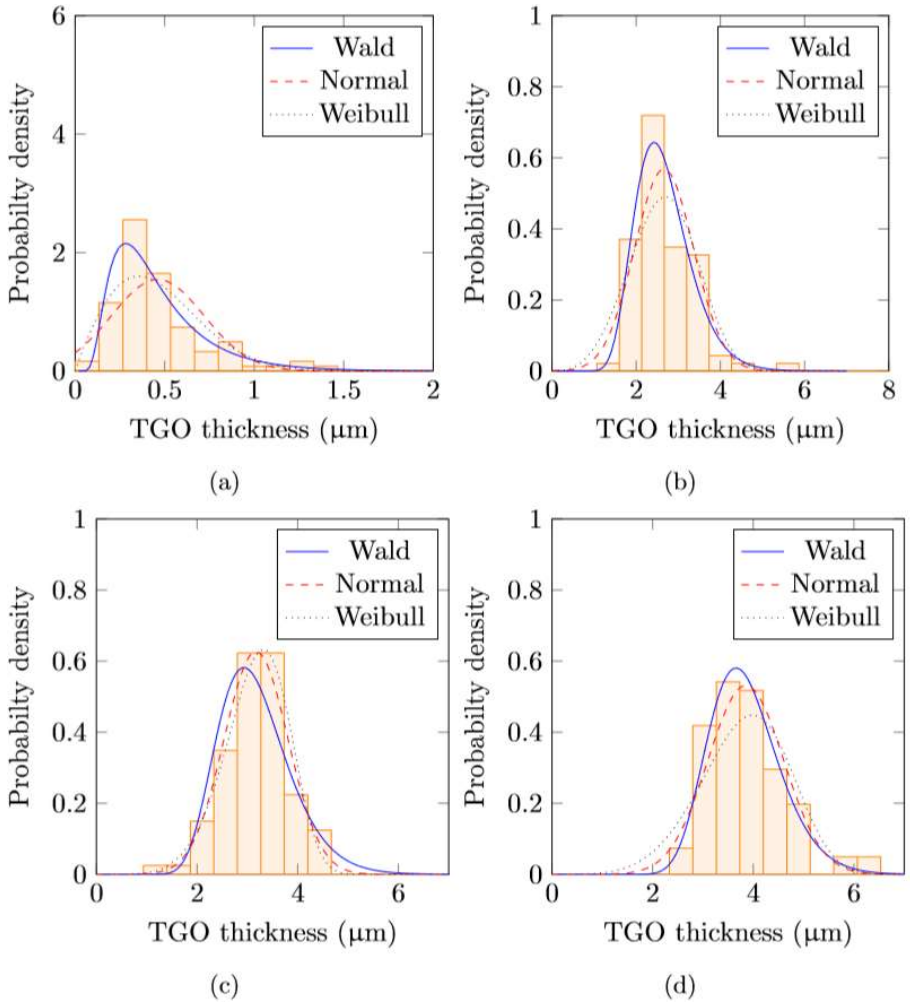

Figure 119 - Probability density functions (Wald or inverse Gaussian, Normal and Weibull) fitted TGO measurements of Rolls-Royce Pt cylindrical micro-specimens (a) as-machined, (b) after 20 hours, (c) after 40 hours and (d) after 80 hours at 1200 °C.

3.2.7 Bondcoat profile analysis

The TGO/bondcoat interface morphology of Pt-aluminide coupons (with topcoats) was investigated using Fiji (ImageJ) for interface extraction and Matlab for profile analysis. This analysis was carried out firstly by isolating the TGO/bondcoat interface profile relative to means and then relating the profile to grit line means. The nature of the profiles and relation to the grit line of the as-received state (Figure 120) indicate an increase in large amplitude undulations with time and a decrease in high frequency features. The distance between the grit line mean and interface mean was seen to decrease from 12.32μm in the as-received state to 11.53μm at 20 hours, 11.42μm at 40 hours and

11.74μm at 80 hours. This decrease suggests a distinct average downward displacement of the TGO/bondcoat interface between 0 and 20 hours that remains constant with further time at temperature.

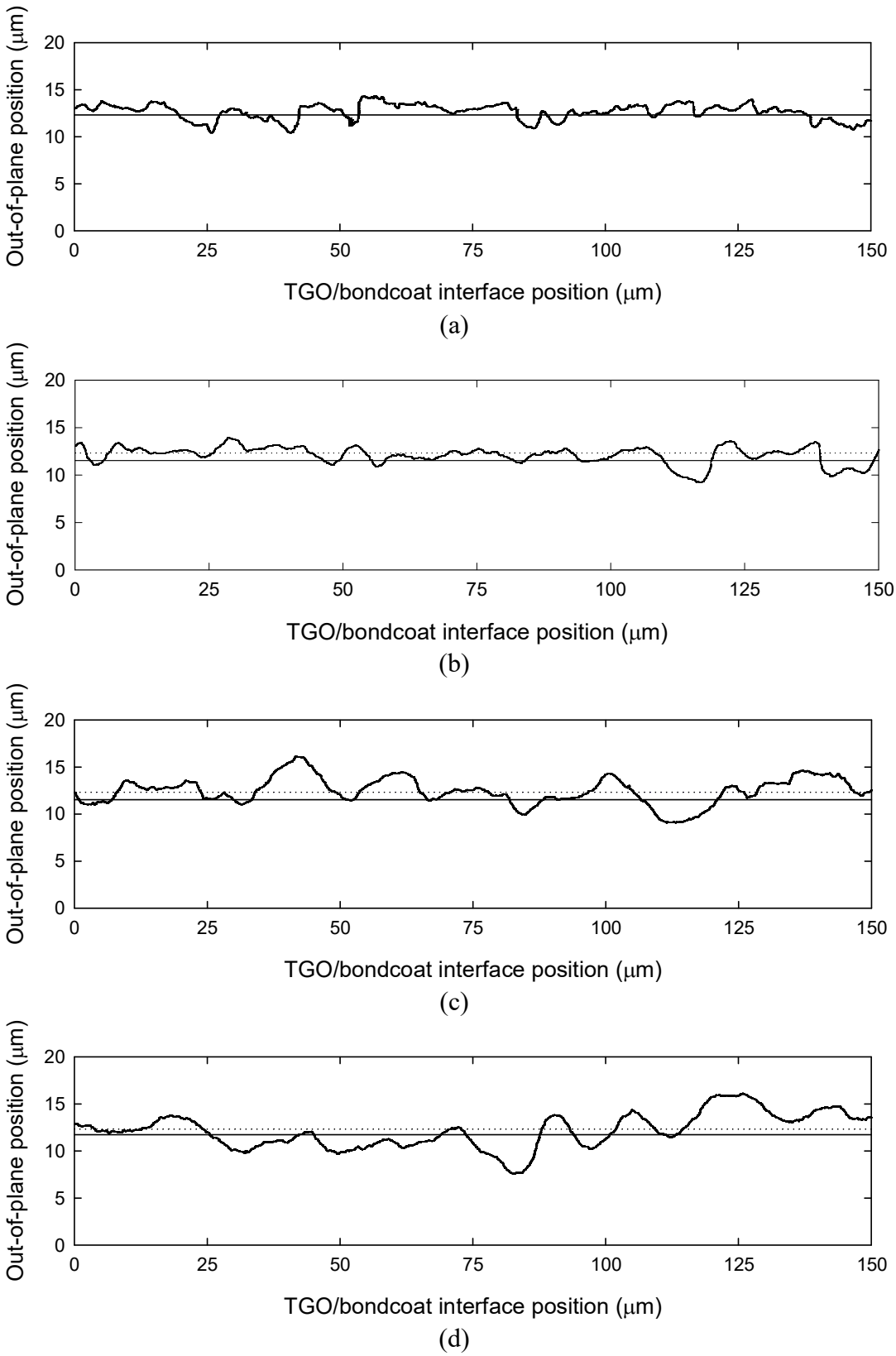

Figure 120 – Bondcoat/TGO interface profile evolution as a function of time (plotted relative to grit line) for Rolls-Royce Pt-Al bondcoats at 1200°C. Dotted lines indicate position of mean bondcoat/TGO interface of the as-received state (a). Subsequent timesteps show profiles at (b) 20 hours, (c) 40 hours and (d) 60 hours.

3.3 Discussion

The time to spallation of aerofoil sections in this work showed considerable scatter at 1175°C. No significant difference within scatter was noted between the time to spallation of Pt-aluminide and Pt-only TBC systems. The time to spallation conformed to an Arrhenius-type rate law (Figure 84b). A comparison of the current work with literature (Figure 121) reveals that this behaviour is in accordance with the work of Wang et al. [96] that examined similar Pt-aluminide aerofoil sections from Rolls-Royce supplied turbine blades. Of the two specimens examined in their work at 1150°C under 20 hour cycles, one aerofoil section was shown to exceed 20% surface spallation after 300 hours (15 cycles) while a second identical aerofoil section failed after 520 hours (26 cycles). The authors also note spallation distribution around all curved portions of the aerofoil of the 300-hour sample and around most of the sample in the 520-hour sample. These observations are consistent with the work herein, in which the single Pt-aluminide blade tested at 1150°C failed at 480 hours (23 cycles). Other Rolls-Royce test data [179,180] on aerofoil sections similar to this work with Pt bondcoats and under the same thermal cycling revealed an equally large scatter in time to spallation. At 1150°C, a time to spallation of greater than 20% was seen ranging from 40 hours to a run-out result of 560 hours. The one-hour cycles at 1135°C of Wu et al. [181] on model samples having both Pt and Pt-aluminide bondcoats on CMSX-4 substrates also showed a wide range of time to spallation. Although the reasons for this large scatter in time to spall are not immediately apparent, the lack of control of bondcoat surface roughness is certainly a contributor (see models by Busso and Evans in section 1.4.3). The work of Chirivì and Nicholls [182] showed the strong effect of substrate surface finish on γ/γ' bondcoat

systems. Yanar et al. [67] showed the strong influence on time to spallation of grit-blasting and hand-polishing of Pt-aluminide bondcoat systems.

The aerofoil sections of the work herein consisted of different aerofoil geometries in that the Pt blades were slightly larger than Pt-aluminide counterparts in all dimensions (Figure 61 for a side-by-side comparison). Specifically, the leading edge of Pt-aluminide aerofoil sections exhibited a sharper radius than Pt counterparts. Aerofoil curvature has been shown to alter the stress state locally within the TGO [96,183]. To isolate the influence of variations in geometry between bondcoat types and local curvature, coupons, flat in visual appearance, and cylindrical micro-specimens were extracted from trailing edge suction surfaces. It was seen that the coupons exhibited some long-range curvature depending on the location along the turbine blade span from which the aerofoil section was derived. Although low magnification micrographs of Pt-aluminide coupons were taken at progressive twenty-hour timesteps, it is implausible for TGO growth to have caused the deflection at, for example 80 hours (Figure 100d) of millimetres thick superalloy substrate. Nonetheless, cylindrical micro-specimens were extracted to completely isolate any curvature effects. Cyclic oxidation of the micro-specimens and comparison with equivalent coupons revealed very similar behaviour both in terms of lateral displacement at free edges and TGO thickening. Between Pt-aluminide and Pt-only TBC systems, very little difference in TGO growth was noted (within scatter, Figure 116 and Figure 117). Transient θ-alumina is known to grow at a faster rate than stable, steady state α-alumina [184]. The TGO formed in both the Pt-aluminide and Pt-only TBC systems during the steady-state growth regions is expected to be α-alumina.

The behaviour of coupons and cylindrical micro-specimens under thermal cycling, both with and without a topcoat proved enlightening as to the stress relief mechanisms under

growth stresses. It was shown for example that a strong bondcoat (Pt) that retains the cuboidal γ/γ' microstructure and limits the displacement in all directions, displays a markedly rougher surface than the Pt-aluminide equivalent (Figure 102 and Figure 110 vs. Figure 111). By contrast, the weaker Pt-aluminide allows upward bowing of the bondcoat in addition to lateral displacement to relieve the TGO growth stress. Atkinson et al. [185] proposed a similar mechanism on Pt-aluminide bondcoats in which a roughening mechanism acts to relieve the growth stress on samples without topcoats.

With the application of an APS mechanical constraint following twenty hours at 1200°C, delamination of the entire TGO/topcoat occurs at the TGO/bondcoat interface (Figure 109). This is in contrast to samples without such a constraint (Figure 108), in which the TGO/bondcoat interface profile is also markedly different. The application of a mechanical constraint clearly supports the mechanism of bondcoat roughening as a means of relieving stress as the TGO/bondcoat interface is noticeably rougher in the mechanically constrained case. The TGO is thicker in the mechanically constrained case despite being exposed to the same temperature for the same duration of time. The role of the topcoat in constraining lateral displacements appears not as significant as the ability of the topcoat to constraint vertical displacements. The appearance of inter-columnar separations as a network of cracks from plan-view micrographs and also noticeable separation in cross-section supports the argument that the TGO is relatively free to extend outwards in Pt-aluminide bondcoats.

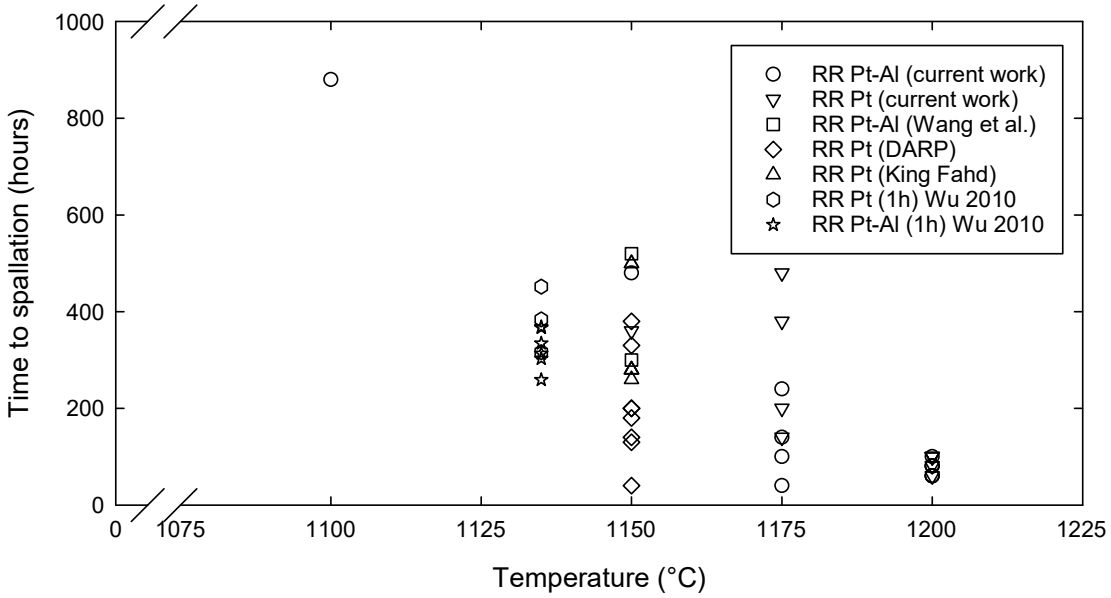

Figure 121 – A comparison of the times to >20% spallation of aerofoil sections derived from Pt and Pt-aluminide HP1 turbine blades with in-house and literature [96,179,180,186] *data. Note that Wu 2010 data is 1 hour cycles on idealised Rolls-Royce discs compared to 20 hour cycles on aerofoil sections in other data sets.*

3.4 Conclusions

Time to spallation of aerofoil sections extracted from turbine blades showed large scatter consistent with literature observations. TGO thickening occurred under the expected rate laws in both Rolls-Royce Pt-aluminide and Pt-only bondcoats, with no significant difference between the two TBC systems. Comparable TGO thicknesses were measured at sample edges and central regions in both cylindrical micro-specimens and flat coupons. Significant lateral displacements at the TGO/bondcoat interface were observed in Pt-aluminide cylindrical micro-specimens and flat coupons. Under the same conditions, Pt-only bondcoats displayed comparatively small lateral displacements owing to the retained γ/γ' superalloy microstructure. Bondcoat phase transformation (β to γ) was noted in Pt-aluminide TBC systems and diffusion of platinum in Pt-only TBC systems.

Cylindrical micro-specimens of both Pt-aluminide and Pt-only bondcoats without topcoats were examined. Pt-aluminide bondcoats without a topcoat displayed wide-

spread cracking in cross-section attributable to the brittle intermetallic nature of the β bondcoat. Pt-only bondcoat exhibited no such cracking however, a non-continuous oxide layer was noted as growing.

Cracking was observed in the presence of mechanical constraints applied in the form of an air plasma sprayed coating on the sides of cylindrical micro-specimens. Pt-only bondcoats displayed cracking through the bondcoat grit-line (the original substrate free surface before bondcoat manufacture), while Pt-aluminide bondcoats exhibited long-range cracking at the TGO bondcoat interface.

Chapter 4 A force balance approach to bondcoat relaxation under TGO growth

4.1 Introduction

Determination of the stress state at temperature within the TGO is of great interest for TBC life prediction. To date, reported TGO stress measurements have mostly been through the use of photo-luminescence piezo-spectroscopy (PLPS) or X-ray diffraction. PLPS, although non-destructively allowing stress inference within the TGO of a TBC system (with a topcoat), is limited to in-situ temperatures of 600°C due to thermal alteration of the observed spectra [90]. This temperature limitation compared to operating temperatures of interest (1000°C to 1250°C) has restricted most literature PLPS experiments [45,89,92,94,96–99,102–104,107,109,187] to carrying out stress measurements at room temperature. Although room temperature stress data is of practical significance, growth stresses at temperature are equally important for modelling and a wider understanding of TGO/bondcoat interaction at temperature. Data acquired at room temperature are subject to large cooling strains that must be accounted for, through an expression for elastic stress generated due to a mismatch in thermal expansion [188,189]:

$$\sigma_{th} = \frac{E_{ox} \cdot \left(\alpha_{ox} - \alpha_{alloy}\right) \cdot \Delta T}{\left(1 - \nu_{ox}\right) + \frac{\xi_{ox}}{\xi_{alloy}} \cdot \frac{E_{ox}}{E_{alloy}} \cdot \left(1 - \nu_{alloy}\right)} \qquad \textit{Eq. 26}$$

where the subscripts o and m represent oxide and underlying metal alloy respectively and the elastic modulus E (Pa) and thermal expansion coefficient α (K^{-1}) are a function of temperature. In cases where the bondcoat is free-standing, that is, a substrate is not present, terms with alloy subscripts may be replaced with terms for the bondcoat.

Estimation and subtraction of thermal expansion mismatch stresses however, introduces further errors compounded to those associated with beam scattering within the topcoat [109]. In an effort to improve spatial resolution, some studies [101,102] have acquired TGO stresses without the presence of a topcoat. Although lack of a topcoat inherently improves measurement accuracy, the influence of the topcoat on TGO stress states is neglected. Other contributions have examined polished cross-sections of thermally exposed specimens, as in the work of Nair et al. [100]. Although this method eliminates the errors introduced by beam scattering, scanning was still carried out at room temperature.

X-ray diffraction offers an alternative to PLPS that may be used at temperatures of 1200°C, significantly above the limitations of PLPS. The high energy and highly-tuned nature of a synchrotron-source X-ray is preferred [190] owing to the high X-ray attenuation of the topcoat [191]. The key drawback of synchrotron XRD on samples with a topcoat in place [192–194] is that the beam is unable to isolate the TGO as the beam width is typically tens of micrometres. Furthermore, diffraction data is collected for the entire through-thickness beam penetration, not for an isolated plane. Through-thickness XRD examination of TBC systems with topcoats have been carried out by Diaz et al. with tensile loading [194], Knipe et al. with thermal gradients [193] and thermo-mechanical loading [192]. In other work on model alloys without a topcoat by Hou and co-workers [41], Heuer et al. [195], Veal et al. [196] and Sarioglu et al. [71] the stress state within the TGO was examined. The work of Heuer et al. [195] showed the strong dependence of the XRD derived strain on the crystal orientation of NiAl.

Here, a new force-balance approach to directly inferring the stress within the TGO from micrographs is presented. The method relies on examining the free-edge of a cylindrical

TBC micro-specimen in cross section and relating the creep deformation of the bondcoat in accommodating the TGO growth stress.

4.2 The force balance approach

The force balance method (Figure 122) relates the total stress required to produce lateral strain of the bondcoat at a free edge, to the relieved stress within the TGO. By considering the lateral strain as a function of vertical position from the TGO/bondcoat interface with time, it is proposed that bondcoat creep rates may be inferred. The computed bondcoat creep rates may then be used with an empirical creep algorithm for a similar TBC system to calculate the bondcoat stress acting over the bondcoat thickness. The resultant total force from this integrated bondcoat stress may then be related to the total force acting on the bondcoat by the TGO. The equated TGO force may, in conjunction with measured TGO thicknesses, subsequently be used to calculate the TGO stress such that

$$\xi\sigma_{ox} + \int_0^y \sigma_y dy = 0 \qquad \textit{Eq. 27}$$

where ξ represents TGO thickness, σ_{ox} is the stress acted upon the bondcoat by the TGO and $\int_0^y \sigma_y dy$ is the integrated bondcoat stress over the vertical bondcoat profile.

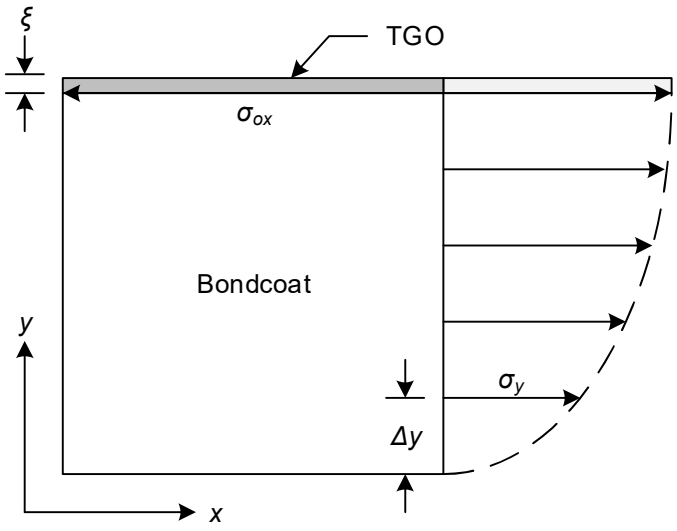

Figure 122 – Schematic diagram of the force balance approach used to equate the estimated total stress acting over the bondcoat and relating this to the stress within the TGO layer.

4.2.1 Displacement profiles from cross-sections

The samples used were Rolls-Royce Pt-aluminide cylindrical micro-specimens, machined to 1000μm diameter using the two-axis slow-speed saw method developed for this work and thermally cycled under 20-hour periods at 1200°C. The cylindrical micro-specimens were exposed for up to 80 hours (4 cycles) with samples removed at 20 hours and 40 hours in addition to the analysis of an as-received sample. The exterior of each thermally cycled specimen was examined in the same position (Figure 123 shows 20-hour sample, Figure 124 the 40-hour sample and Figure 125 the 80-hour sample). Each of these samples (in addition to the as-received sample) was ground and polished in cross-section at the diameter using the sample preparation approach described previously. To ensure that the plane of examination coincided with the sample diameter, external measurements of the diameter were taken from plan-view micrographs. Subsequent grinding and polishing was carried out in an incremental manner with diametric measurements taken at each iteration using a light microscope. Care was exercised to reach and not exceed the diameter during the final polishing stages. Micrographs were

recorded at the free edges of all four samples (Figure 126). A vertical line indicating the reference substrate position was plotted, in addition to the mean position horizontal of the TGO/bondcoat interface. These two reference lines provided a transformed coordinate system from which the bondcoat lateral displacement profile for each time step was derived. In the case of the as-received cross-section (Figure 126a) the initial lateral position is negative with respect to the transformed coordinate system owing to an initial inward curvature at the TGO/bondcoat interface. This inward curvature was present in the as-received condition of all specimens (Figure 123a, Figure 124a and Figure 125a). Lateral displacement profiles were extracted using a combination of Fiji (ImageJ) and a custom MATLAB script (Appendix D) to processed binarised micrographs. A two-term exponential fit of the form

$$\Delta l = a_1 e^{b_1 t} + c_1 e^{d_1 t} \qquad \textit{Eq. 28}$$

was found to accurately represent the evolution of lateral displacement (Δl), as an exponential function e, of time t, related by the constants a_1, b_1, c_1 and d_1 (Figure 127, constants given in Table 9). The profiles at 20, 40 and 80 hours were corrected for initial curvature by summing the total lateral displacement relative to the as-received (Figure 128).

Table 9 – Two-term exponential function constants for lateral displacement and strains as a function of vertical position with time.

Constant	0 hours	20 hours	40 hours	80 hours
$\boldsymbol{a_1}$	-1.78×10^{7}	-0.97	-134.40	-2.24
$\boldsymbol{b_1}$	-0.00080	0.006318	0.002165	0.005688
$\boldsymbol{c_1}$	1.78×10^{7}	1016	1281	1187
$\boldsymbol{d_1}$	0.0008	-4.85×10^{-5}	0.000327	-0.0002721

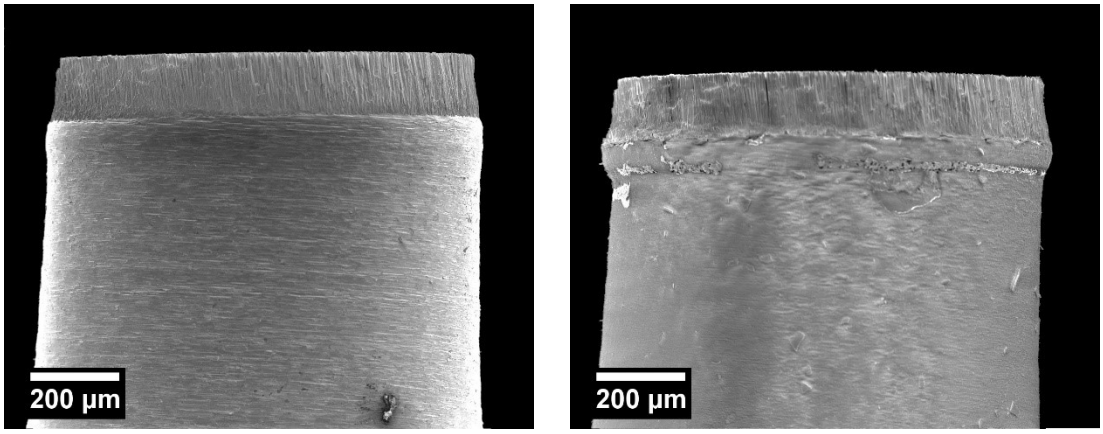

(a) (b)

Figure 123 – Secondary electron micrographs of the same Rolls-Royce Pt-aluminide cylindrical micro-specimen shown in (a) as-received state and following 20 hours at 1200°C.

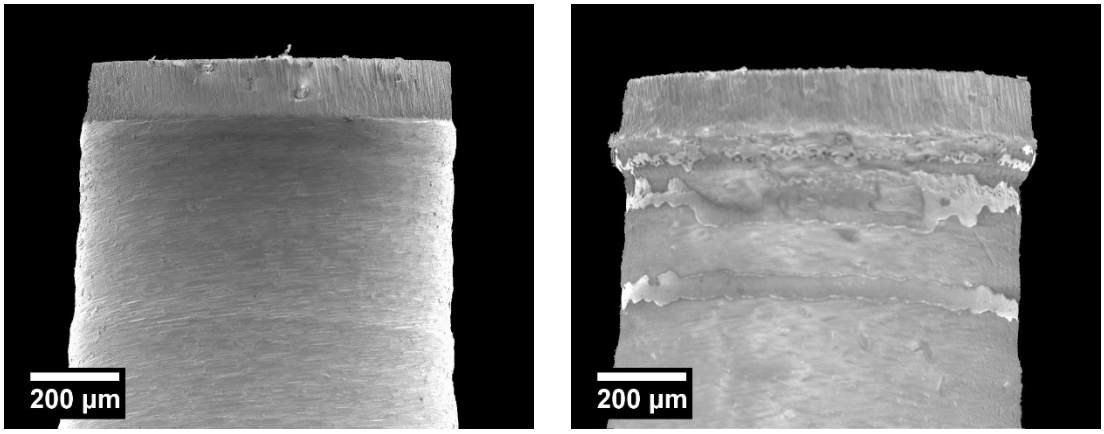

(a) (b)

Figure 124 – Secondary electron micrographs of the same Rolls-Royce Pt-aluminide cylindrical micro-specimen shown in (a) as-received state and following 40 hours (two 20-hour cycles) at 1200°C.

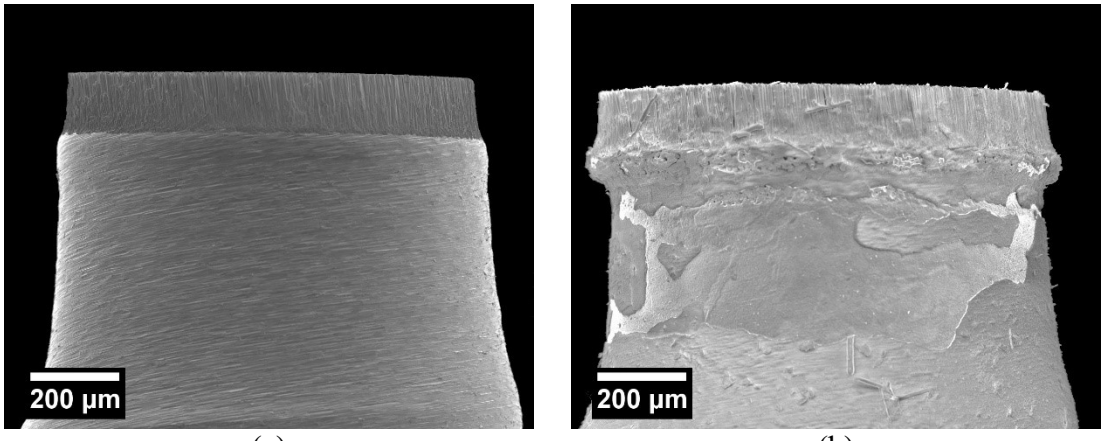

(a) (b)

Figure 125 – Secondary electron micrographs of the same Rolls-Royce Pt-aluminide cylindrical micro-specimen shown in (a) as-received state and following 80 hours (four 20-hour cycles) at 1200°C.

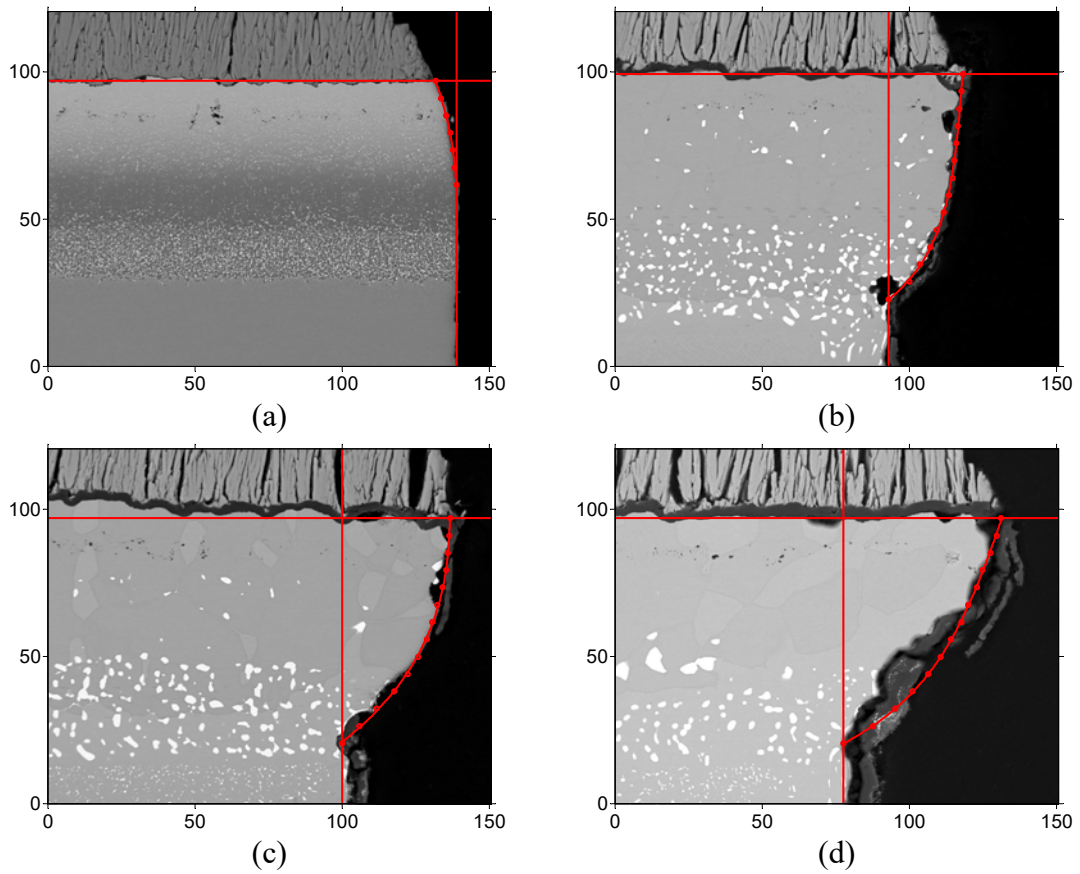

Figure 126 – Backscatter micrographs of cylindrical micro-specimen edges with laterally extended area (red) bound by the approximate original substrate edge and TGO/bondcoat interface. All micrographs are 150µm × 120µm in dimension and show the states of (a) as-received, (b) one 20-hours cycle, (c) two twenty-hour cycles and (d) four 20-hour cycles, all at 1200°C.

4.2.2 Strain rate calculation

At 15µm vertical intervals from the TGO/bondcoat interface, the lateral displacement x as a function of time t was extracted and normalised relative to one half of the initial sample diameter of each sample (536.9µm, 504.6µm and 538.7µm for 20, 40 and 80 hours respectively, measured from exterior micrographs) to reveal lateral strains ε. A power law function of the form

$$\varepsilon = a_2 t^{b_2} + c_2 \qquad \textit{Eq. 29}$$

was found to accurately represent the evolution of lateral strain ε, as a function of time t, related by power law multiplier a_2, time exponent b_2 and constant c_2. Strain rates $\dot{\varepsilon}$, for

each vertical position were then computed by calculating the derivative of the above such that

$$\dot{\varepsilon} = a_2 b_2 t^{b_2 - 1} \qquad \textit{Eq. 30}$$

4.2.3 Bondcoat stress computation

The closest literature experiment on creep of Pt-Aluminide bondcoats to the conditions tested herein was found to be in the work of Taylor et al. [197]. This work deduced a power law creep rate in the range of 800°C to 1000°C to fit the form

$$\dot{\varepsilon} = A\sigma^n e^{\left(-Q/RT\right)} \qquad \textit{Eq. 31}$$

where the stress multiplier A ($MPa^{-n}s^{-1}$), stress exponent n and activation energy Q ($J\ mol^{-1}$), are all a function of total creep strain (values for A, n and Q at 1%, 3% and 9% strain are given in Table 10) and R the universal gas constant (8.314 $Jmol^{-1}K^{-1}$). Solving the above for stress σ, allows computation of the bondcoat stress from the strain rate such that

$$\sigma = \left[\frac{\dot{\varepsilon}}{A} \cdot e^{\left(Q/RT\right)}\right]^{1/n} \qquad \textit{Eq. 32}$$

The total stress (in MPa) for each time step was then calculated at each of 1%, 3% and 9% strain by summing the stress over 714 individual strain profiles of 1pixel width (0.12μm).

Table 10 – Creep law parameters at varying strain levels derived from the work of Taylor et al [197].

Strain (%)	A ($MPa^{-n}s^{-1}$)	n	Q ($J\ mol^{-1}$)
1	8.75×10^{8}	6.82	616,000
3	2.94×10^{7}	8.90	684,200
9	0.126	9.43	537,000

4.3 Results

Micrographs of bondcoat free edges (Figure 126) indicate an increasing lateral displacement at the TGO/bondcoat interface and an increasing profile gradient with time. The extracted profiles (Figure 129) indicate a near doubling of peak lateral extensions between 20 hours and 80 hours from 32µm to 61µm. Strains (shown on the second ordinate axis) computed relative to one half of the sample diameter, also indicate an increase from 6% to approximately 12% between 20 hours and 80 hours. Displacements and strains, plotted for 15µm intervals from the TGO/bondcoat interface as a function of time (Figure 130) indicate higher displacement rates over the first 40µm from the interface, as expected from micrographs (Figure 126). A power law function was found to best fit the data. Derivatives of the two-term exponential fits to strains with respect to time, i.e. creep rates (Figure 131), indicate rates ranging between $1\times10^{-7}\ s^{-1}$ and $4\times10^{-7}\ s^{-1}$ between 20 hours and 80 hours. From these creep rates, the empirical creep algorithms at 1%, 3% and 9% (Table 10) of Taylor et al. [197] were used to compute creep stresses (Figure 132). The computed stresses are in the range 17 MPa to 28 MPa, 9 MPa to 13 MPa and 5MPa to 9MPa for creep parameters at 1%, 3% and 9% strains respectively.

To compute the total force acted upon the bondcoat by the TGO (Figure 133) the creep stresses were integrated over all 714 micrograph pixels in the range 0µm to 84µm from the TGO/bondcoat interface. For each of the three creep law parameters of 1%, 3% and 9%, total forces of 800N to 600N, 1250N to 1000N and 2250N to 2000N were respectively determined in the range 20 hours to 80 hours. The stress in the TGO was

then inferred through force balance using metallographically measured TGO thicknesses (Figure 134) of 0.28µm, 2.22µm, 2.57µm and 3.75µm. The resulting TGO stresses (Figure 135) were determined to be in the range of 180MPa to 280MPa, 280MPa to 500MPa and 520MPa to 940MPa for creep parameters at strains of 1%, 3% and 9% between 20 hours and 80 hours.

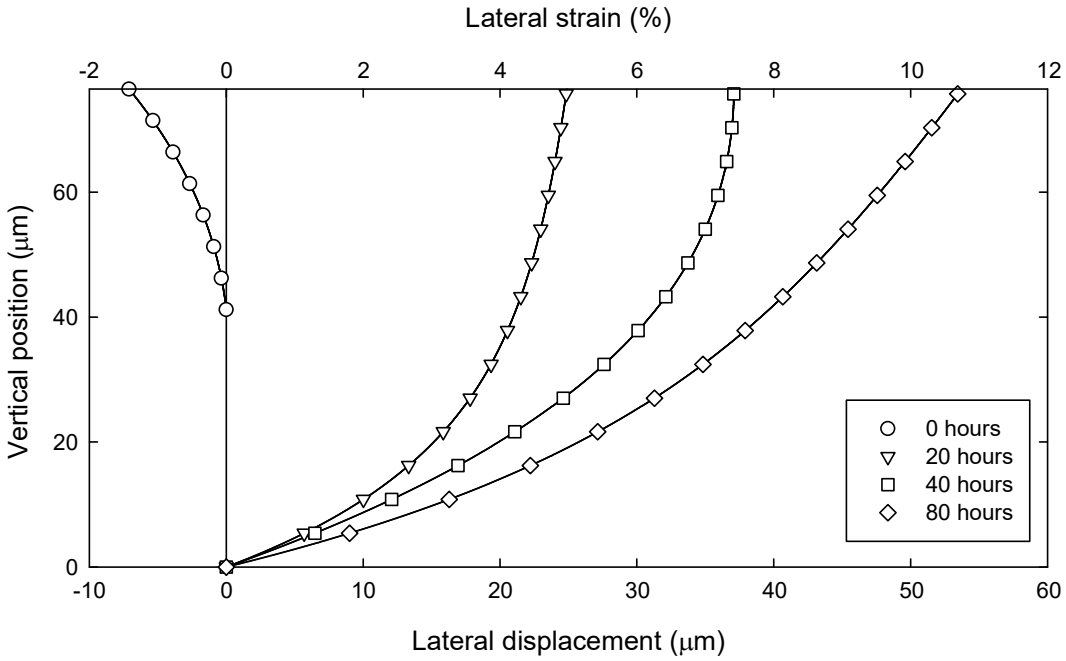

Figure 127 – Lateral displacement profiles from processed micrographs. A fixed initial deflection is assumed for profiles at 20 hours, 40 hours and 80 hours owing to sample-preparation damage.

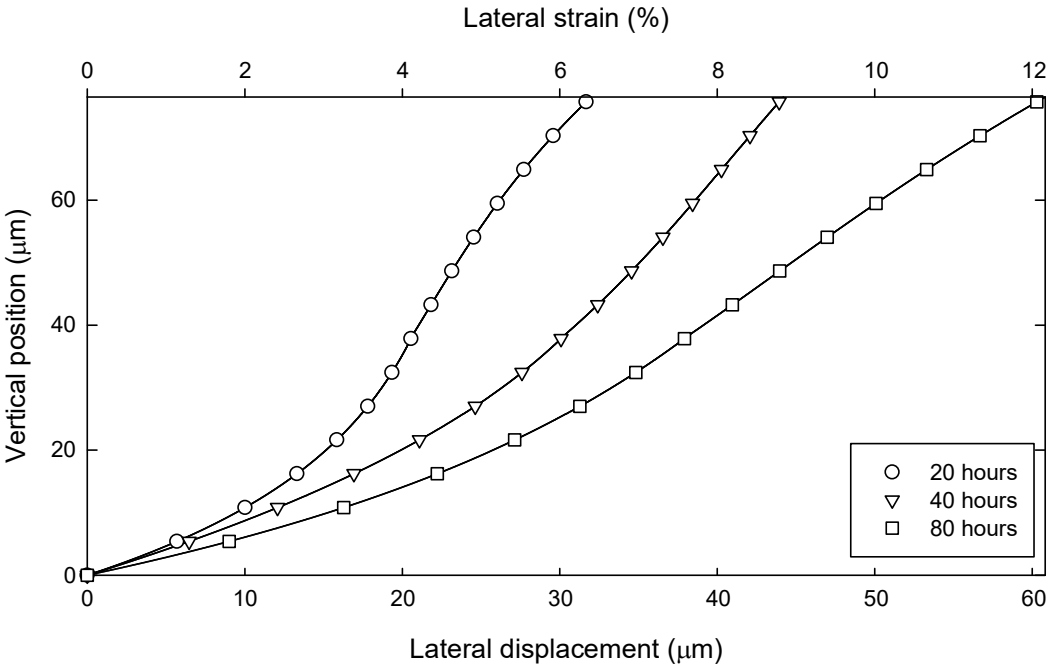

Figure 128 – Lateral displacement profiles from processed micrographs following as-received (0 hours) machining adjustment.

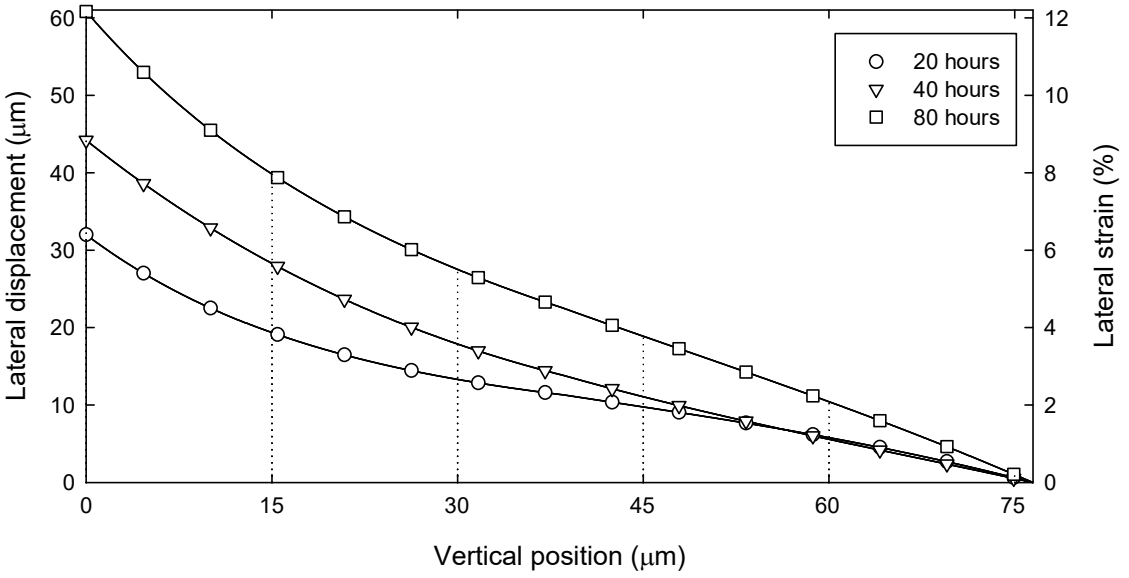

Figure 129 – Lateral displacements and strains profiles as a function of position from the TGO/bondcoat interface for 20-hour cycles at 1200°C. Profiles derived from micrographs of sample free edges and fitted to local turning points of bondcoat edges.

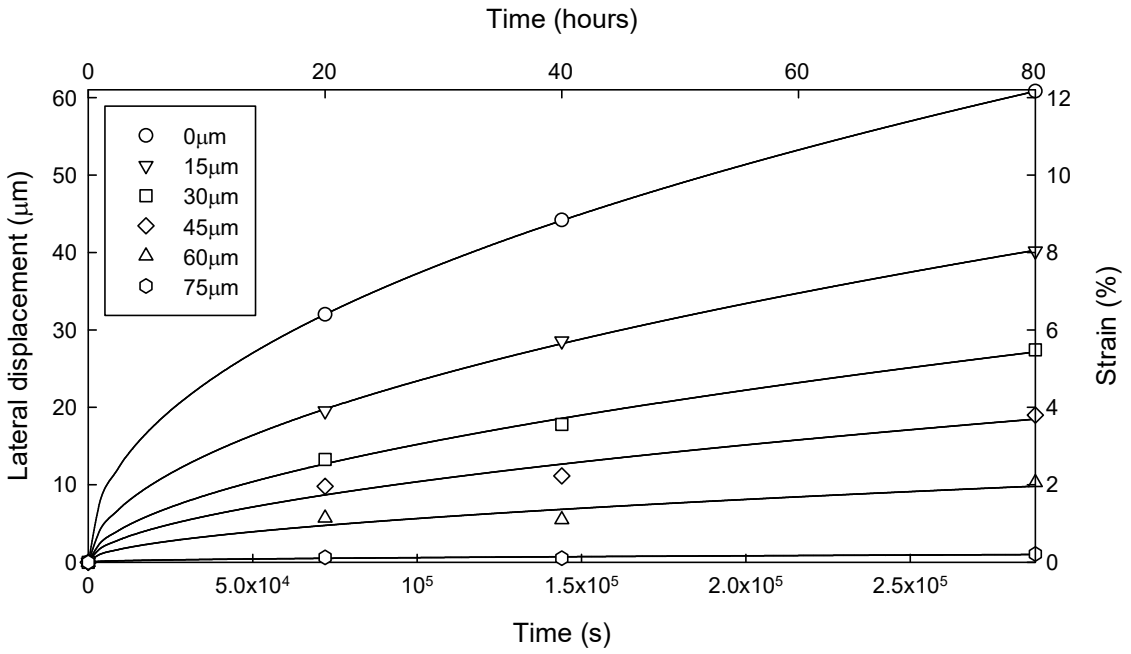

Figure 130 – Lateral displacements and strains as a function of time at 1200°C for 20μm vertical increments from the TGO/bondcoat interface with a power-law fit.

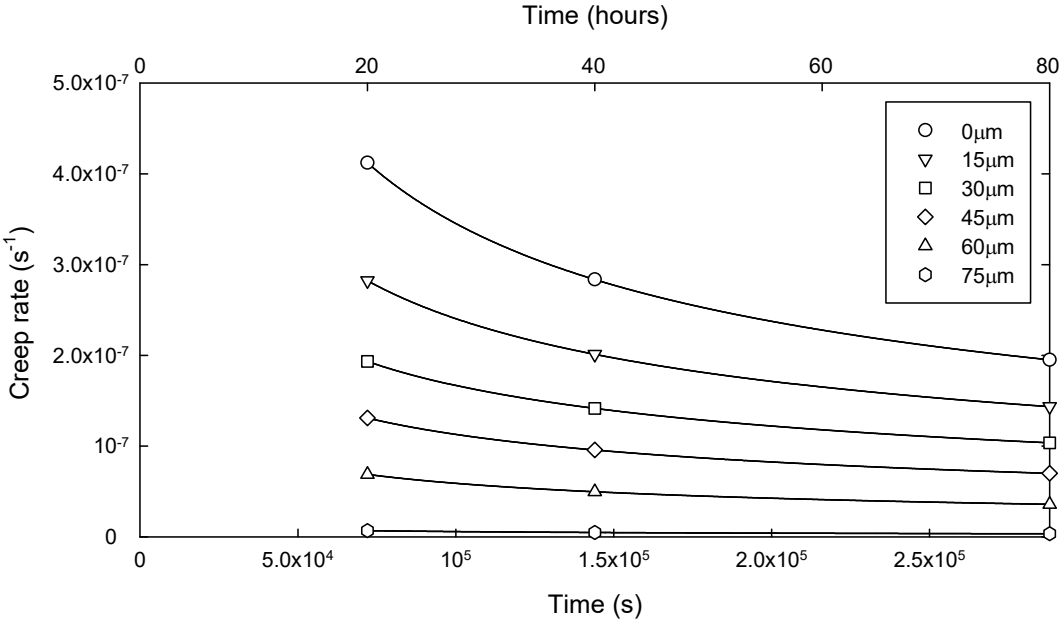

Figure 131 – Creep rates as a function of time for 20μm vertical increments from the TGO/bondcoat interface calculated from derivatives of the two-term exponential fits.

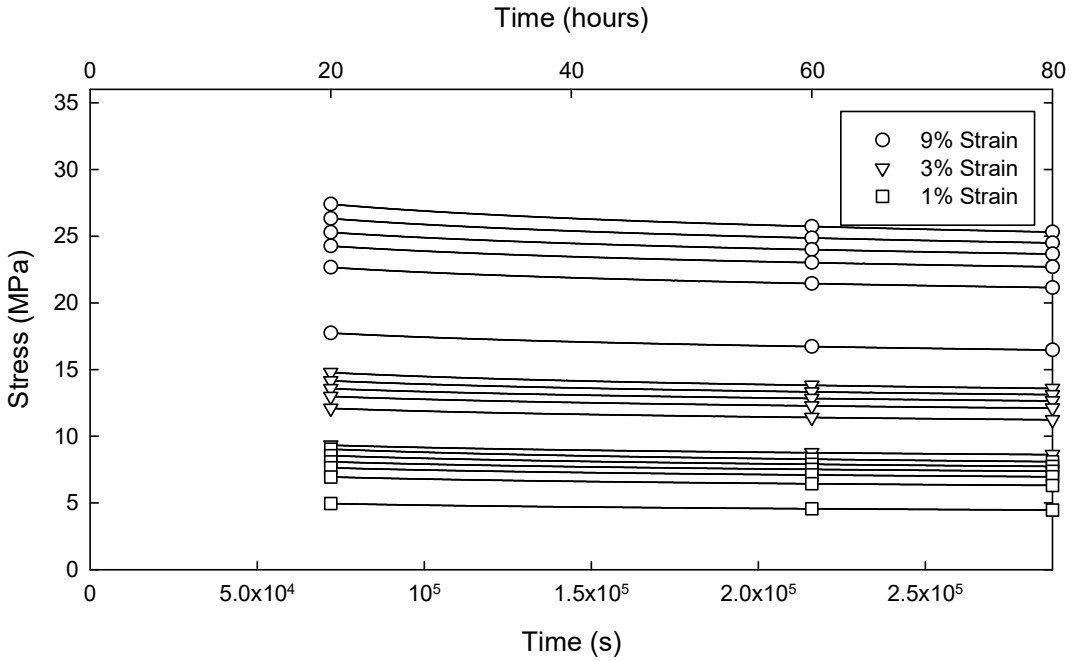

Figure 132 – Creep stress as a function of time for varying strains from the work of Taylor et al. [197]. *The uppermost curve of each set corresponds to the 0μm position (TGO/bondcoat interface) and subsequent curves are at 20μm increments.*

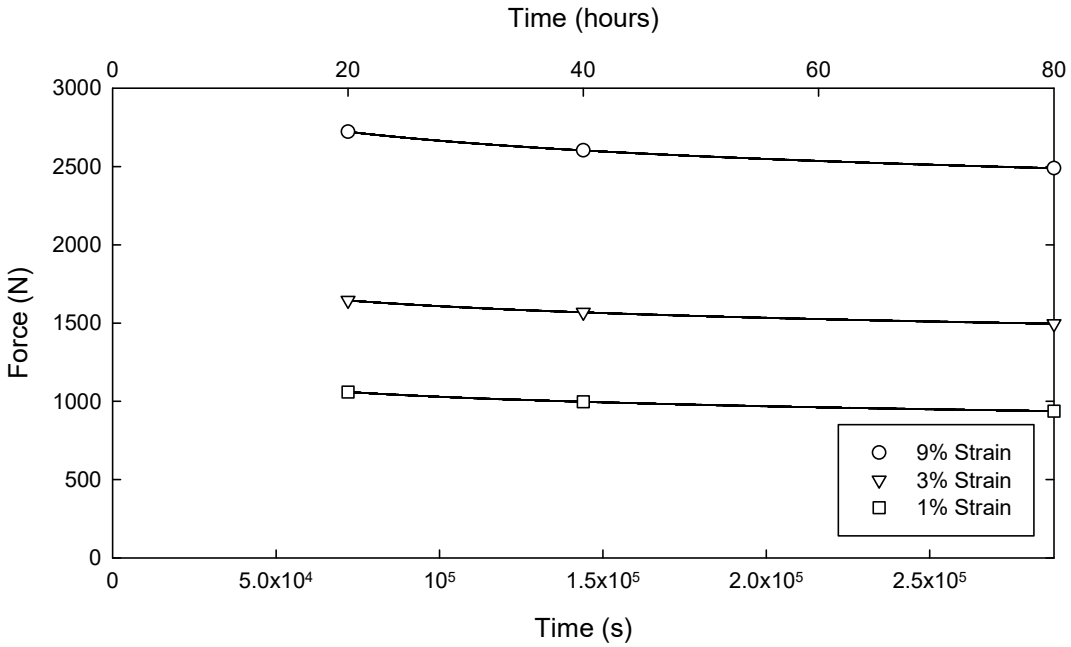

Figure 133 – Total force as a function of time calculated by integrating over the bondcoat thickness at varying creep strains.

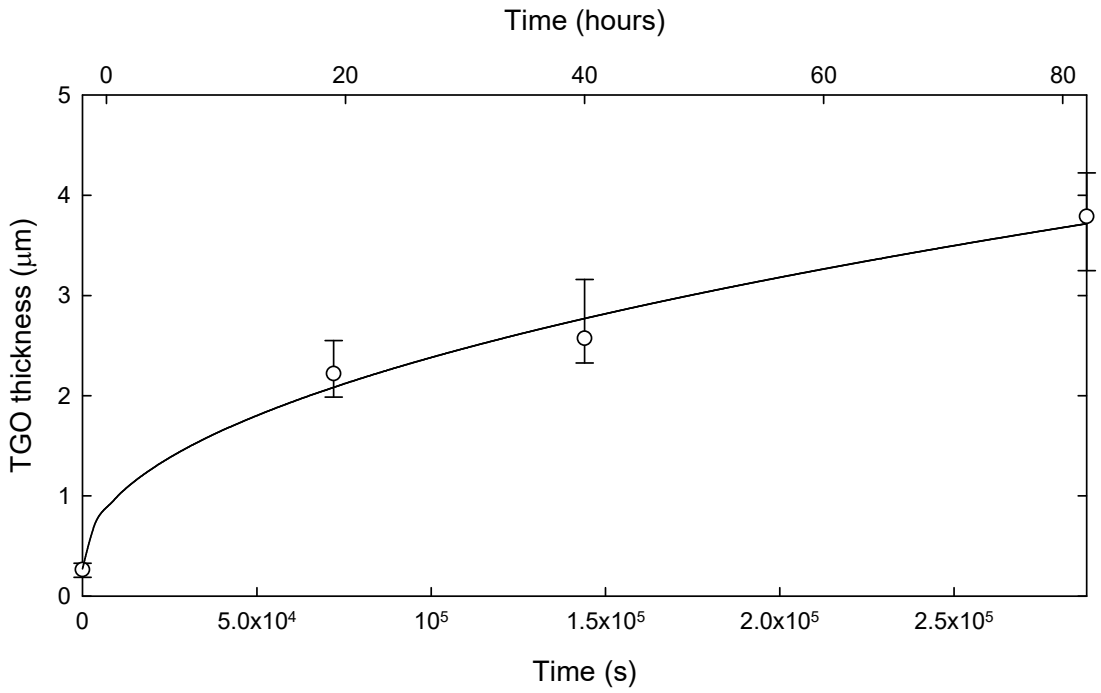

Figure 134 – TGO thickness measurements at right-hand edge of specimen as a function of time (derived from Figure 116). Twenty-five thickness measurements were taken at each time step over a length of 150μm. Median values plotted with errors given by 25th and 75th percentiles. Data fitted to a power law of the form $\xi = at^b + c$.

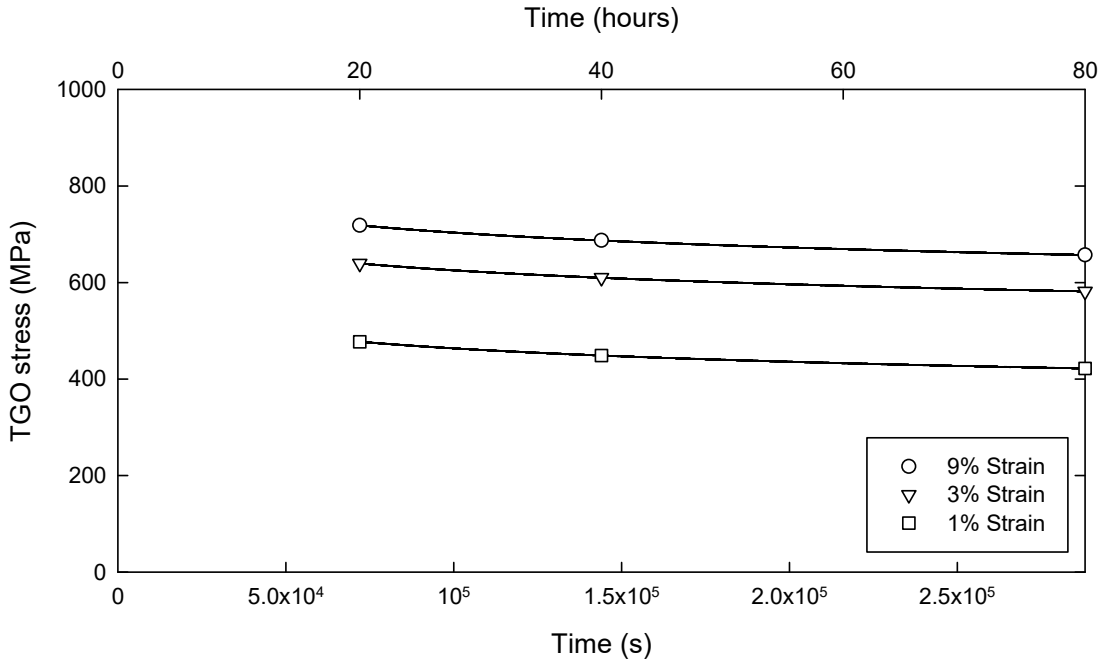

Figure 135 – Calculated TGO stress as a function of time computed using a force balance approach with creep stress and median TGO thickness. Stresses calculated for different creep law parameters.

4.4 Visco-elastic numerical simulation

To further investigate the force balance method, a simple visco-elastic finite element model was developed (Figure 136). The elastic properties of the bondcoat were taken at 1373°K such that E = 92,000MPa and Poisson's ratio = 0.3 (invariant of temperature) [79]. A time-hardening power law creep model of the form

$$\dot{\varepsilon} = A\sigma^n t^m \qquad \textit{Eq. 33}$$

was used as part of the ABAQUS finite element code. In this model, the time exponent (m) was set to zero and the stress multiplier A of Eq. 33 was equated to the product of the stress multiplier and exponential terms of the empirical model of Taylor et al. [197] at 3% strain, that is, $Ae^{\left(-Q/RT\right)}$ of Eq. 31. The stress exponent of the empirical model of Taylor et al. [197] was used directly as the stress exponent n, in the finite element creep model. The bondcoat was modelled by fixing all degrees of freedoms about the lower surface, while the left-hand boundary constituted an axisymmetric axis of rotation. The finite element mesh consisted of 12,000 plane-strain quadrilateral elements with four nodes per element (CPS4). Two boundary conditions representing the topcoat were considered. The first of these assumes the topcoat applies no mechanical constrain to the deformation of the bondcoat (Figure 136a) while the second pins the out-of-plane displacements (Figure 136b) such that only lateral displacements are possible. A surface traction representative of the growth of the oxide as the driver of the lateral displacements was applied to the upper surface in both cases. The magnitude of this applied traction was varied to match the peak lateral displacements following eighty hours.

Three loading steps were executed as part of the model, the first of these settings applied the initial boundary conditions (zero time), the second applying the surface traction load

(over a fraction of a second) and in the third the creep step was applied over 288,000s (eighty hours).

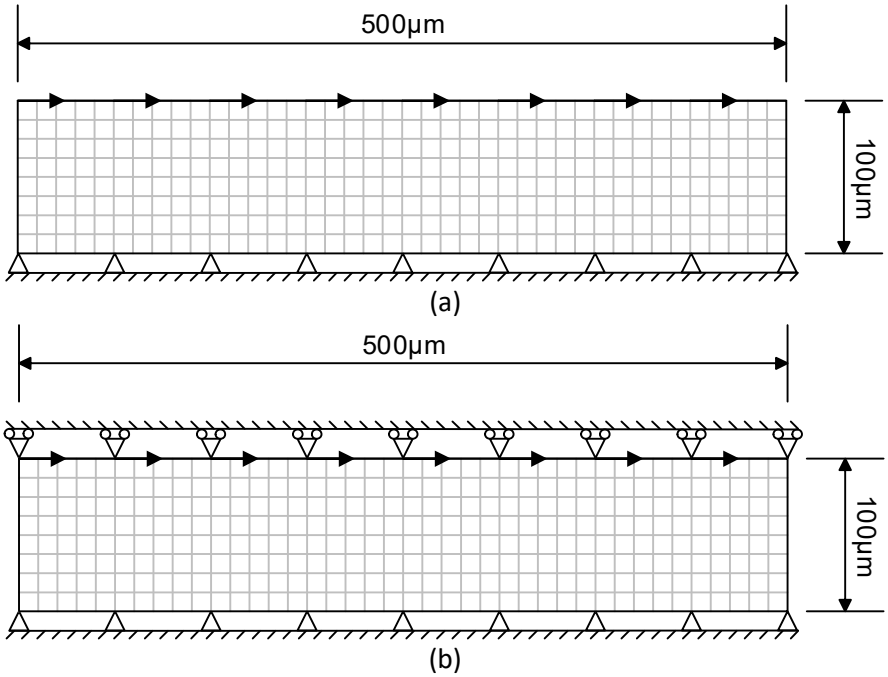

Figure 136 – Schematic diagram of bondcoat finite element models of lateral bondcoat extension under applied surface traction representing TGO growth stress (not to scale).

Results for the model without a topcoat (Figure 137) indicate a maximum lateral displacement of 51.7µm with an applied surface traction of 260MPa. Modifying the boundary conditions such that the top surface was constrained in the vertical direction (simulating the presence of a topcoat), yielded a displacement of 52.6µm at an applied load of 275MPa. A surface traction of 250MPa was then applied to both boundary conditions to compare the resulting lateral displacement of the vertically unconstrained model (Figure 138) and unconstrained (Figure 139) at 20µm nodal intervals. In comparison with displacements as a function of time derived from micrographs (Figure 130), there is significantly more linearity displayed by the finite element model, most notably near the TGO/bondcoat interface. Although final displacements are modelled well, there are numerous physical phenomena that are not accounted for that are likely causes of this discrepancy. Differences may be attributed to the use of a time-hardening

creep law instead of the empirically observed law, the use of fixed bondcoat material definitions that neglect differences in mechanical properties across the bondcoat thickness owing to phase and compositional variations, neglecting residual stress of the TGO in the as-machined state and not allowing for bondcoat roughening. This is also a likely explanation of the lower model TGO stress (250 MPa) required to produce an equivalent lateral displacement than that calculated from empirical creep laws after 80 hours (410 MPa at 1% strain, 590 MPa at 3% strain and 625 MPa at 9% strain).

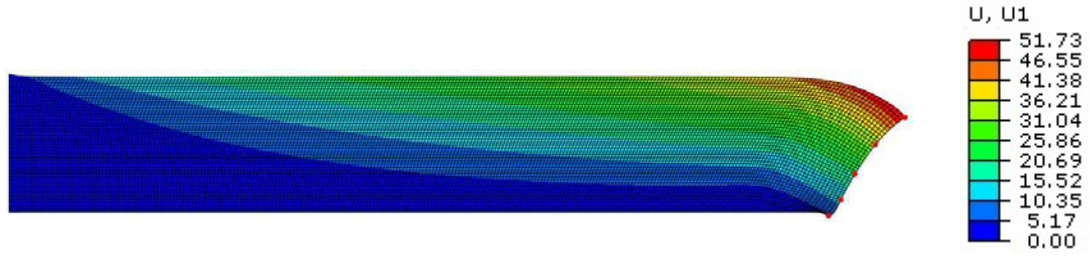

(a)

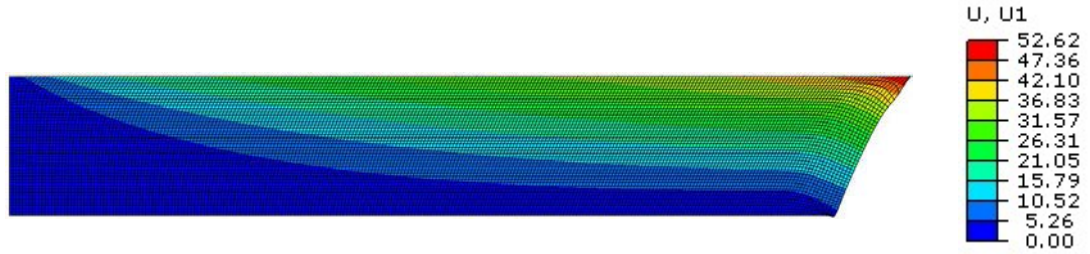

(b)

Figure 137 – Visco-elastic finite element model results of a Pt-aluminide bondcoat (a) with no topcoat and an applied surface traction of 260MPa and (b) with a vertical constraint (zero displacement) along the top surface modelling the presence of a TGO and an applied surface traction of 275MPa. Colour scale indicates magnitude (in micrometres) of lateral displacement parallel to the original plane of the TGO/bondcoat interface.

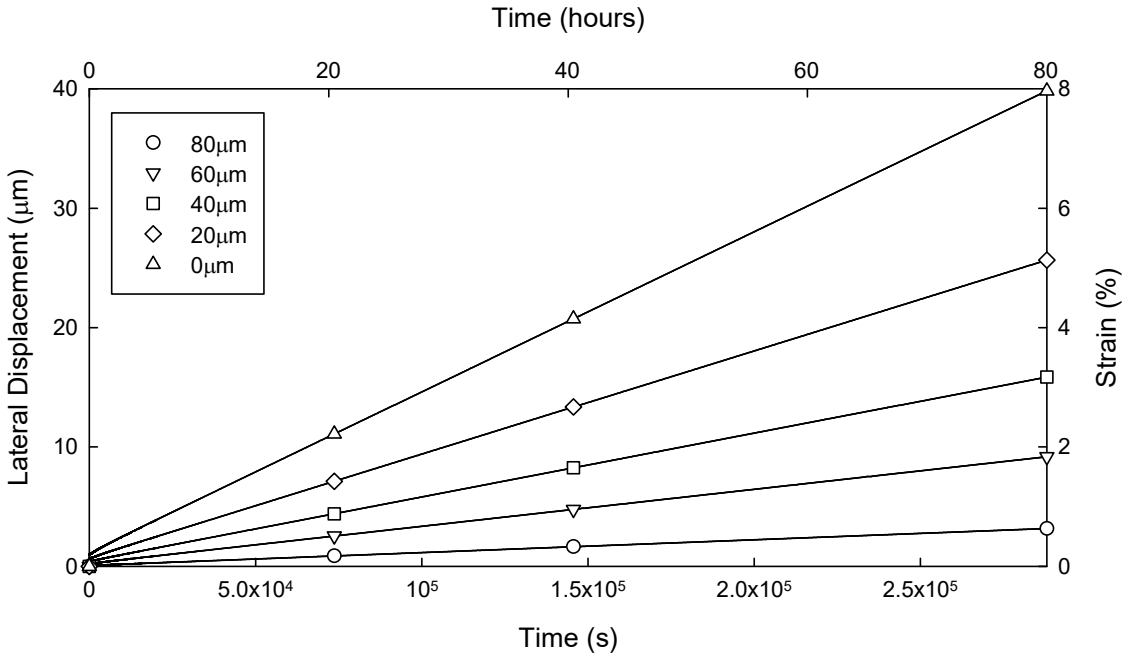

Figure 138 – ABAQUS finite element displacement and strain results of bondcoat model without a topcoat constraint under an applied surface traction load of 250MPa.

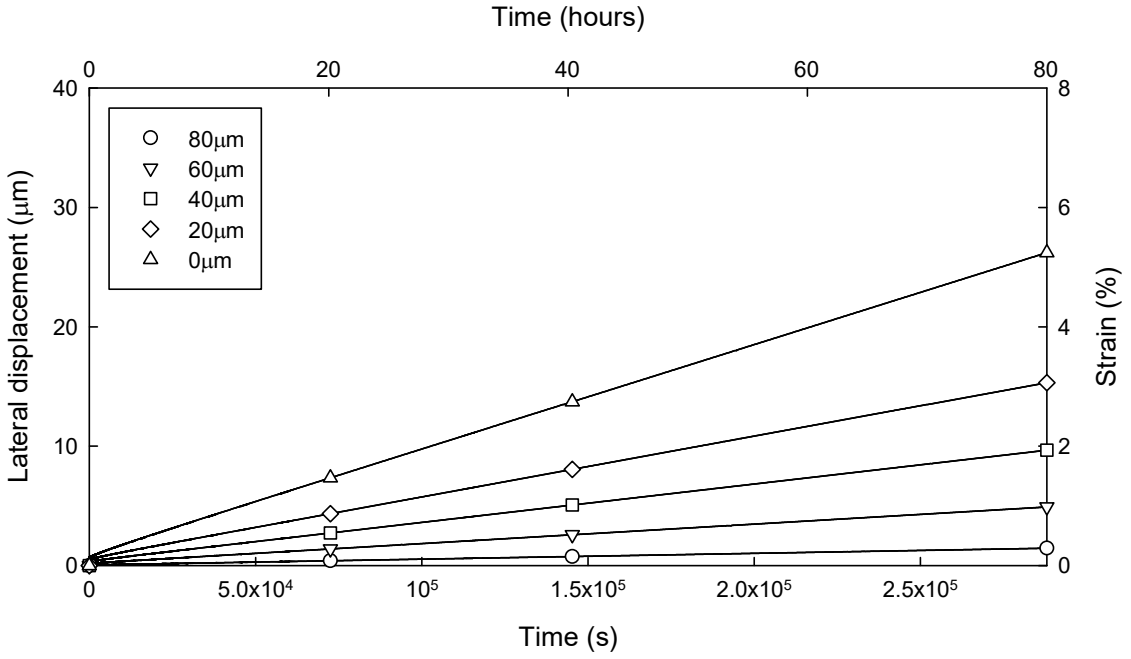

Figure 139 – ABAQUS finite element displacement and strain results of bondcoat model with a vertical topcoat constraint under an applied surface traction load of 250MPa.

4.5 Discussion

The calculated creep rates (Figure 131) in the range of 1×10^{-7} s^{-1} to 1.4×10^{-6} s^{-1} are in accordance with the experimental values of Taylor et al, determined at 3% and 9%

constant strains (Figure 140). Although the experimental work was carried out in the range 800°C to 1000°C, it is reasonable to expect values at 1200°C to lie in the range 1×10^{-8} s^{-1} – 1×10^{-4} s^{-1}. Furthermore, the computed creep stresses from the work herein (Figure 132) of 17 MPa to 28 MPa at 9% strain and 9 MPa to 13 MPa at 3% strain also fall within the experimentally expected stress range around 20MPa beyond 1000°C (Figure 140).

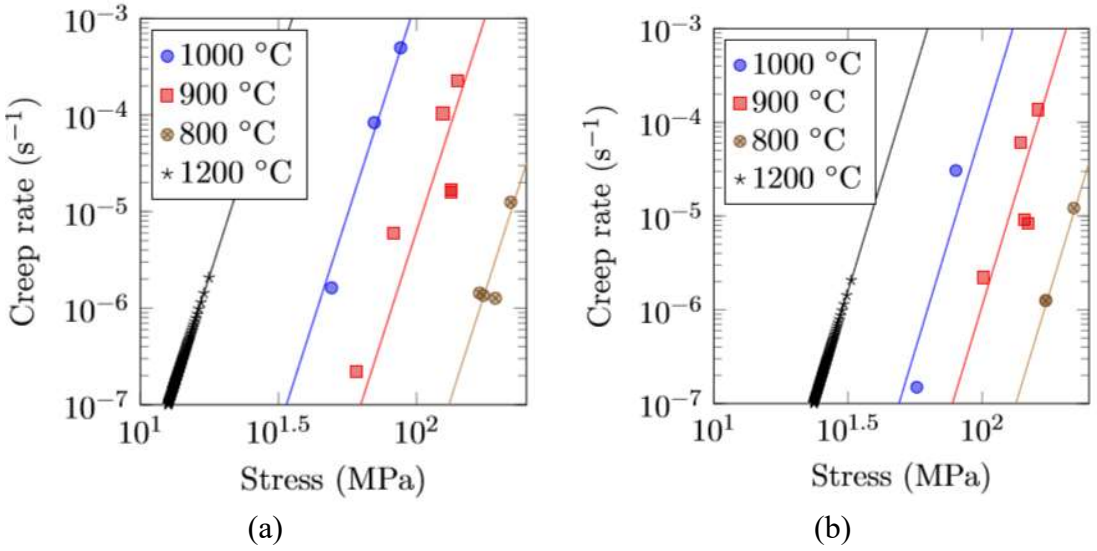

Figure 140 – Creep rates determined experimentally for a Pt-aluminide bondcoat using a constant-stress experimental approach, from the work of Taylor et al. [197] *at (a) 3% strain and (b) 9% strain.*

Early TGO growth stress measurements on NiAl without a topcoat by Sarioglu et al. [71] indicated approximately 100MPa compressive TGO stress after 16 hours. It should be noted however, that the technique used by the authors showed an error range of ±200MPa. Furthermore, measured stresses are expected to be lower in the absence of a superalloy substrate. Synchrotron work by Veal et al. [196] on model (Ni,Pt)-Al alloys without topcoats (Figure 141a) showed compressive stresses of 120MPa to 180MPa for Ni-37Al-10Pt and Ni-25Al-20Pt following 6.7 hours at 1100°C. Comparable values were obtained in the work of Hou et al. [41] and Heuer et al. [195] after 6 and 15 hours respectively, both at 1100°C. In these studies, as with the work of Sarioglu, a superalloy substrate was

not present. Consequently, the reported stresses are lower than those found in this work owing to stress relief by a compliant bondcoat alloy.

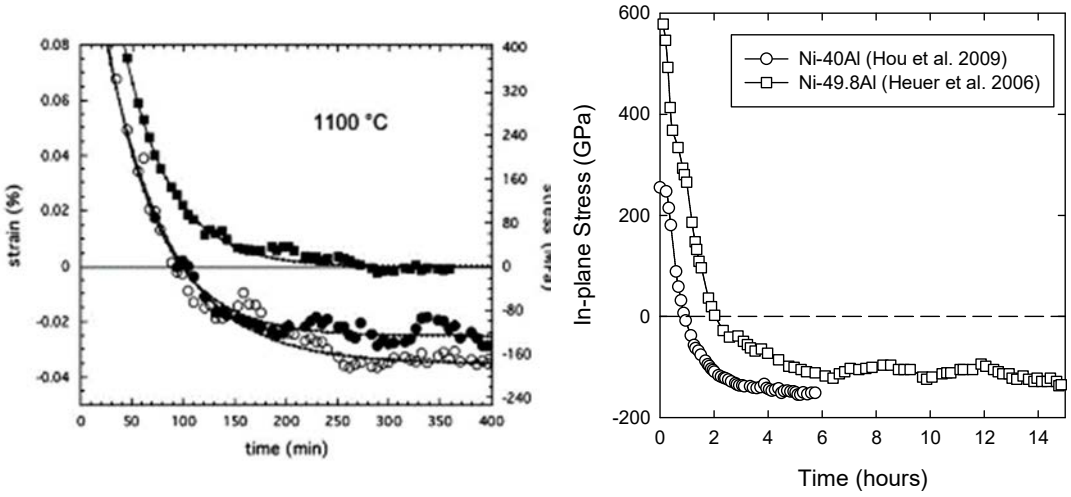

Figure 141 – Synchrotron strain measurements and calculated alumina stresses on model alloys at 1100°C from (a) Veal et al.[196] *for Ni-50Al-10Pt (solid squares), Ni-37Al-10Pt (solid circles) and Ni-25Al-20Pt (open circles) and (b) Hou et al.* [41] *and Heuer et al.* [195].

The PLPS work of Nair et al. [100] estimated growth stresses of approximately 500MPa for an overlay bondcoat system with a topcoat in place, in the range 0 hours to 200 hours (Figure 142). These values are in good agreement with the calculated TGO stresses in this work of 280MPa to 500MPa and 520MPa to 940MPa (Figure 135) for creep parameters at strains of 3% and 9% between 20 hours and 80 hours.

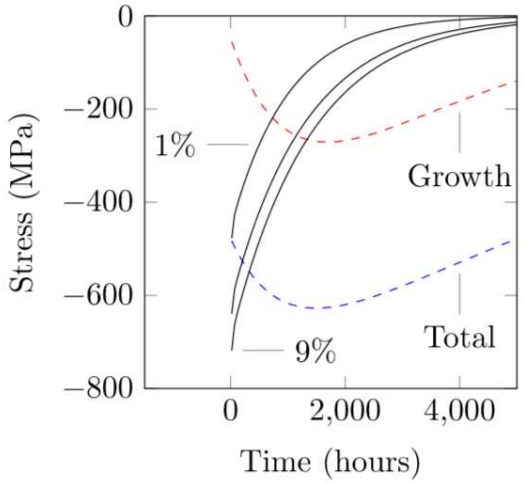

Figure 142 – Estimated TGO Growth stress and measured TGO residual stress at room temperature via PLPS for an overlay TBC system, from the work of Nair et al. [100] *in addition to positions of 1%, 3% (not marked) and 9% empirical strains from the current work.*

For a comparison with TGO stresses from other PLPS measurements that do not take into account cooling stresses (Figure 40), it is necessary to apply an elastic thermal correction. The elastic thermal stress equation presented previously (Eq. 26) holds true for oxides that are thick in relation to the substrate metal. In situations where the substrate is significantly larger than the oxide (as is the case here), the equation reduces to [198]:

$$\sigma_{th} = \frac{E_{alloy} \cdot (\alpha_{ox} - \alpha_{alloy}) \cdot \Delta T}{(1 - \nu_{alloy})} \qquad \textit{Eq. 34}$$

Using CMSX-4 elastic properties of $E_{alloy} = 176GPa$, $\nu_{alloy} = 0.25$ and $\alpha_{alloy} = 13.91\times10^{-6}$ [199] and TGO $\alpha_{ox} = 8.7\times10^{-6}$ [200] and a temperature drop of 1130°C, the elastic strain is found to be 1.71GPa. Applying this correction to literature PLPS measurements and comparing with the calculated force balance TGO stress (Figure 143) suggests good correlation between literature TGO stresses and those from the current work. This is particularly the case in relation to the work of Sridharan et. al [98] and Wen Jordan and Gell [97]. It is noteworthy however, that there is a large range of stress values for each of the reported literature datasets. For example, at 20 hours, the stress range determined by Sridharan et al. shows a range of 0.9GPa to 1.4GPa, equivalent to ±20% of the mean. There is also a large difference in TGO stress between various literature sets, for example, the work of Lee, Atkinson, Selçuk [103] suggest a near-zero TGO stress following 25 hours compared to a corrected TGO stress by Wen, Jordan, Gell [97] of 0.25GPa to 0.5GPa.

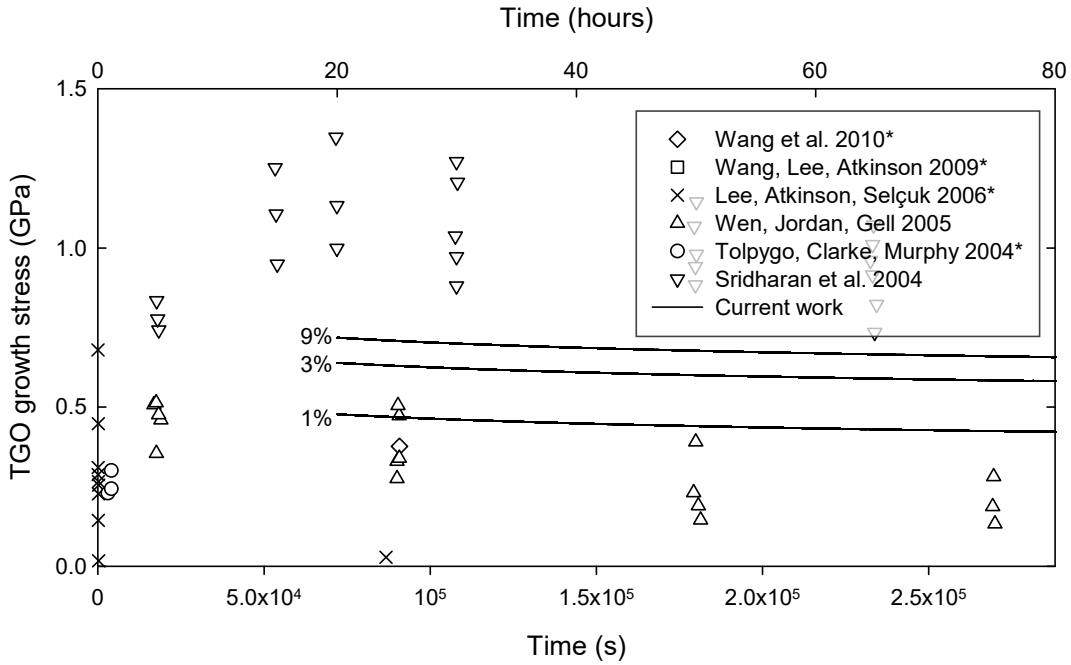

Figure 143 – Literature PLPS data corrected for cooling strains over a temperature drop of 1130°C for Pt-aluminide bondcoats under one-hour cycles (except where noted) from the work of Wang et al. [102]*, Wang, Lee and Atkinson* [96] *(twenty-hour cycles), Lee, Atkinson and Selçuk* [103]*, Wen Jordan and Gell* [97]*, Tolpygo, Clarke and Murphy* [45] *and Sridharan et al.* [98]*. Legend entries denoted by an asterisk indicate TGO stresses calculated from peak shift using Eq. 18. TGO stress from force balance calculated in this work, denoted by solid lines at 1%, 3% and 9% creep strain.*

4.6 Conclusions

A force-balance model has been presented herein that relates fundamental metallographic observation of bondcoat creep to the in-plane TGO stress required to drive such a creep deformation. Empirical creep relationships for similar bondcoats at 1100°C were used to derive creep stresses from strain rates in this work at 1200°C. The TGO stresses computed herein using the force balance approach at 1%, 3% and 9% empirical creep strain experiments were found to be in the range of 400MPa to 500MPa, 600MPa to 700MPa and 700MPa to 750MPa for 1%, 3% and 9% empirical creep strains respectively. A comparison with literature synchrotron XRD shows higher stresses than NiAl alloys owing to a weak substrate alloy in comparison to nickel superalloys. A comparison with PLPS literature shows good agreement with TGO stresses corrected for elastic cooling stresses (calculated at 1.71GPa). An analysis of PLPS literature data reveals a large range

in scatter within data sets and between reported literature values. Furthermore, this analysis has shown the large contribution by cooling strains on the total recorded stresses in PLPS measurements and the need for an analytical method to determine growth stresses, as presented in the force balance herein.

4.7 Further work

It would be advantageous to use creep data specific to the bondcoat system examined and the test temperature, 1200°C in this case. Furthermore, having creep data for entire strain range of 5% to 10% would improve the calculated creep stress at each vertical position from the TGO/bondcoat position. For better comparison to synchrotron XRD and PLPS literature data, it would beneficial to carry out shorter oxidation timesteps, for example, one-hour cycles. Such short-cycle analysis will be useful in determining whether the initial stress increase reported in most literature PLPS experiments is noted using the force balance method.

A refinement of the visco-elastic finite element model with a displacement controlled boundary condition will also allow better modelling of the stress state within the bondcoat. Use of a user subroutine (Appendix F) with accurate creep integration directly utilising the empirical creep relationship as opposed to the time-hardening model used herein will allow better prediction of TGO stresses.

Chapter 5 Temporal 3-D microscopy via synchrotron X-ray tomography

5.1 Introduction

In studies of TBC failure mechanisms, analysis usually involves destructive examination following a period of high-temperature exposure, a certain number of thermal cycles or after failure has occurred. Using such an approach, there is little possibility of tracking initiation features and pre-existing defects. This, combined with the introduction of sample preparation damage limits the ability of such techniques to track changes in the TGO/bondcoat through time, in particular the early defect forming stages.

An alternative strategy is through the use of non-destructive 3-D imaging techniques, for example X-ray tomography. Laboratory-source X-ray tomography imaging [127–129], although relatively inexpensive, provides resolutions on the order of tens of micrometres, too low for analysis in and around the TGO. Synchrotron X-ray tomography [26,131,133,134], uses a high brilliance and monochromatic source of X-rays and has been used to visualise the evolution of TBC and superalloy microstructures at high spatial resolutions. Material phases are distinguished through the difference in X-ray absorption, a function of the mass attenuation coefficient of constituent phases. The majority of the work carried out to date has focused on pre-oxidised samples with a TGO that is sufficiently thick to observe (see section 1.6.4.3). Less emphasis is placed on the initial state of the TBC system and the evolution of the system from the as-coated condition.

In this work, synchrotron X-ray microtomography is used to study the time-dependent evolution of three cylindrical micro-specimen bondcoat systems starting from the as-

received state. Four-dimensional, time-dependent volumetric tomography reconstructions have allowed insights into the behaviour of the bondcoat, TGO, topcoat and substrate. The technique is shown to yield high quality results in the analysis of features with sharp absorption contrast in relation to the surrounding material. Detailed analysis methods are presented to study the TGO/bondcoat interfacial roughness, TGO thickness, substrate porosity and topcoat intercolumnar separation, all as a function of time and all from the same specimens.

5.2 Results

Spatial and temporal microscopy of a β-(Ni,Pt)Al and a platinised γ/γ' coating system was carried out using absorption synchrotron X-ray micro computed tomography (SX μ-CT). The Diamond Light Source Synchrotron facility was used to carry out 3-D imaging of a series of specimen through time, from the as-received state through to 60 hours under 20-hour thermal cycles at 1200°C. The samples were approximately 500μm in diameter and scans were carried out on the same specimen through time. The theoretical imaging resolution was 0.9μm per pixel. Reconstructions were processed using the in-house reconstruction algorithm at the I12 beamline of Diamond Light Source. Avizo Fire was used to produce volumetric reconstructions of the samples (Figure 144, Figure 145). In all 3-D reconstructions, the columnar microstructure of the topcoat is clearly visible. In the as-received state of the Rolls-Royce Pt-aluminide specimen (Figure 144a), the inner and outer regions of the inter-diffusion zone are distinguishable from the substrate. The grit-line is also clearly noted near the TGO/bondcoat interface. With time at temperature, lateral displacement of the TGO/bondcoat interface is noted for all samples resulting in an increase in diameter relative to the original substrate diameter. The Pt bondcoat sample

however, shows significantly less radial lateral displacement. Bondcoat phase transformation with TGO growth is observed with the transition from β to γ' noted in both Pt-aluminide specimens (Figure 144, Figure 145). Reconstructions were orientated such that the micro-drilled holes in the substrate matched the same position between timesteps. The sampling plane was chosen to match the other timesteps of the sample but varied between some timestepts (see Appendix J for full micro-specimen reconstructions.).

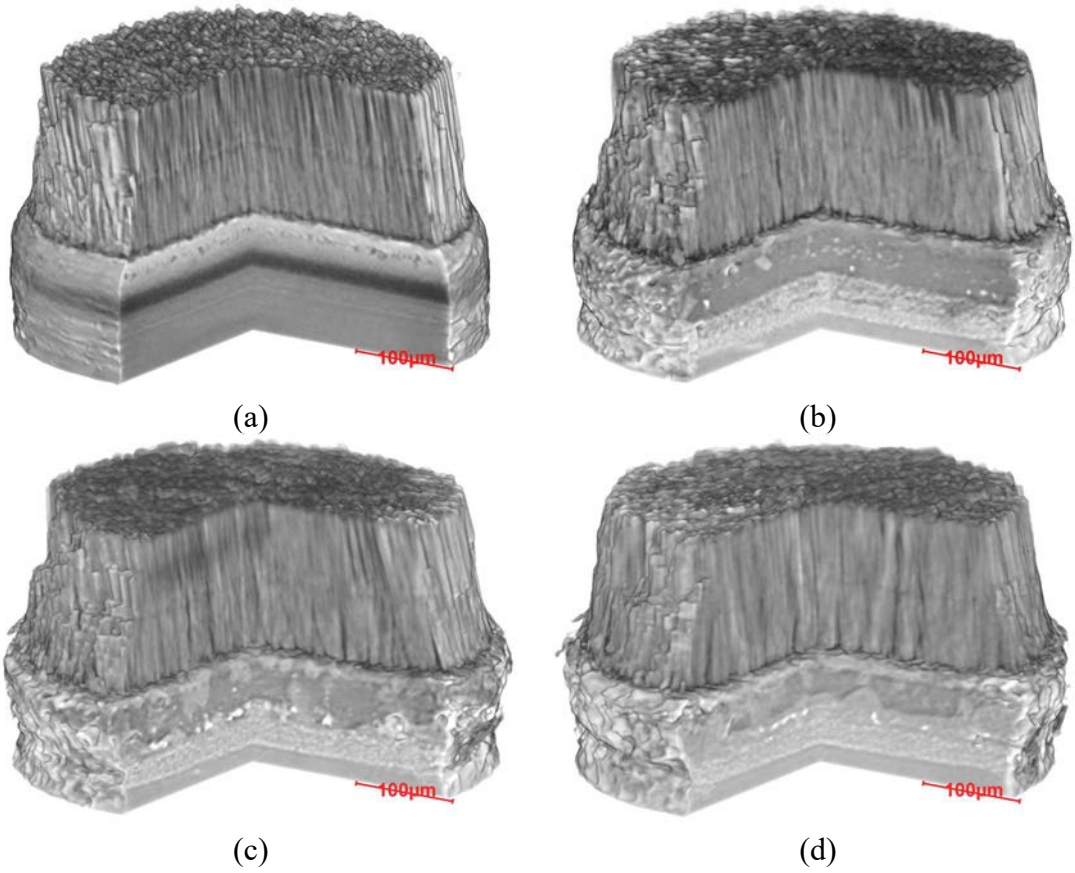

Figure 144 – Cutaways of Rolls-Royce Pt-aluminide reconstructed tomograms showing the (a) as-received scan, (b) the same sample following 20 hours, (c) the same sample at 40 hours and (d) after 60 hours, all under 20-hour cycles at 1200°C. Note that the reconstructions were orientated to match using the micro-drilled holes in the substrate but the virtual sampling plane varied between timesteps. See Appendix J for full micro-specimen reconstructions.

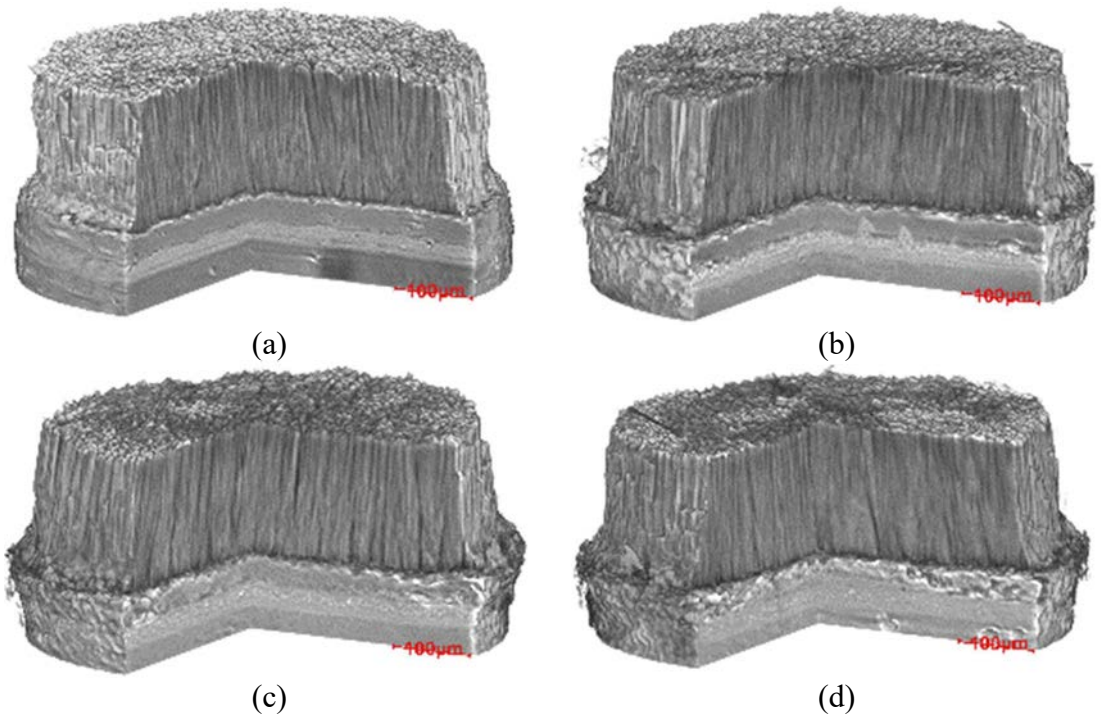

Figure 145 – Cutaways of Alstom Pt-aluminide reconstructed tomograms showing the (a) as-received scan, (b) the same sample following 20 hours, (c) the same sample at 40 hours and (d) after 60 hours, all under 20-hour cycles at 1200°C. Note that the reconstructions were orientated to match using the micro-drilled holes in the substrate but the virtual sampling plane varied between timesteps.See Appendix J for full micro-specimen reconstructions.

Virtual cross-sections derived from volumetric data for Rolls-Royce Pt (Figure 146), Rolls-Royce Pt-aluminide (Figure 147) and Alstom Pt-aluminide (Figure 148) show the extent of microstructural evolution with time. In all cases, thickening of the TGO is noted with associated bondcoat phase transformation. Pt specimens indicate diffusion of platinum from the bondcoat to the substrate. Lateral edge extensions of the bondcoat are pronounced for both Pt-aluminide specimens, more so for the Rolls-Royce specimen than the Alstom variant. Lateral displacements of the Pt specimen indicate restrained behaviour. Substrate porosity is non-existent in the as-received state of both Rolls-Royce specimens, while the Alstom specimen displays some as-received porosity. Substrate porosity with time at temperature is extensively seen in the Alstom Pt-aluminide and Rolls-Royce Pt specimen. Inter-columnar separation is seen to increase for the Alstom and Rolls-Royce Pt-aluminide specimens. At the bondcoat extremities of the Pt-aluminide specimen, distinct voids are noted that are not observed in the equivalent Pt

bondcoat. Similar porosity, albeit confined to a region directly below the TGO is noted in the Alstom specimen.

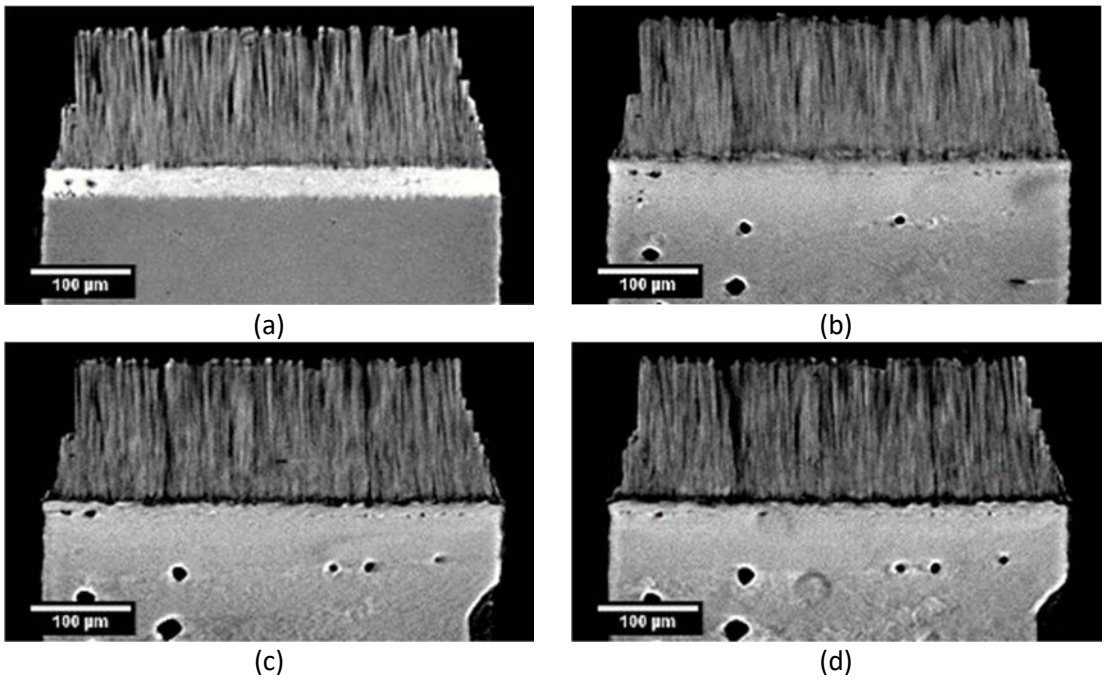

Figure 146 – Reconstructed virtual cross-section of Rolls-Royce Pt specimen undergoing 20-hour cyclic oxidation, (a) as-received, (b) after 20 hours, (c) after 40 hours and (d) after 60 hours.

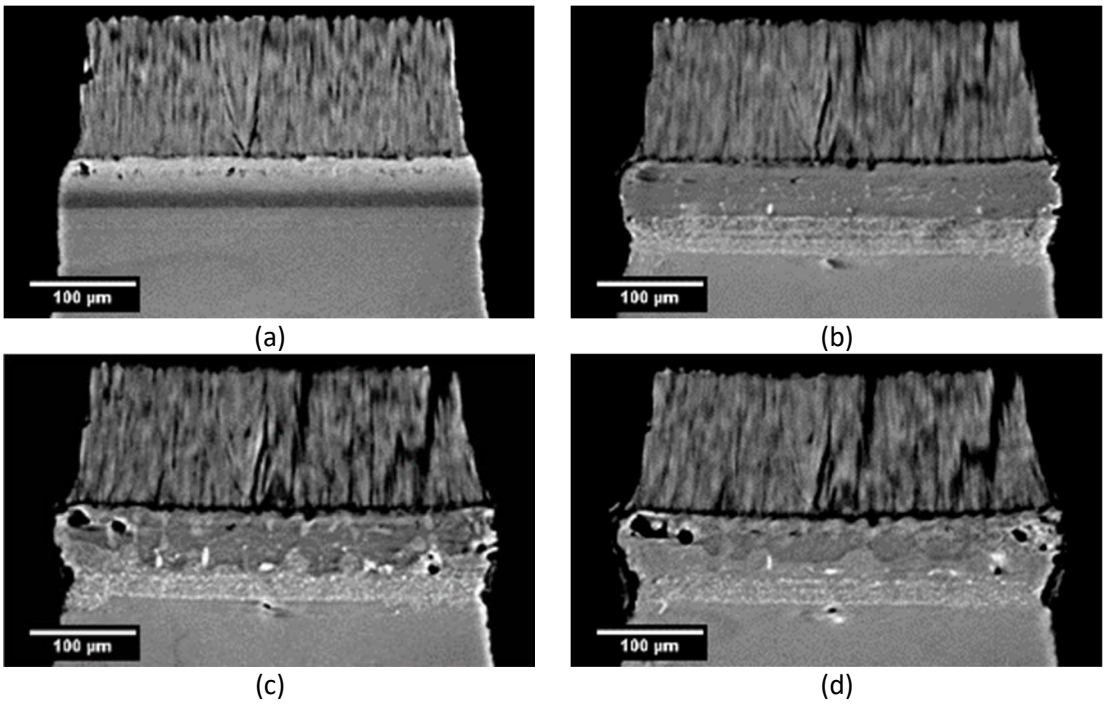

Figure 147 – Reconstructed virtual cross-section of Rolls-Royce Pt-Al specimen undergoing 20-hour cyclic oxidation, (a) as-received, (b) after 20 hours, (c) after 40 hours and (d) after 60 hours.

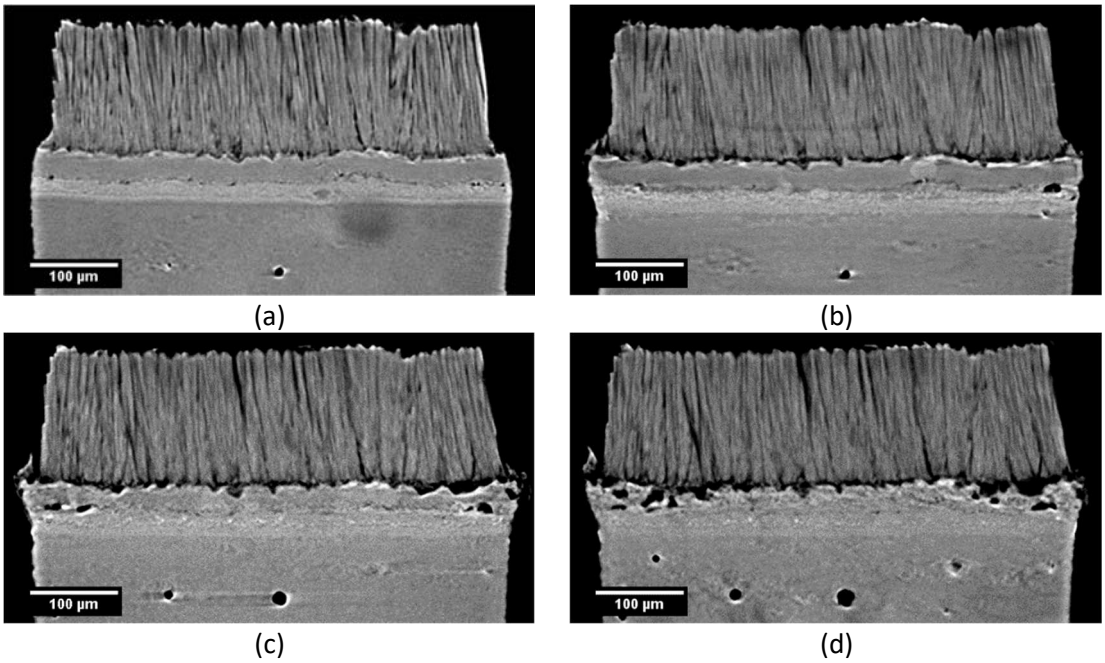

Figure 148 – Reconstructed virtual cross-section of Alstom Pt-Al specimen undergoing 20-hour cyclic oxidation, (a) as-received, (b) after 20 hours, (c) after 40 hours and (d) after 60 hours.

Virtual cross-sections, planar to the TGO/bondcoat interface and approximately through the grit-line of Rolls-Royce Pt (Figure 150), Rolls-Royce Pt-aluminide (Figure 151) and Alstom Pt-aluminide (Figure 152) specimens indicate the extent of bondcoat phase transformation. The Rolls-Royce Pt specimen shows little discernible change, aside from the decrease in contrast associated with platinum diffusion. This specimen however clearly shows off-centre ring-artefacts associated with the tomography reconstruction process. Rolls-Royce Pt-aluminide planar cross-sections (Figure 150) show the transformation of β grains to γ' with depletion of aluminium to form the TGO. Similar behaviour is exhibited by Alstom Pt-aluminide specimens (Figure 152). The extent of bondcoat porosity at radial extremities is most evident following sixty hours for both Alstom (Figure 152d) and Rolls-Royce (Figure 151d) Pt-aluminide specimens.

Detailed visualisation of the TGO of the Rolls-Royce Pt-aluminide specimen (Figure 149) reveals TGO evolution, the thickness of which is clearly seen in the later timesteps of forty and sixty hours. In the as-received condition (Figure 149a) however, distinguishing

between the TGO and bondcoat or topcoat is made difficult by the limited resolution (0.9µm detectable compared to 0.3µm expected) and the presence of bright streak artefacts associated with a sharp change in mass attenuation (at interfaces, for example). Furthermore, the mass attenuation at 53keV (calculated using WinXCom [118]) of the alumina TGO (0.276 cm^2/g) is so close to that of air (0.201 cm^2/g) when compared to say the topcoat (3.960 cm^2/g) that distinguishing between alumina and voids or cracks is impractical.

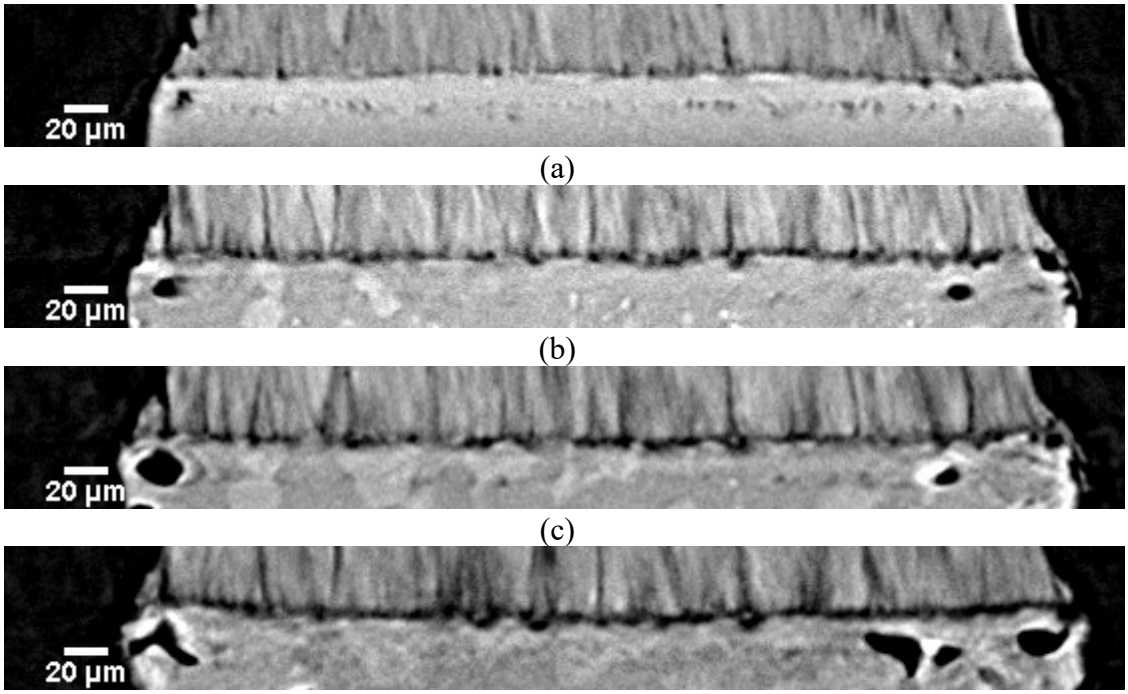

Figure 149 – Virtual cross-sections from 3-D synchrotron X-ray microtomography of the same Rolls-Royce Pt-Al specimen shown through time (a) in the as-received condition, (b) following 20 hours, (c) following 40 hours and (d) following 60 hours, all at 1200°C.

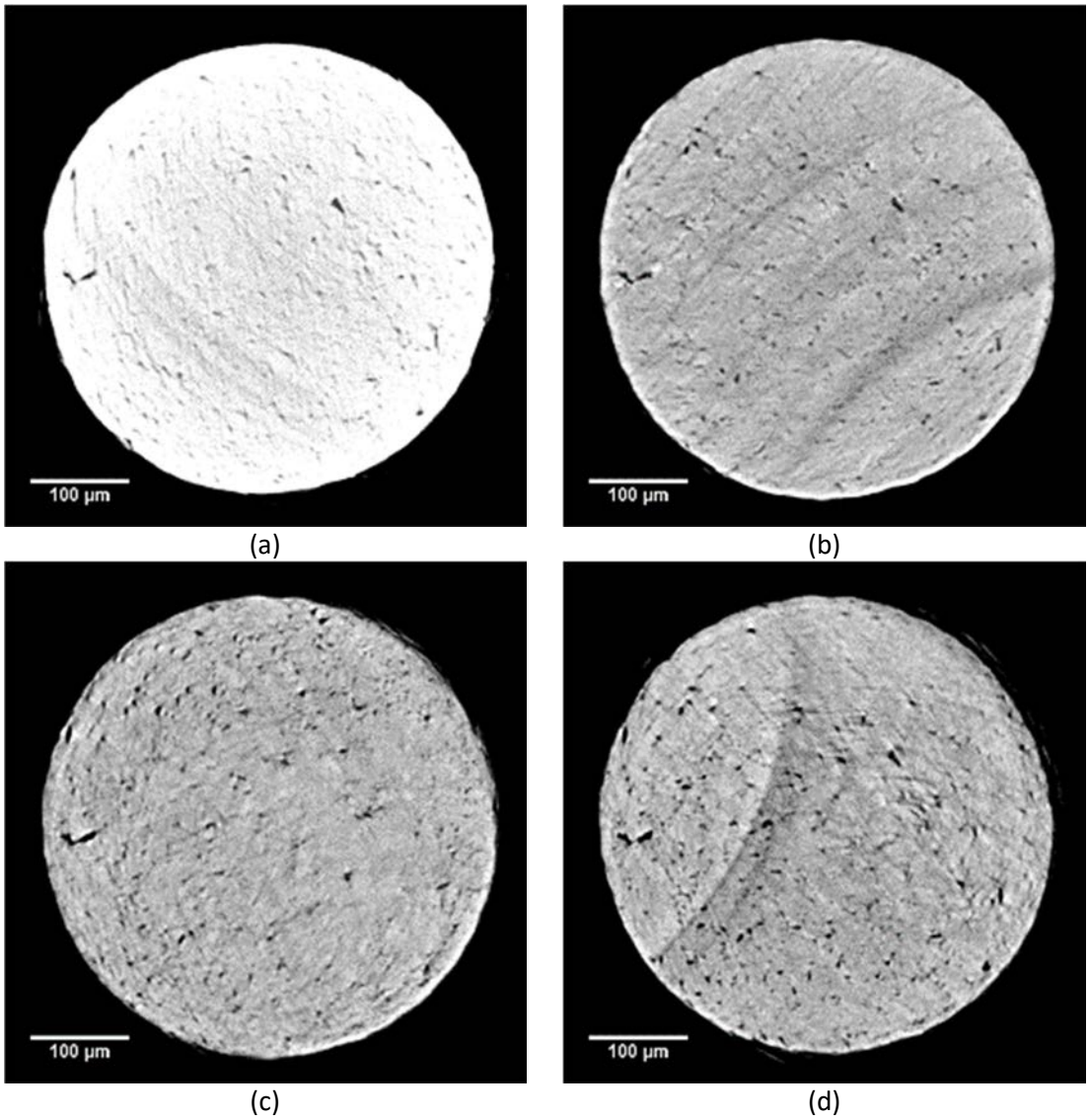

Figure 150 – Reconstructed virtual section through bondcoat of Rolls-Royce Pt specimen undergoing 20-hour cyclic oxidation, (a) as-received, (b) after 20 hours, (c) after 40 hours and (d) after 60 hours.

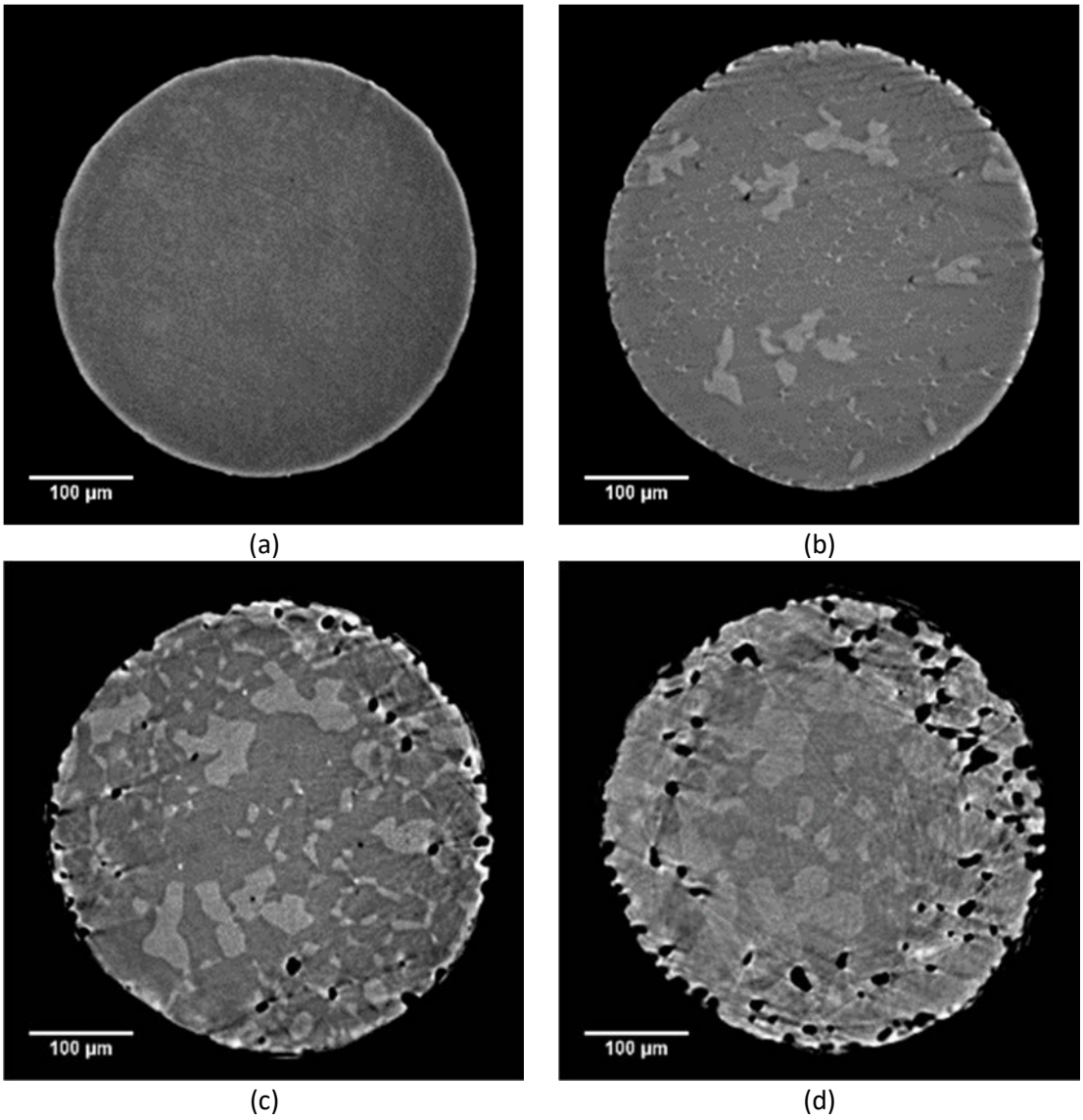

Figure 151 – Reconstructed virtual in-plane section through bondcoat of the same Rolls-Royce Pt-Al cylindrical micro-specimen undergoing 20-hour cyclic oxidation at 1200°C, (a) as-received, (b) after 20 hours, (c) after 40 hours and (d) after 60 hours.

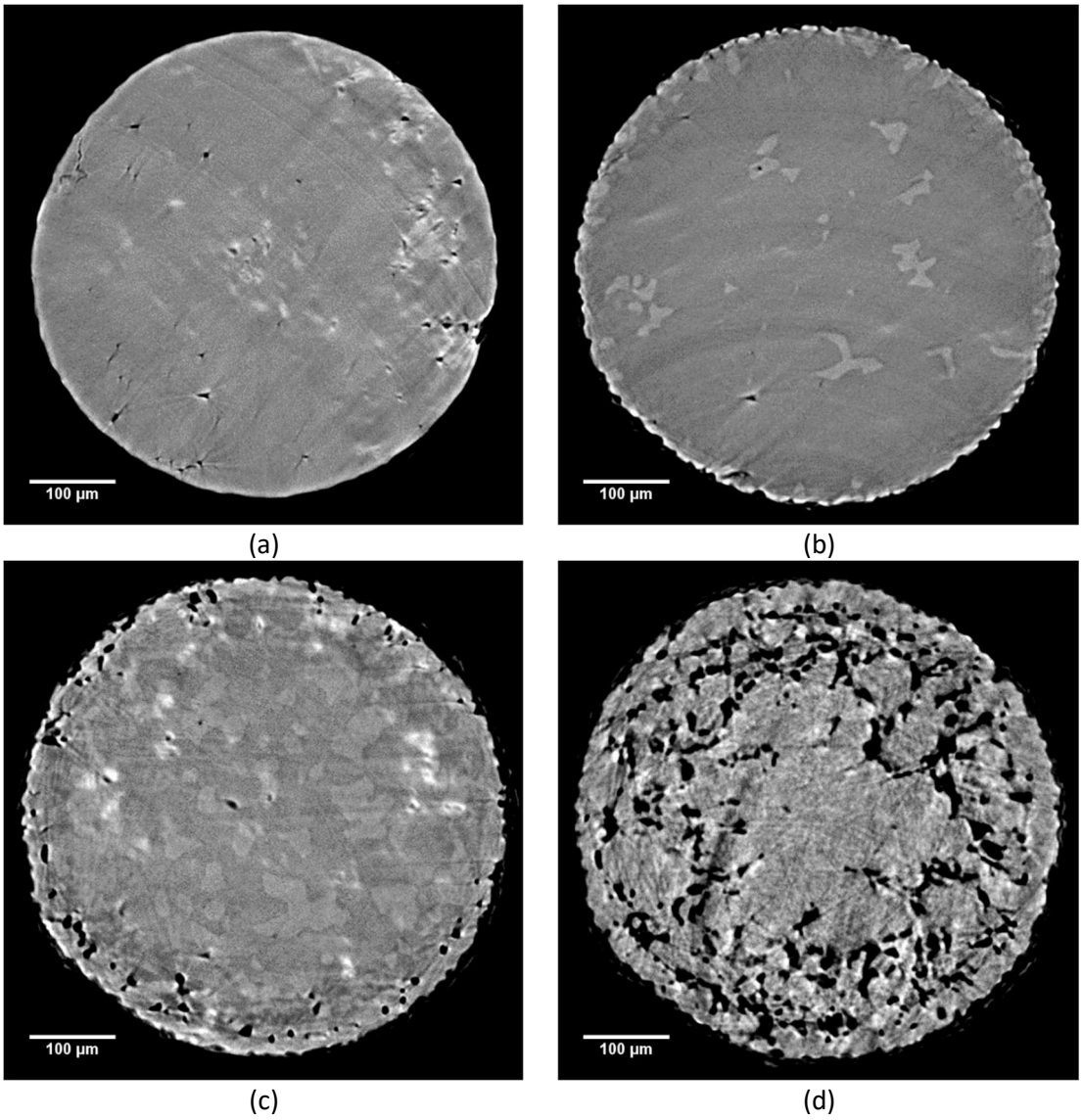

Figure 152 – Reconstructed virtual in-plane section through bondcoat of Alstom Pt-Al specimen undergoing 20-hour cyclic oxidation, (a) as-received, (b) after 20 hours, (c) after 40 hours and (d) after 60 hours.

5.2.1 Line profile analysis of virtual cross-sections

Virtual cross-sections were extracted from the reconstructions of Rolls-Royce Pt-aluminide (Figure 153), Alstom Pt-aluminide (Figure 154) and Rolls-Royce Pt specimens (Figure 155). From these virtual cross-sections, one-dimensional line profiles (Figure 156) were extracted at approximately the same location within the sample. The profiles were normalised relative to the absorption of background air. The first 120µm of each profile corresponds to the thickness of the topcoat and a clear downward trend in

greyscale intensity is noted. This decrease corresponds to an increase in inter-columnar separation and consequently a greater number of voxels (volumetric pixels) taking low 8-bit values (darker). At approximately 120µm to 130µm from the top surface, there is a sharp drop in pixel intensity corresponding to the TGO/bondcoat interface. With time, these troughs are seen to broaden and decrease in pixel intensity. These changes correspond to thickening of the TGO, noted as a well-defined interface between the topcoat and bondcoat in tomographs. To quantify the TGO thickness from these troughs, Gaussian curves were found to best fit the troughs representing the TGO and the full width at half maximum was used to estimate the TGO thickness, given by $2\sqrt{2\ln\sigma}$, where σ is the standard deviation in a Gaussian distribution (Figure 157, ordinate axis inverted). Peak widths indicate TGO thickness, subject to a greyscale cut-off threshold. At 0 hours, the TGO thickness is difficult to estimate owing to the minimum imaging resolution. Ten measurements were taken for each time step of the same specimen followed through time and the TGO thickness computed. Histograms of TGO thicknesses were computed and Wald (inverse Gaussian), normal and Weibull distributions were fitted (Figure 158), with the Wald distribution selected for having the lowest standard error. TGO thickness measurements indicate values of 2.03 µm, 3.43 µm, 3.64 µm and 4.20 µm at 0, 20, 40 and 60 hours respectively at 1200°C. This is contrasted with measurements from cylindrical micro-specimen (pin) and coupon micrographs (Figure 115 and Figure 116) of the same bondcoat (summarised in Table 11, see Figure 173 for plots with rate law).

Table 11 - Summary of TGO thicknesses measured using conventional cross-section and tomographic reconstructions for Rolls-Royce Pt-aluminide bondcoat TBC system.

Time (hours)	0	20	40	60	80
Pin TGO thickness (µm)	0.28	2.22	2.57	-	3.75
Coupon TGO thickness (µm)	0.26	2.25	3.19	3.35	
Tomograph TGO thickness (µm)	2.03	3.43	3.64	4.20	-

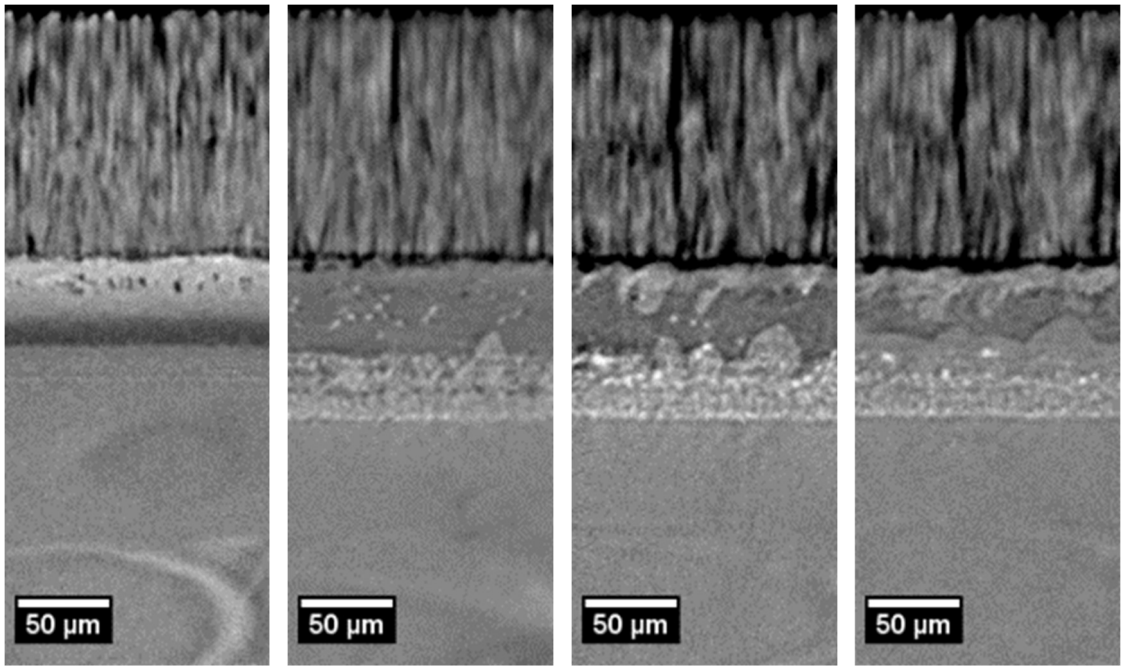

Figure 153 – Virtual cross-sections from the same location within the Rolls-Royce Pt-Al sample indicating the location of greyscale line profiles showing (a) the as-received state, (b) following one 20-hour exposure, (c) two 20-hour exposures and (d) three 20-hour exposures at 1200°C.

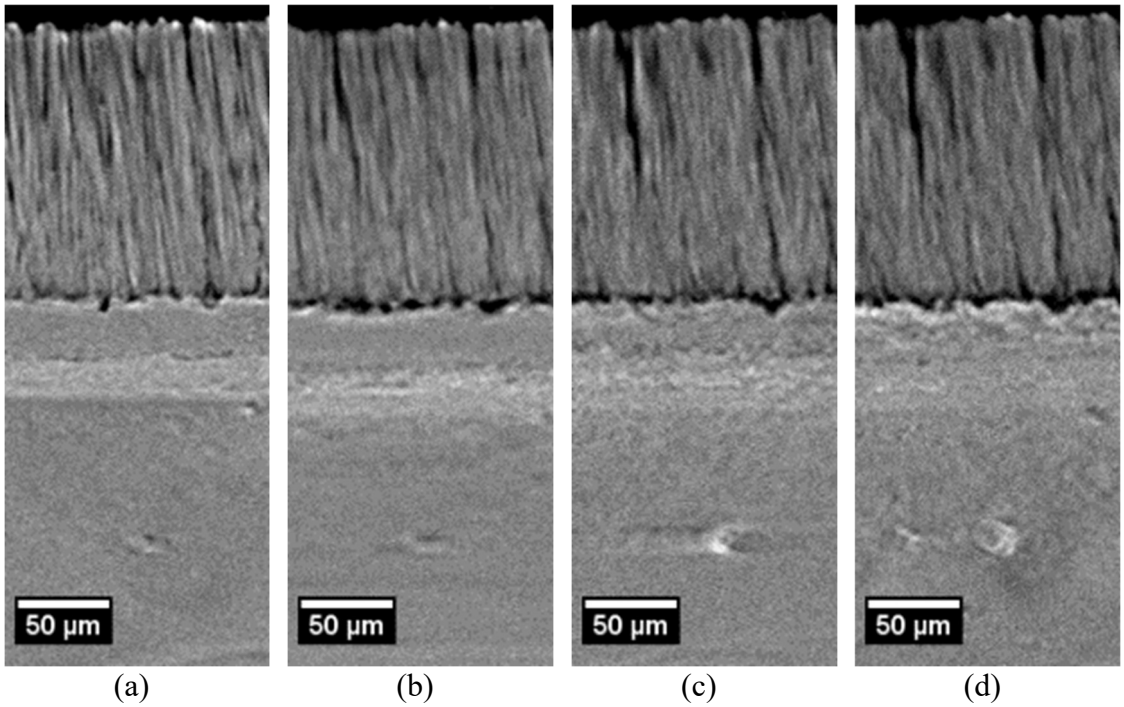

Figure 154 – Virtual cross-sections from the same location within the Alstom Pt-aluminide sample indicating the location of greyscale line profiles showing (a) the as-received state, (b) following one 20-hour exposure, (c) two 20-hour exposures and (d) three 20-hour exposures at 1200°C.

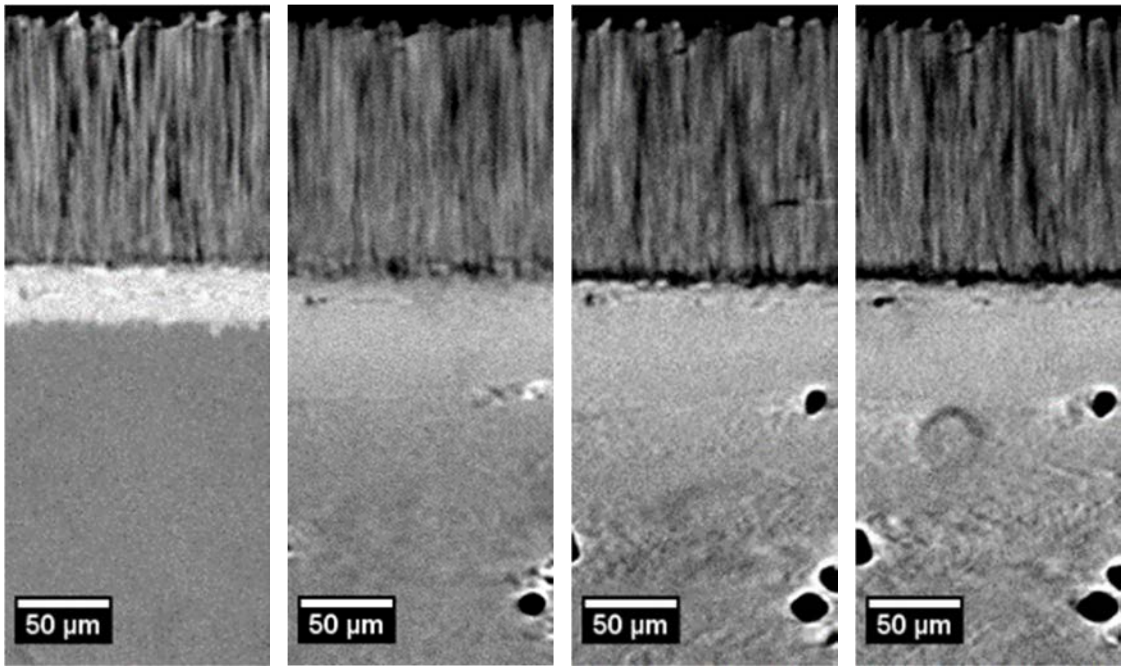

Figure 155 – Virtual cross-sections from the same location within the Rolls-Royce Pt sample indicating the location of greyscale line profiles showing (a) the as-received state, (b) following one 20-hour exposure, (c) two 20-hour exposures and (d) three 20-hour exposures at 1200°C.

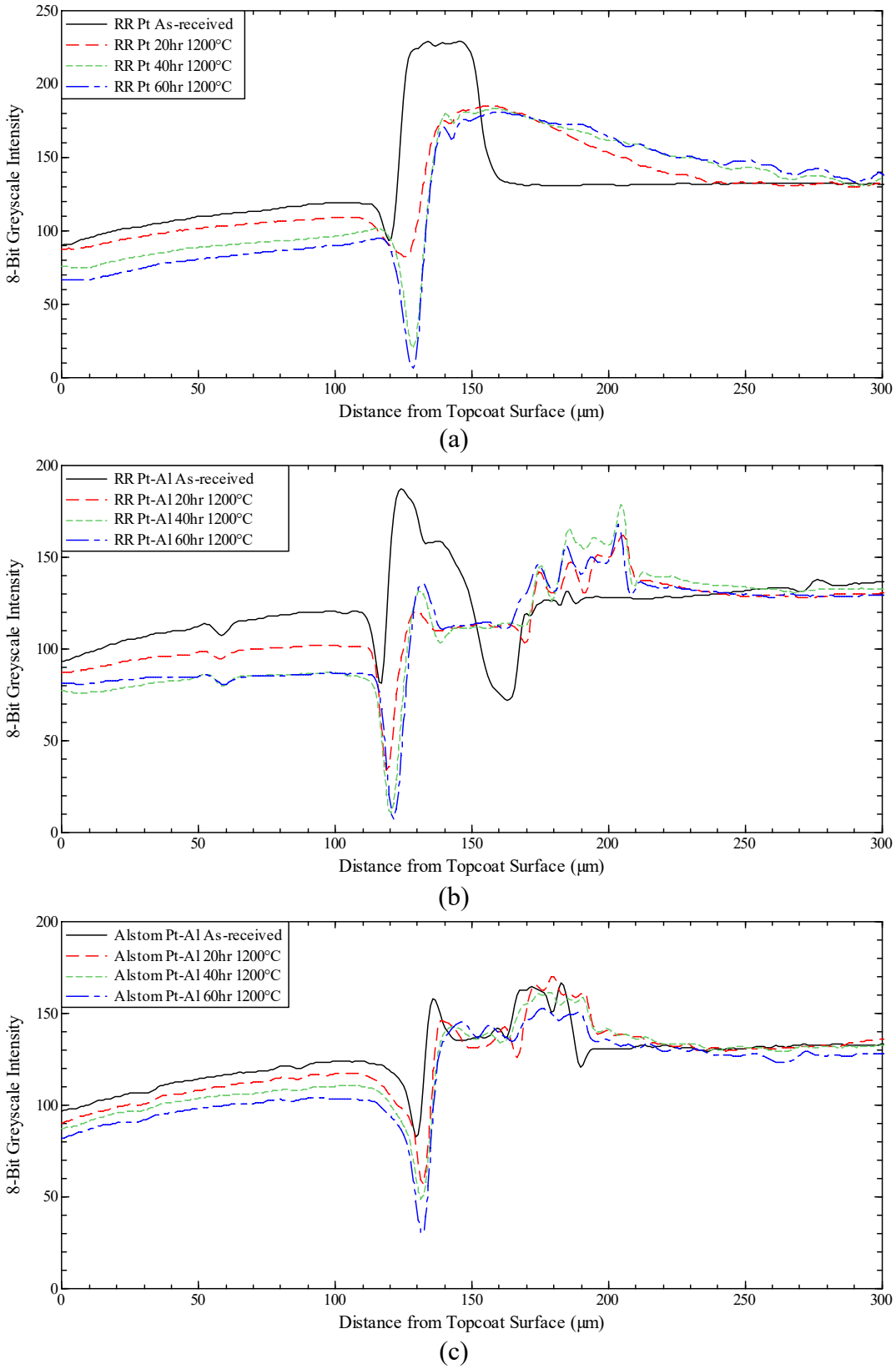

Figure 156 – Greyscale intensity line profiles extracted from virtual cross-sections for (a) Rolls-Royce Pt, (b) Rolls-Royce Pt-Al and (c) Alstom Pt-Al specimens as a function of time. Profiles normalised relative to the background intensity of air.

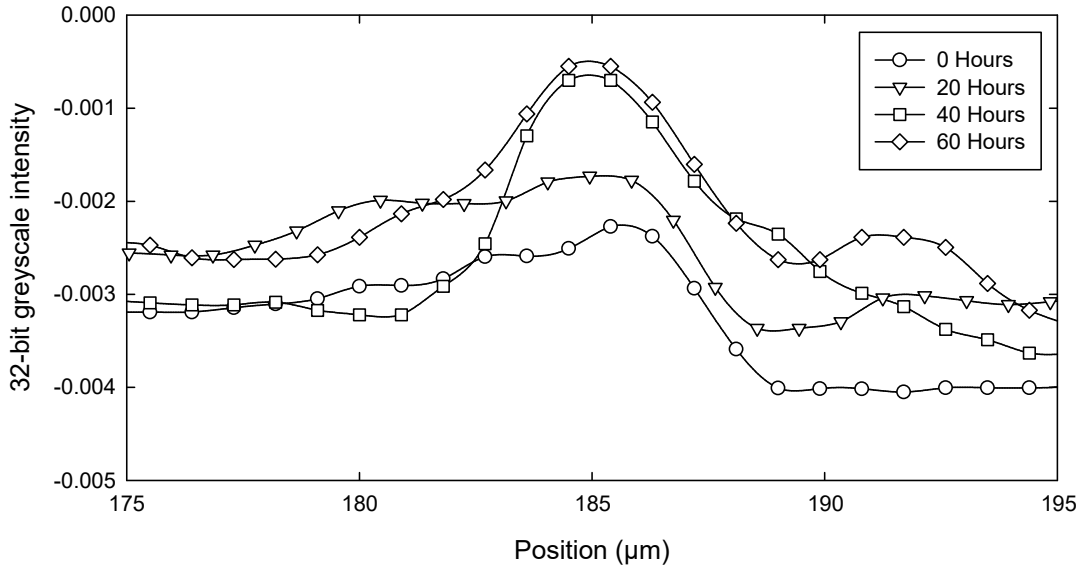

Figure 157 – TGO intensity profiles for the same location within the specimen as a function of time on inverted intensity axis for Rolls-Royce Pt-aluminide specimen. Peak widths indicate TGO thickness, subject to a greyscale cut-off threshold. At 0 hours, the TGO thickness is difficult to estimate owing to the minimum imaging resolution.

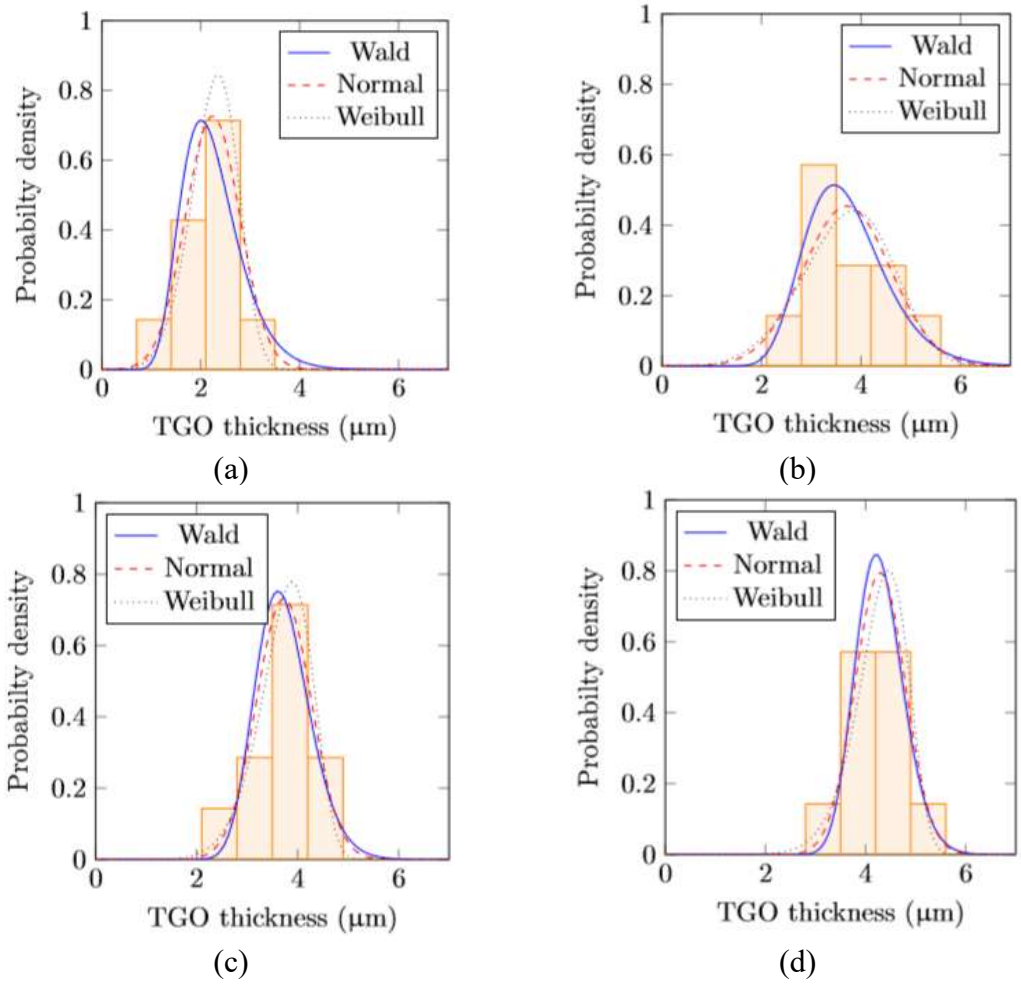

Figure 158- Probability density of TGO thickness measured using line-profiles from tomographs of the same Rolls-Royce Pt-aluminide cylindrical micro-specimens (a) as-machined 0 hours, (b) 20 hours, (c) 40 hours and (d) 60 hours at 1200 °C.

5.2.2 Time-dependent TGO/bondcoat interface evolution

A 100µm×100µm×60µm sub-volume encompassing the TGO and grit line was extracted from the same central portion of the reconstruction for each time step of the same sample. The TGO/bondcoat interface was extracted from within this sub-volume and the heights normalised relative to the mean interface position (Figure 159). These height contours indicate growth of a number of local undulations with an increase in number and area of features ±5µm above and below the mean height. From this 3-D height data, line profiles were extracted at the indicated vertical line on each map (between $X = 70\mu m$ and $X = 75\mu m$), corresponding to approximately the same location as a function of time. These

line profiles (Figure 160) show the evolution of the local undulations, for example between 15µm and 30µm there is an increase in the positive displacement with time while between 30µm and 45µm there is a decrease in negative displacement.

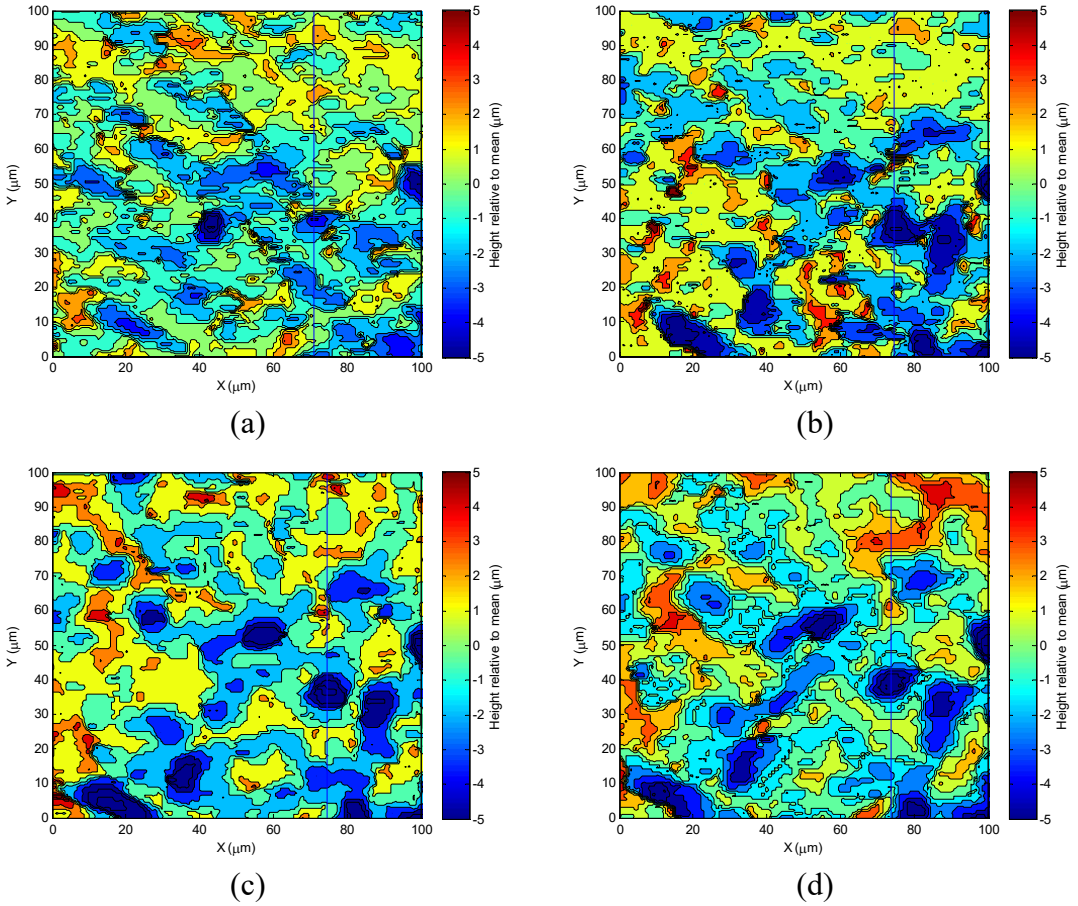

Figure 159 – Contour plots of TGO/bondcoat interface topography extracted from a central 100µm square section from synchrotron X-ray tomography reconstructions of a Rolls-Royce Pt-aluminide specimen showing (a) in the as-received state, (b) following 20 hours, (c) following 40 hours and (d) following 60 hours at 1200°C. All maps are of the same region within the same specimen at the different timesteps. The lines indicated between $X = 70\mu m$ and $X = 75\mu m$ are the position used for line-scans.

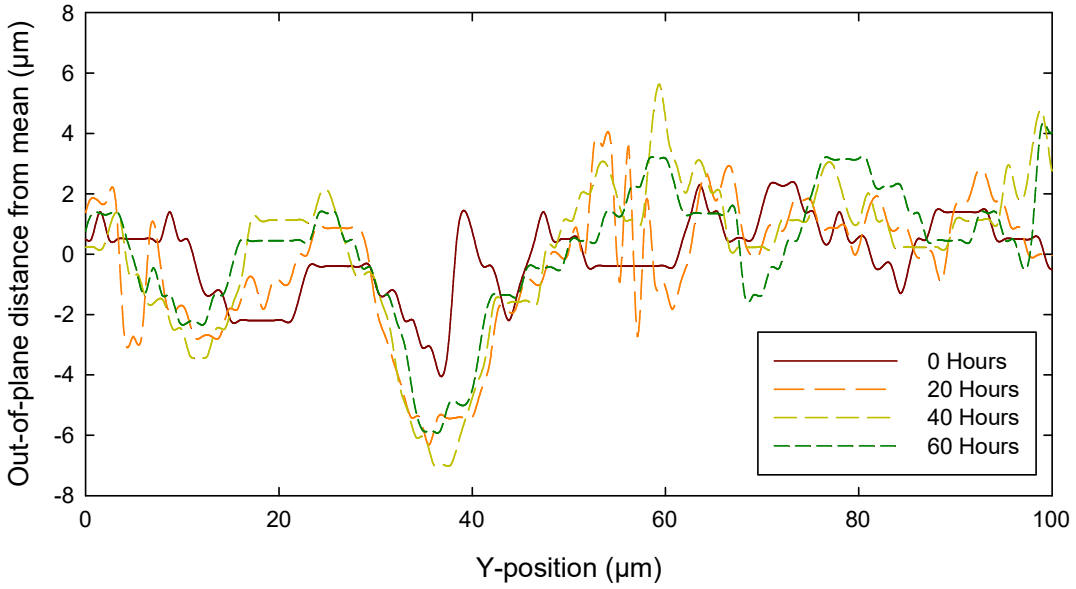

Figure 160 – TGO/Bondcoat line profiles extracted from synchrotron X-ray microtomography reconstructions at approximately the same location from the centre of the specimen.

5.2.3 Segmentation analysis

Segmentation analysis of reconstructions using Avizo fire was carried out on Rolls-Royce Pt (Figure 161), Rolls-Royce Pt-Al (Figure 162) and Alstom Pt-Al specimens (Figure 163). In general, features with well-defined boundaries, e.g. substrate and bondcoat pores lent themselves well to bulk segmentation (using the procedure outlined previously). The evolution of substrate porosity (green) is clearly observed in all three specimens as is radial substrate porosity (pores around the edge of the bondcoat, shown in blue) in the case of both Rolls-Royce and Alstom Pt-aluminide bondcoat specimens. Topcoat intercolumnar separation was segmented but owing to continuity between the background and the intercolumnar spaces combined with high-contrast streak artefacts, consistent observation of segmentation was not possible. This challenge was also present in segmentation of the TGO and bondcoat in which features contiguous with the TGO, such as corn-kernel defects were segmented as the TGO (yellow). Horizontal planes in the topcoat suggests that the topcoat may have been deposited in two layers. Segmentation

statistics of substrate porosity was carried out to reveal pore volume fraction. The lack of substrate porosity in the Rolls-Royce Pt-aluminide specimen compared to the other two variants prompted further investigation into the full scanned sample volume (Figure 164). Planar visualisation of the internal features of this sample as a function of time (Figure 165) indicate a similar porosity as the other two bondcoat types. A volume fraction analysis of the substrate porosity for this sample (Figure 166) reveals an increase from 0.20% to 0.31% to 0.32% following 20, 40 and 60 hours respectively. These values agree with 2-D area fraction calculations from micrographs (Figure 94), with values of 0.26%, 0.47% and 1.32% area fractions for 20, 40 and 80 hours.

Pore volume distribution (Figure 167) was best described by the Logistic distribution function. Pores were seen to increase in volume as a function of time from 296 μm^3 at 20 hours to 553 μm^3 at 40 hours and 634 μm^3 at 60 hours.

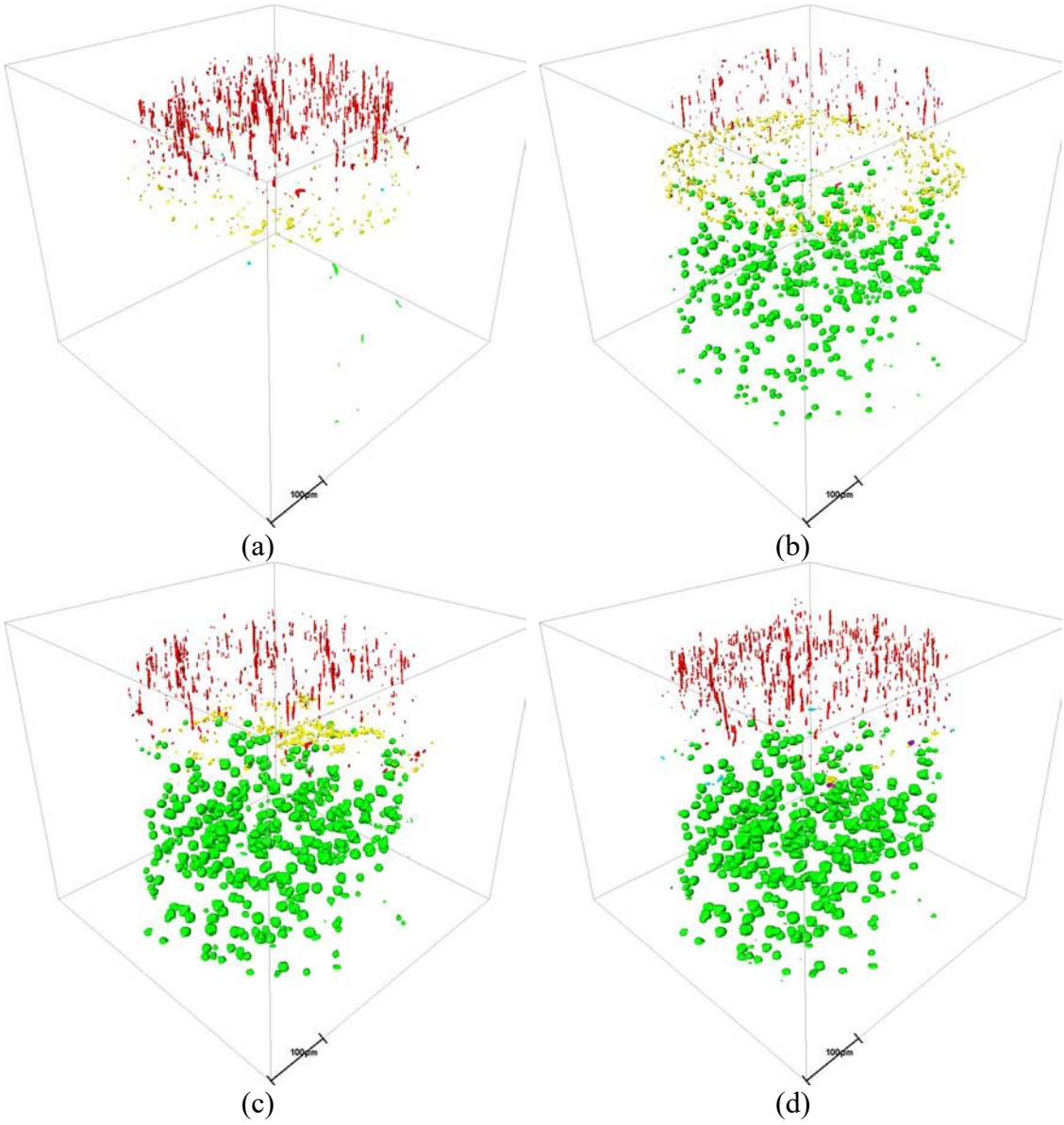

Figure 161 – Segmented visualisation of Rolls-Royce Pt cylindrical micro-specimen (a) as-received, (b) following 20 hours at 1200°C, (c) following 40 hours and (d) after 60 hours. Red pores are inter-columnar voids, yellow voids and pores adjacent to the TGO and green features are pores within the substrate.

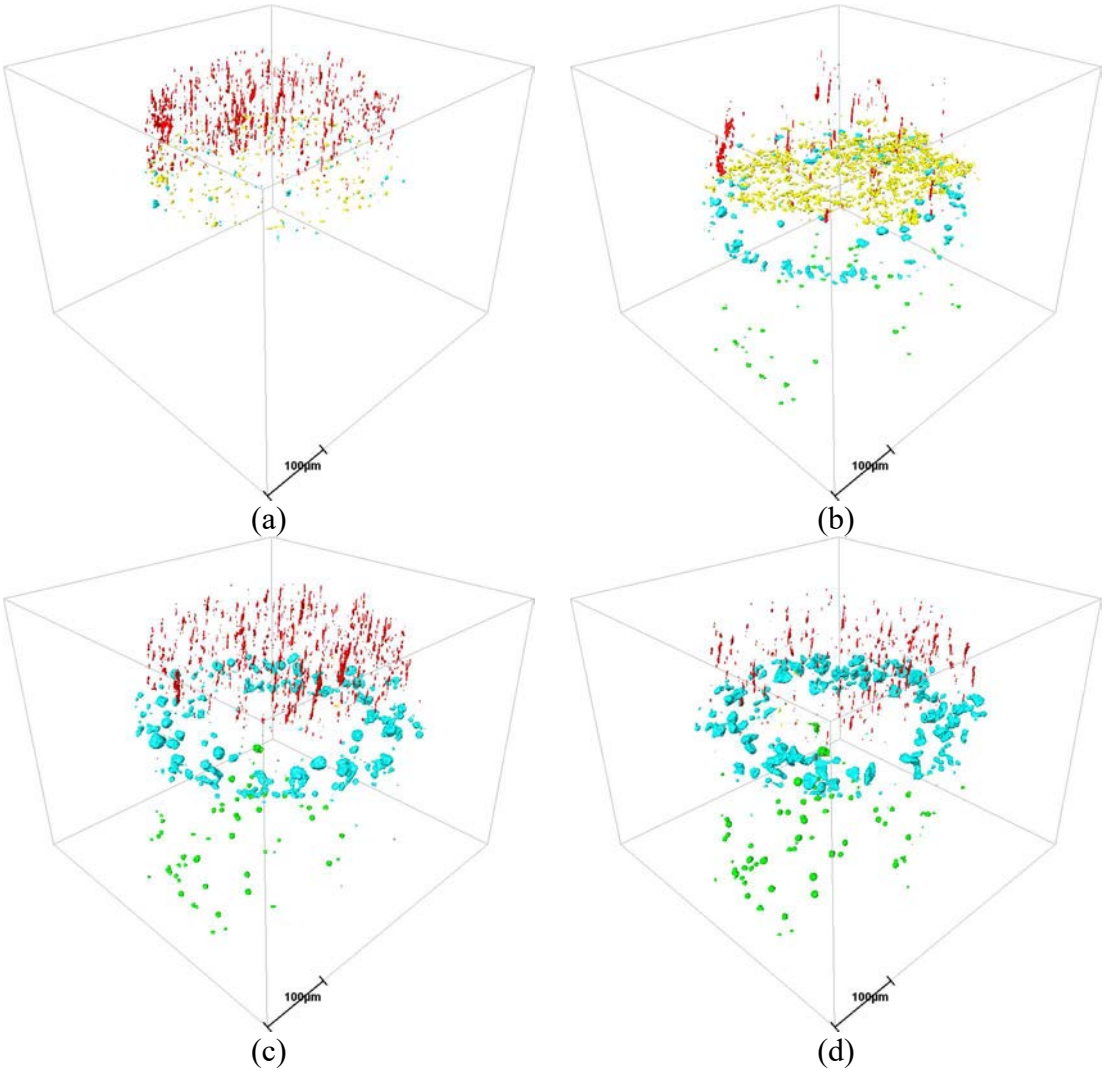

Figure 162 - Segmented visualisation of Rolls-Royce Pt-Al cylindrical micro-specimen (a) as-received, (b) following 20 hours at 1200C, (c) following 40 hours and (d) after 60 hours. Red pores are inter-columnar voids, yellow voids and pores adjacent to the TGO, green features are pores within the substrate and blue are pores within the bondcoat, typically at the bondcoat edge.

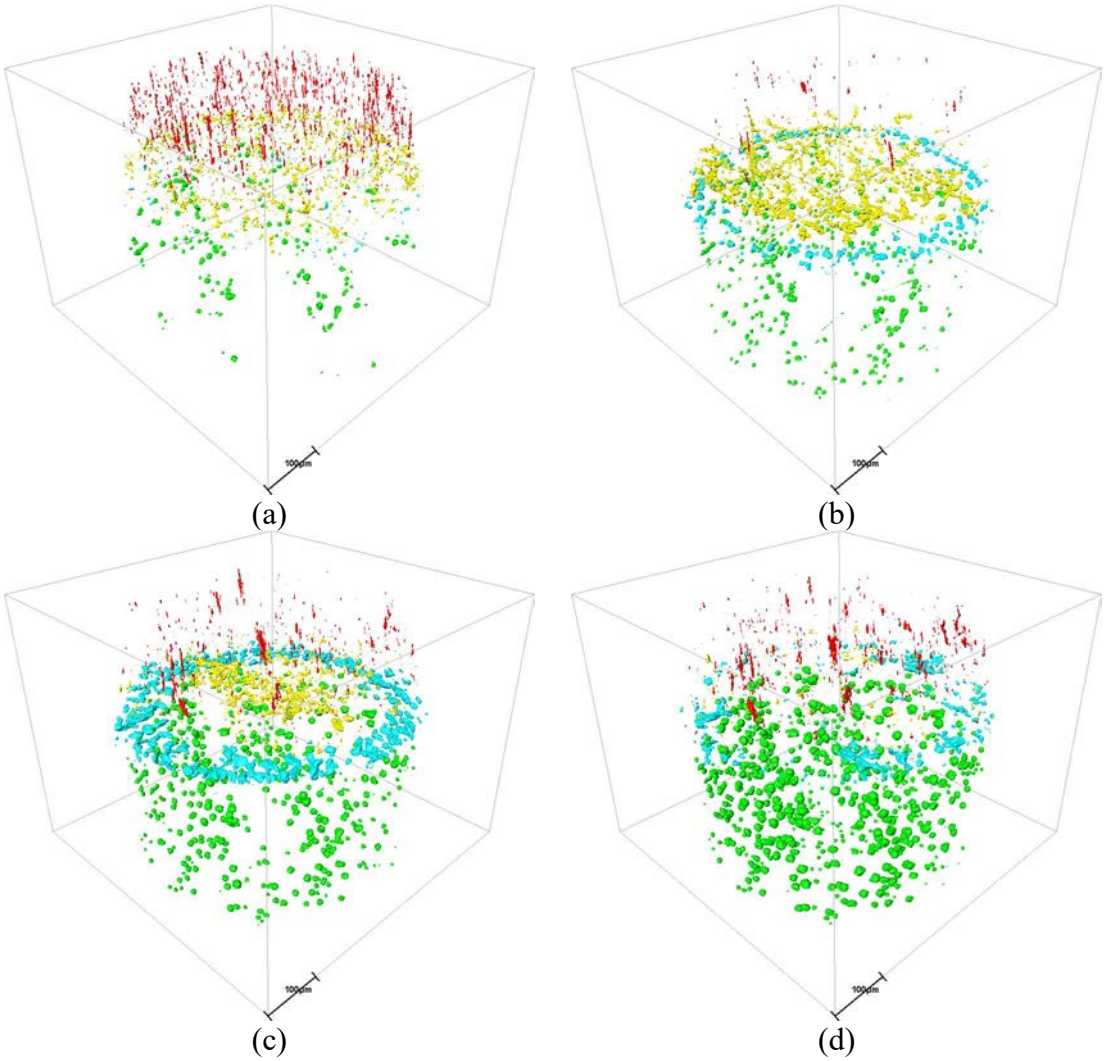

Figure 163 – Segmented visualisation of Alstom Pt-Al cylindrical micro-specimen (a) as-received, (b) following 20 hours at 1200C, (c) following 40 hours and (d) after 60 hours. Red pores are inter-columnar voids, yellow voids and pores adjacent to the TGO, green features are pores within the substrate and blue are pores within the bondcoat, typically at the bondcoat edge.

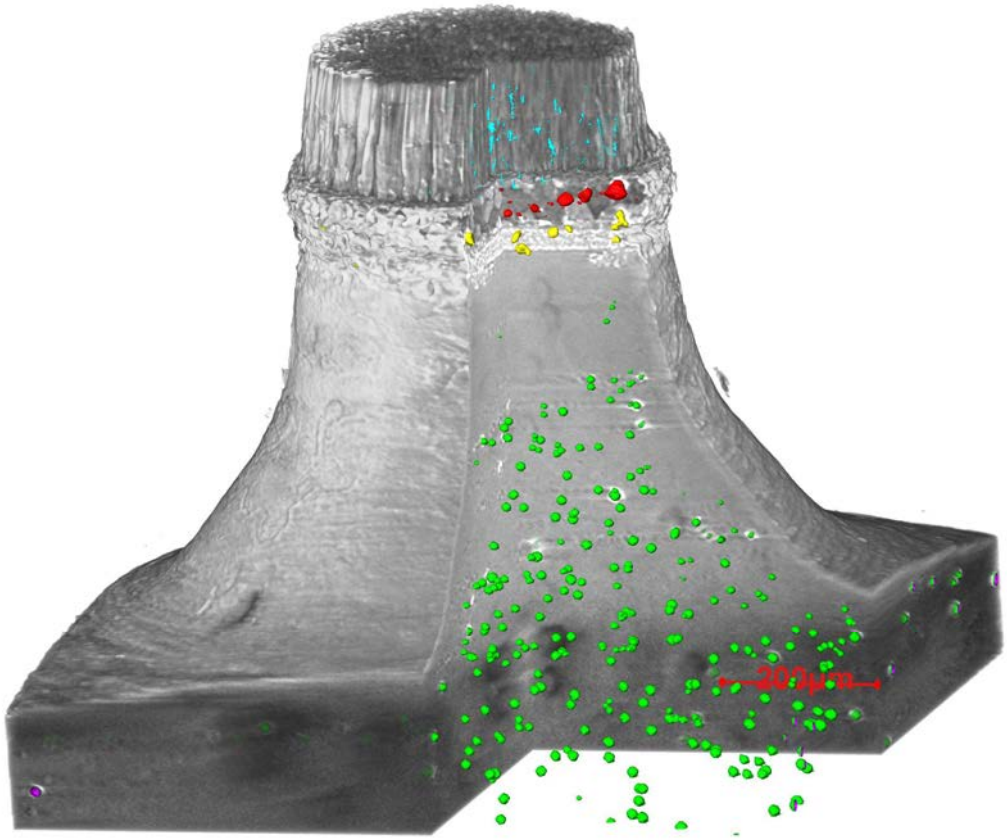

Figure 164 – Cut-away of sample reconstruction revealing segmented substrate porosity (green), bondcoat edge pores (red/yellow) and inter-columnar pores (aqua) for sample exposed for 40-hours (two 20-hour periods) at 1200°C. The horizontal plane in the topcoat suggests that the topcoat may have been deposited in two layers.

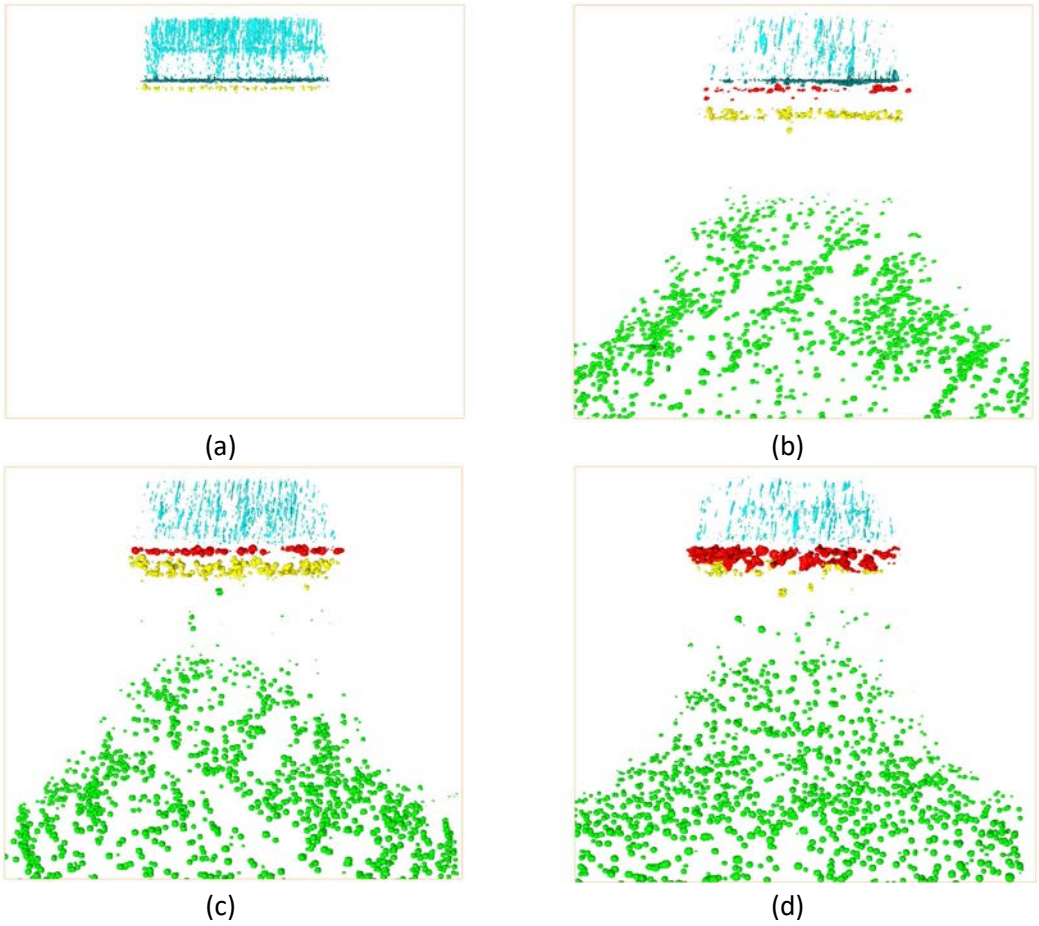

Figure 165 – Planar view of segmentation results showing substrate porosity (green), bondcoat edge pores (red/yellow) and inter-columnar pores (aqua). Note that features from the entire through thickness 3-D segmentation are displayed as a flat 2-D image, giving the impression of higher substrate porosity.

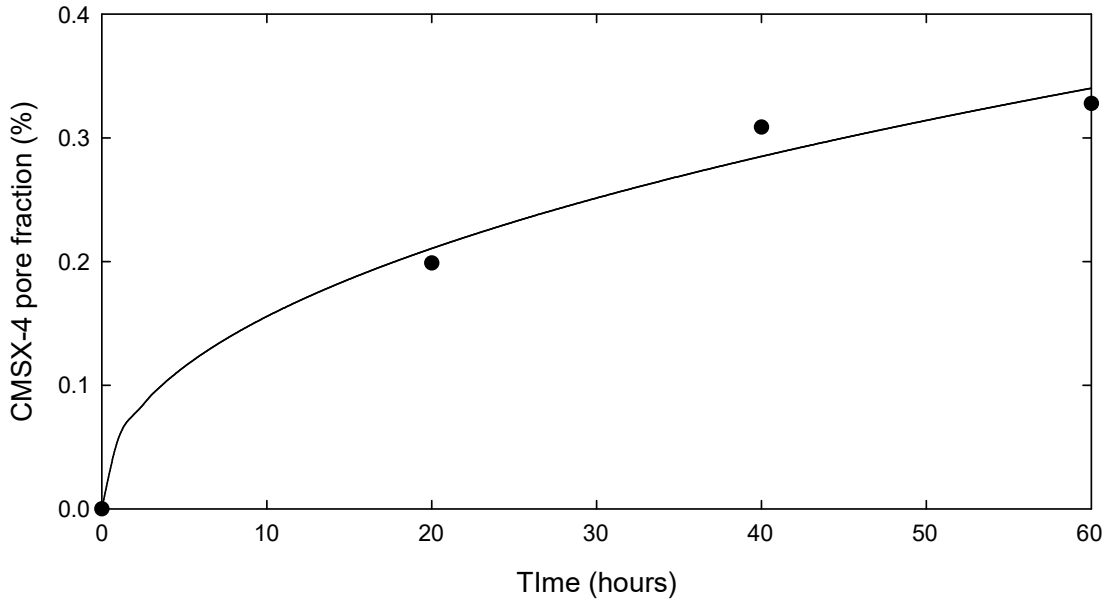

Figure 166 – CMSX-4 pore volume fraction as a function of time computed from temporal 3-D segmentation of synchrotron X-ray reconstructions of Rolls-Royce Pt-aluminide specimen. Fitted power law is of the form $y = ax^b$ *where multiplier* $a = 0.057$ *and exponent* $b = 0.436$*, indicating sub-parabolic kinetics.*

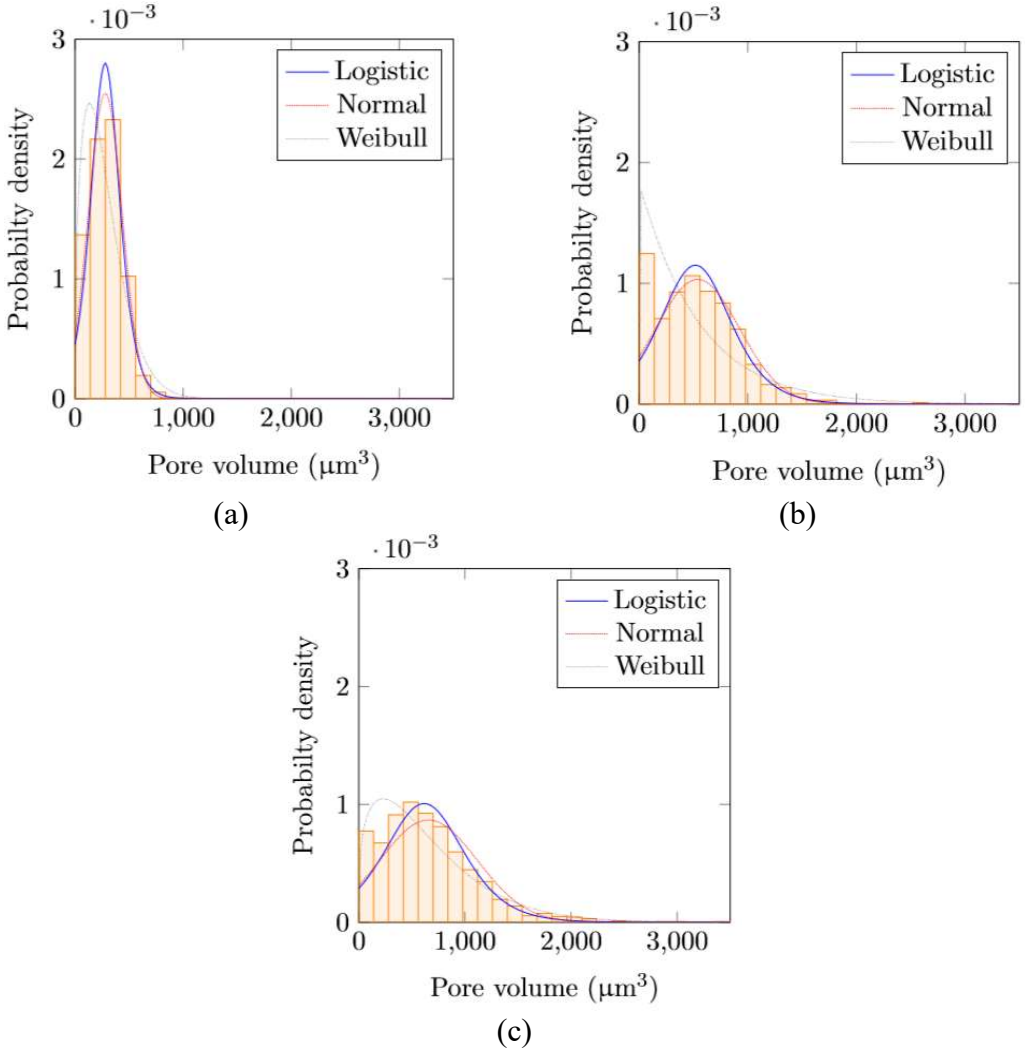

Figure 167 – Substrate CMSX-4 pore volume distributions for Rolls-Royce Pt-Al specimen undergoing 20-hour cycles at 1200°C (a) following 20 hours, (b) 40 hours and (c) 60 hours.

5.2.4 Topcoat inter-columnar separation

A 144µm square cross-section sub-volume was extracted from the centre of the Alstom Pt-aluminide specimen to investigate the development of intercolumnar separation in the topcoat (Figure 168). The inverse surface of the topcoat columnar tips was extracted (green continuous surface) and visualised alongside internal features including the TGO (plus contiguous features - yellow), grit-line (blue) and substrate pores (red). The development of well-defined crack-like intercolumnar separations is noted in the 40-hour

(Figure 168c) and 60-hour (Figure 168d) cases that extend 75µm into the topcoat from the surface.

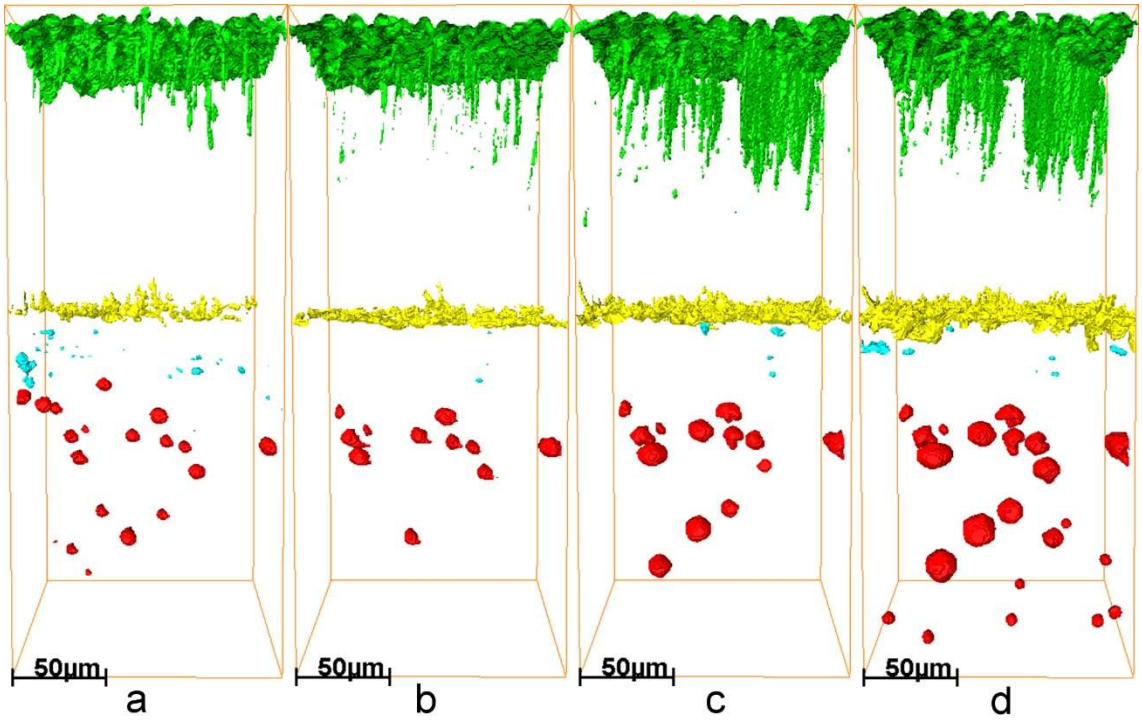

Figure 168 – Alstom Pt-aluminide specimen segmentation of 144µm square cross-section sub-volume showing the evolution of topcoat cracks (green) obtained by combining the topcoat surface with internally segmented features, TGO (yellow), trapped grit-blasting alumina in the bondcoat (blue) and substrate pores (red). Substrate pores are seen to increase in number and size, topcoat cracks to grow in depth and width and the TGO observed to thicken. TGO features are a combination of actual TGO voxels and corn-kernel defects due to likeness in attenuation.

5.2.5 Topcoat influence under 8.5-hour exposure

A set of Rolls-Royce Pt (Figure 169, Figure 170) and Pt-aluminide (Figure 171, Figure 172) samples both with and without topcoats were examined under short-term exposure periods (8.5 hours at 1200°C) using synchrotron X-ray micro-tomography. Substrate porosity was observed for Rolls-Royce Pt specimens (both with and without topcoats) following 8.5 hours but no visible substrate porosity was noted in any of the Pt-aluminide specimens following exposure. This is likely because of the lack of additional aluminium in the Pt-only bondcoat that must rely on substrate aluminium levels. The free bondcoat top surface of the Rolls-Royce Pt sample without a topcoat (Figure 170a, Figure 170b) shows little change following an 8.5-hour exposure while the equivalent Pt-aluminide

sample shows an apparent outward expansion of the bondcoat in all directions away from the substrate. The Rolls-Royce Pt sample with a topcoat displays a lateral displacement at the TGO/bondcoat interface of 5µm to 10µm.

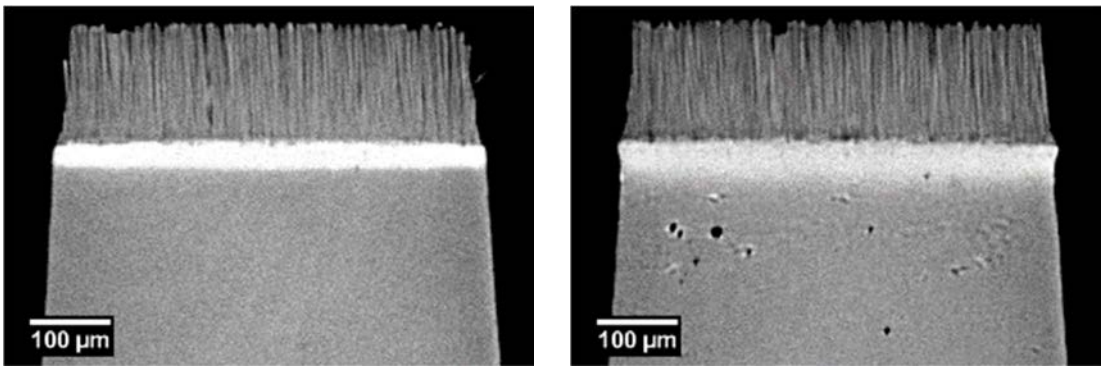

(a) (b)

Figure 169 – Reconstructed virtual cross-sections through Rolls-Royce Pt specimen in (a) as-received condition and (b) following 8.5 hours at 1200°C. Interdiffusion of platinum into the substrate reduces platinum content in the bondcoat, leading to a decrease in X-ray attenuation and an apparently thicker bondcoat. Note creep of bondcoat near TGO at sample edges.

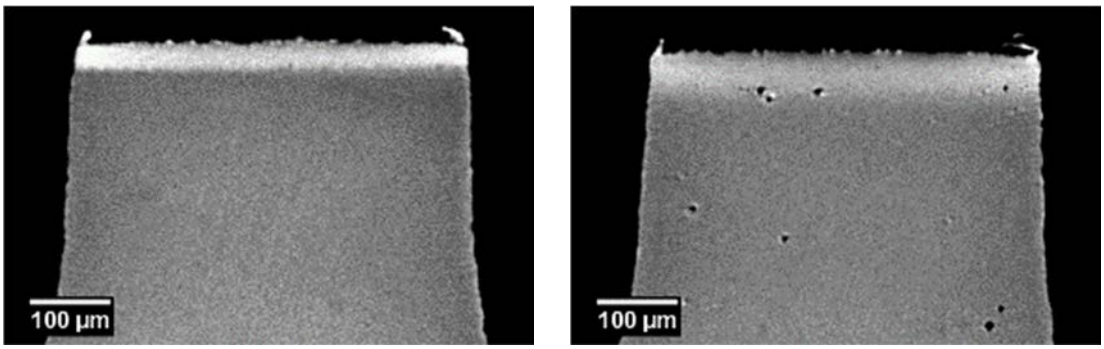

(a) (b)

Figure 170 – Reconstructed virtual cross-sections through Rolls-Royce Pt specimen without a topcoat in (a) as-received condition and (b) following 8.5 hours at 1200°C.

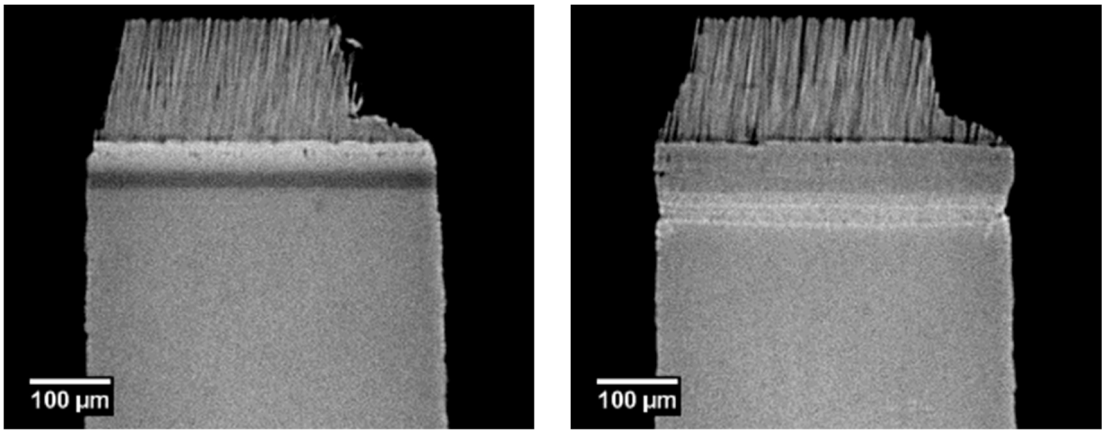

Figure 171 – Reconstructed virtual cross-sections through Rolls-Royce Pt-aluminide specimen in (a) as-received condition and (b) following 8.5 hours at 1200°C. Horizontal bands in topcoat are likely because of topcoat deposition in two stages. Note secondary reaction zone visible in the 8.5 hour exposed reconstruction.

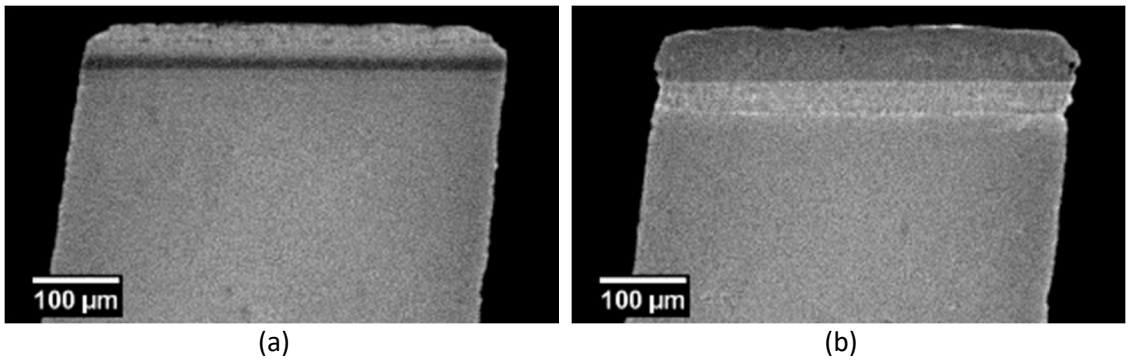

Figure 172 – Reconstructed virtual cross-sections through Rolls-Royce Pt-aluminide specimen without a topcoat in (a) as-received condition and (b) following 8.5 hours at 1200°C.

5.3 Discussion

The key benefit of synchrotron X-ray tomography applied to TBCs is in the inherent non-destructive nature of the technique. This permits examination of the same sample through time and in the experimental schema adopted herein, allowed samples to be monitored from the as-received state. Furthermore, and combined with the sample geometry used, the entire sample volume was imaged. This allowed arbitrary planar slices to be extracted and although orthogonal planes were chosen in the virtual slices displayed herein, any orientation in 3-D space was permissible. The main advantage of this technique over destructive cross-sectioning is therefore preservation of the sample (neglecting X-ray interaction with samples). The two main shortcoming of synchrotron X-ray

microtomography when compared to destructive electron microscopy are firstly the limited resolution and secondly the difficulty in distinguishing between alumina and defects when scanning in air. The resolution limitation becomes apparent when conventional micrographs are compared with tomographs. The configured X-ray optics used at Diamond allowed a maximum resolution of 0.9μm per voxel (also per 2-D pixel). At a modest electron microscope magnification of 20,000× and a working distance of 10mm, the calculated resolution is 0.005μm per pixel. This sizeable difference in resolution meant that features such as micro-cracking within the TGO and grit-line particles that were readily quantifiable from micrographs could not be reliably analysed from tomographs. However, and for features on the order of tens of micrometres, synchrotron tomography provides spatial and temporal visualisation of phase transformation of the bondcoat, depth measurement of intercolumnar separation and substrate porosity evolution that is impractical to obtain using conventional destructive sectioning.

TGO thickness measurements from tomographs (Figure 158, Wald distribution) were found to be 2.03 μm, 3.43 μm, 3.64 μm and 4.20 μm at 0, 20, 40 and 60 hours respectively at 1200°C. This is in contrast to TGO thicknesses measured from micrographs (Figure 116) of 0.27 μm, 2.24 μm, 2.88 μm and 3.35 μm at 0, 20 40 and 60 hours at 1200°C (see Figure 173 for a comparison). It is evident that at 0 hours, the tomograph-measured TGO thickness is an order of magnitude larger than expected. This, of course, is primarily a consequence of the limited 0.9μm resolution meaning that the smallest detectable feature (1 pixel in size) cannot fall below this value. It is thus reasonable to expect the TGO thickness from tomographs at zero hours to be 0.9μm and not over double this value. The reason for this artificially thicker TGO at 0 hours is likely to be inclusion of features

contiguous with the TGO, corn-kernel defects, for example, that are indistinguishable from the TGO owing to the similarity in mass attenuation. This is also the likely cause of a consistently thicker TGO at subsequent time steps.

A power law fit to TGO thicknesses measured from tomographs reveals good agreement of the time exponent (0.3847 compared to 0.3657 from micrographs), suggesting that the sub-parabolic kinetics is captured well.

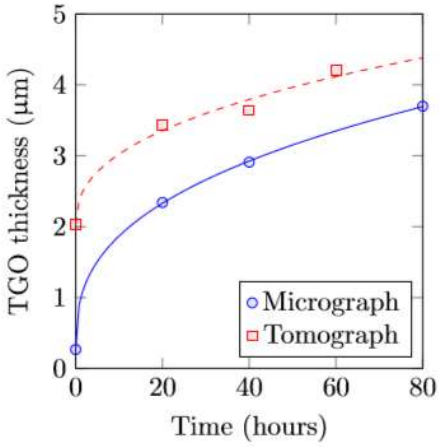

Figure 173 - TGO thickness measurements of Rolls-Royce Pt-aluminide cylindrical micro-specimen via destructive cross-sectioning and synchrotron X-ray microtomography. TGO thickness measurements at each timestep is the Wald (inverse Gaussian) fit peak, with a two-term power law of the form $\xi = at^b + c$ fitted to each data set. Time exponent from micrographs is 0.3657 while time exponent from tomographs is 0.3847, both suggesting sub-parabolic kinetics.

5.4 Conclusions

A novel approach to the tomographic studies of TBC systems has been presented through time-dependent imaging from the as-received condition of Rolls-Royce Pt, Pt-aluminide and Alstom Pt-Al bondcoat cylindrical micro-specimens. The technique allows evolution of the same region to be sampled as a function of time and has afforded quantification of TGO thickening (above 2.5 µm thickness), visualisation of bondcoat phase transformation, the evolution of substrate porosity and the depth of inter-columnar separation. The similarity of alumina and air however, meant distinguishing between air and alumina was challenging. This is reflected in the difference in TGO thickness with

measurements from micrographs at 0 hours appearing almost three times larger. The presence of reconstruction artefacts and distributed noise also presented challenges to segmenting of bondcoat phases.

5.5 Further work

To ascertain the quality of the TGO/bondcoat interface extracted from the tomography data, it will be of great benefit to serial FIB the samples that were scanned at Diamond. A suggested approach is to mount and polish away the topcoat and then serial FIB image a portion of the TGO/bondcoat that corresponds to the 100µm×100µm section extracted from the tomography data (Figure 159).

To overcome the challenge faced in observing the TGO owing to the similarity in mass attenuation of alumina (0.276 cm^2/g) to that of air (0.201 cm^2/g) when compared to say the topcoat (3.960 cm^2/g), it may be of interest to conduct scans in an alternative medium. This may be achieved by evacuating and filling a sealed sample holder with a different gaseous medium, for example Xenon [201].

A future application of this technique may be in quantifying CMAS infiltration. This will allow visualisation of CMAS penetration owing to the difference in absorption between CMAS and a YPSZ topcoat. Using a model composition of 33CaO-9MgO-13$AlO_{1.5}$-45SiO2 (mol%) [202] (equating to 27CaO-19.4MgO-24.6Al_2O_3-29SiO_2 wt%), the attenuation at 50 keV is 4.33 cm^2/g (contrasted to 4.62 cm^2/g for 7-YPSZ) computed using WinXCom [118].

Chapter 6 Digital volume correlation in 3-D strain mapping of TBC oxidation

6.1 Introduction

Digital Image and Digital Volume Correlation (DIC and DVC, respectively) are 2-D and 3-D image analysis techniques that map relative displacements across a time-dependent sequence of images. DIC and DVC divide each data set (images) into smaller subsets, commonly known as interrogation windows. By maximising the correlation coefficient for each interrogation window between successive images, the relative displacement and deformation of each interrogation window is calculated. The computed displacement field can be used to derive total strain fields, from which the position of strain-influencing features such as cracks [146], for instance, may be inferred. It is noteworthy that the inputs are digital images and the technique is consequently independent of the image acquisition technique and hence length scale [203]. Additionally, displacements can be computed beyond the resolution of the imaging technique (i.e., sub-pixel and sub-voxel, respectively) [177]. DIC techniques have previously been used to characterise the mechanical properties of TBCs [151–153] but were limited to 2-D surface imaging and lacked the capability of probing internal volumes.

In the present work, DVC was coupled with high resolution synchrotron X-ray absorption computed micro-tomography (the results of Chapter 5) to study, in a near in-situ fashion, the progressive development of the oxidation induced displacement field within TBC systems undergoing cyclic oxidation.

6.2 Computation of displacement fields

DVC, implemented using the LaVision DaVis Strain Master 8.2.2 software was applied to cropped regions of the X-ray tomographs. The first time step compared the as-received sample to the 20-hour oxidation exposure. The second timestep compared the 20 hours exposure to the 40 hours exposure, and the third time-step compared the 60-hour exposure to the 80-hour exposure (Fig. 1d). The DVC interrogation subsets were iteratively reduced from 128×128×128 voxels to 16×16×16 voxels over 3 iterations with a 50% subset overlap at each stage. Displacement vectors having correlation coefficients less than 50% were excluded. Rigid body translation and fine rotations of the output vector field that arose during sample exchange were corrected using an efficient algorithm [177] (Appendix G), which was also used to obtain the displacement field in a coordinate system that was precisely aligned with the topcoat and TGO interface.

6.3 Displacement visualisation

A set of Matlab scripts (Appendix G, H, I) were written to combine tomography data sets with a computed DVC vector field (Figure 174). Such a script was necessary to determine the location of the TGO within the resulting DVC vector fields in addition to the fact that the DVC data sets were scaled down by approximately a factor of eight. Regions that did not correlate, where the correlation coefficient fell below 0.5, do not display displacement data.

The script also allowed extraction of orthogonal slices from the displacement data. In and around the TGO, an X-Y plane could also be radially analysed with in-plane and out-of-plane displacements extracted. For in-plane displacements, the local Cartesian coordinate system of each vector was transformed into cylindrical coordinates and

determined whether the displacement was negative (inward) or positive (outward). The average strain was computed by fitting a first order polynomial to the displacement set**.**

In general, the initial timesteps of Pt-aluminide specimens (both Rolls-Royce and Alstom), did not show suitable correlation throughout the specimen owing to large deformations and a rapidly evolving microstructure as a function of time. Rolls-Royce Pt specimens showed the highest correlation across all time steps and allowed the distribution of lateral displacement within the specimen to be quantified.

DVC was also applied to tomographs of samples without topcoats but results correlated poorly throughout the substrate and bondcoat.

6.4 Results

Representative planar slices through the obtained displacement fields were extracted from the vicinity of the topcoat and the TGO (Figure 175). The U (in-plane) and W (out-of-plane) components of displacements are shown on X−Z plots, V (in-plane) and W components on Y−Z plots and U, V components shown for X−Y plots. The X−Y plane indicated for The X−Y plane was chosen to coincide with the plane of the TGO. The maps show displacement vectors (indicated by arrows) overlaid on a contour map of displacement magnitude in the plane of the TGO (Figure 175a) and out of plane of the TGO (Figure 175b). White patches on the map indicate regions that did not meet the minimum 50% correlation coefficient criterion. A likely cause of poor correlation within the lower portions of the topcoat is the fine nature and possible sintering of the inter-columnar features, which presents an inherent difficulty in their observations via X-ray attenuation tomography at the current resolution; limited features are thus available for image correlation to operate on. In contrast, the columns, are larger and well-defined in

the upper regions of the topcoat, and hence continuous displacement contours are observed. The majority of the substrate exhibited poor correlation, due to the lack of traceable features in its structure. The in-plane map (Figure 175a) reveals a horizontal gradient in the lateral displacement from the edges of the specimen to the plane centre. There is also a vertical gradient near the sample edges indicating greater lateral displacement within the topcoat competition zone as opposed to the near-surface region. The out of plane map (Figure 175b) suggests a near-uniform upward displacement of the topcoat bulk which, when considered at the horizontal plane of Z=25μm would suggest, is driven by TGO growth. The outer edges of the near-surface region within the topcoat appear to undergo greater out-of-plane displacements that the central near-surface region. To quantify the variation in displacement in and around the TGO, displacement profiles were extracted from the X-Y plane of the TGO region (dashed lines in Figure 175). Although the base of the topcoat did not correlate satisfactorily in all areas, a planar section of the DVC displacement field (7.2 μm thick), encompassing the TGO, provided sufficient displacement vectors to extract in-plane and out-of-plane displacement values (Figure 176). Approximately 55% of the vectors in this section had correlation coefficients below 50% and were not included. The average displacement as a function of the radial position about the specimen cylindrical axis midpoint in the plane of the TGO was extracted and is presented in Figure 177.

The in-plane displacements at the TGO (Figure 177a) show the greatest total outward deformation over the first time step, increasing to the extremities of the specimen with an approximately constant dimensional change rate or strain of 3.3%. An additional outward displacement of up to 2-5 μm (average strain of 0.6%) is observed over the next thermal cycle, mostly near the surface with the third time step causing negligible further

displacements. Sharp changes in contrast, notably at specimen edges can lead to some numerical errors in DVC computations at these locations; this may be seen for example, in the negative in-plane displacements (Figure 177a) at the specimen extremities of the final cycle (40 to 60 hours).

The out of plane displacements along the TGO (Figure 177b) indicate an upward displacement of 1 to 2 μm following the first exposure period which is in accordance with metallographic observations of TGO growth. The displacement gradient following the first exposure period was estimated as 0.7% suggesting that the oxide growth is not uniformly normal and the bondcoat oxidation rate is higher at the exposed surface. As with the in-plane data, the final time step (40 to 60 hours) produced a negligible out-of-plane displacement due to the decrease in oxide growth rate in accordance with expected kinetics; the out of plane displacements for the second time step are not shown in Figure 177b due to a lack of sufficient correlation of microstructural features adjacent to the TGO within the competition zone of the topcoat. Destructive cross-sections show an increase in inter-columnar separations at the base of the topcoat due to bond-coat creep, and thickening of the TGO, which together may be the cause of the measured displacements. This change in the structure may also contribute to the lack of DVC correlation between the 40 hour and 60 hour exposures.

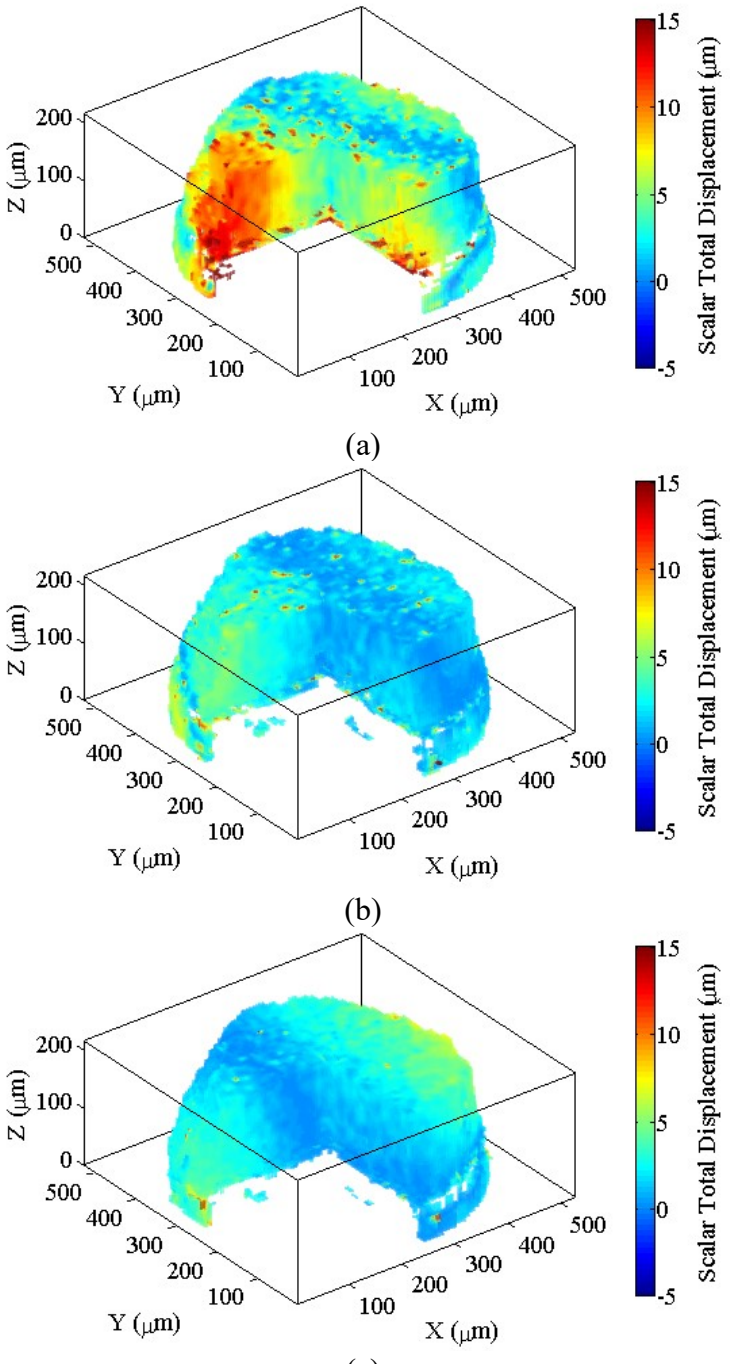

Figure 174 – 3-D visualisation of Rolls-Royce Pt specimen showing corner cut-away of scalar total DVC displacement field of Rolls-Royce Pt-only bondcoat specimens for (a) as-received to 20-hour computation, overlaid onto as-received (b) 20-hour to 40-hour computation overlaid onto 20-hours and (c) 40-hour to 60-hour computation overlaid onto 40-hour reconstruction.

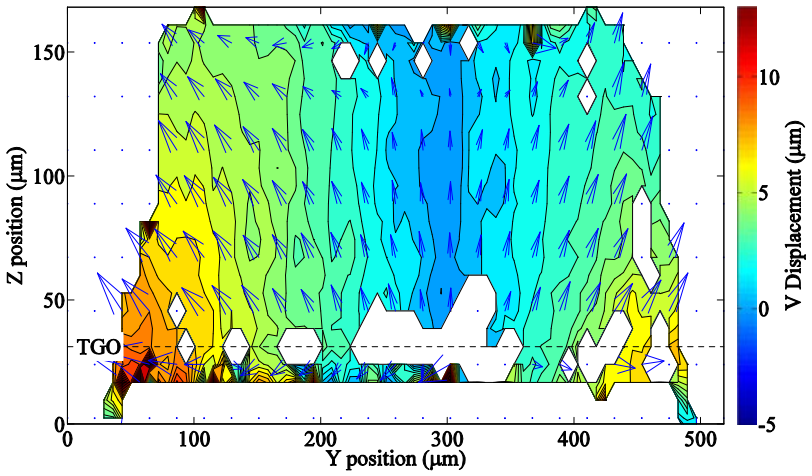

(a)

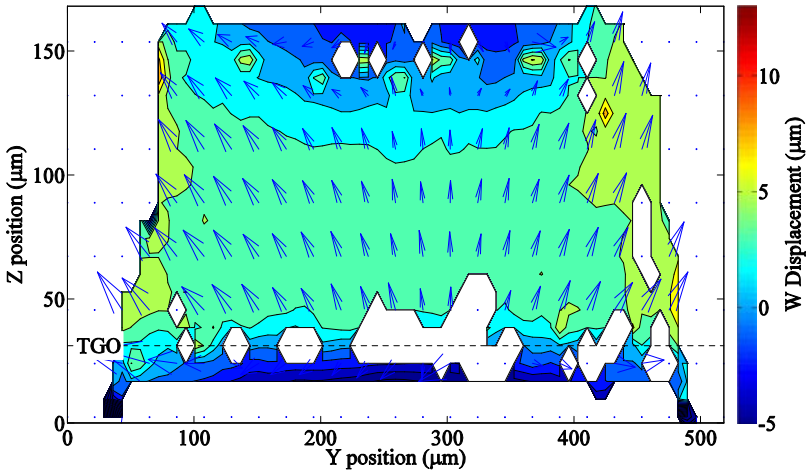

(b)

Figure 175 – Cross section digital volume correlation map of Rolls-Royce Pt cylindrical micro-specimen showing vector arrow field of displacement and (a) in-plane V-component of displacement and (b) out-of-plane W-components of displacement.

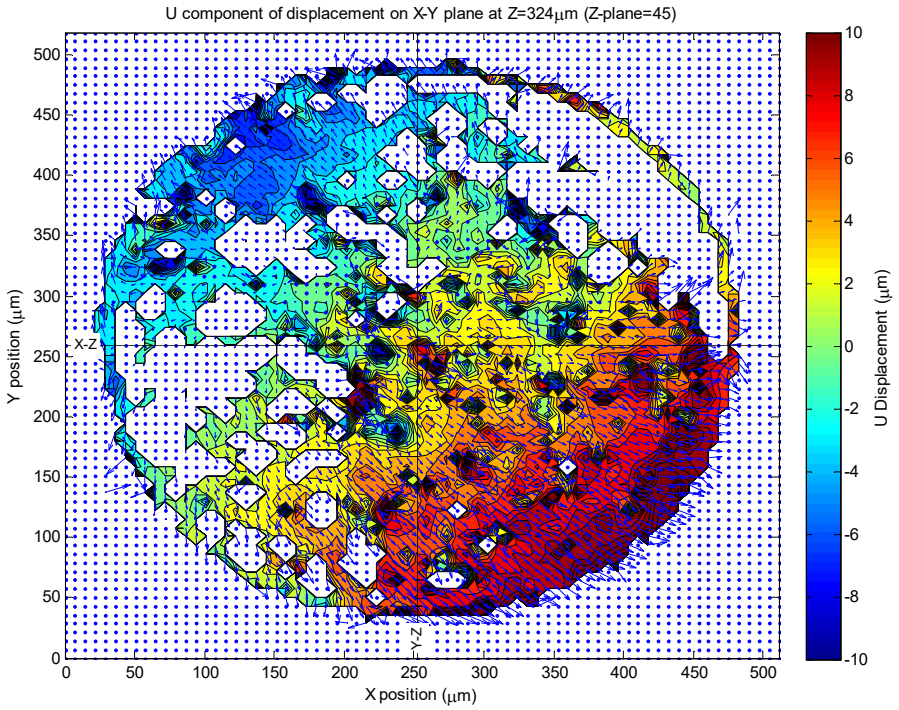

(a)

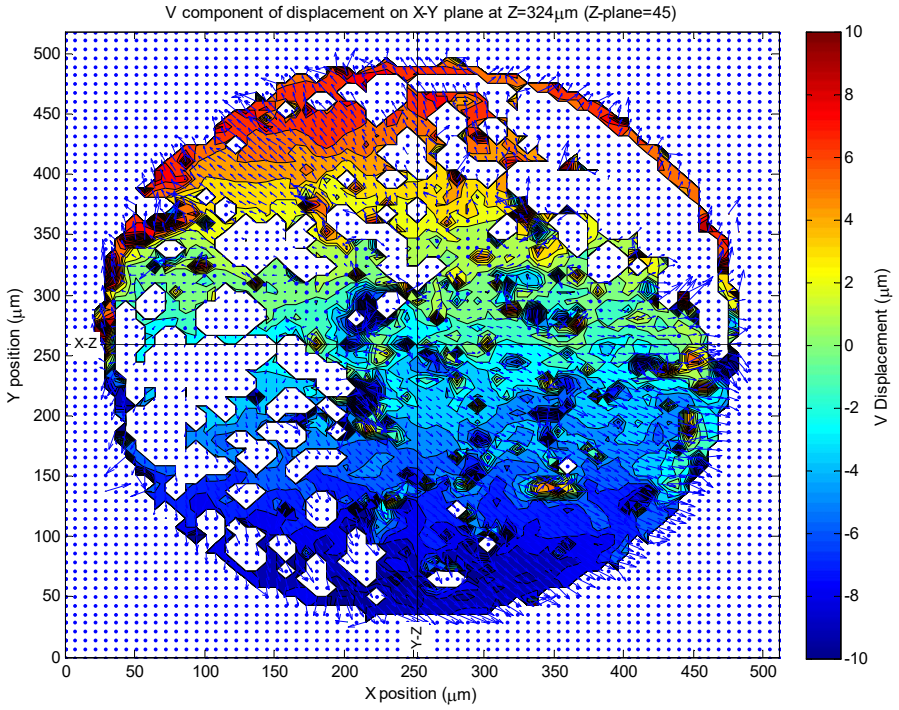

(b)

Figure 176 – Cross-sections through DVC data in and around the TGO for Rolls-Royce Pt cylindrical micro-specimen between 0 hours and 20 hours at 1200°C. White patches indicate areas that did not correlate (correlation coefficient < 0.5).

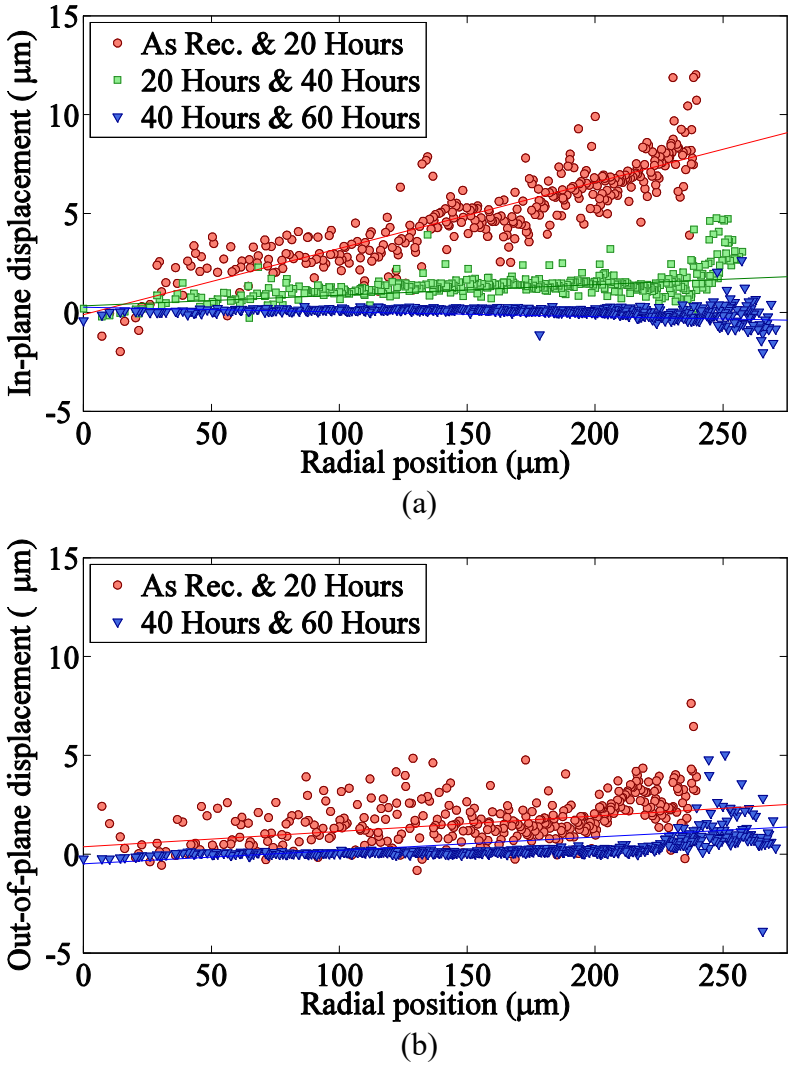

Figure 177 – Average displacement distribution as a function of radial position for Rolls-Royce Pt bondcoat specimen.

An examination of Rolls-Royce Pt-aluminide planar sections (Appendix K) reveals the very low correlation in the first timestep (Figure 187) that increases significantly in the second (Figure 188) and third (Figure 189) timesteps. A similar trend is noted for the Alstom Pt-aluminide sample. This lack of correlation implies that displacements cannot be suitably quantified in the first timestep (as indicated in Figure 178). Subsequent timesteps however, reveal a continuous and well-defined lateral displacement. The formation of voids at the edges of the Pt-aluminide specimens contribute to the large lateral displacements.

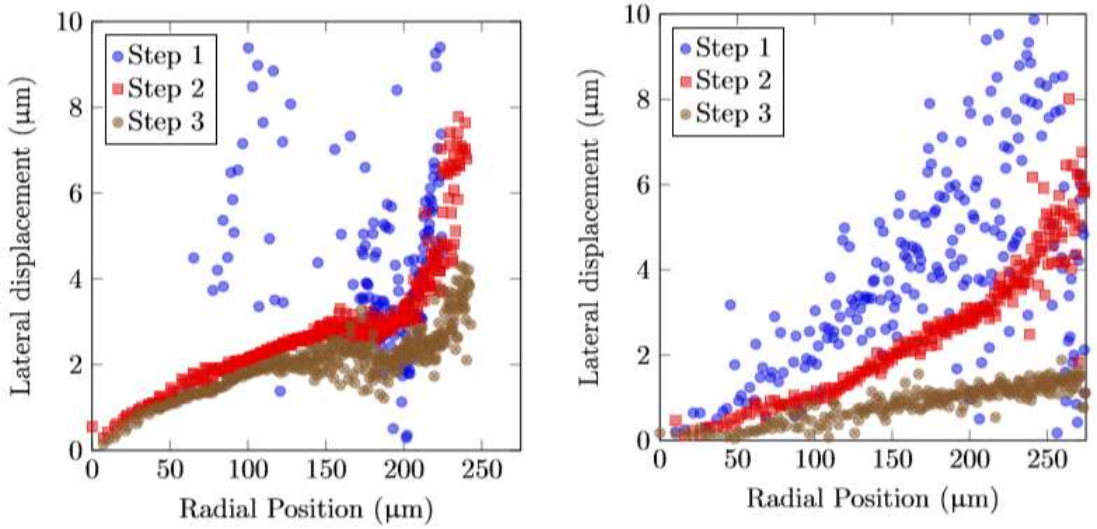

Figure 178 - Displacement data acquired by in-plane radial averaging on X-Y plane of DVC stack showing for (a) Rolls-Royce Pt-aluminide and (b) Alstom Pt-aluminide specimen for timesteps between 0 and 20 hours (step 1), 20 hours to 40 hours (step 2) and 40 hours to 60 hours (step 3) at 1200 °C.

6.5 Discussion

Of the samples analysed via DVC, Pt-only bondcoats displayed superior correlation, particularly in the first timestep. The combination of rapid bondcoat phase transformation and large displacements made computation of displacement fields in Pt-aluminide specimens challenging.

Lateral displacements summed over preceding timesteps from DVC give reasonable agreement with those measured from micrographs (Figure 179) but absolute values are consistently lower. This may be caused by the sharp contrast at the sample edges that leads to numerical instability in certain iterations. The time exponent estimated from a one-term power law fit to the DVC displacements indicates sub-parabolic behaviour (0.2904) as is the case with that measured from micrographs (0.450). A similar comparison was not possible in the case of Pt-aluminide bondcoats because of the very wide spread in lateral displacement in the first timestep.

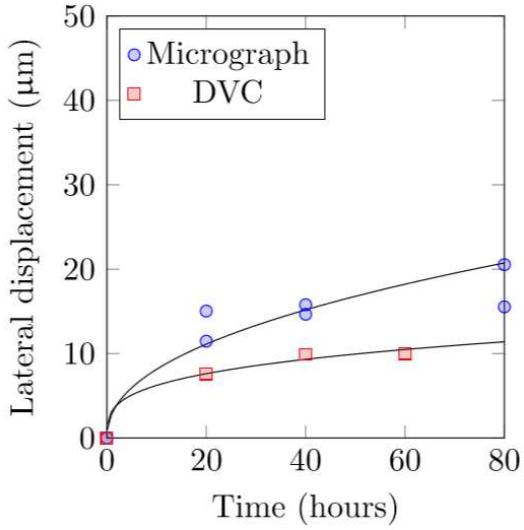

Figure 179 - Lateral extensions at bondcoat/TGO interface for Rolls-Royce Pt cylindrical micro-specimens undergoing 20-hour cyclic oxidation at 1200 °C. Measurements from DVC computations indicate lower lateral displacements than those measured from micrographs. One-term power law fits applied to each data set.

6.6 Conclusions

Rolls-Royce Pt-only specimens showed the highest correlation because of the relatively stable microstructure as a function of time. The rapidly evolving bondcoat microstructure and large displacements of Pt-aluminide bondcoats presented correlation challenges to the DVC method. Microstructural features that are no longer present in a subsequent timestep lead to correlation coefficients that fall below the minimum threshold. At later timesteps, when the bondcoat microstructure stabilises, increased sample domain areas correlate. In general, the topcoat displayed the greatest continuous areas of correlation because of the large number of features that remain detectable between timesteps. To alleviate this difficulty in tracking bondcoat features, shorter timesteps may be used.

The quality of DVC computations rely on the resolution of the input images. In and around the TGO, because of the imaging limitations notable in the first timestep, accurate out-of-plane displacements were difficult to resolve. Global displacements of the TGO/bondcoat interface (Pt-only TBC system), were used to infer lateral displacements and showed good agreement with measurements from micrographs.

Chapter 7 Conclusions and further work

7.1 Summary of conclusions

7.1.1 Thermal cycling

The factor of ten in scatter of time to spallation was shown to still be a challenge in thermal barrier coating systems. Of the sample batch tested, Pt bondcoats had comparable time to spallation lives to Pt-aluminide bondcoat TBC systems. Failure on turbine blade sections occurred most frequently on curved aerofoil surfaces. A novel cylindrical micro-specimen machining technique was devised that allowed isolated samples to be cyclically oxidised and the exterior morphology observed with time. The micro-specimens were shown to be comparable in oxide thickness and bondcoat deformation, to larger coupon specimens.

Thermal cycling of samples without topcoats were investigated and shown to have markedly different morphologies to counterparts with topcoats. Lateral displacement of the bondcoat was seen to occur and a force-balance argument was developed to estimate the TGO growth stress at a few hundred MPa. This is similar to that deduced by other workers.

The application of a mechanical constraint in the form of an APS coating applied to the diametric free surface of micro-specimens prevented any lateral displacements. This was shown to introduce widespread cracking at the TGO/bondcoat interface in Pt-aluminide specimens and through the grit-line in Pt specimens.

7.1.2 Synchrotron X-ray tomography

This study has shown the applicability of synchrotron X-ray microtomography to non-destructive examination of the high temperature cyclic oxidation of TBCs. A significant resolution improvement has been demonstrated over optical flash thermography for imaging and order of magnitude improvement in spatial resolution over photoluminescence piezospectroscopy. The microstructural evolution of diffusion bondcoats with EB-PVD topcoats has been followed over thermal cycles with imaging taking place in the as-received state and after each exposure period. Features that have been tracked in this study include bondcoat phases, substrate pores and topcoat intercolumnar separation.

Direct observation of TGO thickening has been presented in addition to inference of TGO thickness from absorption profiles. The measured average TGO thickness in the as-received case was artificially higher due to voxels associated with corn-kernel defects at the TGO/topcoat interface being counted towards TGO voxels resulting from a similar absorption between air and alumina. Portions of the TGO having smaller thicknesses (notably in the as-received state) occasionally fell below the detectable resolution of the technique and the presence of streak artefacts at times made accurate measurement of TGO thickness difficult.

Absorption profile analysis has allowed monitoring of porosity and intercolumnar separation within the topcoat as well as tracking the IDZ/substrate boundary. The 3-D porosity quantification method presented is an alternative to fluid displacement and precision polishing techniques however there is a requirement for miniature specimens for high resolution imaging.

7.1.3 Digital Volume Correlation

Digital volume correlation was successfully applied to synchrotron X-ray tomographs of TBC systems and allowed full-field quantification of displacements. In-plane and out-of-plane displacements were extracted from a narrow band encompassing the TGO. Interrogation windows within the topcoat exhibited the highest correlation while the homogenous substrate generally did not meet the minimum correlation requirements. Pt specimens showed the highest correlation in and around the TGO owing to the relatively smooth transition from as-received to oxidised bondcoat via platinum diffusion. Lateral displacement distributions were shown to be radially linear and decreased with time as expected. Pt-aluminide specimens, because of the rapidly changing β grain structure, porosity formation and large lateral displacements made correlation inherently difficult.

7.2 Further work

7.2.1 Thermal cycling

To allow detailed investigation of the very different bondcoat and oxide morphologies observed for samples without topcoats (continuous but cracked TGO for Pt-aluminide and alumina islands for Pt only samples without topcoats), further cyclic oxidation tests may be carried out, matching the duration of tests with topcoats. This may be coupled with the creep model presented herein and finite element simulations to better understand the observed difference in oxide and bondcoat morphology.

Further investigation into the effect of the mechanical edge constraint introduced by the APS coating on cylindrical micro-specimens would also help address some of the questions raised by the differing behaviour of the TGO in the presence of this edge constraint.

7.2.2 Bondcoat mechanical properties and finite element modelling

The creep properties of the bondcoat systems need to be accurately measured when modelling oxidation-induced bondcoat deformation. Finite element models should consider the time and temperature dependence of micro-mechanical properties. For such measurements to take place, a possible solution is to carry out micro-cantilever tests on thermally cycled specimens. Samples will need to be prepared for each numerical time step modelled. From this suggested work, derivation of empirical creep properties will be possible that may be used in finite element codes to predict TGO stresses. The model used will need to incorporate visco-plasticity and it is desirable to include strain or time

dependent material hardening. The model could be further adapted to include a mechanical constraint simulating the APS coating applied to the cylindrical sides.

7.2.3 Synchrotron X-ray tomography

To achieve a further improvement in resolution that would allow direct observation of early sub-critical cracks, nano synchrotron X-ray tomography may be explored. This approach is likely to require smaller specimens, but the sample-preparation technique devised in this work has been shown to produce samples on the order of 100 μm (scanned samples in this work were 500 μm and 1000 μm). The addition of electronic measurement control or in-situ machining microscopy would allow samples on the order of 20 μm to be machined, to allow an order of magnitude improvement in spatial resolution. Care will need to be taken to ensure the topcoat is retained.

To avoid the segmentation and DVC issues faced with time-dependent tomography reconstructions, a possible solution is to fill the environment around the samples with an inert gas, for example Xenon, that has a different mass attenuation coefficient to alumina and air or by evacuating the sample holder. This would require adapting or redesigning the sample holder with vacuum seals and/or a one-way gas flow system.

Inter-columnar gaps within the EB-PVD topcoat yield high-contrast with X-ray tomography. The attenuation of CMAS, that is greater than that of the topcoat, should allow high-quality imaging of the penetration depth of CMAS and the evolution with thermal exposure.

7.2.4 Digital Volume Correlation

To overcome the lack of correlation in certain areas of data sets, most notable in the first step of unconstrained correlation pairs, two approaches may be taken. The first approach

involves modifying the experiment that produces the tomographic input data and the second involves changing the DVC code to be aware of microstructural changes. To better capture the evolving bondcoat microstructure and TGO, shorter time steps, for example, 1 hour may be run between scans. Although this fundamentally changes the nature of the experiment, it should allow interrogation windows to better track bondcoat phase transformation and elemental diffusion. To maintain the experimental configuration of 20-hour cycles, another approach is to make use of in-situ furnaces designed for use on synchrotron stages. This would require high-speed scanning to minimise microstructural evolution during each scan, a trade-off with resolution that will negatively impact DVC computations. An alternative is to maintain the experimental configuration used but acquired tomographs with nano-tomography. This increased spatial resolution should allow the lack of traceable features in and around the TGO in the first timestep to be overcome. A further approach is the use of X-ray sensitive markers introduced as dopants in the TBC system. This would require alteration of the TBC manufacturing process and care must be taken to ensure dopants do not alter the microstructural behaviour.

The second overall approach is make the DVC code aware of specific microstructural transformations. Although the commercial DVC code used in this work did not explicitly allow user-modification of the DVC iterations, custom codes may incorporate interface movements and contrast changes between time steps.

Appendix A: Mass gain conversion to oxide thickness

For data obtained using specific mass gain, it is often useful to express this value in terms of oxide thickness. The following derivation allows for converting parabolic rate constants recorded in specific mass gain to a value expressed in oxide thickness. For a metal M supporting the growth of an oxide M_aO_b, it is assumed all the additional mass is gained through the action of adsorption of oxygen and subsequent scale formation. Hence the increase in mass (Δm) equals the amount of oxygen adsorbed. The number of moles of oxygen is then

$$\Delta m/_{M_O} = \Delta m/_{16}$$

Where $M_O = 16$, the molar mass of oxygen. Since b atoms of O are required for each molecule of M.

The number of moles of the oxide must then be divided by the number of atoms of

$$\Delta m/_{M_O \cdot b}$$

The volume of oxide having a thickness ξ over a metal of surface area A is then given by

$$\xi A = \frac{\Delta m \cdot {M_{ox}}/{\rho_{ox}}}{M_O \cdot b} = \frac{\Delta m \cdot M_{ox}}{M_O \cdot b \cdot \rho_{ox}}$$

Using the following substitution

$$\xi = \Delta m/_A$$

the parabolic rate law in terms of mass gain may be rewritten as

$$k_p^m = \frac{\left(\Delta m/_A\right)^2}{t}$$

Additionally, the parabolic rate constant in terms of mass gain may be rewritten in terms of thickness as:

$$k_p = \left(\frac{M_{ox}}{M_O \cdot b \cdot \rho_{ox}}\right)^2 \cdot k_p^m$$

Appendix B: List of turbine blades

Table 12 – List of turbine blades used in this work supplied in production specification. All blades consist of the CMSX-4 nickel superalloy base with a combination of Pt-aluminide and Pt-only bondcoats, with some blades supplied without a topcoat

ID	Serial Part 1	Serial Part 2	Engine	Substrate	Bondcoat	Topcoat
01	FW44488	115661106	Trent 500	CMSX-4	Pt	PYSZ
02	FW44479	116063910	Trent 500	CMSX-4	Pt	PYSZ
03	FW44478	116143511	Trent 500	CMSX-4	Pt	PYSZ
04	FW44484	116143701	Trent 500	CMSX-4	Pt	PYSZ
05	FW44478	116331302	Trent 500	CMSX-4	Pt	PYSZ
06	FW44487	116332112	Trent 500	CMSX-4	Pt	PYSZ
07	FW44478	116379110	Trent 500	CMSX-4	Pt	PYSZ
08	FW21837	116388905	RB211	CMSX-4	Pt-Al	None
09	FW44489	116679408	Trent 500	CMSX-4	Pt	PYSZ
10	FW44482	116754303	Trent 500	CMSX-4	Pt	PYSZ
11	FW44481	116757111	Trent 500	CMSX-4	Pt	PYSZ
12	FW44483	116780008	Trent 500	CMSX-4	Pt	PYSZ
13	TRN101668	131023707	Trent 800	CMSX-4	Pt-Al	PYSZ
14	TRN101668	132313208	Trent 800	CMSX-4	Pt-Al	PYSZ
15	TRN101668	132381203	Trent 800	CMSX-4	Pt-Al	PYSZ
16	TRN101668	132894107	Trent 800	CMSX-4	Pt-Al	PYSZ
17	TRN101668	132894301	Trent 800	CMSX-4	Pt-Al	PYSZ
18	TRN101668	132898111	Trent 800	CMSX-4	Pt-Al	PYSZ
19	TRN101668	132975812	Trent 800	CMSX-4	Pt-Al	PYSZ
20	TRN101668	133673803	Trent 800	CMSX-4	Pt-Al	PYSZ
21	TRN101668	133791302	Trent 800	CMSX-4	Pt-Al	PYSZ
22	FW44486	141609609	Trent 500	CMSX-4	Pt	PYSZ
23	TRN101668	141818002	Trent 800	CMSX-4	Pt-Al	PYSZ
24	FW15154	143478211	Trent 800	CMSX-4	Pt-Al	None
25	FW15759	143855701	Trent 700	CMSX-4	Pt-Al	None
26	FW21837	144155212	RB211	CMSX-4	Pt-Al	None
27	FW15759	144221112	Trent 700	CMSX-4	Pt-Al	None
28	FW63853	144538514	Trent 1000	CMSX-4	Pt	None
29	FW63853	144538905	Trent 1000	CMSX-4	Pt	None

Appendix C: Cyclic oxidation rig source code (C#)

The control software for the cyclic oxidation rig was written and developed in Microsoft Visual Studio. The C# programming language was used (the Microsoft implementation of C++) and four classes were written to manage the application, update status information on the application frontend, control hot/cold cycle timer loops and communicate with the motor controller over an RS-232 serial link.

Front end form

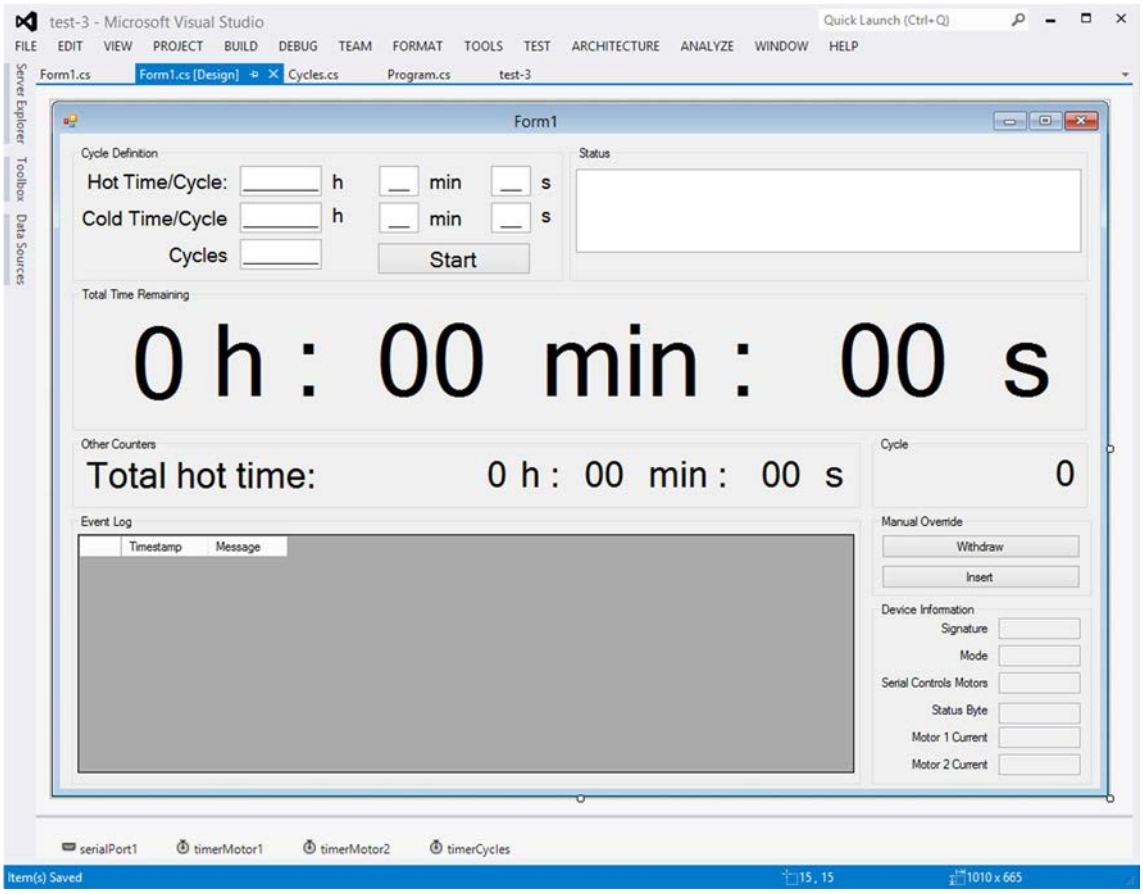

Figure 180 - Cyclic oxidation rig control software, designed and coded in Microsoft Visual Studio. The program communicates with a motor controller over a serial RS-232 link.

User interface Windows form class

```
using System;
using System.Collections.Generic;
using System.ComponentModel;
using System.Data;
using System.Drawing;
using System.Linq;
using System.Text;
using System.Threading.Tasks;
using System.Windows.Forms;

namespace test_3
{
    public partial class Form1 : Form
    {

        // Private variables to measure duration of motor travel
        // measured in milliseconds and updated on timer tick
        private double _motor1Time = 0;
        private double _motor2Time = 0;

        // Booleans if motor is currently moving
        private Boolean _motor1InMotion = false;
        private Boolean _motor2InMotion = false;

        // Motor timeout value, motors are stopped if timeout is reached
        private double _motorTimeout = 6000;

        // Failure Boolean, if timeout or other error has occurred, do not allow
further commands
        private Boolean _failure = false;

        // Cycles class for hot/cold counters
        Cycles cycles = new Cycles();
        ulong hotSeconds = 0; // Total hot time
        ulong coldSeconds = 0; // Total cold time
        ulong cycleCount = 0;
        ulong elapsedSeconds = 0; // Total time since cycle timer started
        ulong totalHotSeconds = 0;

        // Test running Boolean
        private bool testRunning = false;

        // Abort boolean
        private bool abort = false;

        // Status Booleans for inserted/withdrawn
        private bool inserted = true;
        private bool withdrawn = true;

        public Form1()
        {
            InitializeComponent();

            // Log software startup
            dataGridView1.Rows.Insert(0, DateTime.Now.ToString(), "Software
Started");
```

```
            // Initialise class and send in reference to serial port
            // Serial port is configured via visual designer
            Trex trex = new Trex(ref serialPort1);

            // Test if status byte can be retrieved, if not assume
            // connection to device has been lost
            if (trex.getStatusByte())
            {
                // Log connection to device
                dataGridView1.Rows.Insert(0, DateTime.Now.ToString(), "Connected
to motor controller");

                // Run commands to retrieve status data
                trex.getSignature();
                trex.getMode();
                trex.getSerialControlsMotors();

                // Populate status fields on UI form
                textDeviceSignature.Text = trex.deviceSignature;
                textDeviceMode.Text = trex.deviceMode;
                textDeviceSerialControlsMotors.Text =
trex.deviceSerialControlsMotors;
                textStatusByte.Text = trex.deviceStatusByte;

                // Enable inputs
                enableInputs();
            }
            else
            {
                // Log connection error
                dataGridView1.Rows.Insert(0, DateTime.Now.ToString(), "Unable to
connect to device. Please check connections and/or emergency stop button");
                _failure = true;
            }
        }

        /*
         * Manual withdrawal of specimen
         */
        private void btnAccelerateMotor1_Click(object sender, EventArgs e)
        {
            issueWithdraw();
        }

        /*
         * Manual insertion of specimen
         */
        private void btnAccelerateMotor2_Click(object sender, EventArgs e)
        {
            issueInsert();
        }

        /*
         * Enable all user inputs on UI
         */
        private void enableInputs()
        {
            // Enable Masked Text Boxes
            textHotHours.Enabled = true;
            textHotMinutes.Enabled = true;
```

```
            textHotSeconds.Enabled = true;
            textColdHours.Enabled = true;
            textColdMinutes.Enabled = true;
            textColdSeconds.Enabled = true;
            textCycles.Enabled = true;

            // Enable buttons
            btnInsert.Enabled = true;
            btnWithdraw.Enabled = true;
            btnStartProgram.Enabled = true;
        }

        /*
         * Disable all user inputs on UI
         */
        private void disableInputs()
        {
            // Disable Masked Text Boxes
            textHotHours.Enabled = false;
            textHotMinutes.Enabled = false;
            textHotSeconds.Enabled = false;
            textColdHours.Enabled = false;
            textColdMinutes.Enabled = false;
            textColdSeconds.Enabled = false;
            textCycles.Enabled = false;

            // Disable buttons
            btnInsert.Enabled = false;
            btnWithdraw.Enabled = false;
        }

        // Issue insert specimen command via motor 2
        private void issueInsert()
        {
            // Proceed only if a timeout has not occurred
            if (!_failure)
            {
                // Update log
                dataGridView1.Rows.Insert(0, DateTime.Now.ToString(), "Issuing
insert command");
                Trex trex = new Trex(ref serialPort1);

                // Check for connectivity
                if (trex.getStatusByte())
                {
                    // Update Status Label
                    textStatus.Text = "Inserting";

                    withdrawn = false;

                    // Issue accelerate command
                    trex.accelerateMotor2();
                    // Start timer to monitor current and measure time motor has
been moving
                    _motor2InMotion = true;
                    timerMotor2.Start();
                }
                else
                {
                    // Cannot connect to controller, update log
```

```
                    dataGridView1.Rows.Insert(0, DateTime.Now.ToString(), "Unable
to insert specimen. Please check connections and/or emergency stop button");
                    _failure = true;
                    timerCycles.Stop();
                }
            }
            else
            {
                MessageBox.Show("A serious error has occurred, unable to
continue. Please check event log for more information");
                _failure = true;
                timerCycles.Stop();
            }
        }

        // Issue withdraw specimen command via motor 1
        private void issueWithdraw()
        {
            // Proceed only if a timeout or other error has not occurred
            if (!_failure)
            {
                // Update log
                dataGridView1.Rows.Insert(0, DateTime.Now.ToString(), "Issuing
withdraw command");
                Trex trex = new Trex(ref serialPort1);

                // Check for connectivity
                if (trex.getStatusByte())
                {
                    // Update Status Label
                    textStatus.Text = "Withdrawing";

                    inserted = false;
                    // Issue accelerate command
                    trex.accelerateMotor1();
                    _motor1InMotion = true;

                    // Start timer to monitor current and measure time motor has
been moving
                    timerMotor1.Start();
                }
                else
                {
                    // Cannot connect to controller, update log
                    dataGridView1.Rows.Insert(0, DateTime.Now.ToString(), "Unable
to withdraw specimen. Please check connections and/or emergency stop button");
                    _failure = true;
                    timerCycles.Stop();

                }
            }
            else
            {
                MessageBox.Show("A serious error has occurred, unable to
continue. Please check event log for more information");
                _failure = true;
                timerCycles.Stop();
            }
        }
```

```
        // Timer to continuously monitor motor current and stop motor if drops to
zero
        private void timerMotor1_Tick(object sender, EventArgs e)
        {
            Trex trex = new Trex(ref serialPort1);
            if (trex.getStatusByte())
            {
                if (_motor1Time > _motorTimeout)
                {
                    // Timeout has occurred,  Stop motors and reset
                    dataGridView1.Rows.Insert(0, DateTime.Now.ToString(),
"Timeout occurred while attempting to withdraw specimen within " + (_motorTimeout
/ 1000).ToString() + " seconds.");
                    trex.stopMotor1();
                    timerMotor1.Stop();
                    _motor1Time = 0;
                    _motor1InMotion = false;
                    _failure = true;
                }
                else
                {
                    trex.getMotor1current();
                    textMotor1current.Text = trex.motor1current.ToString();

                    // Current has dropped to zero, hit limit switch
                    if (trex.motor1current == 0.0d)
                    {
                        // Stop motor and update log
                        timerMotor1.Stop();
                        dataGridView1.Rows.Insert(0, DateTime.Now.ToString(),
"Specimen has been withdrawn after " + (_motor1Time / 1000).ToString() + "
seconds");
                        _motor1Time = 0;
                        _motor1InMotion = false;
                        textStatus.Text = "Withdrawn";
                        withdrawn = true;

                        if (abort)
                        {
                            // Reset user input fields
                            resetForm();
                        }
                    }
                    else
                    {
                        // If no timeout and current is > 0, increment motor time
for next tick
                        _motor1Time += Convert.ToDouble(timerMotor1.Interval);
                    }
                }
            }
            else
            {
                // Update log
                dataGridView1.Rows.Insert(0, DateTime.Now.ToString(), "Unable to
connect to device. Please check connections and/or emergency stop button");
                timerMotor1.Stop();
                _motor1Time = 0;
                _motor1InMotion = false;
                _failure = true;
```

```
                disableInputs();
            }
        }

        private void timerMotor2_Tick(object sender, EventArgs e)
        {
            Trex trex = new Trex(ref serialPort1);
            if (trex.getStatusByte())
            {
                if (_motor2Time > _motorTimeout)
                {
                    // Timeout has occurred,  Stop motors and reset
                    dataGridView1.Rows.Insert(0, DateTime.Now.ToString(),
"Timeout occurred while attempting to insert specimen within " + (_motorTimeout /
1000).ToString() + " seconds.");
                    trex.stopMotor2();
                    timerMotor2.Stop();
                    _motor2Time = 0;
                    _motor2InMotion = false;
                    _failure = true;
                }
                else
                {
                    // Read motor current from device and update UI Form
                    trex.getMotor2current();
                    textMotor2current.Text = trex.motor2current.ToString();

                    // Current has dropped to zero, hit limit switch
                    if (trex.motor2current == 0.0d)
                    {
                        // Stop motor and update log
                        timerMotor2.Stop();
                        dataGridView1.Rows.Insert(0, DateTime.Now.ToString(),
"Specimen has been inserted after " + (_motor2Time / 1000).ToString() + "
seconds");
                        // Reset motor time
                        _motor2Time = 0;
                        _motor2InMotion = false;
                        textStatus.Text = "Inserted";
                        // Update status boolean
                        inserted = true;
                    }
                    else
                    {
                        // If no timeout and current is > 0, increment motor time
for next tick
                        _motor2Time += Convert.ToDouble(timerMotor2.Interval);
                    }
                }
            }
            else
            {
                // Update log
                dataGridView1.Rows.Insert(0, DateTime.Now.ToString(), "Unable to
connect to device. Please check connections and/or emergency stop button");
                timerMotor2.Stop();
                _motor2Time = 0;
                _motor2InMotion = false;
                _failure = true;
                disableInputs();
```

```
            }
        }

        private void btnStartProgram_Click(object sender, EventArgs e)
        {
            if (testRunning)
            {
                if (MessageBox.Show("Are you sure you want to abort this test?
This will issue a withdraw command to the motors.", "Cyclic rig",
MessageBoxButtons.YesNo) == System.Windows.Forms.DialogResult.Yes)
                {
                    // Set abort boolean to true
                    // Used by withdraw command to reset if aborted
                    abort = true;

                    // Log abortion
                    dataGridView1.Rows.Insert(0, DateTime.Now.ToString(),
"Received request to terminate program.");

                    // Stop cycle timer
                    timerCycles.Stop();

                    // Withdraw specimen
                    issueWithdraw();

                    // Log final statement
                    dataGridView1.Rows.Insert(0, DateTime.Now.ToString(),
"Program aborted prematurely by user.");
                }
            }
            else
            {
                // Retrieve and convert number of cycles
                cycleCount = cycles.cycleCount(textCycles.Text);
                if (cycleCount > 0)
                {
                    // Calculate number of seconds at temperature
                    hotSeconds = cycles.hotTime(textHotHours.Text,
textHotMinutes.Text, textHotSeconds.Text);

                    if (hotSeconds > 0)
                    {
                        // Calculate number of seconds out of furnace
                        coldSeconds = cycles.coldTime(textColdHours.Text,
textColdMinutes.Text, textColdSeconds.Text);

                        if (coldSeconds > 0)
                        {
                            // Confirm user input
                            if (MessageBox.Show("Begin program?", "Cyclic Rig",
MessageBoxButtons.YesNo) == System.Windows.Forms.DialogResult.Yes)
                            {
                                // Set test running boolean to true
                                testRunning = true;

                                // update log
                                dataGridView1.Rows.Insert(0,
DateTime.Now.ToString(), "Defining program with " + cycleCount.ToString() + "
cycles");
```

```
                                dataGridView1.Rows.Insert(0,
DateTime.Now.ToString(), "Defining hot cycle portion with " +
hotSeconds.ToString() + " seconds");
                                dataGridView1.Rows.Insert(0,
DateTime.Now.ToString(), "Defining cold cycle portion with " +
coldSeconds.ToString() + " seconds");

                                //Disable inputs
                                disableInputs();

                                // Begin Program
                                dataGridView1.Rows.Insert(0,
DateTime.Now.ToString(), "Beginning Program.");

                                // Update Button to abort test
                                btnStartProgram.Text = "Abort test";

                                // Update remaining time for first timer tick
                                string[] RemainingTime =
cycles.secondsToTime(cycles.totalTime - elapsedSeconds);
                                textRemainingHours.Text = RemainingTime[0];
                                labelRemainingMinutes.Text = RemainingTime[1];
                                labelRemainingSeconds.Text = RemainingTime[2];

                                // Issue insert command
                                issueInsert();

                                // Start timer
                                timerCycles.Start();
                            }
                        }
                        else
                        {
                            MessageBox.Show("Invalid cold time entered, please
enter a time greater than 0.");
                        }

                    }
                    else
                    {
                        MessageBox.Show("Invalid hot time entered, please enter a
time greater than 0.");
                    }

                }
                else
                {
                    MessageBox.Show("Invalid Cycles entered, please enter a
number greater than 0.");
                }
            }
        }

        private void timerCycles_Tick(object sender, EventArgs e)
        {
            // Update time since start
            if (!_motor1InMotion && !_motor2InMotion)
            {
                if (inserted)
                {
```

```
                    totalHotSeconds++;
                    string[] totalHotTime =
cycles.secondsToTime(totalHotSeconds);
                    textTotalHotHours.Text = totalHotTime[0];
                    labelTotalHotMinutes.Text = totalHotTime[1];
                    labelTotalHotSeconds.Text = totalHotTime[2];
                }
            }

            // Do not increment elapsed time counter if either of the motors are
in motion
            if (!_motor1InMotion && !_motor2InMotion)
            {
                // Increment elapsed time by one second per timer tick. (Assume
timer interval = 1000ms)
                elapsedSeconds++;

                // Calculate remaining seconds for this tick
                ulong remainingSeconds = cycles.totalTime - elapsedSeconds;

                // Make sure not to exceed total number of seconds test is
scheduled to take
                if (elapsedSeconds <= cycles.totalTime)
                {
                    textTotalCycles.Text =
(Math.Ceiling(Convert.ToDouble(elapsedSeconds) / (Convert.ToDouble(hotSeconds) +
Convert.ToDouble(coldSeconds)))).ToString();

                    // Populate remaining times on tick (excluding when motors
are in motion)
                    // by getting string array of hours, minutes and seconds from
Cycles class
                    string[] remainingTime =
cycles.secondsToTime(remainingSeconds);
                    textRemainingHours.Text = remainingTime[0];
                    labelRemainingMinutes.Text = remainingTime[1];
                    labelRemainingSeconds.Text = remainingTime[2];

                    // Retrieve array of time points (in seconds) for insertion
                    // and withdrawals and check for matches with current elapsed
seconds
                    if (Array.IndexOf(cycles.insersions, elapsedSeconds) != -1)
                    {
                        // Issue insert command and log
                        dataGridView1.Rows.Insert(0, DateTime.Now.ToString(),
"Inserting after " + elapsedSeconds.ToString() + " seconds");
                        issueInsert();
                    }
                    else if (Array.IndexOf(cycles.withdrawals, elapsedSeconds) !=
-1)
                    {
                        // Check if should withdraw now and issue withdraw
command and log
                        dataGridView1.Rows.Insert(0, DateTime.Now.ToString(),
"Withdrawing after " + elapsedSeconds.ToString() + " seconds");
                        issueWithdraw();
                    }
                }
                else
                {
```

```
                    // Reached end of run so stop timer
                    timerCycles.Stop();

                    // Only display completed successfully if program was not
aborted
                    if (!abort)
                    {
                        // Log completion
                        dataGridView1.Rows.Insert(0, DateTime.Now.ToString(),
"Program Completed successfully.");
                        MessageBox.Show("Run completed");
                    }
                    resetForm();
                }
            }
        }

        private void resetForm()
        {
            // Reset abort boolean
            abort = false;

            // Create new instance of cycle object
            cycles = new Cycles();

            // Reset timer to allow another run
            elapsedSeconds = 0;

            // Reset inputs to allow another run
            enableInputs();

            // Rest test running boolean
            testRunning = false;

            // Reset cycle counter
            hotSeconds = 0;
            coldSeconds = 0;
            cycleCount = 0;
            elapsedSeconds = 0;
            totalHotSeconds = 0;

            // Reset status label
            textStatus.Text = "Idle";

            // Reset button text
            btnStartProgram.Text = "Start";

            // Reset remaining time labels
            textRemainingHours.Text = "0";
            labelRemainingMinutes.Text = "00";
            labelRemainingSeconds.Text = "00";

            // Reset total hot time labels
            textTotalHotHours.Text = "0";
            labelTotalHotMinutes.Text = "00";
            labelTotalHotSeconds.Text = "00";

            // Reset cycle count
            textTotalCycles.Text = "0";
```

```
            // Reset inserted/withdrawn status Booleans
            inserted = false;
            withdrawn = false;
        }
    }
}
```

Hot/cold cycle timer class

```
/*
 * Class to manage hot/cold cycles
 * Danial Khoshkhou
 * University of Birmingham
 * October 2014
 */

using System;
using System.Collections.Generic;
using System.Collections;
using System.Linq;
using System.Text;
using System.Threading.Tasks;
using System.Windows.Forms;

public class Cycles
{
    private ulong _cycleCount = 0;
    private ulong _hotTime = 0;
    private ulong _coldTime = 0;

    public ulong totalTime = 0;
    public ulong[] insertions; // Array to store seconds for insertions
    public ulong[] withdrawals; // Array to store seconds for withdrawals

    public Cycles()
    {

    }

    /*
     * Set and return converted hot time
     */
    public ulong hotTime(string hotHours, string hotMinutes, string hotSeconds)
    {
        // Convert to seconds
        _hotTime = convertTimeToSeconds(hotHours, hotMinutes, hotSeconds);

        // Update total time
        updateTimes();

        // return to caller
        return _hotTime;
    }

    /*
     * Set and return converted cold time
     */
    public ulong coldTime(string coldHours, string coldMinutes, string coldSeconds)
    {
        // Convert to seconds
        _coldTime = convertTimeToSeconds(coldHours, coldMinutes, coldSeconds);

        // Update total time
        updateTimes();

        // return to caller
        return _coldTime;
    }
```

```
    /*
     * Convert separate string of hours, minutes and seconds into an integer of
seconds
     */
    private ulong convertTimeToSeconds(string hours, string minutes, string seconds)
    {
        // Temporary variables
        ulong _hours = 0;
        ulong _minutes = 0;
        ulong _seconds = 0;
        ulong _time = 0;

        // If empty string, leave as 0
        if (hours != "")
        {
            _hours = Convert.ToUInt64(hours);
        }

        if (minutes != "")
        {
            _minutes = Convert.ToUInt64(minutes);
        }

        if (seconds != "")
        {
            _seconds = Convert.ToUInt64(seconds);
        }

        // Compute total time in seconds
        _time = (_hours * 3600) + (_minutes * 60) + _seconds;

        // return to caller
        return _time;
    }


    private void updateTimes()
    {
        totalTime = (_coldTime + _hotTime) * _cycleCount;

        // Dimension withdrawals and insertions array
        ulong[] _insertions;
        ulong[] _withdrawals;
        _insertions = new ulong[_cycleCount];
        _withdrawals = new ulong[_cycleCount];

        // Calculate time points for insertions and withdrawals
        ulong i;
        for (i = 0; i < _cycleCount; i++)
        {
            _insertions[i] = i * (_hotTime + _coldTime);
            _withdrawals[i] = ((i + 1) * _hotTime) + (i * _coldTime);
        }

        // Set to global values.
        withdrawals = _withdrawals;
        insertions = _insertions;
    }

    /*
     * Set and return converted cycle count
     */
    public ulong cycleCount(string cycleCount)
```

```
    {
        // Retrieve number of cycles
        if (cycleCount != "")
        {
            _cycleCount = Convert.ToUInt64(cycleCount);
        }

        return _cycleCount;
    }

    public string[] getRemainingTime(ulong elapsedSeconds)
    {
        // Return string array
        return (secondsToTime(totalTime - elapsedSeconds));
    }

    /*
     * Total time in seconds to string array
     */
    public string[] secondsToTime(ulong totalSeconds)
    {
        ulong[] _time = new ulong[3];
        string[] _timeStr = new string[3];

        // Hours
        _time[0] = Convert.ToUInt64(Math.Floor(Convert.ToDouble(totalSeconds) /
3600));
        _timeStr[0] = _time[0].ToString();

        // Minutes
        _time[1] = Convert.ToUInt64(Math.Floor((Convert.ToDouble(totalSeconds) -
(_time[0] * 3600)) / 60));
        if (_time[1] < 10)
        {
            _timeStr[1] = "0" + _time[1].ToString();
        }
        else
        {
            _timeStr[1] = _time[1].ToString();
        }
        // Seconds
        _time[2] = Convert.ToUInt64(Convert.ToDouble(totalSeconds) - (_time[0] *
3600) - (_time[1] * 60));
        if (_time[2] < 10)
        {
            _timeStr[2] = "0" + _time[2].ToString();
        }
        else
        {
            _timeStr[2] = _time[2].ToString();
        }


        return _timeStr;
    }

}
```

Motor controller interface class

```
/*
 * Class to interface with TreX Motor Controller
 * Danial Khoshkhou
 * October 2014
 *
 * TODO: add CRC checking to all issued commands
 * TODO: add handling of individual UART error bits
 */

using System;
using System.Collections.Generic;
using System.Collections;
using System.Linq;
using System.Text;
using System.Threading.Tasks;
using System.IO.Ports;
using System.Windows.Forms;

public class Trex
{
    // Private class variables for communicating with device
    private SerialPort _serialPort;
    private string _str;
    private string _echo;
    private string _receive;
    private string _transmit;
    private byte[] _buffer;
    private int _sendBytes;
    private int _readBytes;

    //Public device information variables
    public string deviceSignature;
    public string deviceMode;
    public string deviceSerialControlsMotors;
    public string deviceStatusByte;

    // Public status byte variables
    public bool statusMotor2currentlOverLimit;   // bit 7
    public bool statusMotor2fault;               // bit 6
    public bool statusMotor1currentlOverLimit;   // bit 5
    public bool statusMotor1fault;               // bit 4
    public bool statusUartError;                 // bit 0

    // Public UART byte variables
    public bool uartTimeoutError;               // bit 7
    public bool uartCommandPacketFormatError;   // bit 6
    public bool uartCrcError;                   // bit 5
    public bool uartFrameError;                 // bit 4
    public bool uartDataOverrunError;           // bit 3
    public bool uartParityError;                // bit 2
    public bool uartReadBufferOverrunError;     // bit 1
    public bool uartSendBufferOverrunError;     // bit 0

    // Public Motor current variables
    public double motor1current;
    public double motor2current;

    /*
     * Class Constructor
     * Gets serial port to work with
```

```
     */
    public Trex(ref SerialPort serialPort) {
        // Assign serial port by ref to local variable
        _serialPort = serialPort;
    }

    /*
     * Get Signature Method
     * First 6 bytes are "TrexJr" and the next three firmware version
     */
    public bool getSignature() {
        // Build buffer to send
        _buffer = new byte[32];
        _buffer[0] = 0x81;
        _sendBytes = 1;
        _readBytes = 9;

        if (sendMessage())
        {
            deviceSignature = _str;
            return true;
        }
        else
        {
            return false;
        }
    }

    /*
     * Get Device Mode
     * R = RC mode, A = analogue mode,
     * r = serial mode with channels configured for RC input signals
     * a = serial mode with channels configured for analogue input signals
     */
    public bool getMode()
    {
        // Build buffer to send
        _buffer = new byte[32];
        _buffer[0] = 0x82;
        _sendBytes = 1;
        _readBytes = 1;

        if (sendMessage())
        {
            deviceMode = _str;
            return true;
        }
        else
        {
            return false;
        }
    }

    /*
     * Does Serial Control Motors?
     * 0 = serial is not in control
     * 1 = serial is in control
     * Note that an ASCII 0 or 1 is not returned but a decimal 0 or 1.
     * This is handled in sendCommandPacket where only decimal 32 - 127 are converted
to chars
     */
    public bool getSerialControlsMotors()
    {
```

```
        // Build buffer to send
        _buffer = new byte[32];
        _buffer[0] = 0x83;
        _sendBytes = 1;
        _readBytes = 1;

        if (sendMessage())
        {
            deviceSerialControlsMotors = _str;
            return true;
        }
        else
        {
            return false;
        }
    }

    /*
     * Get Status Byte
     * Need to read individual bits of returned byte:
     * As values are bits (0 or 1), map to boolean
     *
     * bit 7: Motor 2 current over limit
     * bit 6: Motor 2 fault
     * bit 5: Motor 1 current over limit
     * bit 4: Motor 1 fault
     * bits 3-1: not used
     * bit 0: UART error - further error details in getUartErrorByte()
     */
    public bool getStatusByte()
    {
        // Build buffer to send to device
        _buffer = new byte[32];
        _buffer[0] = 0x84;
        _sendBytes = 1;
        _readBytes = 1;

        // Need to wait for bits to be extracted
        // before returning status of sendMessage
        bool boolReturn;
        boolReturn = sendMessage();
        deviceStatusByte = _str;

        // Prepare new array for bit array
        // Note that _buffer get changed from
        // a send byte to a received byte in
        // line above
        byte[] statusByte;
        statusByte = new byte[1];
        statusByte[0] = _buffer[0];

        // Use bit array to separate byte into bits
        BitArray bitArray;
        bitArray = new BitArray(statusByte);
        statusMotor2currentlOverLimit = bitArray.Get(7);
        statusMotor2fault = bitArray.Get(6);
        statusMotor1currentlOverLimit = bitArray.Get(5);
        statusMotor2currentlOverLimit = bitArray.Get(4);
        statusUartError = bitArray.Get(0);

        return boolReturn;
    }
```

```
/*
 * Get UART Error byte
 * Need to read individual bits of returned byte:
 * As values are bits (0 or 1), map to boolean
 *
 * bit 7: timeout
 * bit 6: command packet format error
 * bit 5: CRC error
 * bit 4: frame error (generated by UART hardware)
 * bit 3: data overrun (generated by UART hardware)
 * bit 2: parity error (generated by UART hardware)
 * bit 1: read buffer overrun
 * bit 0: send buffer overrun
 */
public bool getUartErrorByte()
{
    // Build buffer to send to device
    _buffer = new byte[32];
    _buffer[0] = 0x85;
    _sendBytes = 1;
    _readBytes = 1;

    // Need to wait for bits to be extracted
    // before returning status of sendMessage
    bool boolReturn;
    boolReturn = sendMessage();

    // Prepare new array for bit array
    // Note that _buffer get changed from
    // a send byte to a received byte in
    // line above
    byte[] uartByte;
    uartByte = new byte[1];
    uartByte[0] = _buffer[0];

    // Use bit array to separate byte into bits
    BitArray bitArray;
    bitArray = new BitArray(uartByte);

    uartTimeoutError = bitArray.Get(7);
    uartCommandPacketFormatError = bitArray.Get(6);
    uartCrcError = bitArray.Get(5);
    uartFrameError = bitArray.Get(4);
    uartDataOverrunError = bitArray.Get(3);
    uartParityError = bitArray.Get(2);
    uartReadBufferOverrunError = bitArray.Get(1);
    uartSendBufferOverrunError = bitArray.Get(0);

    return boolReturn;
}

/*
 * Get Motor 1 Current
 */
public bool getMotor1current()
{
    // Build buffer to send
    _buffer = new byte[32];
    _buffer[0] = 0x8D;
    _sendBytes = 1;
    _readBytes = 1;
```

```
        if(sendMessage())
        {
            motor1current = Convert.ToDouble(_buffer[0])*0.04;

            if (motor1current == 0)
            {
                stopMotor1();
            }

            return true;
        }
        else{
            return false;
        }

    }

    /*
     * Get Motor 2 Current
     */
    public bool getMotor2current()
    {
        // Build buffer to send
        _buffer = new byte[32];
        _buffer[0] = 0x8E;
        _sendBytes = 1;
        _readBytes = 1;

        if (sendMessage())
        {
            motor2current = Convert.ToDouble(_buffer[0]) * 0.04;

            if (motor2current == 0)
            {
                stopMotor2();
            }
            return true;
        }
        else
        {
            return false;
        }
    }

    /*
     * Accelerate Motor 1 to full speed (127 forward)
     * Must set Motor 2 to 0 first in case normally closed switch is open
     */
    public bool accelerateMotor1()
    {
        stopMotor2();

        // Then build buffer to send and accelerate Motor 1
        _buffer = new byte[32];
        _buffer[0] = 0xC6;
        _buffer[1] = 0x7F;
        _sendBytes = 2;
        _readBytes = 0;
        return sendMessage();
    }

    /*
* Accelerate Motor 2 to full speed (127 forward)
```

```
*/
    public bool accelerateMotor2()
    {
        stopMotor1();

        // Then build buffer to send and accelerate Motor 2
        _buffer = new byte[32];
        _buffer[0] = 0xCE;
        _buffer[1] = 0x7F;
        _sendBytes = 2;
        _readBytes = 0;
        return sendMessage();
    }


    public bool stopMotor1()
    {
        //First set Motor 1 to zero
        _buffer = new byte[32];
        _buffer[0] = 0xC0;
        _buffer[1] = 0;
        _sendBytes = 2;
        _readBytes = 0;
        return sendMessage();
    }

    public bool stopMotor2()
    {
        _buffer = new byte[32];
        _buffer[0] = 0xC8;
        _buffer[1] = 0;
        _sendBytes = 2;
        _readBytes = 0;
        return sendMessage();
    }

    /*
     * Send Message Method
     *
     * Opens and closes serial ports
     * Calls sendCommandPacket Method
     */
    private bool sendMessage() {

        // Reset class strings
        _str = "";
        _echo = "";
        _receive = "";
        _transmit = "";

        try {
            // Open serial port
            _serialPort.Open();

            // Send packet
            if (!(sendCommandPacket(_buffer, _sendBytes, _readBytes))) {
                //MessageBox.Show("Failed to send command to device");
                return false;
            }
            else {
                // Read buffer as string
                for (int i = 0; i < _readBytes; i++) {
```

```
                    // ASCII 32 to 127 are alphanumeric (including space and symbols)
                    // The rest are special ASCII chars so output raw
                    if (_buffer[i] >= 32 && _buffer[i] <= 127) {
                        // Cast to character type
                        _str += (char)_buffer[i];
                    }
                    else {
                        // Convert to string
                        _str += _buffer[i].ToString();
                    }
                }
            }
        }
        catch (Exception) {
            //MessageBox.Show("Exception occurred");
            return false;
        }

        // Close Serial port
        if (_serialPort.IsOpen) {
            _serialPort.Close();
        }
        return true;
    }

    /*
     * Send Command Packet Method
     *
     * Reads and writes to and from serial port
     */
    private bool sendCommandPacket(byte[] packet, int sendBytes, int readBytes)  {

        int i;

        try { // Read any unread bytes in the read buffer
            while (_serialPort.BytesToRead > 0) {
                _serialPort.ReadByte();
            }
        }
        catch{
            //MessageBox.Show("Unable to read unread bytes in read buffer");
            return false;
        }

        try { // Get transmit string
            for (i = 0; i < sendBytes; i++) {
                _transmit += packet[i].ToString("X2") + " ";
            }
        }
        catch {
            //MessageBox.Show("Unable to convert transmit byte packet to string");
            return false;
        }

        try { // Write command packet
            _serialPort.Write(packet, 0, sendBytes);
        }
        catch {
            //MessageBox.Show("Unable to write command packet buffer to serial
port");
            return false;
        }
```

```
        try { // Get echo
            for (i = 0; i < sendBytes; i++) {
                _echo += _serialPort.ReadByte().ToString("X2") + " ";
            }
        }
        catch {
            //MessageBox.Show("Unable to read echo string");
            return false;
        }

        try { // Get receive string
            for (i = 0; i < readBytes; i++) {
                packet[i] = (byte)_serialPort.ReadByte();
                _receive += packet[i].ToString("X2") + " ";
            }
        }
        catch (Exception) {
            //MessageBox.Show("Unable to read receive string");
            return false;
        }

        return true;
    }

}
```

Main Program class

```
/*
 * Main program class
 * Danial Khoshkhou
 * October 2014
 */

using System;
using System.Collections.Generic;
using System.Linq;
using System.Threading.Tasks;
using System.Windows.Forms;

namespace test_3
{
    static class Program
    {
        /// <summary>
        /// The main entry point for the application.
        /// </summary>
        [STAThread]
        static void Main()
        {
            Application.EnableVisualStyles();
            Application.SetCompatibleTextRenderingDefault(false);
            Application.Run(new Form1());
        }
    }
}
```

Appendix D: TGO/bondcoat profiles (MATLAB)

```
%% TGO/Bondcoat interface profile extraction
%  Script to analyse TGO/bondcoat interface from SEM images processed using
%  ImageJ.  2 inputs images are required, both of the same dimensions
%  (5000x750 pixels in this case). The first is the original SEM image and
%  the second is a binarised version of the TGO/bondcoat interface extracted
%  from the SEM image using ImageJ.
%  In addition, the location of the grit line centroids should be placed in
%  the same directory as the SEM and interface images.  The centroids should
%  be located in a variable named grit_line_centroids.
%
%  Author: Danial Khoshkhou, University of Birmingham, June 2015

%% Clean up
%  Close any open figures and clear all variables
clear all;
close all;

%% User inputs
%  SEM scale (microns/pixels)
scale = 10/276;

%% Read image and data files
%  Read original SEM image and binarised interface
I = flipud(imread('MosaicJ_5000x750.jpg'));
B = flipud(imread('MosaicJ_5000x750_interface.tif'));

%  Read grit line centroids (x,y coordinates)
load('grit_line_centroids.mat');

%% Get image dimensions from original SEM image
h = size(I, 1);
w = size(I, 2);

%% Process grit line centroids and interpolate
%  Read X and Y coordinates (Y reverse for read order)
xg = grit_line_centroids(:, 1); %
yg = h - grit_line_centroids(:, 2);

%  Calculate mean grit line position
ygm = mean(yg);

%  Interpolated between grit line coordinates
%  Uses Piecewise Cubic Hermite Interpolating Polynomial
xgi = (1:w);
ygi = interp1(xg, yg, 1:w, 'pchip');

%% Process TGO/Bondcoat interface
%  Create variables to store x and y interface coordinates
xif = 1:w;
yif = zeros(1, w);

%  Loop through columns and get height in pixels (first non-zero pixel)
for i = 1:w
    yif(i) = mean(find(~B(:, i)));
end

%  Calculate mean position
yifm = mean(yif);

%% Display figure
%  Create figure
```

```
figure('Color', 'w');
%  Display image
%  NOTE: MATLAB Image Processing Toolbox is required for this function
imshow(I, 'XData', [0, w*scale], 'YData', [-ygm*scale,(h-ygm)*scale]);
 %  Allow plotting multiple items
hold on;
plot(xif*scale, (yif-ygm)*scale,'color','red','LineWidth',3);
%scatter(xg*scale, (yg-ygm)*scale);
plot(xgi*scale, (ygi-ygm)*scale,'color','blue','LineWidth',3);
line([0, w]*scale,[yifm-ygm, yifm-ygm]*scale,'color','red','LineWidth',3);
line([0, w]*scale, [0, 0],'color','blue','LineWidth',3);
hold off;

%  Use correct axes instead of the default reversed axes for imshow
axis xy;
%  Set font size for axes
set(gca,'FontSize',20);

xlabel('X (\mum)');
ylabel('Y (\mum)');
```

Appendix E: Bondcoat creep profiles (MATLAB)

Main script

```
%% Force balance approach to bondcoat relaxation under TGO growth
%  The purpose of this MATLAB script is to calculate:
%    1. Displacement profiles from micrographs and manual coordinates
%    2. Strains from as-received sample diameters
%    3. Bondcoat creep stress from Empirical models
%    4. Total force acting on bondcoat by TGO
%    5. Equivalent stress in TGO from total force on bondcoat
%
%  This script depends on two functions written as part of this work:
%    1. fn_creep_micrograph to produce profile figures from micrographs
%    2. fn_strain_rate to calculate interpolated derivative of strain

%  This script requires the following MATLAB Toolboxes:
%    1. Image Processing
%    2. Curve Fitting
%
%  Author: Danial Khoshkhou, University of Birmingham, September 2015

%% Clean up
%  Close any open figures and clear all variables
close all;
clear all;

%% User Inputs
%  SEM scale (microns/pixels)
scale = 10/85;

%  Image files
I1 = imread('right0.jpg');
I2 = imread('right20.jpg');
I3 = imread('right40.jpg');
I4 = imread('right80.jpg');

%  Position of TGO (from image top, in pixels)
tgo1 = 200;
tgo2 = 180;
tgo3 = 200;
tgo4 = 200;

%  Position of substrate edge (from image left, in pixels)
sub1 = 1180;
sub2 = 790;
sub3 = 850;
sub4 = 660;

%  Coordinates for profile in x,y pairs
x1 = [1180;1180;1180;1180;1180;1180;1180;1180;1175;1170;1163;1150;1135;1120];
y1 = [850;800;750;700;650;600;550;500;450;400;350;300;250;200];
x2 = [790;850;880;910;930;950;965;975;980;985;990;995;1000;1005];
y2 = [830;780;730;680;630;580;530;480;430;380;330;280;230;180];
x3 = [850;900;950;1000;1040;1070;1095;1110;1125;1140;1150;1155;1160;1162];
y3 = [850;800;750;700;650;600;550;500;450;400;350;300;250;200];
x4 = [660;745;810;860;905;940;970;1000;1020;1045;1060;1085;1102;1115];
y4 = [850;800;750;700;650;600;550;500;450;400;350;300;250;200];

%  As-received sample diameter for strain calculations
```

```
D1 = 1073.83; %  As-received of 20 hour sample (20-C-2)
D2 = 1009.35; %  As-received of 40 hour sample (20-D-1)
D3 = 1077.57; %  As-received of 80 hour sample (20-D-4)

%  Time
time = [72000;144000;288000]; %  20 hours, 40 hours, 80 hours

%  Creep parameters (from Taylor et al. 2006 Acta Mat.) for creep stress
R = 8.314;
T = 1373;
%  n
n1 = 6.82; %  1% strain
n2 = 8.90; %  3% strain
n3 = 9.43; %  9% strain
%  Q (J mol-1)
Q1 = 616000; %  1% strain
Q2 = 684200; %  3% strain
Q3 = 537000; %  9% strain
%  A (MPa-ns-1)
A1 = 8.75E+08; %  1% strain
A2 = 2.94E+07; %  3% strain
A3 = 1.26E-01; %  9% strain

%  TGO thicknesses (for force balance TGO stress calculation)
tgot1 = 2.221E-06; %  20 hours
tgot2 = 2.572E-06; %  40 hours
tgot3 = 3.788E-06; %  80 hours

%% Plot figures on micrographs
%  Call external function to produce figures in pixels and micrometres
[xi1, yi1] = fn_creep_micrograph(scale, I1, tgo1, sub1, x1, y1, false);
[xi2, yi2] = fn_creep_micrograph(scale, I2, tgo2, sub2, x2, y2, false);
[xi3, yi3] = fn_creep_micrograph(scale, I3, tgo3, sub3, x3, y3, false);
[xi4, yi4] = fn_creep_micrograph(scale, I4, tgo4, sub4, x4, y4, false);

%% Adjust displacement profiles for machining damage
%  Correct 20, 40 and 80 hour displacements relative to as-received
yi = yi1-min(yi1);

xi1 = xi1-max(xi1);
xi2 = flipud(xi2-min(xi2)-xi1);
xi3 = flipud(xi3-min(xi3)-xi1);
xi4 = flipud(xi4-min(xi4)-xi1);

%% Calculate interpolated strain rates
%  Calculate strains for each sample
e1 = xi2/(D1/2);
e2 = xi3/(D2/2);
e3 = xi4/(D3/2);

%  Generate time interval in seconds
times = linspace(0,288000, 3600);
timeh = times/3600;

%  Call external function to calculate interpolated strain rates
[ei, dei] = fn_strain_rate(yi,e1,e2,e3,time);

%% Calculate Creep Stress
%  Calculate creep stress from empirical relationships
s1 = ((dei/A1)*exp(Q1/(R*T))).^(1/n1);
s2 = ((dei/A2)*exp(Q2/(R*T))).^(1/n2);
s3 = ((dei/A3)*exp(Q3/(R*T))).^(1/n3);

figure('color', 'w');
hold on;
```

```
plot(times, s1, 'black');
plot(times, s2, 'red');
plot(times, s3, 'blue');
hold off;

%% Calculate Force
%  Calculate force (1-D area)
f1 = sum(s1,2)*(yi(2));
f2 = sum(s2,2)*(yi(2));
f3 = sum(s3,2)*(yi(2));

%  Plot figure
figure('color', 'w');
hold on;
plot(times, f1, 'black');
plot(times, f2, 'black');
plot(times, f3, 'black');
hold off;

%% Calculate TGO stress
%  Calculate 1-D stresses and convert to MPa
ts1 = (f1/tgot1)/1E6;
ts2 = (f2/tgot2)/1E6;
ts3 = (f3/tgot3)/1E6;

%  Plot figure
figure('color', 'w');
hold on;
plot(times, ts1, 'black');
plot(times, ts2, 'black');
plot(times, ts3, 'black');
hold off;
```

Function to calculate transformed displacement profiles

```
function [x_interp_s, y_interp_s] = fn_creep_micrograph(scale, I, tgo, sub, x,
y, pixels)
%FN_CREEP_MICROGRAPH Function to visualise bondcoat creep on micrographs
%   Creates two figures (pixels and microns) and returns interpolated
%   profile fit.
%
%   scale = ratio of microns/pixels
%   I = result of imread function after opening micrograph
%   tgo = pixels from top of image coinciding with TGO plane
%   sub = pixels from left of image coinciding with substrate edge
%   x = [1xn] matrix of discrete profile x coordinates
%   y = [1xn] matrix of discrete profile y coordinates

    %% Calculate profile from coordinates
    %  Calculate image dimensions
    width = size(I, 2);
    height = size(I, 1);

    %  Calculate fitted curve using Two-term exponential fit of the form
    %  f(x)=a*x^b+c
    %  NOTE: MATLAB Curve Fitting toolbox is required for this function
    creep_fit = fit(y, x, 'exp2');

    %  Use 100 equally spaced values to calculated interpolated fit
    y_interp = linspace(y(1), y(end), 100);
    x_interp = feval(creep_fit,y_interp);

    %  The following line (with no semicolon) prints fit model and coeffs
    creep_fit

    %% Scale to micrometres for output and second figure
    x_interp_s = x_interp*scale;
    y_interp_s =((height - y_interp)*scale).';

    %% Create figure (PIXELS)
    %  Create new figure with white background (if option is set)
    if pixels == true
        figure('color', 'w');

        %  Display image
        %  NOTE: MATLAB Image Processing Toolbox is required for this function
        imshow(I);

        %  Allow further plots on this figure
        hold on;
        %  Draw TGO reference line
        line([1, width], [tgo, tgo], 'color', 'red', 'LineWidth', 3)
        %  Draw bondcoat reference line
        line([sub, sub], [1, height], 'color', 'red', 'LineWidth', 3)
        %  Plot interpolated curve
        plot(x_interp, y_interp, 'color', 'red', 'LineWidth', 3);
        %  Plot individual curve points
        scatter(x, y, 'red', 'LineWidth', 3);
        %  Turn off multiple plots per figure
        hold off;
    end
    %% Create figure (MICROMETRES)
    %  Create new figure with white background
    figure('color', 'w');

    %  Display image
    %  NOTE: MATLAB Image Processing Toolbox is required for this function
```

```
    imshow(flipud(I), 'XData', [0, width*scale], 'YData', [0, height*scale]);

    %  Allow further plots on this figure
    hold on;
    %  Draw TGO reference line
    line([1, width]*scale, [(height-tgo), (height-tgo)]*scale, 'color', 'red',
'LineWidth', 3)
    %  Draw bondcoat reference line
    line([sub, sub]*scale, [1, height]*scale, 'color', 'red', 'LineWidth', 3)
    %  Plot interpolated curve
    plot(x_interp*scale, (height-y_interp)*scale, 'color', 'red', 'LineWidth',
3);
    %  Plot individual curve points
    scatter(x*scale, (height-y)*scale, 'red', 'LineWidth', 3);
    %  Turn off multiple plots per figure
    hold off;

    %  Reverse y-axis direction
    set(gca, 'YDir', 'normal');
    % Set axes labels and spacing
    set(gca, 'XTick', [0, 50, 100, 150]);
    set(gca, 'YTick', [0, 50, 100]);
    %  Set font size for axes
    set(gca, 'FontSize', 28);
end
```

Function to calculate strain rates

```
function [ey, dey] = fn_strain_rate(x, y1, y2, y3, time)
%FN_STRAIN_RATE Function to calculate strain rate from strains
%   Calculates interpolated strain as a function of time for various
%   vertical positions from the TGO/bondcoat interface.  These strains are
%   then used to calculate strain rates and both strain and strain rates
%   are returned and plotted.
%

    %  Generate interpolated strain x-coordinates (time in seconds)
    ex = linspace(0,288000, 3600);
    %  Build output array to store interpolated strains
    ey = zeros(numel(ex), numel(time));
    %  Build output array to store interpolated strain rates
    dey = ey;

    %  Loop through input vertical displacement
    for i = 1:numel(x)
        %  Get displacements as a function of time across timesteps
        ei = [y1(i); y2(i); y3(i)];
        %  Fit a 1-term power law fit to these displacements
        efit = fit(time, ei, 'power1');
        %  Calculate interpolated curve at x-values
        ey(:, i) = feval(efit, ex);
        %  Calculate derivative of fit at interpolated x values
        dey(:, i) = differentiate(efit, ex);
    end

    %  Plot strains as a function of time
    figure('color', 'w');
    plot(ex, ey, 'black');
    %  Plot strain rates as a function of time
    figure('color', 'w');
    plot(ex, dey, 'black');
end
```

Appendix F: Bondcoat creep input file (ABAQUS)

Main input file

```
*HEADING
  BONDCOAT CREEP WITH ELASTOPLASTIC MATERIAL DEFINITION
*NODE
 1,1.,0.
 8,8.,0.
 101,1.,10.
 108,8,10.
*NGEN,NSET=BOT
 1,8
*NGEN,NSET=TOP
101,108
*NSET,NSET=LEFT
1,101,3,103,5,105,7,107
*ELEMENT,TYPE=CPS4
 1,1,2,102,101
*ELGEN
1,4,2
*ELSET,ELSET=DATTIM
1,
*ELSET,ELSET=DATSTR
2,
*ELSET,ELSET=USETIM
3,
*ELSET,ELSET=USESTR
4,
*ELSET,ELSET=CREEPERS
1,2,3,4
*SOLID SECTION,ELSET=DATTIM,MATERIAL=A1
*MATERIAL,NAME= A1
*ELASTIC
20E6,.3
*CREEP,LAW=TIME
2.5E-27,5,-0.2
*SOLID SECTION,ELSET=DATSTR,MATERIAL=A2
*MATERIAL,NAME= A2
*ELASTIC
20E6,.3
*CREEP,LAW=STRAIN
2.5E-27,5,-0.2
*SOLID SECTION,ELSET=USETIM,MATERIAL=A3
*MATERIAL,NAME= A3
*ELASTIC
20E6,.3
*CREEP,LAW=USER
*SOLID SECTION,ELSET=USESTR,MATERIAL=A4
*MATERIAL,NAME= A4
```

```
*ELASTIC
20E6,.3
*CREEP,LAW=USER
*DEPVAR
2,
*BOUNDARY
BOT,2
LEFT,1
*****
*****
*RESTART,WRITE,FREQUENCY=20

*STEP
**          STEP 1 ----- ELASTIC LOADING
*STATIC
1.0E-7,1.0E-7
*DLOAD
1,P3,-20000.
2,P3,-20000.
3,P3,-20000.
4,P3,-20000.
*EL FILE,FREQUENCY=20
SDV,
S,
CE,
*END STEP
*STEP,INC=250
**          STEP 2 ----- CREEP TEST
*VISCO,CETOL=5E-6
.01,100000.,1.E-3
*PRINT,FREQUENCY=5,RESIDUAL=NO
*EL
PRINT,ELSET=CREEPERS,FREQUENCY=20,POSITION=CENTROID,SUMMARY=NO
SDV,S
CE,
*EL FILE,ELSET=CREEPERS,FREQUENCY=20,POSITION=CENTROID
SDV,S,CE,
*NODE PRINT,FREQUENCY=20
RF,
*END STEP
```

User subroutine for ABAQUS creep model (FORTRAN)

```
C
      SUBROUTINE CREEP(DECRA,DESWA,STATEV,SERD,EC,ESW,P,QTILD,
     1 TEMP,DTEMP,PREDEF,DPRED,TIME,DTIME,CMNAME,LEXIMP,LEND,
     2 COORDS,NSTATV,NOEL,NPT,LAYER,KSPT,KSTEP,KINC)
C
      INCLUDE 'ABA_PARAM.INC'
C
      CHARACTER*80 CMNAME
C
      DIMENSION DECRA(5),DESWA(5),STATEV(*),PREDEF(*),DPRED(*),
     1 TIME(3),EC(2),ESW(2),COORDS(*)
C
      DIMENSION VARIABLE(1)
      A=0.126
      AN=9.43
      Q=53700
      R=8.314
C
      DECRA(1) = A*(QTILD**AN)*EXP(-Q/(R*1473))*DTIME
C
      IF(LEXIMP.EQ.1) THEN
      DECRA(5) = A*AN*(QTILD**(AN-1))*EXP(-Q/(R*1473))*DTIME
      END IF
C
      READ(*,*), VARIABLE
      RETURN
      END
```

Appendix G: 3-D rigid body rotation correction

Euler rotations and quaternions are used to calculate the centre of rotation and remove rigid body rotations from digital volume correlation (DVC) displacement fields. The centre of interrogation windows, where the displacement vectors are calculated, with respect to a reference Cartesian coordinates can be represented as

$$[X_i^0] = [x_i^0, y_i^0, z_i^0]$$

After oxidation and subsequent deformation, the positions of the centres are denoted by

$$[X_i^1] = [x_i^1, y_i^1, z_i^1]$$

Therefore the displacement vector for each point

$$[U_i] = \left[u_i^x, u_i^y, u_i^z\right]$$

is defined as:

$$[U_i] = [X_i^1] - [X_i^0] \qquad \textit{Eq. 35}$$

The first step is to calculate the rigid body translation, i.e.

$$[\bar{U}] = [\bar{u}^x, \bar{u}^y, \bar{u}^z]$$

The rigid body translations are defined as:

$$\bar{u}^x = \frac{\sum_{i=1}^{N} u_i^x}{n}, \bar{u}^y = \frac{\sum_{i=1}^{N} u_i^y}{n}, \bar{u}^z = \frac{\sum_{i=1}^{N} u_i^z}{n} \qquad \textit{Eq. 36}$$

where N is the number of calculated vectors. The centre of rigid body rotation, i.e.

$$[\bar{X}] = [\bar{x}, \bar{y}, \bar{z}]$$

is assumed to be the point with zero rigid body translation, i.e. the point that minimises the quantity:

$$(\bar{u}^x - \bar{u}_i^x)^2 + \left(\bar{u}^y - \bar{u}_i^y\right)^2 + (\bar{u}^z - \bar{u}_i^z)^2$$

The reference coordinates of the centre of the interrogation windows with respect to the centre of rotation is calculated by:

$$[\bar{X}_i^0] = [X_i^0] - [\bar{X}] \qquad \textit{Eq. 37}$$

The position of each point after deformation, corrected for rigid body translation is therefore described by:

$$\left[X_i^{1,CT}\right] = [\bar{X}_i^0] + [U_i] - [\bar{U}] \qquad \textit{Eq. 38}$$

where CT is the corrected translation. Assuming that the displacements due to loading are negligible compared with the displacements due to rigid body rotation; the final position of each point with respect to its reference position can be described as:

$$[\bar{X}_1^0]_{n\times 3}[M]_{3\times 3} = \left[X_1^{1,CT}\right]_{n\times 3}$$

i.e.

$$\begin{bmatrix} \bar{X}_1^0 \\ \bar{X}_2^0 \\ \vdots \\ \bar{X}_n^0 \end{bmatrix}_{n\times 3} [M]_{3\times 3} = \begin{bmatrix} X_1^{1,CT} \\ X_2^{1,CT} \\ \vdots \\ X_n^{1,CT} \end{bmatrix}_{n\times 3} \qquad \textit{Eq. 39}$$

where n is the number of the calculated vectors and transformation matrix $[M]_{3\times 3}$ is:

$$[M]_{3\times 3} = \begin{bmatrix} m_{11} & m_{12} & m_{13} \\ m_{21} & m_{22} & m_{23} \\ m_{31} & m_{32} & m_{33} \end{bmatrix} \qquad \textit{Eq. 40}$$

If the Euler rotation is considered to be taking place in a sequence of yaw (rotation around z axis, ϕ) followed by pitch (rotation around y axis, θ) followed by roll (rotation around x axis, ψ), the theoretical conversion matrix can be represented as:

$$\begin{bmatrix} \cos\theta\cos\varphi & \cos\theta\sin\varphi & -\sin\theta \\ \sin\psi\sin\theta\cos\varphi - \cos\psi\sin\varphi & \sin\psi\sin\theta\sin\varphi + \cos\psi\cos\theta & \cos\theta\sin\psi \\ \cos\psi\sin\theta\cos\varphi + \sin\psi\sin\varphi & \cos\psi\sin\theta\sin\varphi - \sin\psi\cos\varphi & \cos\theta\cos\psi \end{bmatrix} \qquad \textit{Eq. 41}$$

The provisional conversion matrix can be extracted from the experimentally obtained data:

$$[M]_{3\times3} = [\bar{X}_1^0]^+_{3\times n}[X^{1,CT}]_{n\times3} \quad \textit{Eq. 42}$$

where $[\bar{X}_1^0]^+_{3\times n}$ denotes the Moore-Penrose pseudoinverse of $[\bar{X}_1^0]_{3\times n}$. To avoid numerical instability, ranks of $[\bar{X}_1^0]_{3\times n}$ and $[X^{1,CT}]_{n\times3}$ are calculated at this stage to ensure that none of the three singular values of each matrix are zero. As an additional check, $[M][M]^T$ is calculated which should be an identity matrix. The theoretical rotations angles are extracted from the provisional rotation matrix using Shoemake's method [176]:

$$\varphi = \text{atan2}(m_{12}, m_{11})$$

$$\theta = \text{atan2}(-m_{13}, \sqrt{m_{11}^2 + m_{12}^2}) \quad \textit{Eq. 43}$$

$$\psi = \text{atan2}(m_{23}, m_{33})$$

where $\text{atan2}(m_i, m_j)$ returns the angle between the positive x-axis of a plane and the point given by the coordinates (m_i, m_j); this enables the atan function to return the appropriate quadrant of the computed angle. Using Eq. 41 and Eq. 43, the theoretical displacement due to rigid body rotation is calculated by:

$$[\bar{X}^{1,CT}]_{n\times3} = [\bar{X}_1^0]_{n\times3}[M]_{3\times3} \quad \textit{Eq. 44}$$

Finally, the position of the centre of the interrogation windows after correction for both rigid body translation and rotation $[X^{1,CT,CR}]$ is calculated from:

$$[X^{1,CT,CR}] = [\bar{X}^{1,CT}][\bar{X}^{1,CT}] \quad \textit{Eq. 45}$$

Appendix H: DVC displacement extraction (MATLAB)

2-D plane extraction

```
%% Script to visualise dvc data
%  Danial Khoshkhou
%  University of Birmingham

% v1.0  Initial release
% v1.1  Changed subplots to individual figures
% v1.2  Changed way distance between vector points were calculated from
%       manual to calculated from distance between unique non-nan values
% v1.3  Moved plotting logic into separate function
% v1.4  Added code to fill in NaN values for X, Y and Z coordinate data

%% User inputs for images

% % % % % % % % % % clear
%  Load data from current working directory
load(strcat(pwd, filesep, 'DVC_Corrected_Exp3RRPtUC1200Step1.mat'));
%load(strcat(pwd, filesep, 'DVC_Corrected_Exp3RRPtUC1200Step2.mat'));
%load(strcat(pwd, filesep, 'DVC_Corrected_Exp3RRPtUC1200Step3.mat'));
%load(strcat(pwd, filesep, 'DVC_Corrected_Exp1RRPtAlUC1200Step1.mat'));
%load(strcat(pwd, filesep, 'DVC_Corrected_Exp1RRPtAlUC1200Step2.mat'));
%load(strcat(pwd, filesep, 'DVC_Corrected_Exp1RRPtAlUC1200Step3.mat'));


%  Raw input file (convert from mm to micron)
data = DVC_Corrected_Exp3RRPtUC1200Step1 * 1000;

%  Raw DVC image dimensions (x,y pixel count and number of images in z)
dim_x = 73; % Image x dimension
dim_y = 73; % Image y dimension
dim_z = 67; % Image z dimension (number of images in stack)

%  Image planes (for 2-d planes of interest)
plane_z = 46; % x-y plane number
plane_y = 35; % x-z plane number
plane_x = 35; % y-z plane number

%  Radial averaging centre point
centre_x = 36;
centre_y = 36;

%  Colour bars for contour plots
colourbar_min_u = -5;
colourbar_max_u = 13;
colourbar_min_v = -5;
colourbar_max_v = 13;
colourbar_min_w = -5;
colourbar_max_w = 13;

%% Other user inputs

%  Zoomed in sub-image (rectangle)
zoom_plane = 'xy'; % Options are xy, xz and yz
zoom_x = 155; % x-coordinate
zoom_y = 175; % y-coordinate
zoom_h = 200; % rectangle height
```

```
zoom_w = 200; % rectangle width

%  Units (for axes titles)
units_x = '\mum'; % \mu = micron
units_y = '\mum'; % \mu = micron
units_z = '\mum'; % \mu = micron

%  Contour line density for contour plots
contours_xy = 20;
contours_xz = 20;
contours_yz = 20;
contours_zoom = 10;

%  Contour line units
colorBarUnits_u = 'U Displacement (\mum)';
colorBarUnits_v = 'V Displacement (\mum)';
colorBarUnits_w = 'W Displacement (\mum)';

%  Downsampling for concentric plots
downsampling = 1;
%% Clean-up operations

% Change default axes fonts.
set(0,'DefaultUipanelBackgroundColor',[1 1 1]);
set(0,'DefaultAxesFontName', 'Times New Roman')
set(0,'DefaultAxesFontSize', 24)
% Change default text fonts.
set(0,'DefaultTextFontname', 'Times New Roman')
set(0,'DefaultTextFontSize', 24)

% Close any open figures
delete(findall(0,'Type','figure'));

% Clear command window
clc;

% Start performance stopwatch
tic;

%% Create X, Y and Z coordinate data and U, V, W displacement data

disp('Generating X, Y and Z spatial coordinates.');

%  Get max and min values (used to reposition plots)
min_x = min(data(:, 1));
min_y = min(data(:, 2));
min_z = min(data(:, 3));
min_u = min(data(:, 4));
min_v = min(data(:, 5));
min_w = min(data(:, 6));
max_x = max(data(:, 1));
max_y = max(data(:, 2));
max_z = max(data(:, 3));
max_u = max(data(:, 1));
max_v = max(data(:, 2));
max_w = max(data(:, 3));

%  Select subsets from main data and reset coordinates positions
%  Use reshape to make 3d matrix from columnar data
X = reshape(data(:, 1), dim_x, dim_y, dim_z) - min_x;
Y = reshape(data(:, 2), dim_x, dim_y, dim_z) - min_y;
Z = abs(reshape(data(:, 3), dim_x, dim_y, dim_z) - min_z - max(data(:, 3) -
min_z)); % Z-data is backwards because of image read byte order
U = reshape(data(:, 4), dim_x, dim_y, dim_z);
V = reshape(data(:, 5), dim_x, dim_y, dim_z);
```

```
W = -reshape(data(:, 6), dim_x, dim_y, dim_z); % Negative w because of flipped
z

%% Replace NaNs in coordinates with appropriate values
%  Fill in empty data points with unique values from a single plane
for i = 1:dim_x
    %  Find unique value x for ith plane and replace
    X_i = X(i, :, :);

    % Calculate unique value per plane
    x_i = unique(X_i(~isnan(X_i)));

    %  Use if statement to account for any planes that are all NaN
    if ~isempty(x_i)
        %  Replace all values on plane with unique value
       X(i, :, :) = x_i;
    else
        X(i, :, :) = 0;
    end
end

for j = 1:dim_y
    %  Find unique value y for jth plane and replace
    Y_i = Y(:, j, :);

    % Calculate unique value per plane
    y_i = unique(Y_i(~isnan(Y_i)));

    %  Use if statement to account for any planes that are all NaN
    if ~isempty(y_i)
        %  Replace all values on plane with unique value
       Y(:, j, :) = y_i;
    else
        Y(:, j, :) = 0;
    end
end

for k = 1:dim_z
    %  Find unique value y for jth plane and replace
    Z_i = Z(:, :, k);

    % Calculate unique value per plane
    z_i = unique(Z_i(~isnan(Z_i)));

    %  Use if statement to account for any planes that are all NaN
    if ~isempty(z_i)
        %  Replace all values on plane with unique value
       Z(:, :, k) = z_i;
    else
        Z(:, :, k) = 0;
    end
end

%% Calculate grid spacing from difference between each spatial coordinate
delta_x = min(diff(unique(X(~isnan(X)))));
delta_y = min(diff(unique(Y(~isnan(Y)))));
delta_z = min(diff(unique(Z(~isnan(Z)))));

disp('Spatial coordinates (X, Y, Z) and displacement data (U, V, W)
prepared.');
disp(strcat('Coordinate spacing of x=', num2str(delta_x), ' y=',
num2str(delta_y), ' z=', num2str(delta_z)));

%% Get X-Y, X-Z and Y-Z planar profiles
```

```
disp('Extracting X-Y, X-Z and Y-Z profiles');

%  Invert z and y for image byte read order
plane_z = dim_z - plane_z;
plane_y = dim_y - plane_y;

%  Get x-y plane from specified z
xy_x = fliplr(rot90(X(:, :, plane_z), 3));
xy_y = fliplr(rot90(Y(:, :, plane_z), 3));
xy_u = fliplr(rot90(U(:, :, plane_z), 3));
xy_v = fliplr(rot90(V(:, :, plane_z), 3));
xy_w = fliplr(rot90(W(:, :, plane_z), 3));

%  Get x-z plane from specified y
%  Use squeeze() to get (i x k) from (i x 1 x k)
xz_x = squeeze(X(:, plane_y, :));
xz_z = squeeze(Z(:, plane_y, :));
xz_u = squeeze(U(:, plane_y, :));
xz_v = squeeze(V(:, plane_y, :));
xz_w = squeeze(W(:, plane_y, :));

%  Get y-z plane from specified x
%  Use squeeze() to get (i x k) from (i x 1 x k)
yz_y = squeeze(Y(plane_x, :, :));
yz_z = squeeze(Z(plane_x, :, :));
yz_u = squeeze(U(plane_x, :, :));
yz_v = squeeze(V(plane_x, :, :));
yz_w = squeeze(W(plane_x, :, :));

disp('All planes extracted');

%% Begin figures and plots section

disp('Generating plots');

%  Calculate position of lines
%  X-Y plane lines
line_xy_xz_x = [0 (dim_x * delta_x)]; % X-Z horizontal
line_xy_xz_y = [((dim_y - plane_y) * delta_y) ((dim_y - plane_y) * delta_y)];
line_xy_yz_x = [(plane_x * delta_x) (plane_x * delta_x)]; % Y-Z vertical
line_xy_yz_y = [0 (dim_y * delta_y)];
%  X-Z planes lines
line_xz_xy_x = [0 (dim_x * delta_x)]; % X-Y horizontal
line_xz_xy_y = [((dim_z - plane_z) * delta_z) ((dim_z - plane_z) * delta_z)];
line_xz_yz_x = [(plane_x * delta_x) (plane_x * delta_x)]; % Y-Z vertical
line_xz_yz_y = [0 (dim_z * delta_z)];
%  Y-Z planes lines
line_yz_xy_x = [0 (dim_y * delta_y)]; % X-Y horizontal
line_yz_xy_y = [((dim_z - plane_z) * delta_z) ((dim_z - plane_z) * delta_z)];
line_yz_xz_x = [(plane_y * delta_y) (plane_y * delta_y)]; % X-Z vertical
line_yz_xz_y = [0 (dim_z * delta_z)];

%  Calculate position of line labels
%  X-Y
text_xy_xz_x = delta_x;
text_xy_xz_y = (dim_y - plane_y) * delta_y;
text_xy_yz_x = plane_x * delta_x;
text_xy_yz_y = delta_y;
%  X-Z
text_xz_xy_x = delta_x;
text_xz_xy_y = (dim_z - plane_z) * delta_z;
text_xz_yz_x = plane_x * delta_x;
text_xz_yz_y = delta_z;
%  Y-Z
text_yz_xy_x = delta_y;
```

```
text_yz_xy_y = (dim_z - plane_z) * delta_z;
text_yz_xz_x = plane_y * delta_y;
text_yz_xz_y = delta_y;

%  Prepare figure titles
title_xy_u = strcat('U component of displacement on X-Y plane at Z=',
num2str((dim_z - plane_z) * delta_z), units_z, ' (Z-plane=', num2str(dim_z -
plane_z), ')');
title_xy_v = strcat('V component of displacement on X-Y plane at Z=',
num2str((dim_z - plane_z) * delta_z), units_z, ' (Z-plane=', num2str(dim_z -
plane_z), ')');
title_xy_w = strcat('W component of displacement on X-Y plane at Z=',
num2str((dim_z - plane_z) * delta_z), units_z, ' (Z-plane=', num2str(dim_z -
plane_z), ')');
title_xz_u = strcat('U component of displacement on X-Z plane at Y=',
num2str((dim_y - plane_y) * delta_y), units_y, ' (Y-plane=', num2str(dim_y -
plane_y), ')');
title_xz_w = strcat('W component of displacement on X-Z plane at Y=',
num2str((dim_y - plane_y) * delta_y), units_y, ' (Y-plane=', num2str(dim_y -
plane_y), ')');
title_yz_v = strcat('V component of displacement on Y-Z plane at X=',
num2str(plane_x * delta_x), units_x, ' (X-plane=', num2str(plane_x), ')');
title_yz_w = strcat('W component of displacement on Y-Z plane at X=',
num2str(plane_x * delta_x), units_x, ' (X-plane=', num2str(plane_x), ')');

%  Prepare figure labels
label_xy_x = strcat('X position (', units_x, ')');
label_xy_y = strcat('Y position (', units_y, ')');
label_xz_x = strcat('X position (', units_x, ')');
label_xz_y = strcat('Z position (', units_z, ')');
label_yz_x = strcat('Y position (', units_y, ')');
label_yz_y = strcat('Z position (', units_z, ')');

%  Prepare colourbars
colourbar_axis_u = [colourbar_min_u, colourbar_max_u];
colourbar_axis_v = [colourbar_min_v, colourbar_max_v];
colourbar_axis_w = [colourbar_min_w, colourbar_max_w];

%  Prepare axis limits
lim_x = [0 (max_x - min_x)];
lim_y = [0 (max_y - min_y)];
lim_z = [0 (max_z - min_z)];

%  Invert z and y because of image byte read order
plane_z = dim_z - plane_z;
plane_y = dim_y - plane_y;

%% Plot planes

%  Plot X-Y of U for specified Z plane
plotPlanes(xy_x, xy_y, xy_u, xy_v, xy_u, title_xy_u, label_xy_x, label_xy_y,
colorBarUnits_u, colourbar_axis_u, lim_x, lim_y, 'X-Z', 'Y-Z', plane_y,
delta_y, plane_x, delta_x);

%  Plot X-Y of V for specified Z plane
plotPlanes(xy_x, xy_y, xy_u, xy_v, xy_v, title_xy_v, label_xy_x, label_xy_y,
colorBarUnits_v, colourbar_axis_v, lim_x, lim_y, 'X-Z', 'Y-Z', plane_y,
delta_y, plane_x, delta_x);

%  Plot X-Z of U for specified Y plane
plotPlanes(xz_x, xz_z, xz_u, xz_w, abs(xz_u), title_xz_u, label_xz_x,
label_xz_y, colorBarUnits_u, colourbar_axis_u, lim_x, lim_z, 'X-Y', 'Y-Z',
plane_z, delta_z, plane_x, delta_x);

%  Plot X-Z of W for specified Y plane
```

```
plotPlanes(xz_x, xz_z, xz_u, xz_w, xz_w, title_xz_w, label_xz_x, label_xz_y,
colorBarUnits_w, colourbar_axis_w, lim_x, lim_z, 'X-Y', 'Y-Z', plane_z,
delta_z, plane_x, delta_x);

%  Plot Y-Z of V for specified X plane
plotPlanes(yz_y, yz_z, yz_v, yz_w, abs(yz_v), title_yz_v, label_yz_x,
label_yz_y, colorBarUnits_v, colourbar_axis_v, lim_y, lim_z, 'X-Y', 'X-Z',
plane_z, delta_z, plane_y, delta_y);

%  Plot Y-Z of W for specified X plane
plotPlanes(yz_y, yz_z, yz_v, yz_w, yz_w, title_yz_w, label_yz_x, label_yz_y,
colorBarUnits_w, colourbar_axis_w, lim_y, lim_z, 'X-Y', 'X-Z', plane_z,
delta_z, plane_y, delta_y);

%%  Plot for radially averaged displacements
[out_r, out_i, out_o] = radial_disp(xy_x, xy_y, xy_u, xy_v, xy_w, centre_x,
centre_y, delta_x, delta_y, lim_x, lim_y, downsampling);

%% Clean up

%  Pause stopwatch
executionTime = toc();

disp('Plots generated');
disp(strcat('Script execution time: ', num2str(executionTime)));
```

Function for 2-D planar visualisation

```
function [fig] = plotPlanes(X, Y, U, V, C, plt_title, lbl_x, lbl_y, lbl_cbar,
axs_cbar, lim_x, lim_y, txt_h, txt_v, plane_h, delta_h, plane_v, delta_v)
    %plotPlanes     Plots a 2-d plane for any combination of vertical and
horizontal data
    %  Danial Khoshkhou
    %  University of Birmingham
    %  November 2014
    %  X, Y         Coordinate data for contour and quiver
    %  U, V         Plot data for quiver
    %  C            Plot data for contour
    %  plt_title    Title for figure
    %  lbl_x        Label for vertical x-axis
    %  lbl_y        Label for horizontal y-axis
    %  lbl_cbar     Label for colourbar scale
    %  axs_cbar     Value labels for colourbar scale, given as [min_val
max_val]
    %  lim_x        Limits for horizontal x-axis, given as [min_val max_val]
    %  lim_y        Limits for vertical y-axis, given as [min_val max_val]
    %  txt_h        Text for horizontal line
    %  txt_v        Text for vertical line
    %  plane_h      Plane number for horizontal line
    %  plane_v      Plane number for vertical line

    %  Calculate downsampled matrices for plots
    nx = 3;
    ny = 3;

    X_d = X(1:nx:end, 1:ny:end);
    Y_d = Y(1:nx:end, 1:ny:end);
    U_d = U(1:nx:end, 1:ny:end);
    V_d = V(1:nx:end, 1:ny:end);

    fig = figure('Color','w');
    %[c, h] = contourf(X, Y, C, 40);
    contourf(X, Y, C, 40);
    %[c,h] = contourf(z);
    %clabel(c,h);%, colorbar
    % Set the figure Renderer to OpenGL, which supports transparency
    %set(gcf, 'Renderer', 'OpenGL');
    % Find all the objects that are children of the contourgroup that have the
FaceAlpha property
    %alphable = findobj(h, '-property', 'FaceAlpha');
    %for k = [1:-0.1:0.1 0.1:0.1:1]
        % Change the FaceAlpha property, which will change the objects'
transparency
        %set(alphable, 'FaceAlpha', k);
        %pause(0.5)
    %end

    %  Downsample data


    colormap jet;
    %alpha(0.5)
    hold on
    %pcolor(X, Y, C);
    %shading interp;
    quiv = quiver(X_d, Y_d, U_d, V_d, 4);
    hold off

    %set(quiv, 'LineWidth', 2.0);
    set(quiv, 'LineWidth', 1.0);
```

```
    adjust_quiver_arrowhead_size(quiv, 2.5);

    %  Apply titles and labels
    %title(plt_title);
    xlabel(lbl_x);
    ylabel(lbl_y);

    %  Draw colour bars
    plt_cbar = colorbar;
    ylabel(plt_cbar, lbl_cbar);
    caxis(axs_cbar);

    %  Set limits to be from 0 to corrected max relative to min (max - min)
    %xlim(lim_x);
    %ylim(lim_y);

    %  Draw lines
    disp(strcat('Plotting ', txt_h, ' on plane ' , num2str(plane_h), ' at (',
num2str(lim_x(1)), ', ', num2str(plane_h * delta_h), ')'));
    line(lim_x, [(plane_h * delta_h) (plane_h * delta_h)], 'Color', 'black');
% Horizontal Line
    disp(strcat('Plotting ', txt_v, ' on plane ' , num2str(plane_v), ' at (',
num2str(lim_y(1)), ', ', num2str(plane_v * delta_v), ')'));
    line([(plane_v * delta_v) (plane_v * delta_v)], lim_y, 'Color', 'black');
% Vertical Line

    %  Display text (rotate YZ)
    text(delta_h, (plane_h * delta_h), txt_h, 'Background', 'w'); % Horizontal
line
    text((plane_v * delta_v), delta_v, delta_v, txt_v, 'Background', 'w',
'Rotation', 90); % Vertical Line

end
```

Function for radial displacement averaging

```
function [r_uq, A_I, A_W] = radial_disp(X, Y, U, V, W, cen_x, cen_y, del_x,
del_y, lim_x, lim_y, ds)
    %  Danial Khoshkhou
    %  University of Birmingham
    %  November 2014
    % v1.0  Initial Release
    % v1.1  Fixed second figure hold issue
    % v1.2  Replaced circle drawing method from for loop to single matrix and
    %       grouped plotting operations
    % v1.3  Moved to separate function
    % v1.4  Replaced iterative loops for distance calculations to single
    %       matrix
    % v1.5  Used polar coordinates instead of trig commands
    % v1.6  Added downsampling (ds) to concentric circle plots

    %% Calculate distance and angle of each point from origin

    %  Theta, R for global coordinate system relative to origin
    [T_XY, R_XY] = cart2pol(X-X(cen_x, cen_y), Y - Y(cen_x, cen_y));

    %  set NaN in same nodal positions
    T_XY(isnan(W)) = nan;
    R_XY(isnan(W)) = nan;

    %  Calculate in-plane displacements from U and V

    U_corr = U;
    V_corr = V;

    U_corr(T_XY > pi/2) = -U_corr(T_XY > pi/2);
    U_corr(T_XY < -pi/2) = -U_corr(T_XY < -pi/2);

    V_corr(T_XY <= 0 & T_XY >= -pi/2) = -V_corr(T_XY <= 0 & T_XY >= -pi/2);
    V_corr(T_XY < -pi/2) = -V_corr(T_XY < -pi/2);

    T_XY_corr = abs(T_XY); % Convert all negative values to positive
    %T_XY_corr(T_XY_corr<0) = nan;
    T_XY_corr(T_XY_corr>pi/2) = pi - T_XY_corr(T_XY_corr>pi/2); % Angles >90
stored as 180 - angle
    I = U_corr.*cos(abs(T_XY_corr)) + V_corr.*sin(abs(T_XY_corr));

    %  Get all radii i.e. unique non-repeating equi-distant values
    R_XY = single(R_XY); % Single precision otherwise duplicates remain
    r_uq = unique(R_XY(~isnan(R_XY))); % Column vector of unique radii

    %% Average data values along each radial line
    r = nan(0,1); %  radius single column vector
    d_w = nan(0,1); %  displacement single column vector
    d_i = nan(0,1); %  out-of-plane displacement single column vector

    A_W = zeros(size(r_uq)); %  Averaged out-of-plane displacements
    A_I = zeros(size(r_uq)); %  Averaged in-plane displacements

    for i = 1 : size(r_uq)

        %  Retrieve all displacement values on each unique radial distance
        D_W = W(R_XY == r_uq(i));
        D_I = I(R_XY == r_uq(i));

        %  Store coordinate pairs of displacements and radial distances
        r_tmp = zeros(size(D_W)); %  Temporary array for this iteration
        r_tmp(:,1) = r_uq(i);
```

```
        % Only include radial positions with more than a certain number of
        % data points
        %if(size(D_W, 1) == 1)
            r = vertcat(r, r_tmp); %  Append temporary radii
            d_w = vertcat(d_w, D_W); %  Append temporary out-of-plane
displacements
            d_i = vertcat(d_i, D_I); %  Append temporary in-plane
displacements
        %end

        %  Calculate histogram centres and counts (10 value binning)
        %[counts_w,centers_w] = hist(D_W);
        %[counts_i,centers_i] = hist(D_I);
        %  Retrieve modal value and assign to
        %h_w(i) = centers_w(counts_w == max(counts_w));
        %h_i(i) = centers_i(counts_i == max(counts_i));

        disp(strcat('Number of values on radial line at radius=',
sprintf('%.5f', r_uq(i)), ': ', num2str(size(D_W, 1))));
        %  Calculate average at each radius
        A_W(i) = mean(D_W);
        A_I(i) = mean(D_I(~isnan(D_I)));

    end

    %% Plot figure with concentric circles

    figure('Color','w'); %  Generate figure with white background
    quiver(X, Y, U, V, 0); %  Draw vector field
    hold on %  allow multiple plots
    %  Draw origin
    scatter(cen_x * del_x, cen_y * del_y, 'r');
    %  Draw concentric circles
    theta = linspace(0, 2*pi, 500).';
    plot(cen_x*del_x + cos(theta) * downsample(r_uq.', ds), cen_y*del_y +
sin(theta) * downsample(r_uq.', ds) , 'LineWidth', 0.1);%, 'LineStyle', ':');
    hold off
    %  Draw lines at origin
    line([cen_x * del_x cen_x * del_x], lim_y, 'Color', 'black'); % vertical
line
    line(lim_x, [cen_y * del_y cen_y * del_y], 'Color', 'black') % horizontal
line
    %  Set axes limits
    xlim(lim_x);
    %  Set title
    title('Equidistant radial grid points');
    %  Set labels
    xlabel('X (\mum)');
    ylabel('Y (\mum)');

%% Plot radial out-of plane displacements

    figure('Color','w'); %  Generate figure with white background
    scatter(r, d_w, 2, 'black'); %  Draw
    hold on
    plot(r_uq, A_W);
    xlim(lim_x/2);
    %errorbar(R, A, E);
    %errorbar(R, A, A_min, A_max);
    hold off
    box on
    ylim([-5 15]);

    title('Out-of-plane (vertical) displacement vs radial position');
```

```
    xlabel('Radial position from centre (\mum)');
    ylabel('Displacement (\mum)');

%% Plot radial in-plane displacements

    figure('Color','w'); %  Generate figure with white background
    scatter(r, d_i, 2, 'black');
    hold on
    plot(r_uq, A_I);
    %plot(r_uq, h_i);
    xlim(lim_x/2);
    %errorbar(R, A, E);
    %errorbar(R, A, A_min, A_max);
    hold off
    box on
    ylim([-5 15]);

    title('In-plane (horizontal) displacement vs radial position');
    xlabel('Radial position from centre (\mum)');
    ylabel('Displacement (\mum)');

end
```

Appendix I: DVC 3-D data visualisation (MATLAB)

A MATLAB script was written to combine 3-D displacement field data calculated using DVC and the source tomography data. The number of DVC data points was 16 times fewer in all 3 dimensions, requiring appropriate 3-D matrix scaling. The script was written in two parts, the first to process the tomography and corresponding displacement data stacks and the second for visualisation in 3-D. The visualisation portion of the script used the original tomography stack (Figure 181) and overlaid the displacement field with cutaways at the same positions (Figure 182) to produce an overlay plot (Figure 183).

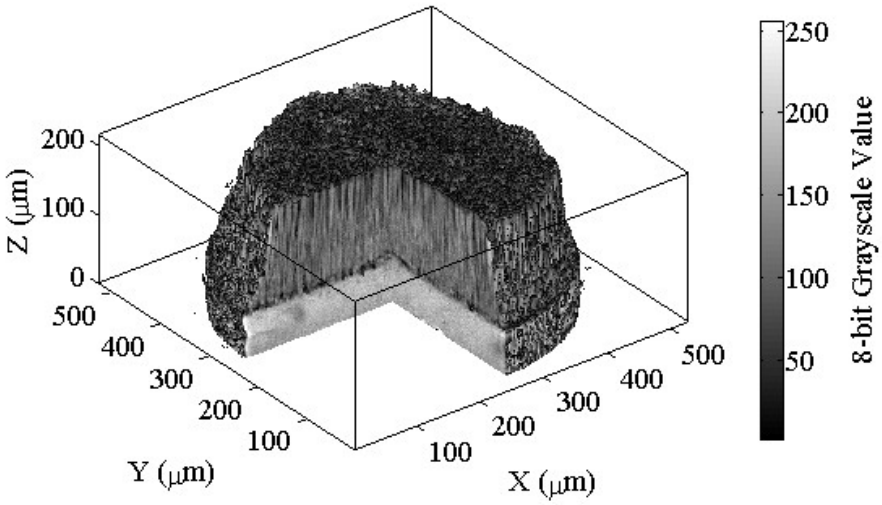

Figure 181 – Cutaway of Rolls-Royce Pt cylindrical micro-specimen in the as-received state visualised in MATLAB

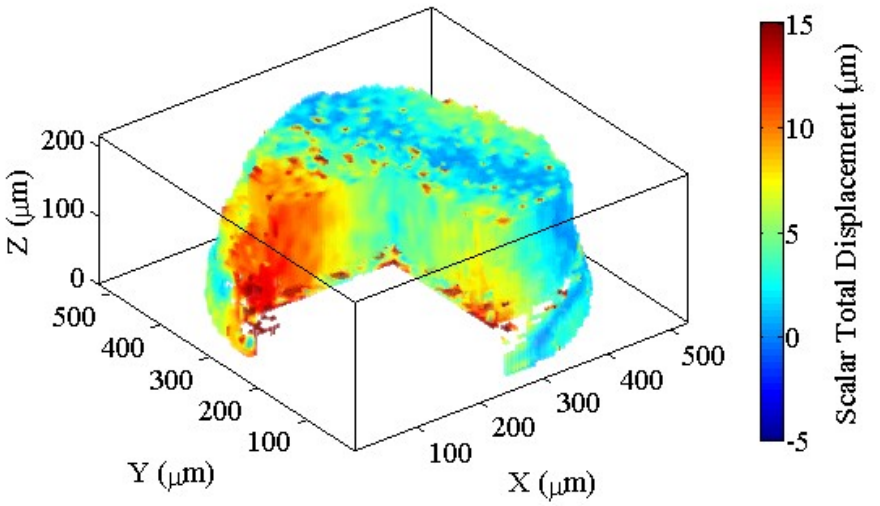

Figure 182 – Cutaway of Rolls-Royce Pt displacement field after a DVC comparison between 0 hours and 20 hours.

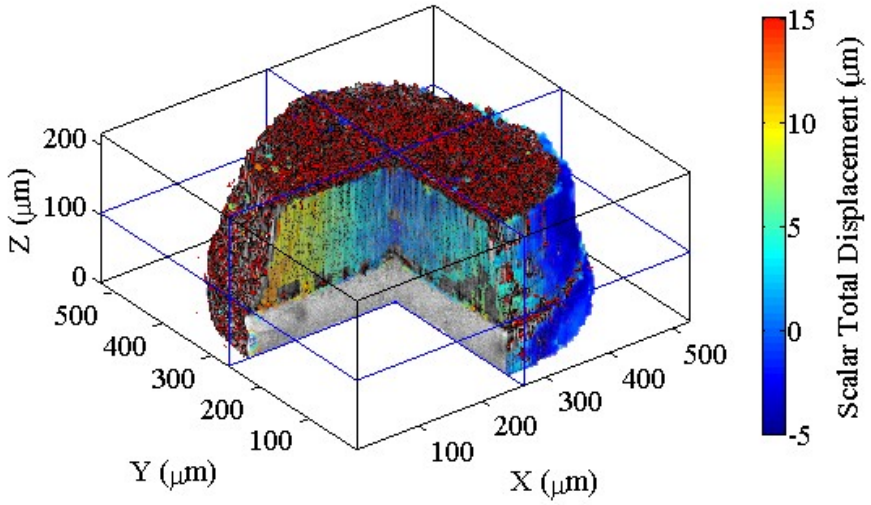

Figure 183 – Cutaway of combined DVC displacement field overlaid onto tomography reconstruction.

DVC and tomography stack processing

```
%% Script to visualise DVC data
%  Danial Khoshkhou
%  University of Birmingham

% v1.0  Initial release
% v1.1  Changed subplots to individual figures
% v1.2  Changed way distance between vector points were calculated from
%       manual to calculated from distance between unique non-nan values
% v1.3  Moved plotting logic into separate function
% v1.4  Added code to fill in NaN values for X, Y and Z coordinate data

%% User inputs for images

%  Load data from current working directory
load(strcat(pwd, filesep, 'DVC_Corrected_Exp3RRPtUC1200Step1.mat'));


%  Raw input file (convert from mm to micron)
data = DVC_Corrected_Exp3RRPtUC1200Step1 * 1000;


%  Raw DVC image dimensions (x,y pixel count and number of images in z)
dim_x = 73; % Image x dimension
dim_y = 73; % Image y dimension
dim_z = 67; % Image z dimension (number of images in stack)

%  Image planes (for 2-d planes of interest)
plane_z = 46; % x-y plane number
plane_y = 35; % x-z plane number
plane_x = 35; % y-z plane number

%  Radial averaging centre point
centre_x = 36;
centre_y = 36;

%  Colour bars for contour plots
colourbar_min_u = -5;
colourbar_max_u = 13;
colourbar_min_v = -5;
colourbar_max_v = 13;
```

```
colourbar_min_w = -5;
colourbar_max_w = 13;

%% Other user inputs

%  Zoomed in sub-image (rectangle)
zoom_plane = 'xy'; % Options are xy, xz and yz
zoom_x = 155; % x-coordinate
zoom_y = 175; % y-coordinate
zoom_h = 200; % rectangle height

zoom_w = 200; % rectangle width

%  Units (for axes titles)
units_x = '\mum'; % \mu = micron
units_y = '\mum'; % \mu = micron
units_z = '\mum'; % \mu = micron

%  Contour line density for contour plots
contours_xy = 20;
contours_xz = 20;
contours_yz = 20;
contours_zoom = 10;



%  Contour line units
colorBarUnits_u = 'U Displacement (\mum)';
colorBarUnits_v = 'V Displacement (\mum)';
colorBarUnits_w = 'W Displacement (\mum)';

%  Downsmapling for concentric plots
downsampling = 1;
%% Clean-up operations

% Change default axes fonts.
set(0,'DefaultUipanelBackgroundColor',[1 1 1]);
set(0,'DefaultAxesFontName', 'Times New Roman')
set(0,'DefaultAxesFontSize', 24)
% Change default text fonts.
set(0,'DefaultTextFontname', 'Times New Roman')
set(0,'DefaultTextFontSize', 24)

% Close any open figures
delete(findall(0,'Type','figure'));

% Clear command window
clc;

% Start performance stopwatch
tic;

%% Create X, Y and Z coordinate data and U, V, W displacement data

disp('Generating X, Y and Z spatial coordinates.');

%  Get max and min values (used to reposition plots)
min_x = min(data(:, 1));
min_y = min(data(:, 2));
min_z = min(data(:, 3));
min_u = min(data(:, 4));
min_v = min(data(:, 5));
min_w = min(data(:, 6));
max_x = max(data(:, 1));
max_y = max(data(:, 2));
```

```
max_z = max(data(:, 3));
max_u = max(data(:, 1));
max_v = max(data(:, 2));
max_w = max(data(:, 3));

%  Select subsets from main data and reset coordinates positions
%  Use reshape to make 3d matrix from columnar data
X = reshape(data(:, 1), dim_x, dim_y, dim_z) - min_x;
Y = reshape(data(:, 2), dim_x, dim_y, dim_z) - min_y;
Z = abs(reshape(data(:, 3), dim_x, dim_y, dim_z) - min_z - max(data(:, 3) -
min_z)); % Z-data is backwards because of image read byte order
U = reshape(data(:, 4), dim_x, dim_y, dim_z);
V = reshape(data(:, 5), dim_x, dim_y, dim_z);
W = -reshape(data(:, 6), dim_x, dim_y, dim_z); % Negative w because of flipped
z

%% Replace NaNs in coordinates with appropriate values
%  Fill in empty data points with unique values from a single plane
for i = 1:dim_x
    %  Find unique value x for ith plane and replace
    X_i = X(i, :, :);

    % Calculate unique value per plane
    x_i = unique(X_i(~isnan(X_i)));

    %  Use if statement to account for any planes that are all NaN
    if ~isempty(x_i)
        %  Replace all values on plane with unique value
       X(i, :, :) = x_i;
    else
        X(i, :, :) = 0;
    end
end

for j = 1:dim_y
    %  Find unique value y for jth plane and replace
    Y_i = Y(:, j, :);

    % Calculate unique value per plane
    y_i = unique(Y_i(~isnan(Y_i)));

    %  Use if statement to account for any planes that are all NaN
    if ~isempty(y_i)
        %  Replace all values on plane with unique value
       Y(:, j, :) = y_i;
    else
        Y(:, j, :) = 0;
    end
end

for k = 1:dim_z
    %  Find unique value y for jth plane and replace
    Z_i = Z(:, :, k);

    % Calculate unique value per plane
    z_i = unique(Z_i(~isnan(Z_i)));

    %  Use if statement to account for any planes that are all NaN
    if ~isempty(z_i)
        %  Replace all values on plane with unique value
       Z(:, :, k) = z_i;
    else
        Z(:, :, k) = 0;
    end
end
```

```
%% Calculate grid spacing from difference between each spatial coordinate
delta_x = min(diff(unique(X(~isnan(X)))));
delta_y = min(diff(unique(Y(~isnan(Y)))));
delta_z = min(diff(unique(Z(~isnan(Z)))));

disp('Spatial coordinates (X, Y, Z) and displacement data (U, V, W)
prepared.');
disp(strcat('Coordinate spacing of x=', num2str(delta_x), ' y=',
num2str(delta_y), ' z=', num2str(delta_z)));

%% Get X-Y, X-Z and Y-Z planar profiles

disp('Extracting X-Y, X-Z and Y-Z profiles');

%  Invert z and y for image byte read order
plane_z = dim_z - plane_z;
plane_y = dim_y - plane_y;

%  Get x-y plane from specified z
xy_x = fliplr(rot90(X(:, :, plane_z), 3));
xy_y = fliplr(rot90(Y(:, :, plane_z), 3));
xy_u = fliplr(rot90(U(:, :, plane_z), 3));
xy_v = fliplr(rot90(V(:, :, plane_z), 3));
xy_w = fliplr(rot90(W(:, :, plane_z), 3));

%  Get x-z plane from specified y
%  Use squeeze() to get (i x k) from (i x 1 x k)
xz_x = squeeze(X(:, plane_y, :));
xz_z = squeeze(Z(:, plane_y, :));
xz_u = squeeze(U(:, plane_y, :));
xz_v = squeeze(V(:, plane_y, :));
xz_w = squeeze(W(:, plane_y, :));

%  Get y-z plane from specified x
%  Use squeeze() to get (i x k) from (i x 1 x k)
yz_y = squeeze(Y(plane_x, :, :));
yz_z = squeeze(Z(plane_x, :, :));
yz_u = squeeze(U(plane_x, :, :));
yz_v = squeeze(V(plane_x, :, :));
yz_w = squeeze(W(plane_x, :, :));

disp('All planes extracted');

%% Begin figures and plots section

disp('Generating plots');

%  Calculate position of lines
%  X-Y plane lines
line_xy_xz_x = [0 (dim_x * delta_x)]; % X-Z horizontal
line_xy_xz_y = [((dim_y - plane_y) * delta_y) ((dim_y - plane_y) * delta_y)];
line_xy_yz_x = [(plane_x * delta_x) (plane_x * delta_x)]; % Y-Z vertical
line_xy_yz_y = [0 (dim_y * delta_y)];
%  X-Z planes lines
line_xz_xy_x = [0 (dim_x * delta_x)]; % X-Y horizontal
line_xz_xy_y = [((dim_z - plane_z) * delta_z) ((dim_z - plane_z) * delta_z)];
line_xz_yz_x = [(plane_x * delta_x) (plane_x * delta_x)]; % Y-Z vertical
line_xz_yz_y = [0 (dim_z * delta_z)];
%  Y-Z planes lines
line_yz_xy_x = [0 (dim_y * delta_y)]; % X-Y horizontal
line_yz_xy_y = [((dim_z - plane_z) * delta_z) ((dim_z - plane_z) * delta_z)];
line_yz_xz_x = [(plane_y * delta_y) (plane_y * delta_y)]; % X-Z vertical
line_yz_xz_y = [0 (dim_z * delta_z)];
```

```
%  Calculate position of line labels
%  X-Y
text_xy_xz_x = delta_x;
text_xy_xz_y = (dim_y - plane_y) * delta_y;
text_xy_yz_x = plane_x * delta_x;
text_xy_yz_y = delta_y;
%  X-Z
text_xz_xy_x = delta_x;
text_xz_xy_y = (dim_z - plane_z) * delta_z;
text_xz_yz_x = plane_x * delta_x;
text_xz_yz_y = delta_z;
%  Y-Z
text_yz_xy_x = delta_y;
text_yz_xy_y = (dim_z - plane_z) * delta_z;
text_yz_xz_x = plane_y * delta_y;
text_yz_xz_y = delta_y;

%  Prepare figure titles
title_xy_u = strcat('U component of displacement on X-Y plane at Z=',
num2str((dim_z - plane_z) * delta_z), units_z, ' (Z-plane=', num2str(dim_z -
plane_z), ')');
title_xy_v = strcat('V component of displacement on X-Y plane at Z=',
num2str((dim_z - plane_z) * delta_z), units_z, ' (Z-plane=', num2str(dim_z -
plane_z), ')');
title_xy_w = strcat('W component of displacement on X-Y plane at Z=',
num2str((dim_z - plane_z) * delta_z), units_z, ' (Z-plane=', num2str(dim_z -
plane_z), ')');
title_xz_u = strcat('U component of displacement on X-Z plane at Y=',
num2str((dim_y - plane_y) * delta_y), units_y, ' (Y-plane=', num2str(dim_y -
plane_y), ')');
title_xz_w = strcat('W component of displacement on X-Z plane at Y=',
num2str((dim_y - plane_y) * delta_y), units_y, ' (Y-plane=', num2str(dim_y -
plane_y), ')');
title_yz_v = strcat('V component of displacement on Y-Z plane at X=',
num2str(plane_x * delta_x), units_x, ' (X-plane=', num2str(plane_x), ')');
title_yz_w = strcat('W component of displacement on Y-Z plane at X=',
num2str(plane_x * delta_x), units_x, ' (X-plane=', num2str(plane_x), ')');

%  Prepare figure labels
label_xy_x = strcat('X position (', units_x, ')');
label_xy_y = strcat('Y position (', units_y, ')');
label_xz_x = strcat('X position (', units_x, ')');
label_xz_y = strcat('Z position (', units_z, ')');
label_yz_x = strcat('Y position (', units_y, ')');
label_yz_y = strcat('Z position (', units_z, ')');

%  Prepare colourbars
colourbar_axis_u = [colourbar_min_u, colourbar_max_u];
colourbar_axis_v = [colourbar_min_v, colourbar_max_v];
colourbar_axis_w = [colourbar_min_w, colourbar_max_w];

%  Prepare axis limits
lim_x = [0 (max_x - min_x)];
lim_y = [0 (max_y - min_y)];
lim_z = [0 (max_z - min_z)];

%  Invert z and y because of image byte read order
plane_z = dim_z - plane_z;
plane_y = dim_y - plane_y;

%% Plot planes

%  Plot X-Y of U for specified Z plane
```

```
plotPlanes(xy_x, xy_y, xy_u, xy_v, xy_u, title_xy_u, label_xy_x, label_xy_y,
colorBarUnits_u, colourbar_axis_u, lim_x, lim_y, 'X-Z', 'Y-Z', plane_y,
delta_y, plane_x, delta_x);

%  Plot X-Y of V for specified Z plane
plotPlanes(xy_x, xy_y, xy_u, xy_v, xy_v, title_xy_v, label_xy_x, label_xy_y,
colorBarUnits_v, colourbar_axis_v, lim_x, lim_y, 'X-Z', 'Y-Z', plane_y,
delta_y, plane_x, delta_x);


%  Plot X-Z of U for specified Y plane
plotPlanes(xz_x, xz_z, xz_u, xz_w, abs(xz_u), title_xz_u, label_xz_x,
label_xz_y, colorBarUnits_u, colourbar_axis_u, lim_x, lim_z, 'X-Y', 'Y-Z',
plane_z, delta_z, plane_x, delta_x);

%  Plot X-Z of W for specified Y plane
plotPlanes(xz_x, xz_z, xz_u, xz_w, xz_w, title_xz_w, label_xz_x, label_xz_y,
colorBarUnits_w, colourbar_axis_w, lim_x, lim_z, 'X-Y', 'Y-Z', plane_z,
delta_z, plane_x, delta_x);

%  Plot Y-Z of V for specified X plane
plotPlanes(yz_y, yz_z, yz_v, yz_w, abs(yz_v), title_yz_v, label_yz_x,
label_yz_y, colorBarUnits_v, colourbar_axis_v, lim_y, lim_z, 'X-Y', 'X-Z',
plane_z, delta_z, plane_y, delta_y);

%  Plot Y-Z of W for specified X plane
plotPlanes(yz_y, yz_z, yz_v, yz_w, yz_w, title_yz_w, label_yz_x, label_yz_y,
colorBarUnits_w, colourbar_axis_w, lim_y, lim_z, 'X-Y', 'X-Z', plane_z,
delta_z, plane_y, delta_y);

%%  Plot for radially averaged displacements
[out_r, out_i, out_o] = radial_disp(xy_x, xy_y, xy_u, xy_v, xy_w, centre_x,
centre_y, delta_x, delta_y, lim_x, lim_y, downsampling);

%% Clean up

%  Pause stopwatch
executionTime = toc();

disp('Plots generated');
disp(strcat('Script execution time: ', num2str(executionTime)));
```

Function to plot 2-D planes with transparency

```
function [fig] = plotPlanes(X, Y, U, V, C, plt_title, lbl_x, lbl_y, lbl_cbar,
axs_cbar, lim_x, lim_y, txt_h, txt_v, plane_h, delta_h, plane_v, delta_v)
    %plotPlanes     Plots a 2-d plane for any combination of vertical and
horizontal data
    %  Danial Khoshkhou
    %  University of Birmingham
    %  November 2014
    %  X, Y         Coordinate data for contour and quiver
    %  U, V         Plot data for quiver
    %  C            Plot data for contour
    %  plt_title    Title for figure
    %  lbl_x        Label for vertical x-axis
    %  lbl_y        Label for horizontal y-axis
    %  lbl_cbar     Label for colourbar scale
    %  axs_cbar     Value labels for colourbar scale, given as [min_val
max_val]
    %  lim_x        Limits for horizontal x-axis, given as [min_val max_val]
    %  lim_y        Limits for vertical y-axis, given as [min_val max_val]
    %  txt_h        Text for horizontal line
    %  txt_v        Text for vertical line
    %  plane_h      Plane number for horizontal line
    %  plane_v      Plane number for vertical line

    %  Calculate downsampled matrices for plots
    nx = 3;
    ny = 3;

    X_d = X(1:nx:end, 1:ny:end);
    Y_d = Y(1:nx:end, 1:ny:end);
    U_d = U(1:nx:end, 1:ny:end);
    V_d = V(1:nx:end, 1:ny:end);

    fig = figure('Color','w');
    %[c, h] = contourf(X, Y, C, 40);
    contourf(X, Y, C, 40);
    %[c,h] = contourf(z);
    %clabel(c,h);%, colorbar
    % Set the figure Renderer to OpenGL, which supports transparency
    %set(gcf, 'Renderer', 'OpenGL');
    % Find all the objects that are children of the contourgroup that have the
FaceAlpha property
    %alphable = findobj(h, '-property', 'FaceAlpha');
    %for k = [1:-0.1:0.1 0.1:0.1:1]
        % Change the FaceAlpha property, which will change the objects'
transparency
        %set(alphable, 'FaceAlpha', k);
        %pause(0.5)
    %end

    %  Downsample data


    colormap jet;
    %alpha(0.5)
    hold on
    %pcolor(X, Y, C);
    %shading interp;
    quiv = quiver(X_d, Y_d, U_d, V_d, 4);
    hold off

    %set(quiv, 'LineWidth', 2.0);
    set(quiv, 'LineWidth', 1.0);
```

```
    adjust_quiver_arrowhead_size(quiv, 2.5);

    %  Apply titles and labels
    %title(plt_title);
    xlabel(lbl_x);
    ylabel(lbl_y);

    %  Draw colour bars
    plt_cbar = colorbar;
    ylabel(plt_cbar, lbl_cbar);
    caxis(axs_cbar);

    %  Set limits to be from 0 to corrected max relative to min (max - min)
    %xlim(lim_x);
    %ylim(lim_y);

    %  Draw lines
    disp(strcat('Plotting ', txt_h, ' on plane ' , num2str(plane_h), ' at (',
num2str(lim_x(1)), ', ', num2str(plane_h * delta_h), ')'));
    line(lim_x, [(plane_h * delta_h) (plane_h * delta_h)], 'Color', 'black');
% Horizontal Line
    disp(strcat('Plotting ', txt_v, ' on plane ' , num2str(plane_v), ' at (',
num2str(lim_y(1)), ', ', num2str(plane_v * delta_v), ')'));
    line([(plane_v * delta_v) (plane_v * delta_v)], lim_y, 'Color', 'black');
% Vertical Line

    %  Display text (rotate YZ)
    text(delta_h, (plane_h * delta_h), txt_h, 'Background', 'w'); % Horizontal
line
    text((plane_v * delta_v), delta_v, delta_v, txt_v, 'Background', 'w',
'Rotation', 90); % Vertical Line

end
```

Plotting in 3-D with multiple surfaces

```
%% Set figure defaults

% Change default axes fonts.
set(0,'DefaultUipanelBackgroundColor',[1 1 1]);
set(0,'DefaultAxesFontName', 'Times New Roman')
set(0,'DefaultAxesFontSize', 14)

% Change default text fonts.
set(0,'DefaultTextFontname', 'Times New Roman')
set(0,'DefaultTextFontSize', 14)

%% Draw DVC only figure

%  Create new figure;
figure('color', 'w');

%  Enable borders
box on;

%  Draw surface
surfdvc = surface(X2d, Y2d, Z2d, D2d);

%  Remove edges and gridlines
set(surfdvc, 'EdgeColor', 'none');

%  Add transparency
alpha(surfdvc, 0.5);

%  Show color bar
cb = colorbar;

%  Set colorbar range
caxis([dvc_min dvc_max]);

ax = gca;
axpos = get(ax, 'Position');
%axpos = ax.Position;
cpos = get(cb, 'Position');

%  Move colorbar further to the right
cpos(1) = 1.05*cpos(1);

%  Reduce height of colorbar
oldHeight = cpos(4); % Store old height to calculate increase in y-position
newHeight = 0.75*cpos(4);
cpos(4) = newHeight;

%  Move colorbar further up (also reduce height later)
cpos(2) = cpos(2) + (oldHeight - newHeight)/2;

%  Reduce width of colorbar
cpos(3) = 0.5*cpos(3);

%  Apply new colorbar position
set(cb, 'Position',cpos);

%  Re-apply existing axis position
set(ax, 'Position', axpos);

%  Set colorbar label
ylabel(cb, 'Scalar Total Displacement (\mum)');
```

```
%  Set axes labels
xlabel('X (\mum)');
ylabel('Y (\mum)');
zlabel('Z (\mum)');

%  Set aspect ratio
daspect([1,1,1])

%  Remove extra space
axis tight

%  Set 3-D view
view(3)

%%  Get DVC colormap

%  Get figure colormap
CMapSingleDvc = get(gcf,'Colormap');

%  Get number of colors in current colormap
mSingleDvc = size(colormap,1);

%  Get matrix of colors at every point
CDataSingleDvc = get(surfdvc,'CData');

%  Get minimum color value
cSingleMinDvc = min(CDataSingleDvc(:));

%  Get maximum color value
cSingleMaxDvc = max(CDataSingleDvc(:));

%  Get integer values that range from 1 to the length of the colormap
%indexSingleDvc = min(mSingleDvc,round((mSingleDvc-1)*(D2d-
cSingleMinDvc)/(cSingleMaxDvc-cSingleMinDvc))+1);
indexSingleDvc = min(mSingleDvc,round((mSingleDvc-1)*(D2d - dvc_min)/(dvc_max
- dvc_min))+1);

%% Draw image only figure

%  Create new figure;
figure('color', 'w');

%  Enable borders
box on;

%  Draw surface
surfimg = surface(X2d, Y2d, Z2d, I2d);

%  Remove edges and gridlines
set(surfimg, 'EdgeColor', 'none');

%  Set colormap
colormap gray;

%  Create colorbar
cb = colorbar;

%  Set colorbar label
ylabel(cb, '8-bit Grayscale Value');

ax = gca;

axpos = get(ax, 'Position');
%axpos = ax.Position;
cpos = get(cb, 'Position');
```

```
%  Move colorbar further to the right
cpos(1) = 1.05*cpos(1);

%  Reduce height of colorbar
oldHeight = cpos(4); % Store old height to calculate increase in y-position
newHeight = 0.75*cpos(4);
cpos(4) = newHeight;

%  Move colorbar further up (also reduce height later)
cpos(2) = cpos(2) + (oldHeight - newHeight)/2;

%  Reduce width of colorbar
cpos(3) = 0.5*cpos(3);

%  Apply new colorbar position
set(cb, 'Position',cpos);

%  Re-apply existing axis position
set(ax, 'Position', axpos);

%  Set axes labels
xlabel('X (\mum)');
ylabel('Y (\mum)');
zlabel('Z (\mum)');

%  Set aspect ratio
daspect([1,1,1])

%  Remove extra space
axis tight

%  Set 3-D view
view(3)

%%  Get Image colormap

%  Get figure colormap
CMapSingleImg = get(gcf,'Colormap');

%  Get number of colors in current colormap
mSingleImg = size(colormap,1);

%  Get matrix of colors at every point
CDataSingleImg = get(surfimg,'CData');

%  Get minimum color value
cSingleMinImg = min(CDataSingleImg(:));

%  Get maximum color value
cSingleMaxImg = max(CDataSingleImg(:));

%  Get integer values that range from 1 to the length of the colormap
indexSingleImg = 64 + min(mSingleImg,round((mSingleImg-1)*(I2d-
cSingleMinImg)/(cSingleMaxImg-cSingleMinImg))+1);


%% 3-D Draw combined (DVC and image) figure

%  Create new figure;
figure('color', 'w');

%  Combine two previous colormaps
CMapCombined = colormap([CMapSingleDvc; CMapSingleImg]);
```

```
%  Enable borders
box on;

%  Draw DVC surface
surfdvc = surface(X2d, Y2d, Z2d, D2d);

%  Remove DVC edges and gridlines
set(surfdvc, 'EdgeColor', 'none');

%  Add transparency
alpha(surfdvc, 0.5);

%  Draw Image surface
surfimg = surface(X2d, Y2d, Z2d, I2d);

%  Remove Image edges and gridlines
set(surfimg, 'EdgeColor', 'none');

%  Set axes labels
xlabel('X (\mum)');
ylabel('Y (\mum)');
zlabel('Z (\mum)');

%  Set aspect ratio
daspect([1,1,1])

%  Remove extra space
axis tight

%  Set 3-D view
view(3)

%  Get number of colors in combined colormap
mCombined = size(colormap,1);

%  Hide background pixels
indexSingleDvc(indexSingleDvc == 64) = NaN;
indexSingleImg(indexSingleImg == 128) = NaN;

%  Update color values of surface
set(surfdvc,'CData', indexSingleDvc);
set(surfimg,'CData', indexSingleImg);

%  Get minimum color value
cCombinedDvcMin = min(indexSingleDvc(:));

%  Get maximum color value
cCombinedDvcMax = max(indexSingleDvc(:));

%  Set axes labels
xlabel('X (\mum)');
ylabel('Y (\mum)');
zlabel('Z (\mum)');

%  Create colorbar
cb = colorbar;

% Set limits
set(cb, 'YLim', [cCombinedDvcMin, 64]);

% Set tick positions
set(cb, 'YTick', [cCombinedDvcMin, cCombinedDvcMin + ((64 -
cCombinedDvcMin)/4), cCombinedDvcMin + 2*(((64 - cCombinedDvcMin)/4)),
cCombinedDvcMin + 3 *(((64 - cCombinedDvcMin)/4)), 64]);
```

```
%  Set tick labels
set(cb, 'YTickLabel', [dvc_min, 0, 5, 10, dvc_max]);

%  Set colorbar label
ylabel(cb, 'Scalar Total Displacement (\mum)');

ax = gca;
axpos = get(ax, 'Position');
%axpos = ax.Position;
cpos = get(cb, 'Position');

%  Move colorbar further to the right
cpos(1) = 1.05*cpos(1);

%  Reduce height of colorbar
oldHeight = cpos(4); % Store old height to calculate increase in y-position
newHeight = 0.75*cpos(4);
cpos(4) = newHeight;

%  Move colorbar further up (also reduce height later)
cpos(2) = cpos(2) + (oldHeight - newHeight)/2;

%  Reduce width of colorbar
cpos(3) = 0.5*cpos(3);

%  Apply new colorbar position
set(cb, 'Position',cpos);

%  Re-apply existing axis position
set(ax, 'Position', axpos);

%  Draw orthogonal planes
patchxy = patch([xmin xmin, xmax, xmax], [ymin, ymax, ymax, ymin], [plane_xy,
plane_xy, plane_xy, plane_xy], [1 1 1]);
patchxz = patch([xmin xmin, xmax, xmax], [Y(crop_x_end+1, 1, 1),
Y(crop_x_end+1, 1, 1), Y(crop_x_end+1, 1, 1), Y(crop_x_end+1, 1, 1)], [zmin,
zmax, zmax, zmin], [1 1 1]);
patchyz = patch([X(1, crop_y_end+1, 1), X(1, crop_y_end+1, 1), X(1,
crop_y_end+1, 1), X(1, crop_y_end+1, 1)], [ymin, ymax, ymax, ymin], [zmin,
zmin, zmax, zmax], [1 1 1]);

%  Set border colors of planes
set(patchxy, 'EdgeColor', 'b');
set(patchxz, 'EdgeColor', 'b');
set(patchyz, 'EdgeColor', 'b');

%  Remove plane fill
set(patchxy, 'FaceColor', 'none');
set(patchxz, 'FaceColor', 'none');
set(patchyz, 'FaceColor', 'none');

%% 2-D Image only figure;

figure('color', 'w');

colormap gray;

surfimg2d = surface(Xdxy, Ydxy, Zdxy, Idxy);
set(surfimg2d, 'EdgeColor', 'none');

%  Enable borders
box on;

%  Set aspect ratio
daspect([1,1,1])
```

```
%  Remove extra space
axis tight

%  Set 2-D view
view(2)

%  Create colorbar
cb = colorbar;

%%  Get Image colormap

%  Get figure colormap
CMapSingleImg2d = get(gcf,'Colormap');

%  Get number of colors in current colormap
mSingleImg2d = size(colormap,1);

%  Get matrix of colors at every point
CDataSingleImg2d = get(surfimg2d,'CData');

%  Get minimum color value
cSingleMinImg2d = min(CDataSingleImg2d(:));

%  Get maximum color value
cSingleMaxImg2d = max(CDataSingleImg2d(:));

%  Get integer values that range from 1 to the length of the colormap
indexSingleImg2d = 64 + min(mSingleImg2d,round((mSingleImg2d-1)*(Idxy-
cSingleMinImg2d)/(cSingleMaxImg2d-cSingleMinImg2d))+1);

%% 2-D DVC only figure;
figure('color', 'w');

colormap jet;

surfdvc2d = surface(Xdxy, Ydxy, Zdxy, Ddxy);
set(surfdvc2d, 'EdgeColor', 'none');

%  Enable borders
box on;

%  Set aspect ratio
daspect([1,1,1])

%  Remove extra space
axis tight

%  Set 2-D view
view(2)

%  Create colorbar
cb = colorbar;

%%  Get 2-d DVC colormap

%  Get figure colormap
CMapSingleDvc2d = get(gcf,'Colormap');

%  Get number of colors in current colormap
mSingleDvc2d = size(colormap,1);

%  Get matrix of colors at every point
CDataSingleDvc2d = get(surfdvc2d,'CData');
```

```
%  Get minimum color value
cSingleMinDvc2d = min(CDataSingleDvc2d(:));

%  Get maximum color value
cSingleMaxDvc2d = max(CDataSingleDvc2d(:));

%  Get integer values that range from 1 to the length of the colormap
indexSingleDvc2d = min(mSingleDvc2d,round((mSingleDvc2d-1)*(Ddxy -
dvc_min)/(dvc_max - dvc_min))+1);

%% 2-D Draw combined (DVC and image) figure

%  Create new figure;
figure('color', 'w');

%  Combine two previous colormaps
CMapCombined2d = colormap([CMapSingleDvc2d; CMapSingleImg2d]);

%  Enable borders
box on;

%  Draw Image surface
surfimg2d = surface(Xdxy, Ydxy, Zdxy, Idxy);

%  Remove Image edges and gridlines
set(surfimg2d, 'EdgeColor', 'none');

%  Draw DVC surface
surfdvc2d = surface(Xdxy, Ydxy, Zdxy, Udxy);



%  Remove DVC edges and gridlines
set(surfdvc2d, 'EdgeColor', 'none');

hold on

quiver3(Xdxy, Ydxy, Zdxy, Udxy, Vdxy, Wdxy);
%contour(Xdxy, Ydxy, Udxy);

hold off;

%  Add transparency
alpha(surfdvc2d, 0.5);

%  Set axes labels
xlabel('X (\mum)');
ylabel('Y (\mum)');
zlabel('Z (\mum)');

%  Set aspect ratio
daspect([1,1,1])

%  Remove extra space
axis tight

%  Set 3-D view
view(2)

%  Get number of colors in combined colormap
mCombined2d = size(colormap,1);

%  Hide background pixels
indexSingleDvc2d(indexSingleDvc2d == 64) = NaN;
indexSingleImg2d(indexSingleImg2d == 128) = NaN;
```

```
%  Update color values of surface
set(surfdvc2d,'CData', indexSingleDvc2d);
set(surfimg2d,'CData', indexSingleImg2d);

%  Get minimum color value
cCombinedDvcMin2d = min(indexSingleDvc2d(:));

%  Get maximum color value
cCombinedDvcMax2d = max(indexSingleDvc2d(:));
```

Appendix J: Tomography Reconstructions

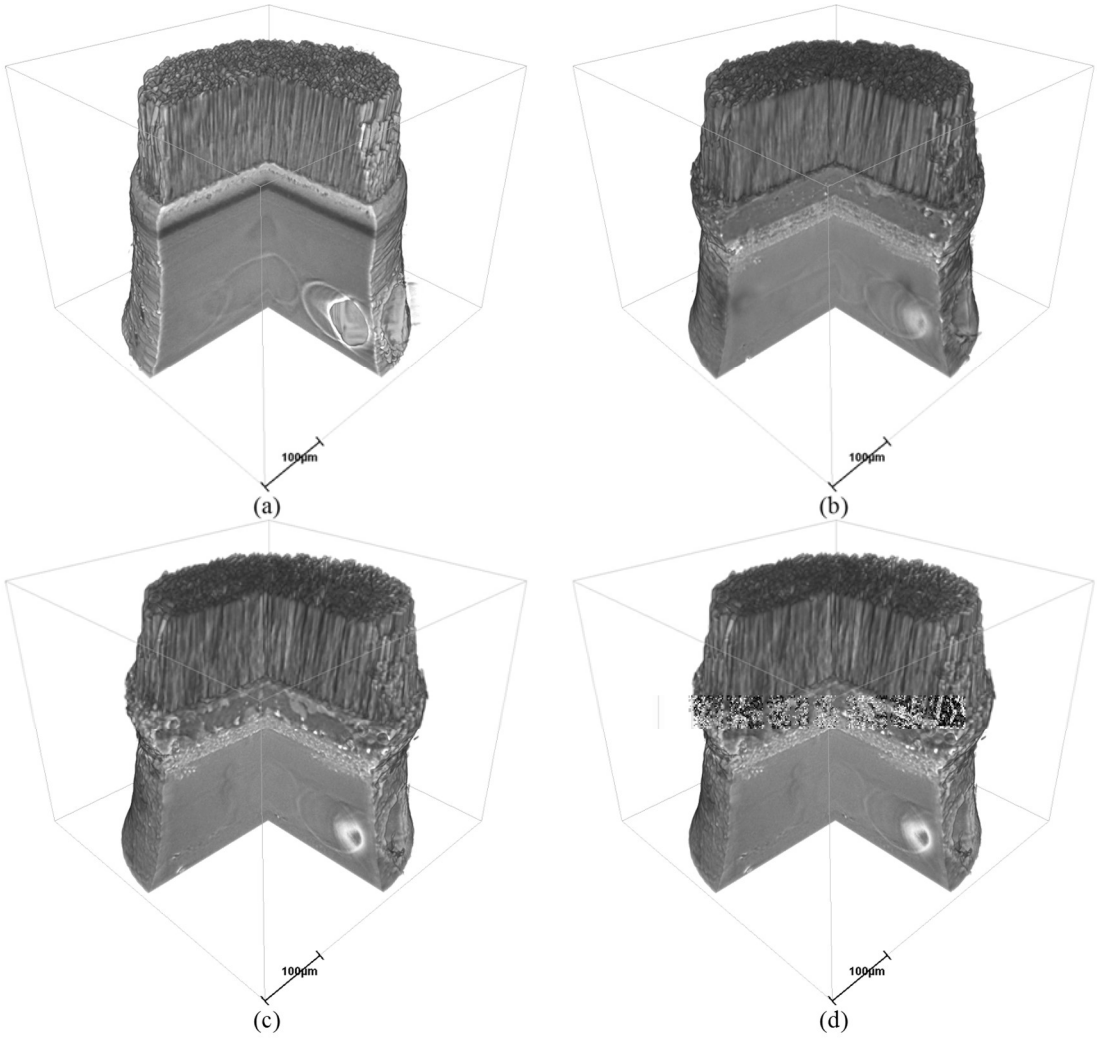

Figure 184 - Reconstructions of diffused Rolls-Royce Pt-Al specimens (a) as-received condition, (b) following 20 hours at 1200°C (c) following 40 hours and (d) after 60 hours.

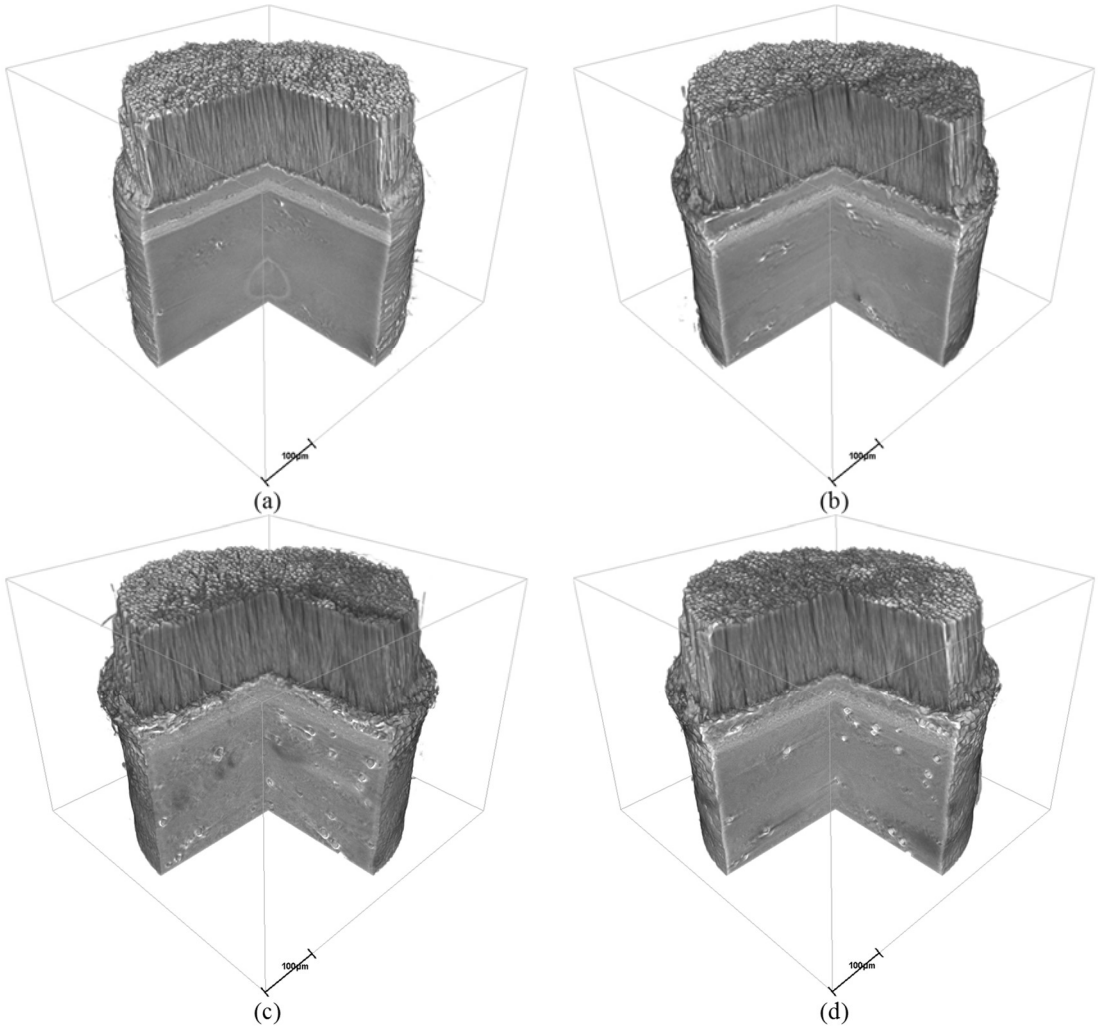

Figure 185 - Reconstructions of Alstom Pt-Al specimens (a) as-received condition, (b) following 20 hours at 1200°C (c) following 40 hours and (d) after 60 hours.

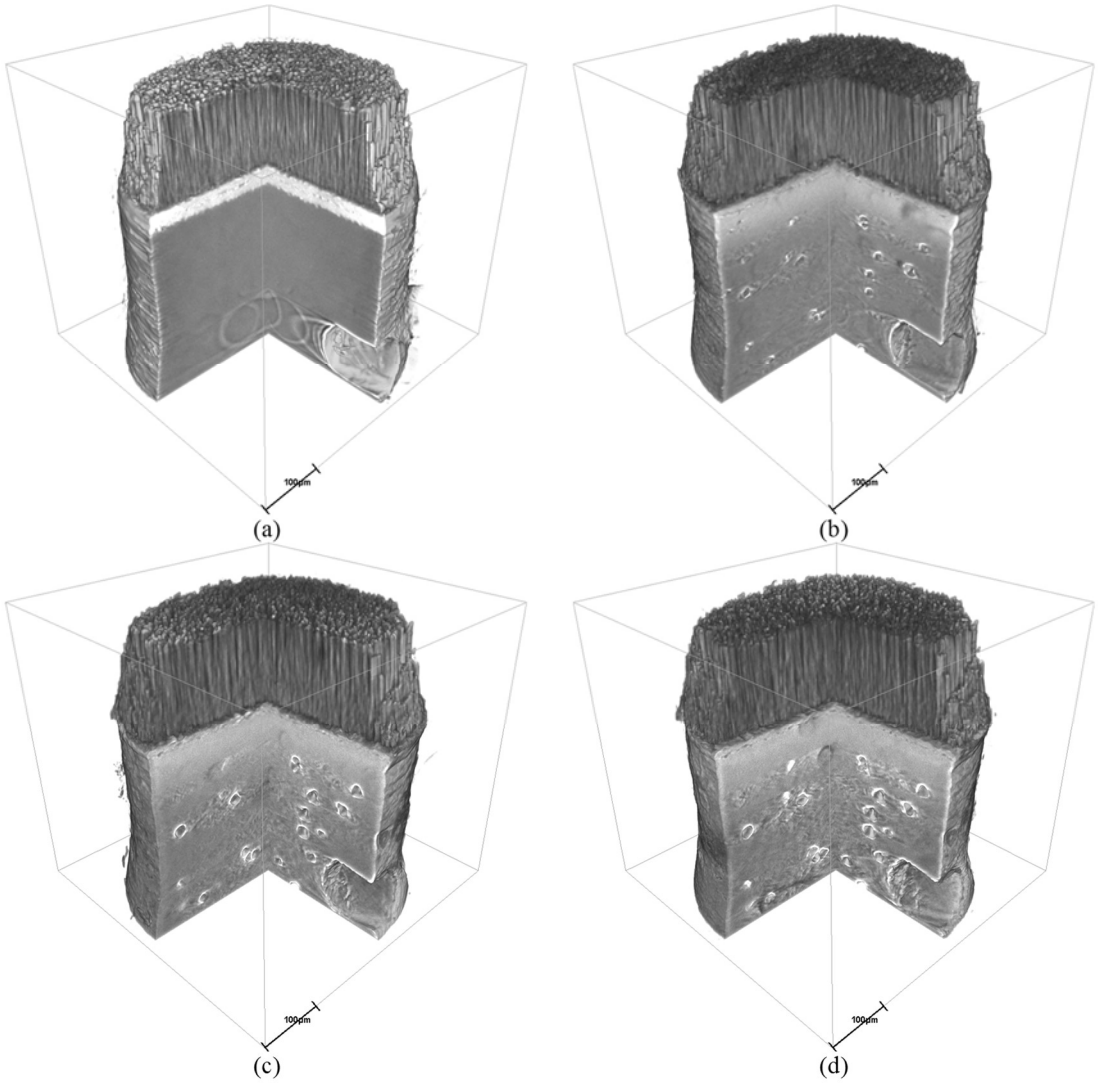

Figure 186 – Reconstructions of Rolls-Royce diffused platinum specimens (a) as-received condition, (b) following 20 hours at 1200°C (c) following 40 hours and (d) after 60 hours.

Appendix K: DVC Plots

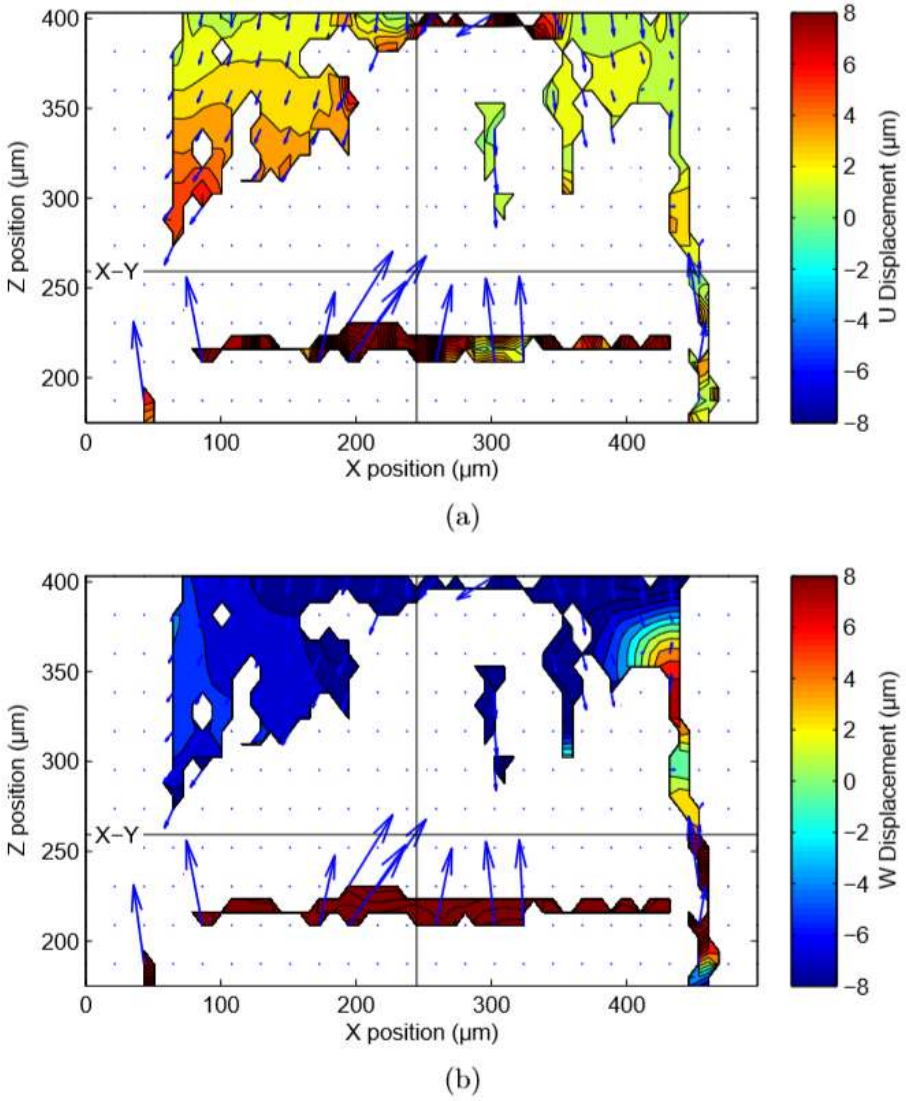

Figure 187 - Planar X-Z displacement field for Rolls-Royce Pt-aluminide specimen at step 1 (as-machined to 20 hours) at 1200 °C showing (a) U component of displacement and (b) W component displacement.

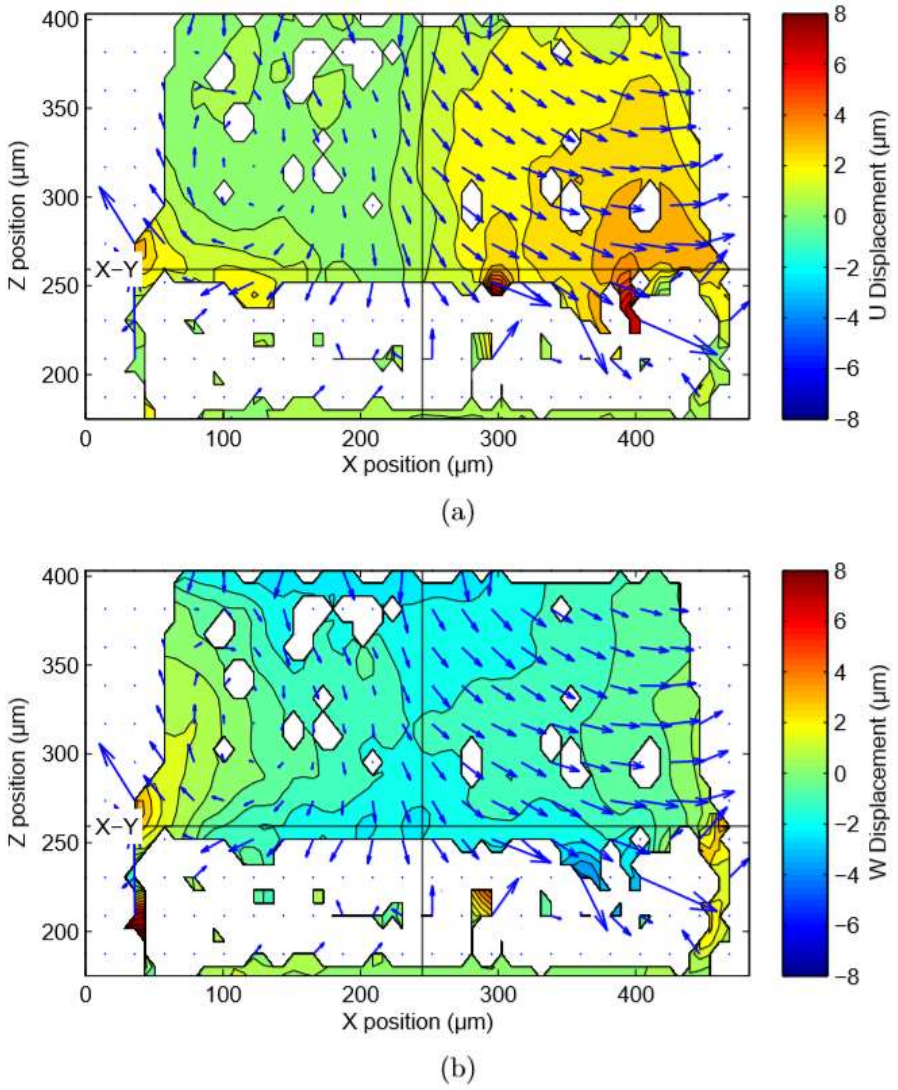

Figure 188 - Planar X-Z displacement field for Rolls-Royce Pt-aluminide specimen at step 2 (20 hours to 40 hours) at 1200 °C showing (a) U component of displacement and (b) W component displacement.

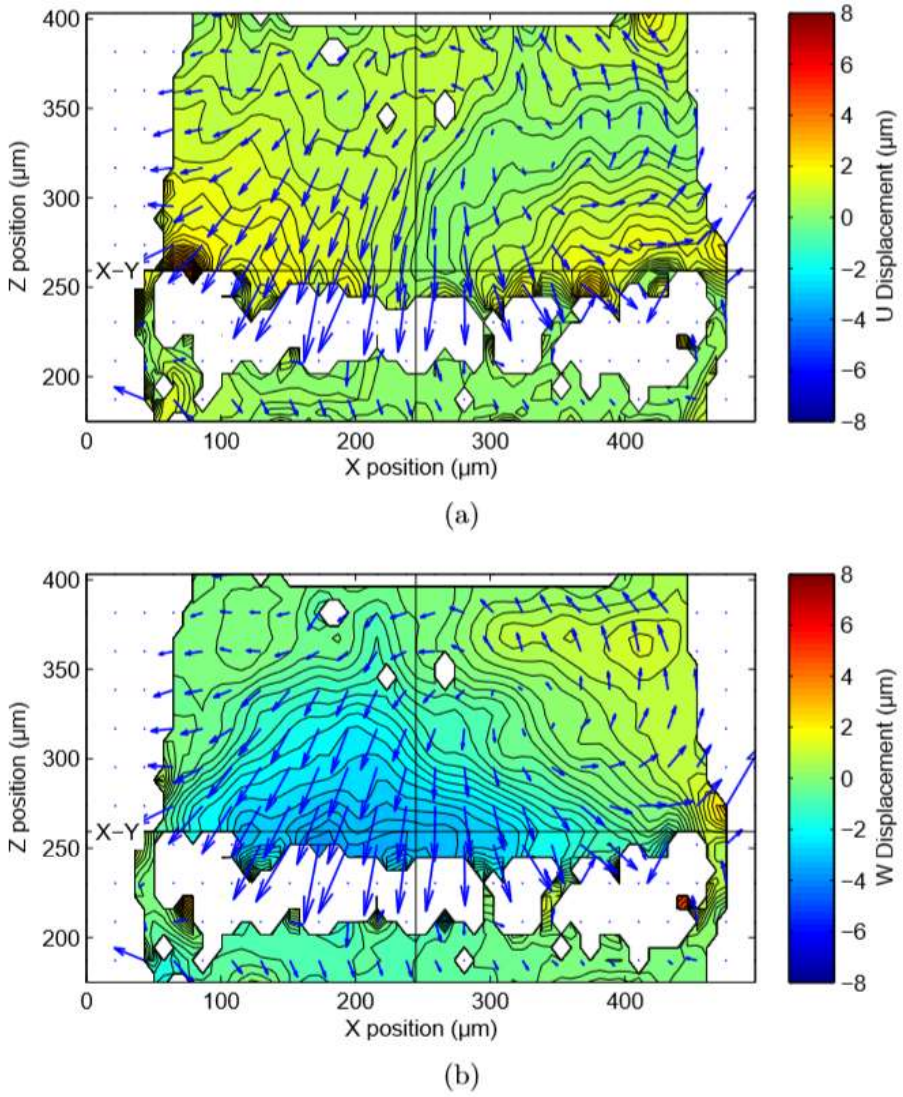

Figure 189 - Planar X-Z displacement field for Rolls-Royce Pt-aluminide specimen at step 3 (40 hours to 60 hours) at 1200 °C showing (a) U component of displacement and (b) W component displacement.

References

[1] S.L. Dixon, C. Hall, Introduction: Basic Principles 1, 7th ed., Butterworth-Heinemann, Oxford, 2014. doi:10.1016/B978-1-85617-793-1.00001-8.

[2] S. Gudmundsson, Selecting the Power Plant, in: Gen. Aviat. Aircr. Des. Appl. Methods Proced., 1st ed., Butterworth-Heinemann, Oxford, 2014: pp. 181–234. doi:http://dx.doi.org/10.1016/B978-0-12-397308-5.00007-6.

[3] M.P. Boyce, Theoretical and Actual Cycle Analyses, in: Gas Turbine Eng. Handb., 4th ed., Butterworth-Heinemann, Oxford, 2012: pp. 89–137. http://books.google.com/books?id=zPAFHyHctRUC.

[4] FAA, Exhaust Emissions (New Aircraft Gas Turbine Engines), U.S. Government Publishing Office, USA, 2013. http://www.ecfr.gov/cgi-bin/text-idx?SID=6cff8346f718c41b9e7c96e346088beb&node=sp14.1.34.c&rgn=div6#se14.1.34_123.

[5] C. Soares, Gas Turbine Major Components and Modules, in: Gas Turbines A Handb. Air, L. Sea Appl., 2nd ed., Butterworth-Heinemann, Oxford, 2015: pp. 173–254. doi:10.1016/B978-0-12-410461-7.00004-3.

[6] J. Moxon, T. Hall, Trent 500 Shapes Up, Flight Int. 158 (2000) 82–87.

[7] R.C. Reed, Introduction, in: Superalloys Fundam. Appl., 1st ed., Cambridge University Press, Cambridge, 2008: pp. 1–32. doi:10.2105/AJPH.50.1.21.

[8] G.E. Fuchs, D.U. Furrer, Designing with Ni-Base Alloys, in: G.E. Totten, L. Xie, K. Funatani (Eds.), Handb. Mech. Alloy Des., CRC Press, New York, 2003: pp. 585–617.

[9] P. Caron, T. Khan, Evolution of Ni-based superalloys for single crystal gas turbine blade applications, Aerosp. Sci. Technol. 3 (1999) 513–523. doi:10.1016/S1270-9638(99)00108-X.

[10] K. Harris, G.L. Erickson, S.L. Sikkenga, W.D. Brentnall, J.M. Aurrecoechea, K.G. Kubarych, Development of the rhenium containing superalloy CMSX-4 and CM 186 LC for single crystal blade and directionally solidified vane applications in advanced turbine engines, in: S.D. Antolovich, R.W. Stusrud, R.A. MacKay, D.L. Anton, T. Khan, R.D. Kissinger, D.L. Klarstrom (Eds.), Superalloys 1992 (Proceedings Seventh Int. Symp. Superalloys), TMS, 1992: pp. 297–306.

[11] M.J. Donachie, S.J. Donachie, Understanding Superalloy Metallurgy, in: Superalloys A Tech. Guid., 2nd ed., ASM International, 2002: pp. 25–39.

[12] R.E. Smallman, A.H.W. Ngan, Advanced alloys, in: Phys. Metall. Adv. Mater., 7th ed., Butterworth-Heinemann, Oxford, 2007: pp. 447–480.

[13] R.C. Reed, Single-crystal superalloys for blade applications, in: Superalloys Fundam. Appl., 1st ed., Cambridge University Press, Cambridge, 2008: pp. 121–216.

[14] M. Gell, D.N. Duhl, A.F. Giamei, The Development of Single Crystal Superalloy Turbine Blades, in: J.K. Tien (Ed.), Superalloys 1980 (Proceedings Fourth Int. Symp. Superalloys), American Society for Metals, 1980: pp. 205–214.

[15] W. Wang, P.D. Lee, M. McLean, A model of solidification microstructures in nickel-based superalloys: Predicting primary dendrite spacing selection, Acta Mater. 51 (2003) 2971–2987. doi:10.1016/S1359-6454(03)00110-1.

[16] S. Miller, Advanced materials mean advanced engines, Interdiscip. Sci. Rev. 21 (1996) 117–129.

[17] R. Diaz, M. Mossaddad, A. Bozan, S. Raghavan, J. Almer, J. Okasinski, H. Pelaez-Perez, P.K. Imbrie, In-Situ Strain Measurements of EB-PVD Thermal Barrier Coatings using Synchrotron X-Ray Diffraction under Thermo-Mechanical Loading, in: 49th AIAA Aerosp. Sci. Meet. Incl. New Horizons Forum Aerosp. Expo., American Institute of Aeronautics and Astronautics, Orlando, 2011.

[18] A. Szczotok, B. Chmiela, Effect of Heat Treatment on Chemical Segregation in CMSX-4 Nickel-Base Superalloy, J. Mater. Eng. Perform. 23 (2013) 2739–2747. doi:10.1007/s11665-013-0843-1.

[19] H.U. Hong, B.G. Choi, I.S. Kim, Y.S. Yoo, C.Y. Jo, Characterization of deformation mechanisms during low cycle fatigue of a single crystal nickel-based superalloy, J. Mater. Sci. 46 (2011) 5245–5251. doi:10.1007/s10853-011-5462-3.

[20] A. Kruk, A. Czyrska-Filemonowicz, Contribution of Electron Tomography to Development of Innovative Materials for Clean Energy Systems and Aeronautics, Arch. Metall. Mater. 58 (2013) 387–392. doi:10.2478/amm-2013-0005.

[21] A. Epishin, T. Link, M. Nazmy, M. Staubli, G. Nolze, Microstructural degradation of CMSX-4: kinetics and effect on mechanical properties, in: R.C. Reed, K.A. Green, P. Caron, T.P. Gabb, M.G. Fahrmann, E.S. Huron, S.A. Woodard (Eds.), Proceeding Superalloy 2008, TMS, 2008: pp. 725–731.

[22] J.-C. Chang, Y.-H. Yun, C. Choi, J.-C. Kim, Development of Microstructure and Mechanical Properties of a Ni-Base Single-Crystal Superalloy by Hot-Isostatic Pressing, J. Mater. Eng. Perform. 12 (2003) 420–425. doi:10.1361/105994903770342953.

[23] F. Wang, D.X. Ma, J. Zhang, S. Bogner, A. Bührig-polaczek, A high thermal gradient directional solidification method for growing superalloy single crystals, J. Mater. Process. Technol. 214 (2014) 3112–3121. doi:10.1016/j.jmatprotec.2014.07.020.

[24] B.S. Bokstein, A. Epishin, T. Link, V.A. Esin, A.O. Rodin, I.L. Svetlov, Model for the porosity growth in single-crystal nickel-base superalloys during homogenization, Scr. Mater. 57 (2007) 801–804. doi:10.1016/j.scriptamat.2007.07.012.

[25] J. Jaroszewicz, H. Matysiak, J. Michalski, K. Matuszewski, K. Kubiak, K.J. Kurzydłowski, Characterization of Single-Crystal Dendrite Structure and Porosity in Nickel-Based Superalloys Using X-Ray Micro-Computed Tomography, Adv. Mater. Res. 278 (2011) 66–71. doi:10.4028/www.scientific.net/AMR.278.66.

[26] T. Link, S. Zabler, A. Epishin, A. Haibel, M. Bansal, X. Thibault, Synchrotron tomography of porosity in single-crystal nickel-base superalloys, Mater. Sci. Eng. A. 425 (2006) 47–54. doi:10.1016/j.msea.2006.03.005.

[27] A. Epishin, B. Fedelich, T. Link, T. Feldmann, I.L. Svetlov, Pore annihilation in a single-crystal nickel-base superalloy during hot isostatic pressing: Experiment and

modelling, Mater. Sci. Eng. A. 586 (2013) 342–349. doi:10.1016/j.msea.2013.08.034.

[28] W.J. Evans, R. Lancaster, A. Steele, M. Whittaker, N. Jones, Plain and notched fatigue in nickel single crystal alloys, Int. J. Fatigue. 31 (2009) 1709–1718. doi:10.1016/j.ijfatigue.2009.03.010.

[29] J.J. Moore, E.A. Boyce, B. Perry, P.J. Sheridan, Chemical Metallurgy, 2nd ed., Butterworth-Heinemann, Oxford, 1997.

[30] R.E. Smallman, A.H.W. Ngan, Physical Metallurgy and Advanced Materials, 7th ed., Elsevier, 2010.

[31] N. Birks, G.H. Meier, F.S. Pettit, Introduction to the High-Temperature Oxidation of Metals, 2nd ed., Cambridge University Press, Cambridge, 2006.

[32] P. Sarrazin, A. Galerie, J. Fouletier, Mechanisms of High Temperature Corrosion - A Kinetic Approach, Trans Tech Publications Ltd, 2008.

[33] S. Bose, Oxidation, in: High Temp. Coatings, Elsevier, 2007: pp. 29–51.

[34] G. Zhou, J.C. Yang, Initial oxidation kinetics of copper (1 1 0) film investigated by in situ UHV-TEM, Surf. Sci. 531 (2003) 359–367. doi:10.1016/S0039-6028(03)00539-9.

[35] A.S. Khanna, High Temperature Oxidation, in: M. Kutz (Ed.), Handb. Environ. Degrad. Mater., 2nd ed., William Andrew Publishing, Oxford, 2012: pp. 127–194.

[36] C. Wagner, Beitrag zur theorie des anlaufvorgangs, Zeitschrift Für Phys. Chemie B. 21 (1933) 25.

[37] A. Atkinson, R.I. Taylor, A.E. Hughes, A quantitative demonstration of the grain boundary diffusion mechanism for the oxidation of metals, Philos. Mag. A Phys. Condens. Matter, Struct. Defects Mech. Prop. 45 (1982) 823–833. doi:10.1080/01418618208239905.

[38] N. Birks, G.H. Meier, F.S. Pettit, Mechanisms of Oxidation, in: Introd. to High Temp. Oxid. Met., 2nd ed., Cambridge, 2006: pp. 39–74. doi:10.1038/168123a0.

[39] P.Y. Hou, Segregation Phenomena at Thermally Grown Al2O3/Alloy Interfaces, Annu. Rev. Mater. Res. 38 (2008) 275–298. doi:10.1146/annurev.matsci.38.060407.130323.

[40] H.J. Grabke, Oxidation of NiAl and FeAl, Intermetallics. 7 (1999) 1153–1158. doi:10.1016/S0966-9795(99)00037-0.

[41] P.Y. Hou, A.P. Paulikas, B.W. Veal, Growth strains in thermally grown Al2O3 scales studied using synchrotron radiation, JOM. 61 (2009) 51–55. doi:10.1007/s11837-009-0103-x.

[42] A.H. Heuer, D.B. Hovis, J.L. Smialek, B. Gleeson, Alumina Scale Formation: A New Perspective, J. Am. Ceram. Soc. 94 (2011) 146–153. doi:10.1111/j.1551-2916.2011.04573.x.

[43] D.B. Hovis, L. Hu, A. Reddy, A.H. Heuer, A.P. Paulikas, B.W. Veal, In-situ studies of the TGO growth stresses and the martensitic transformation in the B2 phase in commercial Pt-modified NiAl and NiCoCrAlY bond coat alloys, Int. J. Mater. Res. 98 (2007) 1209–1213. http://www.hanser-

elibrary.com/doi/abs/10.3139/146.101586.

[44] H.E. Evans, Stress effects in high temperature oxidation of metals, Int. Mater. Rev. 40 (1995) 1–40. doi:10.1179/095066095790151124.

[45] V.K. Tolpygo, D.R. Clarke, K.S. Murphy, Evaluation of interface degradation during cyclic oxidation of EB-PVD thermal barrier coatings and correlation with TGO luminescence, Surf. Coatings Technol. 188–189 (2004) 62–70. doi:10.1016/j.surfcoat.2004.08.001.

[46] C.M. Younes, G.C. Allen, J.A. Nicholson, High temperature oxidation behaviour of single crystal superalloys RR3000 and CMSX-4, Corros. Eng. Sci. Technol. 42 (2007) 80–88. doi:10.1179/174327807X159925.

[47] H.E. Evans, High temperature coatings: Protection and breakdown, in: B. Cottis, M. Graham, R. Lindsay, S. Lyon, T. Richardson, D. Scantlebury, H. Stott (Eds.), Shreir's Corros., Elsevier, Amsterdam, 2010: pp. 691–724. doi:10.1016/B978-044452787-5.00080-9.

[48] J.R. Nicholls, K.J. Lawson, L.H. Al Yasiri, P. Hancock, Vapour phase alloy design of corrosion-resistant overlay coatings, Corros. Sci. 35 (1993). doi:10.1016/0010-938X(93)90341-D.

[49] J.R. Nicholls, N.J. Simms, W.Y. Chan, H.E. Evans, Smart overlay coatings - Concept and practice, Surf. Coatings Technol. 149 (2002) 236–244. doi:10.1016/S0257-8972(01)01499-2.

[50] R.G. Wellman, A. Scrivani, G. Rizzi, A. Weisenburger, F.H. Tenailleau, J.R. Nicholls, Pulsed electron beam treatment of MCrAlY bondcoats for EB PVD TBC systems part 2 of 2: Cyclic oxidation of the coatings, Surf. Coatings Technol. 202 (2007) 709–713. doi:10.1016/j.surfcoat.2007.06.037.

[51] A. Bradshaw, N.J. Simms, J.R. Nicholls, Development of hot corrosion resistant coatings for gas turbines burning biomass and waste derived fuel gases, Surf. Coatings Technol. 216 (2013) 8–22. doi:10.1016/j.surfcoat.2012.10.047.

[52] S. Hayashi, S.I. Ford, D.J. Young, D.J. Sordelet, M.F. Besser, B. Gleeson, α-NiPt(Al) and phase equilibria in the Ni-Al-Pt system at 1150°C, Acta Mater. 53 (2005) 3319–3328. doi:10.1016/j.actamat.2005.03.046.

[53] R.C. Reed, R.T. Wu, M.S. Hook, C.M.F. Rae, R.G. Wing, On oxidation behaviour of platinum aluminide coated nickel based superalloy CMSX-4, Mater. Sci. Technol. 25 (2009) 276–286. doi:10.1179/174328408X361481.

[54] E.P. Busso, H.E. Evans, Z.Q. Qian, M.P. Taylor, Effects of breakaway oxidation on local stresses in thermal barrier coatings, Acta Mater. 58 (2010) 1242–1251. doi:10.1016/j.actamat.2009.10.028.

[55] D.K. Das, Microstructure and high temperature oxidation behavior of Pt-modified aluminide bond coats on Ni-base superalloys, Prog. Mater. Sci. 58 (2013) 151–182. doi:10.1016/j.pmatsci.2012.08.002.

[56] J.H. Chen, J.A. Little, Degradation of the platinum aluminide coating on CMSX4 at 1100 °C, Surf. Coatings Technol. 92 (1997) 69–77. doi:10.1016/S0257-8972(96)03117-9.

[57] H.E. Evans, M.P. Taylor, Oxidation of high-temperature coatings, Proc. Inst.

Mech. Eng. Part G J. Aerosp. Eng. 220 (2006) 1–10. doi:10.1243/095441005X33420.

[58] J.R. Nicholls, K.J. Lawson, A. Johnstone, D.S. Rickerby, Methods to reduce the thermal conductivity of EB-PVD TBCs, Surf. Coatings Technol. 151–152 (2002) 383–391. doi:10.1016/S0257-8972(01)01651-6.

[59] E. Hejrani, D. Sebold, W.J. Nowak, G. Mauer, D. Naumenko, R. Vaßen, W.J. Quadakkers, Isothermal and cyclic oxidation behavior of free standing MCrAlY coatings manufactured by high-velocity atmospheric plasma spraying, Surf. Coatings Technol. 313 (2017) 191–201. doi:10.1016/j.surfcoat.2017.01.081.

[60] G. Mauer, R. Vaßen, D. Stöver, Controlling the oxygen contents in vacuum plasma sprayed metal alloy coatings, Surf. Coatings Technol. 201 (2007) 4796–4799. doi:10.1016/j.surfcoat.2006.10.008.

[61] A. Feuerstein, J. Knapp, T. Taylor, A. Ashary, A. Bolcavage, N. Hitchman, Technical and economical aspects of current thermal barrier coating systems for gas turbine engines by thermal spray and EBPVD: A review, J. Therm. Spray Technol. 17 (2008) 199–213. doi:10.1007/s11666-007-9148-y.

[62] M. Leoni, R.L. Jones, P. Scardi, Phase stability of scandia–yttria-stabilized zirconia TBCs, Surf. Coatings Technol. 108–109 (1998) 107–113.

[63] J.R. Brandon, R. Taylor, Thermal properties of ceria and yttria partially stabilized zirconia thermal barrier coatings, Surf. Coatings Technol. 39/40 (1989) 143–151.

[64] D.E. Wolfe, J. Singh, R.A. Miller, J.I. Eldridge, D.M. Zhu, Tailored microstructure of EB-PVD 8YSZ thermal barrier coatings with low thermal conductivity and high thermal reflectivity for turbine applications, Surf. Coatings Technol. 190 (2005) 132–149. doi:10.1016/j.surfcoat.2004.04.071.

[65] K. Suzuki, T. Shobu, K. Wada, H. Matsubara, M. Kawamura, Microstructure and Residual Stress of EB-PVD TBCs Grown under Substrate Rotation, J. Soc. Mater. Sci. Japan. 57 (2008) 674–680. doi:10.2472/jsms.57.674.

[66] A.M. Limarga, D.R. Clarke, Characterization of electron beam physical vapor-deposited thermal barrier coatings using diffuse optical reflectance, Int. J. Appl. Ceram. Technol. 6 (2009) 400–409. doi:10.1111/j.1744-7402.2008.02349.x.

[67] N.M. Yanar, F.S. Pettit, G.H. Meier, Failure characteristics during cyclic oxidation of yttria stabilized zirconia thermal barrier coatings deposited via electron beam physical vapor deposition on platinum aluminide and on NiCoCrAlY bond coats with processing modifications for improved perfo, Metall. Mater. Trans. A. 37 (2006) 1563–1580. doi:10.1007/s11661-006-0100-4.

[68] H.E. Evans, Oxidation failure of TBC systems: An assessment of mechanisms, Surf. Coatings Technol. 206 (2011) 1512–1521. doi:10.1016/j.surfcoat.2011.05.053.

[69] H.E. Evans, R.C. Lobb, Conditions for the initiation of oxide-scale cracking and spallation, Corros. Sci. 24 (1984) 209–222. doi:10.1016/0010-938X(84)90051-9.

[70] K.L. Luthra, C.L. Briant, Mechanism of adhesion of alumina on MCrAlY alloys, Oxid. Met. 26 (1986) 397–416. doi:10.1007/BF00659344.

[71] C. Sarioglu, E. Schumann, J.R. Blachere, F.S. Pettit, G.H. Meier, X-ray

determination of stresses in alumina scales on high temperature alloys, Mater. High Temp. 17 (2000) 109–115.

[72] S. Gray, M.P. Taylor, E. Chau, H.E. Evans, Evaluation of the Critical Oxide Thickness to Initiate Spallation from a LPPS CoNiCrAlY Coating, in: B. Cottis (Ed.), Corros. Sci. 21st Century, Journal of Corrosion Science and Engineering, Manchester, 2003: p. H016.

[73] V.K. Tolpygo, D.R. Clarke, On the rumpling mechanism in nickel-aluminide coatings part I: An experimental assessment, Acta Mater. 52 (2004) 5115–5127. doi:10.1016/j.actamat.2004.07.019.

[74] V.K. Tolpygo, D.R. Clarke, Surface rumpling of a (Ni, Pt)Al bond coat induced by cyclic oxidation, Acta Mater. 48 (2000) 3283–3293. doi:10.1016/S1359-6454(00)00156-7.

[75] I.T. Spitsberg, D.R. Mumm, A.G. Evans, On the failure mechanisms of thermal barrier coatings with diffusion aluminide bond coatings, Mater. Sci. Eng. A. 394 (2005) 176–191. doi:10.1016/j.msea.2004.11.038.

[76] A.G. Evans, M.Y. He, J.W. Hutchinson, Mechanics-based scaling laws for the durability of thermal barrier coatings, Prog. Mater. Sci. 46 (2001) 249–271. doi:10.1016/S0079-6425(00)00007-4.

[77] A.G. Evans, D.R. Clarke, C.G. Levi, The influence of oxides on the performance of advanced gas turbines, J. Eur. Ceram. Soc. 28 (2008) 1405–1419. doi:10.1016/j.jeurceramsoc.2007.12.023.

[78] J.L. Smialek, Compiled furnace cyclic lives of EB-PVD thermal barrier coatings, Surf. Coatings Technol. 276 (2015) 31–38. doi:10.1016/j.surfcoat.2015.06.018.

[79] E.P. Busso, Z.Q. Qian, M.P. Taylor, H.E. Evans, The influence of bondcoat and topcoat mechanical properties on stress development in thermal barrier coating systems, Acta Mater. 57 (2009) 2349–2361. doi:10.1016/j.actamat.2009.01.017.

[80] R.G. Wellman, J.R. Nicholls, Erosion, corrosion and erosion-corrosion of EB PVD thermal barrier coatings, Tribol. Int. 41 (2008) 657–662. doi:10.1016/j.triboint.2007.10.004.

[81] N. Vialas, D. Monceau, Substrate effect on the high-temperature oxidation behavior of a Pt-modified aluminide coating. Part I: Influence of the initial chemical composition of the coating surface, Oxid. Met. 66 (2006) 155–189. doi:10.1007/s11085-006-9024-z.

[82] N. Vialas, D. Monceau, Substrate effect on the high temperature oxidation behavior of a Pt-modified aluminide coating. Part II: Long-term cyclic-oxidation tests at 1,050 °C, Oxid. Met. 68 (2007) 223–242. doi:10.1007/s11085-007-9072-z.

[83] D.S. Rickerby, S.R. Bell, R.G. Wing, Article Including Thermal Barrier Coated Superalloy Substrate, US5981091, 1999.

[84] M. Jönsson, B. Rendahl, I. Annergren, The use of infrared thermography in the corrosion science area, Mater. Corros. 61 (2010) 961–965. doi:10.1002/maco.200905525.

[85] S.A. Grammatikos, E.Z. Kordatos, N.-M. Barkoula, T.E. Matikas, A.S. Paipetis,

Innovative non-destructive evaluation and damage characterisation of composite aerostructures using thermography, Plast. Rubber Compos. 40 (2011) 342–348. doi:10.1179/1743289810Y.0000000013.

[86] K. Blessley, C. Young, J. Nunn, J. Coddington, S. Shepard, The Feasibility of Flash Thermography for the Examination and Conservation of Works of Art, Stud. Conserv. 55 (2010) 107–120.

[87] S.M. Shepard, Flash thermography of aerospace composites, in: IV Conf. Panam. END Buenos Aires, Buenos Aires, 2007: p. 7. http://212.8.206.21/article/panndt2007/papers/132.pdf.

[88] J.B. Abbiss, B. Heeg, Imaging piezospectroscopy, Rev. Sci. Instrum. 79 (2008) 123105. doi:10.1063/1.3030776.

[89] B.W. Kempshall, Y.H. Sohn, S.K. Jha, S. Laxman, R.R. Vanfleet, J. Kimmel, A microstructural observation of near-failure thermal barrier coating: A study by photostimulated luminescence spectroscopy and transmission electron microscopy, Thin Solid Films. 466 (2004) 128–136. doi:10.1016/j.tsf.2004.02.046.

[90] D.M. Lipkin, D.R. Clarke, Measurement of the stress in oxide scales formed by oxidation of alumina-forming alloys, Oxid. Met. 45 (1996) 267–280. doi:10.1007/BF01046985.

[91] C.R.C. Lima, S. Dosta, J.M. Guilemany, D.R. Clarke, The application of photoluminescence piezospectroscopy for residual stresses measurement in thermally sprayed TBCs, Surf. Coatings Technol. 318 (2016) 147–156. doi:10.1016/j.surfcoat.2016.07.084.

[92] A. Selçuk, A. Atkinson, Residual stress measurement by Piezo spectroscopy of cross sections through thermal barrier coatings, Proc. Fifth Int. Conf. Microsc. Oxidation, Limerick, 26-28 August 2002. 20 (2003) 241–248.

[93] C. De Michelis, C. Rinaldi, C. Sampietri, R. Vario, Condition monitoring and assessment of power plant components, in: J.E. Oakey (Ed.), Power Plant Life Manag. Perform. Improv., 1st ed., Woodhead Publishing, Cambridge, 2011: pp. 38–109.

[94] B. Heeg, V.K. Tolpygo, D.R. Clarke, Damage Evolution in Thermal Barrier Coatings with Thermal Cycling, J. Am. Ceram. Soc. 94 (2011) 112–119. doi:10.1111/j.1551-2916.2011.04496.x.

[95] J.A. Nychka, D.R. Clarke, Damage quantification in TBCs by photo-stimulated luminescence spectroscopy, Surf. Coatings Technol. 146–147 (2001) 110–116. doi:10.1016/S0257-8972(01)01455-4.

[96] X. Wang, G. Lee, A. Atkinson, Investigation of TBCs on turbine blades by photoluminescence piezospectroscopy, Acta Mater. 57 (2009) 182–195. doi:10.1016/j.actamat.2008.08.053.

[97] M. Wen, E.H. Jordan, M. Gell, Evolution of photo-stimulated luminescence of EB-PVD/(Ni, Pt)Al thermal barrier coatings, Mater. Sci. Eng. A. 398 (2005) 99–107. doi:10.1016/j.msea.2005.03.020.

[98] S. Sridharan, L. Xie, E.H. Jordan, M. Gell, Stress variation with thermal cycling in

the thermally grown oxide of an EB-PVD thermal barrier coating, Surf. Coatings Technol. 179 (2004) 286–296. doi:10.1016/S0257-8972(03)00858-2.

[99] X. Wang, A. Atkinson, Piezo-spectroscopic mapping of the thermally grown oxide in thermal barrier coatings, Mater. Sci. Eng. A. 465 (2007) 49–58. doi:10.1016/j.msea.2007.04.081.

[100] B.G. Nair, J.P. Singh, M. Grimsditch, Stress analysis in thermal barrier coatings subjected to long-term exposure in simulated turbine conditions, J. Mater. Sci. 39 (2004) 2043–2051. doi:10.1023/B:JMSC.0000017767.36955.5c.

[101] N. Mu, J. Liu, J.W. Byeon, Y.H. Sohn, Y.L. Nava, Long-term oxidation and phase transformations in aluminized CMSX-4 superalloys, Surf. Coatings Technol. 188–189 (2004) 27–34. doi:10.1016/j.surfcoat.2004.07.091.

[102] X. Wang, A. Atkinson, L. Chirivì, J.R. Nicholls, Evolution of stress and morphology in thermal barrier coatings, Surf. Coatings Technol. 204 (2010) 3851–3857. doi:10.1016/j.surfcoat.2010.04.065.

[103] G. Lee, A. Atkinson, A. Selçuk, Development of residual stress and damage in thermal barrier coatings, Surf. Coatings Technol. 201 (2006) 3931–3936. doi:10.1016/j.surfcoat.2006.08.010.

[104] A. Selçuk, A. Atkinson, Analysis of the Cr3+ luminescence spectra from thermally grown oxide in thermal barrier coatings, Mater. Sci. Eng. A. 335 (2002) 147–156. doi:10.1016/S0921-5093(01)01911-6.

[105] H. Kimachi, W. Ota, K. Fujiyama, S. Yamamoto, K. Niwa, M. Uchimura, Evaluation of Thermal Damage of Thermal Barrier Coatings by Using Raman Microspectroscopy, J. Soc. Mater. Sci. Japan. 59 (2010) 455–461.

[106] Y. Zhao, C. Ma, F. Huang, C. Wang, S. Zhao, Q. Cui, X. Cao, F. Li, Residual stress inspection by Eu3+ photoluminescence piezo-spectroscopy : An application in thermal barrier coatings, J. Appl. Phys. 114 (2013) 1–5. doi:10.1063/1.4818500.

[107] S. Zhu, K. Fukuda, T. Osaki, Residual Stress in TGO and Interfacial Damage in Thermal Barrier Coating after Thermal Exposure and Cyclic Indentation, J. Solid Mech. Mater. Eng. 4 (2010) 244–251. doi:10.1299/jmmp.4.244.

[108] E.P. Busso, L. Wright, H.E. Evans, L.N. McCartney, S.R.J. Saunders, S. Osgerby, J. Nunn, A physics-based life prediction methodology for thermal barrier coating systems, Acta Mater. 55 (2007) 1491–1503. doi:10.1016/j.actamat.2006.10.023.

[109] A. Selçuk, A. Atkinson, The evolution of residual stress in the thermally grown oxide on Pt diffusion bond coats in TBCs, Acta Mater. 51 (2003) 535–549. doi:10.1016/S1359-6454(02)00436-6.

[110] J. Baruchel, J.-Y. Buffière, E. Maire, P. Merle, G. Peix, Microtomography at a third generation synchrotron radiation facility, in: X-Ray Tomogr. Mater. Sci., Hermes Science Publications, Paris, 2000: pp. 45–59.

[111] P. Willmot, Synchrotron Physics, in: An Introd. to Synchrotron Radiat. Tech. Appl., 1st ed., Wiley, Chichester, 2011: pp. 39–86.

[112] H. Winick, Introduction and Overview, in: Synchrotron Radiat. Sources A Prim., World Scientific Publishing Co Pte Ltd, Singapore, 1995: pp. 1–15.

[113] G. Margaritondo, Synchrotron Radiation Sources and Instrumentation, in: Introd.

to Synchrotron Radiat., Oxford University Press, Oxford, 1988: pp. 9–91.

[114] G. Choppin, J.-O. Liljenzin, J. Rydberg, C. Ekberg, Particle Accelerators, in: Radiochem. Nucl. Chem., 4th ed., Academic Press, Oxford, 2013: pp. 493–512.

[115] J. Banhart, Radiation Sources and Interaction of Radiation with Matter, in: J. Banhart (Ed.), Adv. Tomogr. Methods Mater. Res. Eng., 1st ed., Oxford University Press, Oxford, 2008: pp. 107–140.

[116] T. Donath, Quantitative X-ray Microtomography with Synchrotron Radiation, GKSS-Forschungszentrum, Geesthacht, 2007.

[117] M.J. Berger, J.H. Hubbell, S.M. Seltzer, J. Chang, J.S. Coursey, R. Sukumar, D.S. Zucker, K. Olsen, XCOM: Photon Cross Sections Database, NIST Stand. Ref. Database 8. (1998).

[118] L. Gerward, N. Guilbert, K.B. Jensen, H. Levring, WinXCom—a program for calculating X-ray attenuation coefficients, Radiat. Phys. Chem. 71 (2004) 653–654. doi:10.1016/j.radphyschem.2004.04.040.

[119] L. Gerward, N. Guilbert, K. Bjørn Jensen, H. Levring, X-ray absorption in Matter. Reengineering XCOM, Radiat. Phys. Chem. 60 (2001) 23–24.

[120] M. Bech, O. Bunk, C. David, R. Ruth, J. Rifkin, R. Loewen, R. Feidenhansl, F. Pfeiffer, Hard X-ray phase-contrast imaging with the Compact Light Source based on inverse Compton X-rays, J. Synchrotron Radiat. 16 (2008) 43–47. doi:10.1107/S090904950803464X.

[121] J. Radon, On determination of functions by their integral values along certain multiplicities, Ber. Der Sachische Akad. Der Wissenschaften Leipzig. 69 (1917) 262–277.

[122] P. Willmot, Beamlines, in: An Introd. to Synchrotron Radiat. Tech. Appl., 1st ed., Wiley, Chichester, 2011: pp. 87–131.

[123] P. Willmot, Imaging Techniques, in: An Introd. to Synchrotron Radiat. Tech. Appl., 1st ed., John Wiley & Sons, Ltd, Chichester, 2011: pp. 303–337.

[124] L. Helfen, F. Xu, H. Suhonen, P. Cloetens, T. Baumbach, Laminographic imaging using synchrotron radiation – challenges and opportunities, in: P. Dumas, J. Susini (Eds.), J. Phys. Conf. Ser., IOP Publishing, 2013: pp. 1–6. doi:10.1088/1742-6596/425/19/192025.

[125] G. Borstnar, M.N. Mavrogordato, L. Helfen, I. Sinclair, S.M. Spearing, Interlaminar fracture micro-mechanisms in toughened carbon fibre reinforced plastics investigated via synchrotron radiation computed tomography and laminography, Compos. Part A Appl. Sci. Manuf. 71 (2015) 176–183. doi:10.1016/j.compositesa.2015.01.012.

[126] M. Hoshino, K. Uesugi, A. Takeuchi, Y. Suzuki, N. Yagi, I. McNulty, C. Eyberger, B. Lai, Development of an X-ray Micro-Laminography System at SPring-8, in: I. McNulty, C. Eyberger, B. Lai (Eds.), 10th Int. Conf. X-Ray Microsc., AIP, 2011: pp. 250–253. doi:10.1063/1.3625351.

[127] S. Ahmadian, A. Browning, E.H. Jordan, Three-dimensional X-ray micro-computed tomography of cracks in a furnace cycled air plasma sprayed thermal barrier coating, Scr. Mater. 97 (2015) 13–16.

doi:10.1016/j.scriptamat.2014.10.026.

[128] Y. Zhao, A. Shinmi, X. Zhao, P.J. Withers, S. Van Boxel, N. Markocsan, P. Nylen, P. Xiao, Investigation of interfacial properties of atmospheric plasma sprayed thermal barrier coatings with four-point bending and computed tomography technique, Surf. Coatings Technol. 206 (2012) 4922–4929. doi:10.1016/j.surfcoat.2012.05.099.

[129] N. Asadizanjani, S. Shahbazmohamadi, E.H. Jordan, Investigation of Surface Geometry Thermal Barrier Coatings using Computed X-Ray Tomography, in: M.W. Kriven, D. Zhu, K. Il Moon, T. Hwang, J. Wang, C.A. Lewinsohn, Y. Zhou, A.L. Gyekenyesi, M. Halbig (Eds.), Dev. Strateg. Mater. Comput. Des. V A Collect. Pap. Present. 38th Int. Conf. Adv. Ceram. Compos. January 27-31, 2014 Daytona Beach, Florida, John Wiley & Sons, 2015: pp. 175–187.

[130] Z. Yan, O. Guillon, S. Wang, C.L. Martin, C.S. Lee, D. Bouvard, Synchrotron x-ray nano-tomography characterization of the sintering of multilayered systems, Appl. Phys. Lett. 100 (2012) 2631071–2631074. doi:10.1063/1.4730625.

[131] A.A. Kulkarni, A. Goland, H. Herman, A.J. Allen, T. Dobbins, F. DeCarlo, J. Ilavsky, G.G. Long, S. Fang, P. Lawton, Advanced neutron and X-ray techniques for insights into the microstructure of EB-PVD thermal barrier coatings, Mater. Sci. Eng. A. 426 (2006) 43–52. doi:10.1016/j.msea.2006.03.070.

[132] A.A. Kulkarni, H. Herman, F. Decarlo, Microstructural Characterization of Electron Beam – Physical Vapor Deposition Thermal Barrier Coatings through High-Resolution Computed Microtomography, Metall. Mater. Trans. A. 35 (2004) 1945–1952.

[133] V. Maurel, L. Helfen, F. N'Guyen, A. Köster, M. Di Michiel, T. Baumbach, T.F. Morgeneyer, Three-dimensional investigation of thermal barrier coatings by synchrotron-radiation computed laminography, Scr. Mater. 66 (2012) 471–474. doi:10.1016/j.scriptamat.2011.12.021.

[134] V. Maurel, L. Helfen, R. Soulignac, T.F. Morgeneyer, A. Köster, L. Rémy, Three-Dimensional Damage Evolution Measurement in EB-PVD TBCs Using Synchrotron Laminography, Oxid. Met. 79 (2013) 313–323. doi:10.1007/s11085-012-9333-3.

[135] F. Fiori, F. Spinozzi, Microstructural Investigations by Small Angle Scattering of Neutrons and X-rays, in: F. Rustichelli, J.J. Skrzypek (Eds.), Innov. Technol. Mater. Struct. Prop. by Neutron Scatt. Synchrotron Radiat. Model., Springer-Verlag, Dordrecht, 2010: pp. 35–73.

[136] A.J. Allen, Characterization of ceramics by X-ray and neutron small-angle scattering, J. Am. Ceram. Soc. 88 (2005) 1367–1381. doi:10.1111/j.1551-2916.2005.00463.x.

[137] J. Ilavsky, F. Zhang, A.J. Allen, L.E. Levine, P.R. Jemian, G.G. Long, Ultra-Small-Angle X-ray Scattering Instrument at the Advanced Photon Source: History, Recent Development, and Current Status, Metall. Mater. Trans. A. 44 (2012) 68–76. doi:10.1007/s11661-012-1431-y.

[138] J. Ilavsky, P.R. Jemian, A.J. Allen, F. Zhang, L.E. Levine, G.G. Long, Ultra-small-angle X-ray scattering at the Advanced Photon Source, J. Appl. Crystallogr. 42

(2009) 469–479. doi:10.1107/S0021889809008802.

[139] A.F. Renteria, B. Saruhan, J. Ilavsky, A.J. Allen, Application of USAXS analysis and non-interacting approximation to determine the influence of process parameters and ageing on the thermal conductivity of electron-beam physical vapor deposited thermal barrier coatings, Surf. Coatings Technol. 201 (2007) 4781–4788. doi:10.1016/j.surfcoat.2006.10.020.

[140] D.D. Hass, H. Zhao, T. Dobbins, A.J. Allen, A.J. Slifka, H.N.G. Wadley, Multi-scale pore morphology in directed vapor deposited yttria-stabilized zirconia coatings, Mater. Sci. Eng. A. 527 (2010) 6270–6282. doi:10.1016/j.msea.2010.06.033.

[141] F. Hild, S. Roux, Digital image correlation: From displacement measurement to identification of elastic properties - A review, Strain. 42 (2006) 69–80. doi:10.1111/j.1475-1305.2006.00258.x.

[142] B. Pan, D. Wu, Z. Wang, Internal displacement and strain measurement using digital volume correlation: a least-squares framework, Meas. Sci. Technol. 23 (2012) 1–13. doi:10.1088/0957-0233/23/4/045002.

[143] B.K. Bay, T.S. Smith, D.P. Fyhrie, M. Saad, Digital volume correlation: Three-dimensional strain mapping using X-ray tomography, Exp. Mech. 39 (1999) 217–226. doi:10.1007/BF02323555.

[144] K. Madi, G. Tozzi, Q.H. Zhang, J. Tong, A. Cossey, A. Au, D. Hollis, F. Hild, Computation of full-field displacements in a scaffold implant using digital volume correlation and finite element analysis, Med. Eng. Phys. 35 (2013) 1298–1312. doi:10.1016/j.medengphy.2013.02.001.

[145] LaVision, Product Manual - DAVIS 8.2 Software, Göttingen, 2014.

[146] M. Mostafavi, S.A. McDonald, P.M. Mummery, T.J. Marrow, Observation and quantification of three-dimensional crack propagation in poly-granular graphite, Eng. Fract. Mech. 110 (2013) 410–420. doi:10.1016/j.engfracmech.2012.11.023.

[147] J.Q. Da Fonseca, P.M. Mummery, P.J. Withers, Full-field strain mapping by optical correlation of micrographs acquired during deformation, J. Microsc. 218 (2005) 9–21. doi:10.1111/j.1365-2818.2005.01461.x.

[148] B. Pan, K. Qian, H. Xie, A. Asundi, Two-dimensional digital image correlation for in-plane displacement and strain measurement: a review, Meas. Sci. Technol. 20 (2009) 1–17. doi:10.1088/0957-0233/20/6/062001.

[149] N. Lenoir, M. Bornert, J. Desrues, P. Bésuelle, G. Viggiani, Volumetric Digital Image Correlation Applied to X-ray Microtomography Images from Triaxial Compression Tests on Argillaceous Rock, Strain. 43 (2007) 193–205.

[150] A. Germaneau, P. Doumalin, J.C. Dupré, 3D Strain Field Measurement by Correlation of Volume Images Using Scattered Light: Recording of Images and Choice of Marks, Strain. 43 (2007) 207.

[151] C. Eberl, D.S. Gianola, X. Wang, M.Y. He, A.G. Evans, K.J. Hemker, A method for in situ measurement of the elastic behavior of a columnar thermal barrier coating, Acta Mater. 59 (2011) 3612–3620. doi:10.1016/j.actamat.2011.02.034.

[152] C. Eberl, D.S. Gianola, K.J. Hemker, Mechanical Characterization of Coatings

Using Microbeam Bending and Digital Image Correlation Techniques, Exp. Mech. 50 (2010) 85–97. doi:10.1007/s11340-008-9187-4.

[153] C. Eberl, X. Wang, D.S. Gianola, T.D. Nguyen, M.Y. He, A.G. Evans, K.J. Hemker, In situ measurement of the toughness of the interface between a thermal barrier coating and a Ni alloy, J. Am. Ceram. Soc. 94 (2011) 120–127. doi:10.1111/j.1551-2916.2011.04588.x.

[154] W.G. Mao, D.J. Wu, W.B. Yao, M. Zhou, C. Lu, Multiscale monitoring of interface failure of brittle coating/ductile substrate systems: A non-destructive evaluation method combined digital image correlation with acoustic emission, J. Appl. Phys. 110 (2011) 1–5. doi:10.1063/1.3651378.

[155] X.S. Yang, J. Wan, C.Y. Dai, Y. Zhang, W.G. Mao, Y.C. Zhou, C. Lu, Finite element analysis of crack propagation and fracture mechanical properties of freestanding 8wt.% Y2O3-ZrO2 coatings, Surf. Coatings Technol. 223 (2013) 87–91. doi:10.1016/j.surfcoat.2013.02.034.

[156] X. Yang, Z. Liu, H. Xie, A real time deformation evaluation method for surface and interface of thermal barrier coatings during 1100 °C thermal shock, Meas. Sci. Technol. 23 (2012) 1–12. doi:10.1088/0957-0233/23/10/105604.

[157] J. Wan, M. Zhou, X.S. Yang, C.Y. Dai, Y. Zhang, W.G. Mao, C. Lu, Fracture characteristics of freestanding 8wt% Y2O3-ZrO2 coatings by single edge notched beam and Vickers indentation tests, Mater. Sci. Eng. A. 581 (2013) 140–144. doi:10.1016/j.msea.2013.05.086.

[158] C. Pfeiffer, E. Affeldt, M. Göken, Miniaturized bend tests on partially stabilized EB-PVD ZrO2 thermal barrier coatings, Surf. Coatings Technol. 205 (2011) 3245–3250. doi:10.1016/j.surfcoat.2010.11.047.

[159] E.M. Donohue, N.R. Philips, M.R. Begley, C.G. Levi, Thermal barrier coating toughness: Measurement and identification of a bridging mechanism enabled by segmented microstructure, Mater. Sci. Eng. A. 564 (2013) 324–330. doi:10.1016/j.msea.2012.11.126.

[160] D.J. Wu, W.G. Mao, Y.C. Zhou, C. Lu, Digital image correlation approach to cracking and decohesion in a brittle coating/ductile substrate system, Appl. Surf. Sci. 257 (2011) 6040–6043. doi:10.1016/j.apsusc.2011.01.119.

[161] R.J. Thompson, K.J. Hemker, Thermal Expansion Measurements on Coating Materials by Digital Image Correlation, in: 2007 SEM Annu. Conf. Expo. Exp. Appl. Mech., 2007.

[162] J. Zhu, H. Xie, Z. Hu, P. Chen, Q. Zhang, Residual stress in thermal spray coatings measured by curvature based on 3D digital image correlation technique, Surf. Coatings Technol. 206 (2011) 1396–1402. doi:10.1016/j.surfcoat.2011.08.062.

[163] V. Maurel, P. de Bodman, L. Rémy, Influence of substrate strain anisotropy in TBC system failure, Surf. Coatings Technol. 206 (2011) 1634–1639. doi:10.1016/j.surfcoat.2011.06.041.

[164] R.C. Reed, N. Matan, D.C. Cox, M.A. Rist, C.M.F. Rae, Creep of CMSX-4 superalloy single crystals: effects of rafting at high temperature, Acta Mater. 47 (1999) 3367–3381. doi:10.1016/S1359-6454(99)00217-7.

[165] K. Harris, G.L. Erickson, Single Crystal Alloy Technology, US4643782, 1987.

[166] A. Thompson, I. Lindau, D. Attwood, Y. Liu, E. Gullikson, P. Pianetta, M. Howells, A. Robinson, K.-J. Kim, J. Scofield, J. Kirz, J. Underwood, J. Kortright, G. Williams, H. Winick, X-Ray Data Booklet, 3rd ed., Lawrence Berkeley National Laboratory, Berkeley, 2009.

[167] Oxford Instruments, INCA Energy Operator Manual, 2nd ed., Oxford Instruments Analytical, High Wycombe, 2006. http://www.iitk.ac.in/meesa/SEM/EDS_manual.pdf.

[168] J. Schindelin, I. Arganda-Carreras, E. Frise, V. Kaynig, M. Longair, T. Pietzsch, S. Preibisch, C. Rueden, S. Saalfeld, B. Schmid, J.-Y. Tinevez, D.J. White, V. Hartenstein, K.W. Eliceiri, P. Tomancak, A. Cardona, Fiji: an open-source platform for biological-image analysis., Nat. Methods. 9 (2012) 676–682. doi:10.1038/nmeth.2019.

[169] P. Thévenaz, M. Unser, User-Friendly Semiautomated Assembly of Accurate Image Mosaics in Microscopy, Microsc. Res. Tech. 70 (2007) 135–146.

[170] W. Rasband, Grid Overlay Plugin, (2010). http://rsb.info.nih.gov/ij/plugins/graphic-overlay.html.

[171] J. Angenete, K. Stiller, A comparative study of two inward grown Pt modified Al diffusion coatings on a single crystal Ni base superalloy, Mater. Sci. Eng. A. 316 (2001) 182–194. doi:10.1016/S0921-5093(01)01236-9.

[172] X. Zhao, I.P. Shapiro, P. Xiao, Spinel formation in thermal barrier systems with a Pt-enriched γ-Ni + γ′-Ni3Al bond coat, Surf. Coatings Technol. 202 (2008) 2905–2916. doi:10.1016/j.surfcoat.2007.10.030.

[173] J.H. Hubbell, S.M. Seltzer, Tables of X-Ray Mass Attenuation Coefficients and Mass Energy-Absorption Coefficients from 1 keV to 20 MeV for Elements Z = 1 to 92 and 48 Additional Substances of Dosimetric Interest, Gaithersburg, 2004.

[174] S. Titarenko, P.J. Withers, A. Yagola, An analytical formula for ring artefact suppression in X-ray tomography, Appl. Math. Lett. 23 (2010) 1489–1495. doi:10.1016/j.aml.2010.08.022.

[175] C.A. Schneider, W.S. Rasband, K.W. Eliceiri, NIH Image to ImageJ: 25 years of image analysis, Nat. Methods. 9 (2012) 671–675. doi:10.1038/nmeth.2089.

[176] K. Shoemake, Animating rotation with quaternion curves, in: ACM SIGGRAPH Comput. Graph., San Francisco, 1985: pp. 245–254. doi:10.1145/325165.325242.

[177] M. Mostafavi, D.M. Collins, B. Cai, R. Bradley, R.C. Atwood, C. Reinhard, X. Jiang, M. Gelano, P.D. Lee, T.J. Marrow, Yield behavior beneath hardness indentations in ductile metals , measured by three-dimensional computed X-ray tomography and digital volume correlation, Acta Mater. 82 (2015) 468–482. doi:10.1016/j.actamat.2014.08.046.

[178] D. Monceau, B. Pieraggi, Determination of Parabolic Rate Constants from a Local Analysis of Mass-Gain Curves, Oxid. Met. 50 (1998) 477–493. doi:10.1023/A:1018860909826.

[179] M.P. Taylor, H.E. Evans, DARP Lifing of TBCs, 2005.

[180] H.M. Tawancy, Advanced Thermal Barrier Coating Systems: Comparative

Performance of Low-Cost Pt and CN122+Pt on Alloy CMSX-4, Dhahran, 1997.

[181] R.T. Wu, K. Kawagishi, H. Harada, R.C. Reed, The retention of thermal barrier coating systems on single-crystal superalloys: Effect of substrate composition, Acta Mater. 56 (2008) 3622–3629.

[182] L. Chirivì, J.R. Nicholls, Influence of surface finish on the cyclic oxidation lifetime of an EV-PVD TBC, deposited on PtAl and Pt-diffused bondcoats, Oxid. Met. 81 (2014) 17–31. doi:10.1007/s11085-013-9429-4.

[183] D. Liu, C. Rinaldi, P.E.J. Flewitt, Effect of substrate curvature on the evolution of microstructure and residual stresses in EBPVD-TBC, J. Eur. Ceram. Soc. 35 (2015) 2563–2575. doi:10.1016/j.jeurceramsoc.2015.02.024.

[184] H. Hindam, D.P. Whittle, Microstructure, adhesion and growth kinetics of protective scales on metals and alloys, Oxid. Met. 18 (1982) 245–284. doi:10.1007/BF00656571.

[185] A. Atkinson, A. Selçuk, S.J. Webb, Variability of stress in alumina corrosion layers formed in thermal-barrier coatings, Oxid. Met. 54 (2000) 371–384. doi:10.1023/A:1004613332338.

[186] R.T. Wu, X. Wang, A. Atkinson, On the interfacial degradation mechanisms of thermal barrier coating systems: Effects of bond coat composition, Acta Mater. 58 (2010) 5578–5585.

[187] M. Wen, E.H. Jordan, M. Gell, Analysis of localized damage in EB-PVD/(Ni, Pt)Al thermal barrier coatings, Surf. Coatings Technol. 200 (2006) 5193–5202. doi:10.1016/j.surfcoat.2005.05.044.

[188] S.J. Bull, Modeling of Residual Stress in Oxide Scales, Oxid. Met. 49 (1998) 1–17. http://dx.doi.org/10.1023/A:1018822222663.

[189] V.K. Tolpygo, D.R. Clarke, Competition Between Stress Generation and Relaxation During Oxidation of an Fe-Cr-Al-Y Alloy, Oxid. Met. 49 (1998) 187–212. doi:10.1023/A:1018828619028.

[190] K. Suzuki, K. Tanaka, Y. Akiniwa, Estimation of Spalling Stress in Thermal Barrier Coatings Using Hard Synchrotron X-Rays, Trans. Japan Soc. Mech. Eng. Ser. A. 47 (2004) 318–323. doi:10.1299/kikaia.70.724.

[191] K. Vaidyanathan, D. Pease, E.H. Jordan, H. Canistraro, M. Gell, T. Watkins, A Diffractometer for X-Ray Studies of TBC Bond Coats Beneath Zirconia Top Coats, Adv. X-Ray Anal. 45 (2002) 48–53.

[192] K. Knipe, A.C. Manero, S.F. Siddiqui, S. Sofronsky, P. Fouquet, C. Meid, J. Schneider, J. Okasinski, J. Almer, A.M. Karlsson, M. Bartsch, S. Raghavan, Synchrotron XRD Measurements of Thermal Barrier Coatings Subjected to Loads Representing Operational Conditions of Rotating Gas Turbine Blades, in: 52nd Aerosp. Sci. Meet., American Institute of Aeronautics and Astronautics, 2014.

[193] K. Knipe, A.C. Manero, S.F. Siddiqui, C. Meid, J. Wischek, J. Okasinski, J. Almer, A.M. Karlsson, M. Bartsch, S. Raghavan, Strain response of thermal barrier coatings captured under extreme engine environments through synchrotron X-ray diffraction., Nat. Commun. 5 (2014) 1–7. doi:10.1038/ncomms5559.

[194] R. Diaz, M. Jansz, M. Mossaddad, S. Raghavan, J. Okasinski, J. Almer, H. Pelaez-

Perez, P.K. Imbrie, Role of mechanical loads in inducing in-cycle tensile stress in thermally grown oxide, Appl. Phys. Lett. 100 (2012) 1–4. doi:10.1063/1.3692592.

[195] A.H. Heuer, A. Reddy, D.B. Hovis, B.W. Veal, A.P. Paulikas, A. Vlad, M. Rühle, The effect of surface orientation on oxidation-induced growth strains in single crystal NiAl: An in situ synchrotron study, Scr. Mater. 54 (2006) 1907–1912. doi:10.1016/j.scriptamat.2006.02.021.

[196] B.W. Veal, a. P. Paulikas, B. Gleeson, P.Y. Hou, Creep in α-Al2O3 thermally grown on β-NiAl and NiAlPt alloys, Surf. Coatings Technol. 202 (2007) 608–612. doi:10.1016/j.surfcoat.2007.05.093.

[197] M.P. Taylor, H.E. Evans, E.P. Busso, Z.Q. Qian, Creep properties of a Pt-aluminide coating, Acta Mater. 54 (2006) 3241–3252. doi:10.1016/j.actamat.2006.03.010.

[198] J. Laconte, D. Flandre, J.-P. Raskin, Thin dielectric films stress extraction, in: Micromachined Thin-Film Sensors for SOI-CMOS Co-Integration, Springer US, 2006: pp. 47–103. doi:10.1007/0-387-28843-0_3.

[199] G.C. Chang, W. Phucharoen, R. a. Miller, Behavior of thermal barrier coatings for advanced gas turbine blades, Surf. Coatings Technol. 30 (1987) 13–28. doi:10.1016/0257-8972(87)90004-1.

[200] J. Cheng, E.H. Jordan, B. Barber, M. Gell, Thermal/residual stress in an electron beam physical vapor deposited thermal barrier coating system, Acta Mater. 46 (1998) 5839–5850. doi:10.1016/S1359-6454(98)00230-4.

[201] S. Mayo, M. Josh, Y. Nesterets, L. Esteban, M. Pervukhina, M. Ben Clennell, A. Maksimenko, C. Hall, Quantitative micro-porosity characterization using synchrotron micro-CT and xenon K-edge subtraction in sandstones, carbonates, shales and coal, Fuel. 154 (2015) 167–173. doi:10.1016/j.fuel.2015.03.046.

[202] S. Krämer, J. Yang, C.G. Levi, C.A. Johnson, Thermochemical interaction of thermal barrier coatings with molten CaO-MgO-Al 2O 3-SiO 2 (CMAS) deposits, J. Am. Ceram. Soc. 89 (2006) 3167–3175. doi:10.1111/j.1551-2916.2006.01209.x.

[203] A. Germaneau, P. Doumalin, J.C. Dupré, Comparison between X-ray micro-computed tomography and optical scanning tomography for full 3D strain measurement by digital volume correlation, NDT E Int. 41 (2008) 407–415. doi:10.1016/j.ndteint.2008.04.001.